Spin Hall effect of light in transversally disordered media

Federico Carlini

SCIENCES SORBONNE UNIVERSITÉ

Laboratoire Kastler Brossel
Physique quantique et applications

THÈSE DE DOCTORAT DE SORBONNE UNIVERSITÉ

Spécialité : Physique

École doctorale nº 564 : Physique en Île-de-France

réalisée

au Laboratoire Kastler Brossel

sous la direction de Nicolas Cherroret

présentée par

Federico Carlini

pour obtenir le grade de :

DOCTEUR DE SORBONNE UNIVERSITÉ

Sujet de la thèse :

Spin Hall effect of light in transversally disordered media

soutenue le 13 février 2023

devant le jury composé de :

M.	Matthieu BELLEC	Examinateur
M.	Nicolas CHERRORET	Directeur de thèse
M^{me}	Agnès MAITRE	Présidente du jury
M.	Allard MOSK	Rapporteur
M.	Romain PIERRAT	Examinateur
M.	Bart VAN TIGGELEN	Rapporteur

Contents

General introduction

A medium is said to be "disordered" when it presents a complex spatial inhomogeneity of a certain parameter affecting the propagation of waves in the medium (e.g., the refractive index for electromagnetic waves). Examples of disordered materials are ubiquitous in nature: liquids with suspended particles like proteins in a glass of milk, biological tissues, classical or quantum gases like the atmosphere or cold atomic vapors, or solids with defects. All these media can be seen as composed of a large ensemble of scatterers with the waves propagating inside them undergoing a multiple scattering process. On average, waves entering a disordered medium propagate "ballistically" only up to a certain distance called the scattering mean free path. The corresponding ballistic portion of the signal, named coherent mode, gets depleted by the disorder as the wave penetrates deeper in the medium, with the multiple scattering component quickly becoming dominant at large optical thicknesses.

Wave propagation in disordered media typically generates, as a result of the process of multiple scattering, an apparently random distribution of the wave field, known as a speckle pattern. Naively, one could think that from such speckle patterns no interesting physics could be extracted. But, starting from the 70s, it was shown that at scales where the coherence of the propagating wave is preserved, the interference between scattered wavelets in the multiple scattering process could produce interesting and non-trivial phenomena. In the context of coherent transport of electrons in mesoscopic disordered conductors, a first example is the appearance of a small negative correction to the Drude conductivity, known as weak localization [1, 2]. In optics, another example is the enhancement of the average intensity in the exact backscattering direction for electromagnetic waves scattered from a disordered dielectric medium, known as coherent backscattering [3, 4]. Both phenomena turn out to stem from the constructive interference between reversed multiple scattering trajectories in the medium, the only difference being their respective global (for weak localization) and local (for coherent backscattering) character. Another interesting phenomenon arising for waves in disordered media is Anderson localization, which corresponds to the absence of diffusion at strong enough disorder, originating from the proliferation of destructive interference in the multiple scattering process [5, 6]. Interestingly, in three dimensions Anderson localization manifests itself as a phase transition, with the transport being diffusive below a certain disorder threshold, and localized above. In the regime where Anderson localization shows up, other relevant interference phenomena surviving disorder averaging can appear like, for example, the coherent forward scattering effect [7], the mesoscopic echo [8, 9] and the quantum boomerang effect [10, 11] that were discovered recently. Even in the diffusive regime, the speckle patterns themselves are generated by the interference between scattered waves and, as such, were shown to exhibit non-

trivial long-range temporal [12, 13] and spatial [14, 15] correlations, making them not as random as they seem.

Many mechanisms of wave propagation in a random medium, such as diffusion or the aforementioned wave interference effects, are shared by many types of waves, from quantum (e.g., electrons or cold atoms) to classical (e.g., sound and light) waves. Nevertheless, in practice the peculiar features of a given wave system can affect, sometimes drastically, the manifestation of these phenomena. The propagation of electromagnetic waves in disordered dielectric media is, in this respect, representative. Indeed, because in the course of the diffusion process pertained to multiple scattering light polarization is typically randomized after a few scattering events, it was for long time assumed that the polarization degree of freedom could be completely discarded in disordered media, and light propagation treated within a scalar approximation [16, 17]. While the scalar description brings a significant simplification in the theoretical computations, it turns out that light polarization can actually play a relevant role in photon transport in disorder. In this regard, Anderson localization in three dimensions provides a striking example. The latter was experimentally observed for electrons in disordered solids [18, 19, 20], for acoustic waves in random elastic networks [21, 22] and atomic waves in cold atoms immersed in a random potential [23, 24, 25]. First observations of three-dimensional Anderson localization of electromagnetic waves [26, 27] were, on the other hand, questioned due to the presence of absorption in the samples, effectively mimicking the effect of Anderson localization [28], and more recent time-resolved measurements [29, 30] also hampered by fluorescence [31]. In the end, even if it was initially thought that transport of photons in disordered media should constitute an ideal system for studying Anderson localization [32], to date an experimental demonstration of three-dimensional localization of light is still lacking. Interestingly, theoretical works have suggested that the reason for this lack could precisely reside in the peculiar vectorial nature of electromagnetic waves. Indeed, it was demonstrated numerically within a model of random ensemble of point scatterers, that the vector nature of light, specifically its near-field component, was preventing localization [33, 34, 35]. This constitutes an evocative theoretical example of the decisive impact that polarization can have on light propagation in a random medium. Generally speaking, the dependence of optical transport phenomena in disorder upon polarization can have two different origins. First, multiple scattering can be directly affected via the dependence of the single-scattering process on the polarization of light. The latter can originate, for example, from the anisotropic nature of the elementary scatterers (e.g., their shape) or from their internal structure (e.g., the quantum selection rules for atomic scatterers). Therefore, the incident light polarization, by fixing the relative weight of each single-scattering channel, can modify, for example, the mean free path characterizing the disorder. Second, polarization affects the properties of reciprocity of the system. For example, the phenomenon of coherent backscattering, which is related to the interference between time-reversed multiple scattering paths, strongly depends on polarization. In particular, the shape of the coherent backscattering, its contrast, and even its very existence are crucially dependent on the choice of the "polarization channel" in which the effect is detected [36, 37, 38, 39, 40, 41, 42]. Among other effects where the vector nature of electromagnetic waves is relevant, one may also cite the photon Hall effect [43], the memory of rotation of incident polarization [44] and the polarization structure of

spatial and temporal correlations in the speckle patterns [45, 46, 47].

Beyond the context of disordered materials, another fundamental mechanism related to the vector nature of light is known to occur for electromagnetic waves in inhomogeneous media: spin-orbit interactions (SOI) of light, which corresponds to a coupling between the spatial and polarization degrees of freedom of the optical wavefront [48]. This phenomenon, well known in photonics, constitutes an optical analogue of the spin-orbit interactions affecting electrons in condensed matter, where the light helicity plays the role of the electron spin. An important manifestation of SOI is the optical spin Hall effect (SHE), which refers to an helicity dependent sub-wavelength lateral shift of the trajectory of circularly polarized beams, in analogy with its electronic counterpart [49]. In simple geometries, the spin Hall effect is today understood in terms of geometric phases and angular momentum conservation [50], and it has been experimentally observed mainly at optical interfaces [51, 52] and in smoothly inhomogeneous dielectric media [53]. Generally speaking, the SHE and SOI phenomena typically occur at sub-wavelength scales. However, the rapid development of nano-optics, photonics and plasmonics have made the wavelength-scale processes crucially important for the manipulation and control of light. In particular, in the last years the SHE of light has sparked significant interest in these communities due to its promising applications in the control of light at the nanoscale [54, 55].

In the context of disordered media, the concept of spin-orbit interactions of light remained unexplored until recently. Investigating spin-orbit physics in disordered media constitutes *per se* an interesting fundamental question, but it could also lead to some potential applications. Indeed, recent progresses in wave control and imaging have shown the great potential of treating disorder as a tool rather than as a nuisance in general [56, 57, 58, 59, 60, 61]. With spin-orbit interactions, it is on paper possible to some extent control the wave trajectory via the polarization. Whether this idea could be pushed to the realm of wave control in disordered media is still an open but interesting question. A first evidence of spin-orbit interactions of light surviving disorder averaging was theoretically predicted in 2019 [62]. Within a simple model, the existence of an optical spin Hall effect affecting the coherent mode in transversally disordered media was demonstrated. Transversally disordered optical media are three-dimensional media characterized by spatial fluctuations in the refractive index in two directions only, the medium being homogeneous along the third dimension. The concept of transverse disorder [63] and its experimental implementation was originally driven with profit by the search of transverse (2D) Anderson localization of light [64]. Generally speaking, light propagation in transversally disordered media is typically described within the paraxial approximation, which is a scalar approximation of the Helmholtz equation. The phenomenon of SOI, however, precisely involves polarization corrections to the paraxial solution, which require the development of a proper vectorial treatment of light scattering [42, 62, 65, 66].

The goals of this thesis are (i) to further investigate theoretically the phenomenon of spin Hall effect in transversally disordered media, employing realistic disorder models, (ii) to find out a realistic disorder configuration where the optical spin Hall effect could be experimentally observable, and (iii) to explore signatures of SOI in multiple scattering. Specifically, the thesis is organized as follows. In chapter 1, a brief overview of the phenomenon of spin-orbit interactions of light and their role in producing a spin

Hall effect of light in inhomogeneous media is given. In chapter 2, we introduce the problem of light propagation in disordered media, focusing on the case of transverse disorder. In this chapter we also introduce the theoretical tools specific to disordered systems within the relatively simple framework of the paraxial approximation, and derive a few relevant results which constitute a benchmark for the following chapters. In the rest of the thesis, by employing a vectorial, i.e., beyond-paraxial, description of light propagation, we explore the effect of spin-orbit interactions of light in two kinds of transversally disordered media. The first one is a model of correlated, continuous disorder model which we study in chapter 3. There we demonstrate the existence of a novel, oscillating spin Hall effect of light affecting the coherent mode, tunable via the disorder correlation length and the polarization of the incident beam [67]. In chapter 4, we study a second model of transverse disorder: a random photonic array of tubes, in which we demonstrate the existence of a resonant spin Hall effect, tunable via the incident laser frequency and *a priori* observable experimentally [68]. Last, in chapter 5, we develop a vectorial treatment of multiple scattering of light in transversally disordered media. This allows us to demonstrate the existence of a spin Hall effect of light not only in the coherent mode, but also in the multiple scattering signal as well. Additional information and technical details are finally collected in 6 appendices.

A large fraction of results presented in this thesis has been collected in the following papers:

- F. Carlini and N. Cherroret. Tailoring propagation of light via spin-orbit interactions in correlated disorder. Phys. Rev. A, 105:053508, 2022.

- F. Carlini and N. Cherroret. Resonant Spin Hall Effect of Light in Random Photonic Arrays, https://arxiv.org/abs/2210.16379, 2022 (accepted for publication in SciPost Physics).

Chapter 1

Spin Hall effect of light in inhomogeneous media

In this chapter, we introduce the spin Hall effect of light, a sub-wavelength optical phenomenon appearing in inhomogeneous dielectric media which constitutes an optical analogue to the standard spin Hall effect of electrons in conductors. In the following, we highlight its physical origin, namely the spin-orbit interactions of light, and its geometrical nature, i.e., its description in term of a Berry phase. We end the chapter with two recent experimental measurements, and finally introduce the concept in the context of random media.

1.1 Hall effects for electrons

1.1.1 Ordinary Hall effect

Edwin Hall discovered in 1879 [69] that the passage of an electric current $\boldsymbol{j}_{\text{el}}$ through a planar electronic conductor, to which an external magnetic field $\boldsymbol{B}_{\text{ext}}$ perpendicular to the conductor plane is applied, is accompanied by the production of a voltage difference transverse to both the electric current and the applied magnetic field.

The explanation of such phenomenon is simple. A charge in motion immersed in a magnetic field is subjected to the Lorentz force ($\boldsymbol{F} = q\boldsymbol{v} \times \boldsymbol{B}_{\text{ext}}$), whose action generates a transverse current $\boldsymbol{j}_H$. Such current is responsible for a transverse voltage difference, which appears as a result of the accumulation of charges having an opposite sign on the lateral boundaries of the conductor.

The Hall effect not only proved to be relevant for a certain number of applications [70], but it also paved the way to the discovery of numerous related phenomena, such as the anomalous Hall effect [71], the integer and fractional quantum Hall effects [72, 73, 74], and the spin Hall effect.

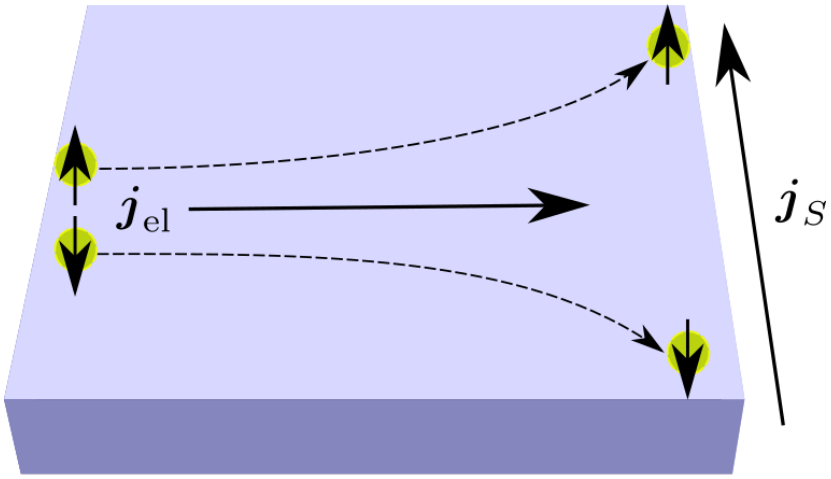

Figure 1.1: Schematic representation of the spin Hall effect for electrons.

1.1.2 Spin Hall effect

The spin Hall effect (SHE) was first predicted by Dyakonov and Perel in 1971 [75], but it was only in 1999 with a paper by Hirsch [76] that the phenomenon acquired the deserved attention. The setup is similar to the one of the ordinary Hall effect, i.e., an electric current $\boldsymbol{j}_{\mathrm{el}}$ flows through a thin conductive plate, but with the difference that this time no external magnetic field is present. The spin Hall effect corresponds to the emergence of a transverse spin current $\boldsymbol{j}_S$, which leads to the accumulation of electron spins on the lateral surfaces of the electric current-carrying sample, with electrons at opposing boundaries having opposite spins (see Fig. 1.1).

This peculiar transport phenomenon originates from the presence of spin-orbit interactions (SOI) [77]. SOI is a type of physical interaction that couples the spin of a particle with its trajectory, causing spatial and internal degrees of freedom to influence each other. Spin-orbit interactions can have an extrinsic nature, as originally discussed by Dyakonov and Perel, where carriers with opposite spin scatter in opposite directions when colliding with impurities in the material (spin-dependent Mott scattering [78]); but they can also originate as a consequence of certain asymmetries in the material and, hence, constitute an intrinsic property of the material itself [79, 80, 81]. The phenomenon of SHE was first detected by optical means in both the extrinsic [82] and the intrinsic regime [83] (see Fig. 1.2).

Theoretically, the phenomenon can be easily captured within a semi-classical approach starting from the simple Hamiltonian [84]:

$$H = \frac{\boldsymbol{p}^2}{2m} + qV(\boldsymbol{r}) + \mathcal{A}_{\text{s-o}} \left[\boldsymbol{p} \times \boldsymbol{\nabla} V(\boldsymbol{r})\right] \cdot \boldsymbol{S} \,, \tag{1.1}$$

where any form of electron-electron interaction is neglected and $\mathcal{A}_{\text{s-o}}$ is the spin-orbit coefficient whose value depends on the material under examination. m and q are, respectively, the electron mass and charge, $V(\boldsymbol{r})$ and $\boldsymbol{S}$ are, respectively, the electric potential and the spin of electrons (the latter being treated as a classical momentum).

Assuming a uniform electric potential gradient, from (1.1) one derives the following

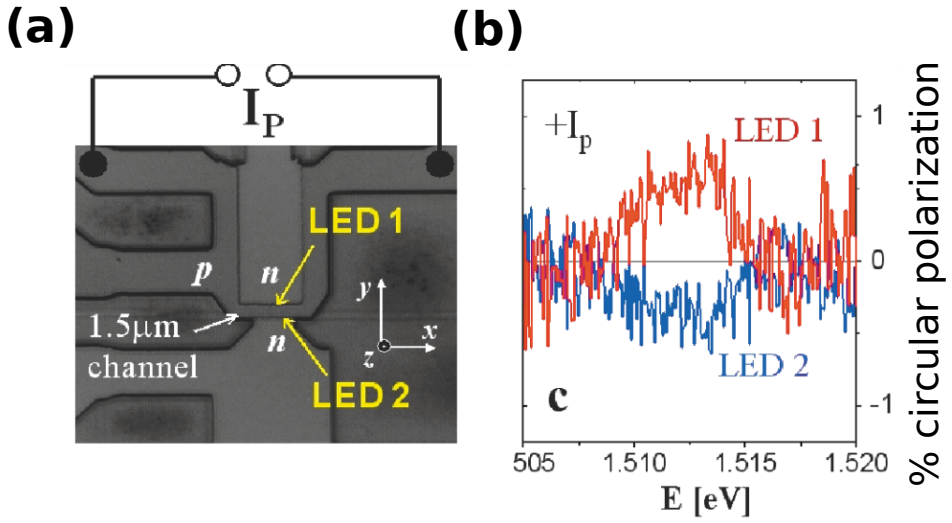

Figure 1.2: Observation of the spin Hall effect in a spin-orbit coupled semiconductor. Figures taken from [83]. (a) The sample. Scanning electron microscopy image of the device. The top (LED 1) or bottom (LED 2) n contacts are used to measure the electroluminescence at opposite edges of the 2D hole gas ("p-channel") parallel to the driving current. (b) The measurement. Polarization along z axis measured for LED 1 and LED 2. Opposite polarizations at opposite edges of the 2D hole gas channel are observed, demonstrating the spin Hall effect for electrons.

Hamilton equations:

$$\begin{cases} \dfrac{d\boldsymbol{r}}{dt} = \dfrac{\boldsymbol{p}}{m} + \mathcal{A}_{\text{s-o}} \left[\boldsymbol{\nabla} V(\boldsymbol{r}) \times \boldsymbol{S} \right] \\ \dfrac{d\boldsymbol{p}}{dt} = -q \boldsymbol{\nabla} V(\boldsymbol{r}) \ . \end{cases} \tag{1.2}$$

The term $\mathcal{A}_{\text{s-o}} \left[\boldsymbol{\nabla} V(\boldsymbol{r}) \times \boldsymbol{S} \right]$, coming from the spin-orbit interaction term of the Hamiltonian (1.1), is responsible for a shift of the electron trajectories orthogonal to the electric potential gradient, with its direction only depending on the value of the electron spin. Spin up and down are deviated in opposite directions, explaining the accumulation of spin on the lateral surfaces.

Nowadays, the spin Hall effect has been experimentally measured in numerous configurations [84] and has acquired a great interest due to the possibility of exploiting it to create and control spin currents. Indeed, the generation, manipulation, and detection of spin currents constitutes some key aspects of spintronics, a field which exploits both the spin and charge degrees of freedom with the aim of controlling devices and properties of materials [85].

1.2 Spin-orbit interactions of light

1.2.1 Maxwell's equations

Light consists of electromagnetic waves which propagate through space carrying electromagnetic energy. It is described by Maxwell's equations, which are a set of equations governing the evolution of the electric $\boldsymbol{E}(\boldsymbol{r},t)$ and magnetic $\boldsymbol{B}(\boldsymbol{r},t)$ vector fields. Remarkably, Maxwell theory constitutes an *ante litteram* relativistic, quantum theory [1] and, as Planck said during the commemoration of 100th anniversary of Maxwell's birth [87], "remains for all time one of the greatest triumphs of intellectual endeavor". The Maxwell's equations for a dielectric (non-magnetic) medium read [88]:

$$\boldsymbol{\nabla}\cdot\boldsymbol{D}(\boldsymbol{r},t)=0 \tag{1.3a}$$
$$\boldsymbol{\nabla}\cdot\boldsymbol{B}(\boldsymbol{r},t)=0 \tag{1.3b}$$
$$\boldsymbol{\nabla}\times\boldsymbol{E}(\boldsymbol{r},t)=-\partial_t\boldsymbol{B}(\boldsymbol{r},t) \tag{1.3c}$$
$$\boldsymbol{\nabla}\times\boldsymbol{B}(\boldsymbol{r},t)=\mu_0\partial_t\boldsymbol{D}(\boldsymbol{r},t)\ , \tag{1.3d}$$

where μ_0 is the vacuum permeability and $\boldsymbol{D}(\boldsymbol{r},t)$ is the electric displacement or electric induction field, which accounts for the electric field interaction with the dielectric medium. Assuming a local and instantaneous medium response, $\boldsymbol{D}(\boldsymbol{r},t)$ is related to the electric field as follows:

$$\boldsymbol{D}(\boldsymbol{r},t)=\epsilon_0\boldsymbol{E}(\boldsymbol{r},t)+\epsilon_0\boldsymbol{\chi}(\boldsymbol{r},t)\boldsymbol{E}(\boldsymbol{r},t)\ , \tag{1.4}$$

where ϵ_0 is the vacuum permittivity and $\boldsymbol{\chi}(\boldsymbol{r},t)$ is the electric susceptibility tensor of the dielectric medium. The second term in Eq. (1.4), given by the contraction between the electric susceptibility tensor and the electric field, is called dielectric polarization and defines the medium's response to the applied electric field.

In the following, we will consider linear (i.e., the electric susceptibility does not depend on the applied electric field), scalar (i.e., the response does not depend on the direction of the wave propagation direction) and time-independent media. Under these hypotheses, Eq. (1.4) reduces to

$$\boldsymbol{D}(\boldsymbol{r},t)=\epsilon_0\epsilon(\boldsymbol{r})\boldsymbol{E}(\boldsymbol{r},t)\ , \tag{1.5}$$

which is known in the literature as the dielectric constitutive relation, where $\epsilon(\boldsymbol{r})=1+\chi(\boldsymbol{r})$ is the relative permittivity of the medium.

1.2.2 Helmholtz equation

We now focus on the evolution of the electric field since, once known, the evolution of the magnetic field can be deduced straightforwardly from Eq. (1.3c). Introducing the temporal Fourier transform of the electric field $\boldsymbol{E}(\boldsymbol{r},t)$ as

$$\boldsymbol{E}(\boldsymbol{r},t)=\int_{-\infty}^{\infty}\frac{d\omega}{2\pi}\boldsymbol{E}(\boldsymbol{r},\omega)e^{-i\omega t}\ , \tag{1.6}$$

[1] Although it is of course a classical theory, after a second quantization procedure, Maxwell's equations give the correct Dirac equation used in quantum optics [86].

and combining the two Maxwell's equations (1.3c) and (1.3d), one obtains the following wave equation governing the spatial evolution of the Fourier components $\boldsymbol{E}(\boldsymbol{r},\omega)$:

$$\left[\Delta + \frac{\omega^2}{c^2}\epsilon(\boldsymbol{r})\right]\boldsymbol{E}(\boldsymbol{r},\omega) - \boldsymbol{\nabla}[\boldsymbol{\nabla}\cdot\boldsymbol{E}(\boldsymbol{r},\omega)] = 0\ , \tag{1.7}$$

where $c = 1/\sqrt{\epsilon_0\mu_0}$ is the vacuum speed of light. Eq. (1.7) is called the vector Helmholtz equation and, as the name suggests, it describes light propagation taking fully into account its vectorial nature. Making use of Maxwell's equation (1.3a), one can rewrite the vector Helmholtz equation in the following form:

$$\left[\Delta + \frac{\omega^2}{c^2}\epsilon(\boldsymbol{r})\right]\boldsymbol{E}(\boldsymbol{r},\omega) + \boldsymbol{\nabla}[\boldsymbol{\nabla}\ln\epsilon(\boldsymbol{r})\cdot\boldsymbol{E}(\boldsymbol{r},\omega)] = 0\ . \tag{1.8}$$

The last term in the left-hand side couples the components of the electric field $\boldsymbol{E}$, namely the light polarization, with the spatial degree of freedom $\boldsymbol{\nabla}\ln\epsilon(\boldsymbol{r})$, which governs the trajectory of light in the material. This precisely shows how intrinsic SOI of light fundamentally originate from Maxwell's equations, and are thus naturally present in all basic optical processes involving inhomogeneous media. However, akin to the Planck constant smallness that controls electron spin-orbit coupling, SOI of light arise at a scale of the order of a fraction of the wavelength, which is typically small compared with macroscopic scales. Nevertheless, SOI of light turn out to play a crucial role in modern optics where, with the miniaturization of optical devices and the need for high-precision performances, they attract a lot of attention in the nanophotonics community [48, 54, 55].

SOI of light manifest under various phenomena in both simple optical elements, like planar interfaces, lenses, anisotropic plates, waveguides and small particles, and complex nano-structures, like photonic crystals, metamaterials and plasmonics structures. Among them, a phenomenon plays a special role: the so-called spin Hall effect of light. As we will show in the following, this phenomenon consists in a transverse, spin-dependent sub-wavelength shift of light analogous to the spin Hall effect for electrons.

1.3 Geometrical optics in inhomogeneous media

Typically, SOI of light give rise to sub-wavelength effects. Therefore, in numerous situations, it is customary to neglect the "SOI term" in Eq. (1.8). The three components of the electric field, hence, decouple and obey the scalar Helmholtz equation:

$$\left[\Delta + \frac{\omega^2}{c^2}\epsilon(\boldsymbol{r})\right]\mathcal{E}(\boldsymbol{r},\omega) = 0\ , \tag{1.9}$$

where $\mathcal{E}$ here refers to a generic component of the field $\boldsymbol{E}$. Eq. (1.9) constitutes the starting point of scalar wave optics in inhomogeneous media.

In the following we show that, by performing an eikonal approximation of Eq. (1.9), one can derive the ray equation which constitutes the core of geometrical optics. The latter is a branch of optics which describes light propagation by means of rays, neglecting any form of spin-orbit interaction, diffraction and interference. Mathematically,

geometrical optics is given by the zero-order approximation with respect to the wavelength in vacuum $\lambda_v = 2\pi/k_v = 2\pi\omega/c$ (i.e., $\lambda_v \to 0$). It is able to properly describe in a simple fashion light phenomena occurring at a macroscopic scale, i.e., at spacial scales much larger than λ_v.

Putting the following Ansatz for the electric field:

$$\mathcal{E}(\boldsymbol{r},t) = \mathcal{E}_0(\boldsymbol{r}) \exp\big[-i(\omega t - k_v S(\boldsymbol{r}))\big] \ , \tag{1.10}$$

where $\mathcal{E}_0(\boldsymbol{r})$ varies weakly over the wavelength scale λ_v, and the function $S(\boldsymbol{r})$ is known as the eikonal function, into the scalar Helmholtz equation (1.9), we find [89]

$$\begin{cases} k^{-2}\Delta\mathcal{E}_0 - \mathcal{E}_0(\boldsymbol{\nabla}S)^2 + \epsilon\mathcal{E}_0 = 0 & \text{(1.11a)} \\ 2(\boldsymbol{\nabla}S\cdot\boldsymbol{\nabla})\mathcal{E}_0 - \mathcal{E}_0\Delta S = 0 \ . & \text{(1.11b)} \end{cases}$$

Within geometrical optics, the term $k^{-2}\Delta\mathcal{E}_0$ in Eq. (1.11a), being proportional to λ_v^2, is neglected. Eq. (1.11a) thus becomes

$$(\boldsymbol{\nabla}S)^2 = n(\boldsymbol{r})^2 \tag{1.12}$$

with $n(\boldsymbol{r}) = \sqrt{\epsilon(\boldsymbol{r})}$ the medium refractive index profile. Eq. (1.12), known as the eikonal equation, constitutes the fundamental equation of geometrical optics, and can be rewritten as

$$\boldsymbol{\nabla}S = n(\boldsymbol{r})\boldsymbol{t} \ . \tag{1.13}$$

Integrating Eq. (1.13) over a scale small compared to λ_v, i.e. a spatial scale where the refractive index is approximately constant, and substituting the result in Eq. (1.10), one realizes that $\boldsymbol{t}$ is the local unit vector normal to the local wavefront and thus gives the local propagation direction of light. The light rays are field lines along which the electromagnetic energy flows. Mathematically, a light ray is described by the position vector field $\boldsymbol{r}(l)$, where l is the curvilinear abscissa that parameterizes the ray. By definition, the unit vector $\boldsymbol{t} = d\boldsymbol{r}/dl$ is tangent to the ray at each point $\boldsymbol{r}(l)$. By simply differentiating Eq. (1.13), one derives the ray equation [89, 90]:

$$\frac{d}{dl}\left(n(\boldsymbol{r})\frac{d\boldsymbol{r}}{dl}\right) = \boldsymbol{\nabla}n(\boldsymbol{r}) \ , \tag{1.14}$$

which correctly describes the macroscopic ray trajectories followed by light passing through inhomogeneous media. From Eq. (1.14), the laws of geometrical optics, such as the well-known Snell-Descartes law [91], follow and, given $n(\boldsymbol{r})$, any ray trajectory can be determined. Note that the same equation can be derived within an Hamiltonian formalism based on the following "geometrical optics" Hamiltonian [89]:

$$\mathcal{H}_{GO}(\boldsymbol{r},\boldsymbol{p}) = \frac{1}{2}\left[\boldsymbol{p}^2 - n^2(\boldsymbol{r})\right] \ , \tag{1.15}$$

where $\boldsymbol{p} = \boldsymbol{\nabla}S = \boldsymbol{k}/k_v$ is the dimensionless wave vector. From Eq. (1.15), we obtain the following equations of motion:

$$\begin{cases} \dfrac{d\boldsymbol{r}}{dl} = \dfrac{\boldsymbol{p}}{n} \\ \dfrac{d\boldsymbol{p}}{dl} = \boldsymbol{\nabla}n(\boldsymbol{r}) \ , \end{cases} \tag{1.16}$$

where the relation $p = dl/(cdt) = n$ was used. Eq.s (1.16) also lead to (1.14), and elucidate the simplest effect a dielectric inhomogeneity, i.e. $\boldsymbol{\nabla} n(\boldsymbol{r}) \neq 0$, has on light propagation: a deviation of the optical wave vector, i.e., of the ray trajectory.

1.4 Beyond geometrical optics: spin-orbit interactions

Even in a simple optical phenomenon such as light impinging on an interface, as soon as one considers optical beams having a finite width, geometrical optics fails to capture a variety of shifts affecting both the reflected and transmitted beams occurring at the wavelength scale [92]. Such shifts, first observed for total internal reflection [93, 94], are generally associated with two distinct fundamental effects. The first, known under the name of Goos–Hänchen effect, consists of a spacial shift in the plane of incidence involving linearly polarized light. As shown by Artmann in 1948 [95], it originates from the dispersion of the reflection and transmission coefficients associated with the different Fourier components of the incident beam. The other effect, called in the literature Imbert–Fedorov effect, involves instead an out-of-plane displacement existing for elliptically-polarized beams only. Even though, similarly to the Goos–Hänchen effect, Fedorov and Imbert originally explained the Imbert–Fedorov effect with Poynting energy-flow arguments [94, 96], with Schilling in 1965 being the first to relate the effect to plane-wave decomposition and interference inside the beams [97], it was only later that the deeper, more sophisticated origin of the Imbert–Fedorov effect was revealed. Indeed, around 1987, Player and Fedoseyev showed the intimate relation between the Imbert–Fedorov shift and the balance and conservation of the total angular momentum of light, including the intrinsic spin angular momentum associated with circularly polarized light [98, 99]. In 1992, finally, Liberman and Zel'dovich traced the phenomenon back to spin–orbit interactions of light [100].

While the Imbert–Fedorov effect takes place at optical interfaces, similar phenomena have been theoretically predicted and experimentally observed in smoothly inhomogeneous media, i.e., optical media where the condition $\lambda|\boldsymbol{\nabla} n|/n \ll 1$ holds true [101] (on the contrary, $\boldsymbol{\nabla} n$ strictly speaking diverges at the interface between two homogeneous dielectric media). While propagating in such materials, optical beams progressively exhibit a displacement in a direction transverse to the optical wave vector. Such an effect was originally dubbed "optical Magnus effect" because it can be seen as the optical analogue of the Magnus effect [102], a displacement phenomenon associated with spinning objects moving through fluids as a result of a pressure gradient. Likewise, circularly-polarized light is described by a rotating electric field and, as it propagates in a refractive-index gradient, it undergoes a transverse shift. However, the fundamental origin of the optical Magnus effect lies in spin–orbit interactions of light. Indeed, as stated in the original paper [101], the optical Magnus effect, where the light polarization degree of freedom affects the beam trajectory, can be framed as the "inverse" of the Rytov-Vladimirski rotation, a rotation of the polarization plane acquired by electromagnetic waves in smoothly inhomogeneous media and related to the change of the wave-vector direction -namely the optical trajectory- affecting the polarization [103, 104]. Furthermore, the Imbert–Fedorov effect and the optical Magnus effect can

be directly connected by considering a smoothly inhomogeneous medium as composed of the superimposition of multiple interfaces having slightly different refractive indices, highlighting their common origin, the spin-orbit interactions of light [100].

The optical Magnus effect can be theoretically described within a "semi-classical" approach, where one constructs a modified geometrical-optics theory that takes into account the leading-order ($\propto k_v^{-1}$) vectorial correction corresponding to spin-orbit coupling. The adjective semi-classical here comes from the fact that such a modified geometrical-optics approach constitutes an optical analogue of the semi-classical description of topological spin transport in condensed matter [105, 106, 107]: in the optical domain, discrete spin projections are replaced by right-handed and left-handed circularly-polarized waves and the Planck constant $\hbar$ is replaced by k_v^{-1}. Within this description, the following equations of motion for the light rays are obtained [50, 53, 100]

$$\begin{cases} \dfrac{d\boldsymbol{r}}{dl} = \dfrac{\boldsymbol{p}}{n} + \dfrac{\sigma}{k_v}\dfrac{\boldsymbol{\nabla} n \times \boldsymbol{p}}{p^3} \\ \dfrac{d\boldsymbol{p}}{dl} = \boldsymbol{\nabla} n(\boldsymbol{r}) \ , \end{cases} \tag{1.17}$$

where $\sigma = \pm 1$ is the helicity of right-handed (left-handed) photons, respectively. These equations correctly describe the optical Magnus effect. Comparing with the standard geometrical-optics result (1.16), we notice here the appearance of the extra term $\propto \sigma/k_v$ in the equation governing the evolution of the position of the ray. Such a term couples the photon "spin" $\sigma\boldsymbol{p}/p$ with the refractive index gradient $\boldsymbol{\nabla} n$. Interestingly, Eq.s (1.17) are completely analogous to Eq.s (1.2) that describe the spin Hall effect for electrons: the refractive-index gradient plays the role of the electric-potential gradient, while the helicity plays the role of the electron spin. For this reason, the optical Magnus effect is today dubbed "spin Hall effect of light". Note that, strictly speaking, Eq.s (1.17) can only be applied when the refractive index varies slowly at the wavelength scale. Nevertheless, it was shown that they are able to reproduce the correct shift of light transmitted through sharp interfaces as well, because of the conservation of the total angular momentum [50]. Hence, nowadays both the Imbert–Fedorov and the optical Magnus effects are seen as similar manifestations of the spin Hall effect of light [49].

1.5 Berry phase

At a fundamental level, the spin Hall effect of light in inhomogeneous media is currently understood in term of a geometric phase [108]. The latter consists in a phase factor of geometrical origin acquired by the electric field over a cyclic adiabatic evolution of the system affecting the dynamics of observables. This phenomenon, first pointed out by Pancharatnam in the optical domain [109], was later generalized and formalized in the context of quantum mechanics by Berry [110]. Geometric phases, nowadays referred to as Berry phases, constitute an ubiquitous concept in both classical and quantum physics. The concept of Berry phase was also extended to acyclic, non-adiabatic and non-Hermitian processes [111, 112].

In optics, the geometric phase originates from the coupling between local coordinates rotations, i.e., wave-vector variations, and the optical spin. Indeed, in free space or weakly inhomogeneous media, light is described by transverse waves, implying that the polarization depends on the direction of the wave vector. A cyclic light process can be pictured as a closed curve lying on the surface of unit sphere $\boldsymbol{p}/p$. The light polarization vector, tangent by definition to this sphere, follows a parallel transport along this curve, inevitably acquiring a rotation with respect to the original polarization vector. Such a geometrical rotation is associated with the accumulation of a Berry phase diagonal in the basis of circular polarizations. Decomposing the transverse field in such basis ($\boldsymbol{E} = \boldsymbol{E}^{+}\boldsymbol{e}^{+} + \boldsymbol{E}^{-}\boldsymbol{e}^{-}$), the Berry phase Φ_B is defined as [113]:

$$\begin{cases} \Phi_B = \sigma \int_C \boldsymbol{A}(\boldsymbol{p}) \cdot d\boldsymbol{p} \\ \boldsymbol{A}(\boldsymbol{p}) = -ie_i^{-}\boldsymbol{\nabla}_{\boldsymbol{p}} e_i^{+} \ , \end{cases} \tag{1.18}$$

where C represents the considered closed path taking place in the unit sphere, $\sigma = \pm 1$ stands here for the helicity eigenvalues and $\boldsymbol{A}(\boldsymbol{p})$ is known as the Berry connection. The latter describes the infinitesimal parallel transport process of light polarization vector $\boldsymbol{E}$, performed between the points $\boldsymbol{p}$ and $\boldsymbol{p} + d\boldsymbol{p}$ in momentum space. The Berry curvature associated with the Berry connection is given by

$$\boldsymbol{F}(\boldsymbol{p}) = \boldsymbol{\nabla}_{\boldsymbol{p}} \times \boldsymbol{A}(\boldsymbol{p}) = \frac{\boldsymbol{p}}{p^3} \ . \tag{1.19}$$

The Berry curvature, contrary to the Berry connection, is gauge invariant. Hence, $\boldsymbol{F}(\boldsymbol{p})$ is the geometrical object entering the evolution of all physical quantities, independent of the coordinate system. Looking at Eq. (1.19), it is evident that, despite their geometric nature, the Berry connection and Berry curvature can be effectively seen, respectively, as a vector potential and a magnetic field, with the helicity playing the role of the electric charge and the Berry phase generating a topological monopole in momentum space. This analogy highlights the existing connection between the Berry phase and the famous Aharonov-Bohm effect [114, 115]. It also enables us to naturally construct an Hamiltonian formalism where the vector potential $\boldsymbol{A}(\boldsymbol{p})$ coming from the Berry phase enters directly [116, 117]:

$$\mathcal{H}_B(\boldsymbol{r}, \boldsymbol{p}) = \frac{1}{2}\left[\boldsymbol{p}^2 - n^2(\boldsymbol{r} - \sigma k_v^{-1}\boldsymbol{A}(\boldsymbol{p}))\right] \ , \tag{1.20}$$

from which, remarkably, one recovers Eq.s (1.17). This highlights the geometric nature of the SOI correction term appearing in Eq.s (1.17), which in term of the Berry curvature is rewritten as $\sigma k_v^{-1}\left[d\boldsymbol{p}/dl \times \boldsymbol{F}(\boldsymbol{p})\right]$. Remarkably, the Berry approach also allows to derive an evolution equation for the light polarization, which in the geometrical-optics framework is neglected, obtaining

$$\frac{d\boldsymbol{e}^{\pm}}{dl} = -i\sigma\left[\frac{d\boldsymbol{p}}{dl} \cdot \boldsymbol{A}(\boldsymbol{p})\right]\boldsymbol{e}^{\pm} \ . \tag{1.21}$$

Eq. (1.21) describes the different geometrical rotations that the components $\boldsymbol{e}^{\pm}$ undergo during the parallel transport process.

1.6 Spin Hall effect of light: examples

1.6.1 At optical interfaces

The simplest configuration where a SHE of light takes place is at an optical interface. Let θ_I be the angle between the normal to the interface, directed along the z axis, and the momentum of the incident beam, lying in the (x, z) plane. The beam, being of finite size, is composed of multiple Fourier components with slightly different wave vectors $\boldsymbol{k}$. Thus, despite the average wave vector component along y of the incident beam is zero ($\langle k_y \rangle = 0$), in general each Fourier component of the incident beam has a tiny finite k_y. During the reflection and/or transmission occurring at the interface, a rotation of the wave vectors occurs, inducing a geometric phase whose value depends on k_y. In the simplest case of total reflection, one has the formation of a Berry phase $\Phi_B = \sigma k_y \cot\theta_I$, whose k_y-gradient generates an out-of-plane beam shift along y equals to:

$$\delta^R = -\frac{\sigma + \sigma'}{k} \cot\theta_I \ , \tag{1.22}$$

where σ' is the helicity of the reflected beam. This constitutes the Berry-phase explanation of the Imbert–Fedorov effect [50]. The effect was first experimentally measured by Imbert in 1972 in the case of total reflection, who actually used successive reflections to amplify the shift [96].

Much later, in 2008, the spin Hall effect of light at an interface was experimentally measured by Hosten and Kwiat [51] in transmission, using an optical analogue of the quantum weak-measurement technique (see Sec. 3.9.1). The shift in transmission, which depends on the incident polarization due to the polarization-dependence of the Fresnel reflections at the interface, is given by:

$$\begin{aligned} \delta^H &= \frac{\sigma}{k} \frac{\cos\theta_T - (t_s/t_p)\cos\theta_I}{\sin\theta_I} \\ \delta^V &= \frac{\sigma}{k} \frac{\cos\theta_T - (t_p/t_s)\cos\theta_I}{\sin\theta_I} \ , \end{aligned} \tag{1.23}$$

where H and V stand for horizontal (TM) and vertical (TE) incident light polarizations, θ_I and θ_T are, respectively, the central incident and transmitted angles related by Snell's law, and t_s and t_p are the Fresnel transmission coefficients. The experimental measurement performed for an air-glass interface is reported in Fig. 1.3.

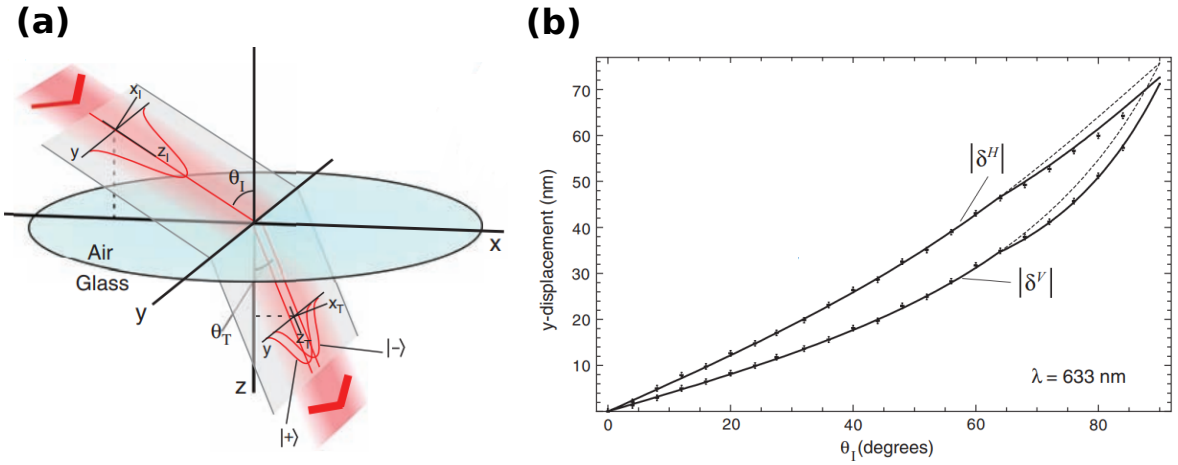

Figure 1.3: (a) Experimental measurement of the spin Hall effect of light taking place during the refraction process at an air-glass interface. In panel (b), the two different displacement curves show clearly the polarization dependence of the effect. Figures taken from [51].

1.6.2 In smoothly inhomogeneous media

In the context of smoothly inhomogeneous media, a remarkable example highlighting the interplay between the Berry phase and the spin Hall effect of light is light propagation along an helical trajectory in a cylindrically-symmetric medium, i.e., having a refractive index depending solely on the cylindrical radial coordinate r. A helical trajectory is uniquely characterized by its radius R in the transverse plane and the angle θ between its tangent vector and the cylindrical axis z, satisfying the relation $\sin^2\theta = -R\partial_r n(r)|_{r=R}/n(R)$ coming from geometrical optics. In the unit sphere $\boldsymbol{k}/k$, it is described by the closed circular path with fixed polar angle θ. The Berry phase accumulated during a helix period, i.e., a ray length $l = 2\pi R/\sin\theta$, is $\Phi_B = -2\pi\sigma\cos\theta$. Such a geometric phase is responsible for a shift transverse to both the refractive-index gradient and the axis z given by:

$$\Delta = -\frac{2\pi\sigma\sin\phi}{k}N\ , \tag{1.24}$$

where N is the number of helical turns performed by light before detection. Such shift, resulting in a splitting between right-handed and left-handed circularly polarized light, has been experimentally observed in helical light beams propagating at a grazing angle inside a glass cylinder [53], see Fig. 1.4a. The expression of the shift (1.24), as well as the Berry phase formalism of Sec. 1.5, actually assumes isotropy and, hence, conservation of helicity during the evolution. The isotropy approximation is not satisfied in total reflection in glass cylinder, where a phase difference occurs between the p and s linearly-polarized modes reflected from the surface. Once the effect on the transverse shift of such linear birefringence is taken into account, the theory very well captures the experimental results, see Fig. 1.4b.

Note that a similar manifestation of the Berry phase in optical helical trajectories was also observed in an early experience [118] using a single-mode, helically wound

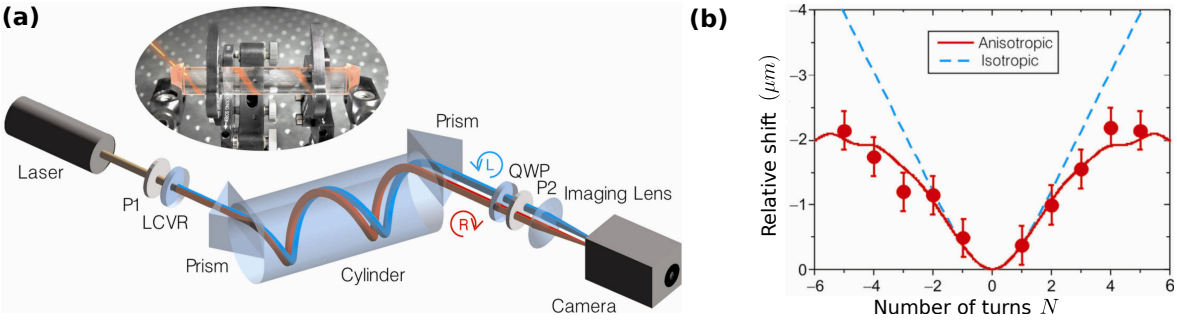

Figure 1.4: (a) Experimental setup for the observation of spin Hall effect of light at a glass cylinder surface. The upper inset shows a real picture of the spiral light beam inside the cylinder. (b) The measured relative shift between the output beam positions of $\sigma = 1$ and $\sigma = -1$ light (red dots) as a function of the number of helical turns. The solid red curve is the theory prediction taking into account the effect of the material anisotropy on the displacement, while the dashed blue line represents the theory prediction within the isotropic approximation, see Eq.(1.24). Figures taken from [53].

optical fiber.

1.7 Spin Hall effect of light in random media

So far, we have discussed the spin Hall effect of light in the context of "simple" inhomogeneous optical geometries such as optical interfaces or smoothly inhomogeneous media. Recently, however, the concept of spin Hall effect of light has been extended to disordered optical systems as well. In [62], a spin Hall effect of light affecting the "coherent mode" of light (see next chapter) propagating in a transversally disordered system has been theoretically predicted (see Fig. 1.5). Upon impinging on a dielectric material disordered in the (x, y) plane with a tilt angle θ with respect to the z axis, it has been shown that a beam acquires a lateral shift $R_y(z)$ as it evolves within the material at a distance z from the interface. This shift was found to be given by

$$R_y(z) = -\frac{\sigma}{k_0}\left(1 - \frac{1}{\cosh z/2z_S}\right) , \tag{1.25}$$

where $k_0 = k \sin\theta$ is the projection of the incident wave vector on the interface, σ is the helicity of the incident beam and z_S is a characteristic longitudinal length over which the phenomenon occurs.

This result was obtained starting from first principles, i.e., from a direct resolution of the vector Helmholtz equation. This approach will also be the one used throughout the thesis, where we will revisit this problem by considering more sophisticated disorder models or computing R_y in more complicated scenarios. The coherent mode, as will be seen in the following chapters, is indeed typically a wave phenomenon, originating from the interference between the initial beam and the light scattered from the spatial disorder in the forward direction. This makes a geometrical-optics-like formulation of

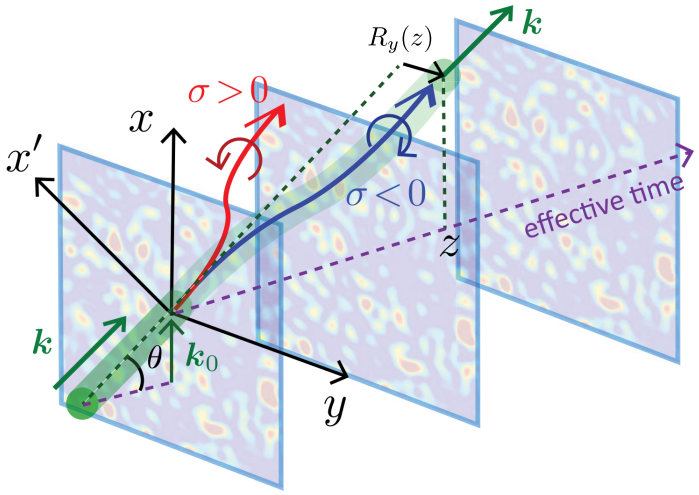

Figure 1.5: The centroid of the coherent mode, generated from the light propagation of a tilted collimated beam in a transversally disordered medium, undergoes a lateral shift R_y. Such a shift, proportional to the beam helicity σ, can be seen as a spin Hall effect of light. Figure taken from [62].

the spin Hall effect of the type of Eq. (1.25) a priori inadequate, although the same mechanism of SOI is at play.

1.8 Conclusion

In this introductory chapter, we have briefly reviewed the physical origin, the history and the theoretical description of the spin Hall effect of light in inhomogeneous media. In the thesis, we will address this physics in the context of transversally disordered media where a similar effect was recently predicted. Before exploring this problem, however, we will start by recalling a few elements about light propagation in such materials.

Chapter 2

Light propagation in transversally disordered media

The physics on which this thesis focuses concerns light propagation in transversally disordered -or (2+1)-dimensional- dielectric media beyond the paraxial approximation. In this chapter, we will describe general properties of wave transport in this geometry, staying at the paraxial level. In detail, after general considerations on light scattering in disordered media, we will introduce the paraxial approximation and the paraxial wave equation, which effectively describes light propagation in (2+1)-dimensional media, and discuss a few experimental examples with and without disorder. Then, we will apply the general theoretical tools used to describe transport in disordered media to the specific case of transverse disorder within the paraxial approximation. These results will serve as a basis for the physics of spin-orbit interactions of light discussed in the next chapters, which typically involves vectorial corrections beyond the paraxial framework.

2.1 Light propagation in disordered media

2.1.1 Disorder in dielectric media

In the previous chapter, we discussed several examples where light propagates in dielectric structures in which the spatial variations of the permittivity are known and controlled. In the real world, however, one often does not have the exact knowledge of the microscopic structure of many materials. Among them, media characterized by complex spatial inhomogeneities where the refractive index profile appears to be more or less random at the sample's scale are referred to as disordered dielectric media.

In optics, examples of disordered media are semiconductor powders, biological tissues, classical gases like the atmosphere, quantum gases like clouds of ultracold atoms, and even liquids with suspended particles. The distinction between "controlled" inhomogeneous media, where the permittivity variations can be modeled through a simple profile, and disordered media, is important because, even if in both cases at the fundamental level the same underlying physics occurs (typically, light is deviated by the dielectric inhomogeneities), the observed macroscopic physical phenomena as well as the theoretical tools used to describe them are significantly different. One can sum-

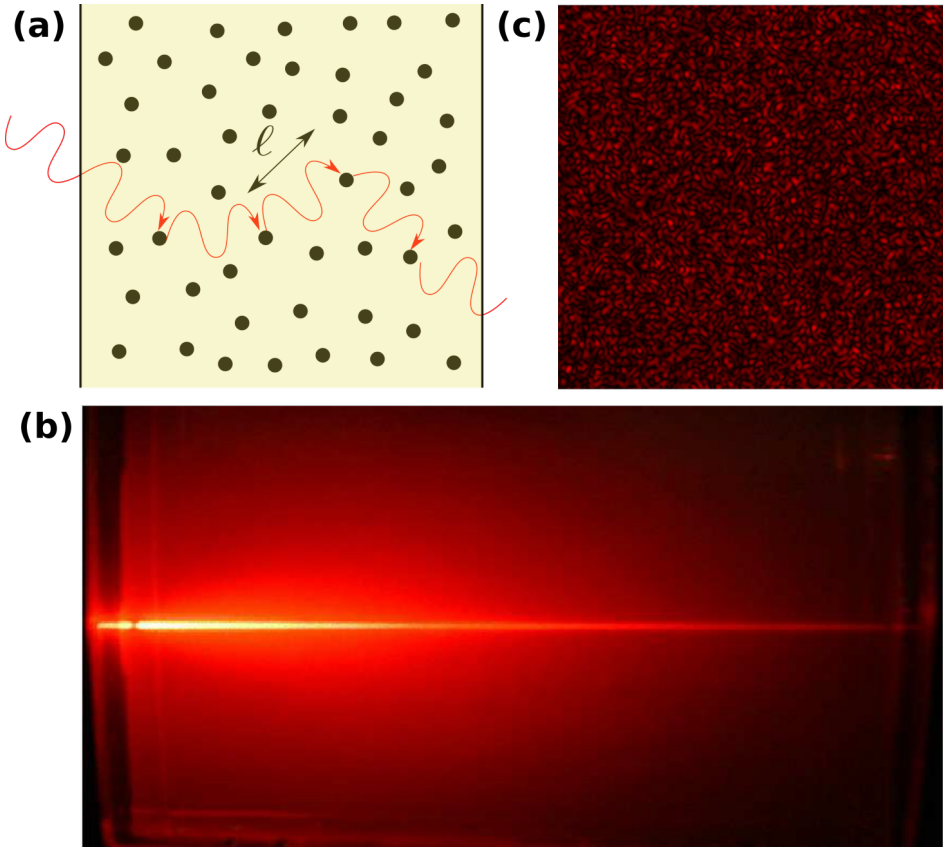

Figure 2.1: (a) Scheme of multiple light scattering through a discrete ensemble of scatterers (ℓ is the mean free path). (b) Picture of light propagating inside a disordered medium, more precisely a laser beam in a glass of milk. The coherent beam is well visible, with its intensity getting attenuated as a diffusive halo emerges all around. (c) Example of speckle pattern observed at the output of an optically-thick medium ($L \gg \ell$).

marize this with the celebrated Anderson's statement "More is different" [119]. In the case of disordered media, an original physics especially stems from the interference developed by a wave as it propagates through a large ensemble of scattering objects [61]. This physics, incidentally, goes beyond the field of optics and covers a large variety of disordered systems such as electron transport in dirty metals or semiconductors [120, 121, 122, 123], or cold atoms in random potentials [124].

2.1.2 A qualitative description

Imagine a coherent beam of light, e.g. a laser, impinging on a disordered dielectric medium. The latter can be viewed as a set of scatterers randomly distributed in space, from which the light gets scattered (see Fig. 2.1a). As the beam penetrates inside the medium, light propagates in a straight line until it comes across a scatterer and gets deviated. The average distance over which a photon propagates without being scattered is called the scattering mean free path. It is usually denoted by ℓ and represents a first key parameter which characterizes a disordered medium. The deeper light propagates

inside the medium, the more probable it gets scattered. As a result, the intensity of the portion of light propagating ballistically attenuates with the distance. This portion is called the "coherent mode". At a macroscopic level, it manifests itself as an exponential decay of the laser intensity along the forward direction (see Fig. 2.1b). The light depleted from the coherent mode undergoes a multiple scattering process. If one measures the light transmitted through a medium of size L much greater than the mean free path ($L \gg \ell$), only these scattered photons contribute to the detection and one only observes an apparently random distribution of bright and dark area called a speckle pattern (see Fig. 2.1c). The speckle pattern constitutes a sort of fingerprint of the disordered medium and originates from the interference between optical waves scattered in all directions [125]. Mathematically, the intensity at a given point is the sum of many complex amplitudes associated to the light waves arriving at the point after having followed a certain multiple scattering trajectory.

At weak enough disorder, precisely when the wavelength $\lambda = 2\pi/k$ is much smaller than ℓ, the multiply scattered light can be described, at large scale, by a diffusive process with diffusion coefficient D. If a short pulse is sent through the medium at $t = 0$ and light is collected in transmission at a later time t, this process manifests itself as a halo of width $\sim \sqrt{Dt}$. The diffusive description is in general a good approximation, except in cases one is interested in fine details of light scattering taking place at the scale of the mean free path. Special care then has to be taken to treat such short scales. This question will be especially important in this thesis. A second case where the diffusive description breaks down is in strongly scattering media, where $k\ell$ is not very large. In this limit, interference corrections to diffusion must be accounted for. Those include a variety of phenomena such as coherent backscattering [3, 4, 40, 126] or Anderson localization [5, 6, 127]. Coherent backscattering (CBS) corresponds to an enhancement of the probability of photons to be backscattered by the medium due to constructive interference between paths travelled in opposite directions in the disorder. Anderson localization, on the other hand, is a multi-wave interference phenomenon which typically occurs at strong disorder ($k\ell \sim 1$). In three dimensions, it manifest itself as a phase transition triggered by the proliferation of destructive interference between scattering paths and occurring below a certain critical value of $k\ell$ [128]. This leads to the total inhibition of diffusive propagation, with D vanishing at the transition point.

We have here given a qualitative description of what happens when light propagates through a disordered medium. At a theoretical level, the complex problem of multiple scattering is usually treated within a statistical perspective where the disorder is modeled by a random function. Transport through the disorder is then characterized by computing statistical averages of observables using dedicated theoretical tools that were developed and refined during the second half of the last century. The averaging is performed over the set of all different microscopic realizations of the medium disorder which share the same statistical features.

2.2 Light propagation in (2+1)-dimensional media

Generally speaking, in physics the symmetry and the dimension of a system can strongly affect its physical properties. Disordered systems are no exception. As we will show in this thesis, an example of this is the phenomenon of spin-orbit interactions of light, which show up in transversally disordered dielectric media but are averaged out if one considers a standard three-dimensional isotropic disorder.

In this section, we will introduce the paraxial approximation and the notion of (2+1)-dimensional dielectric medium. We will then review some relatively recent experiments exploiting the (2+1)-dimensional geometry (both without and with disorder), within the framework of the paraxial wave equation.

2.2.1 Paraxial approximation

Light beams weakly deviating from a fixed propagation direction defining an optical axis are effectively well described by the paraxial wave equation. This equation comes from the application of the paraxial approximation to the Helmholtz equation. It is equivalent to a slowly-varying envelope approximation, and usually holds as long as the Fourier components $\boldsymbol{k}$ of the light beam make a small angle with the optical axis. It is customary to choose the coordinate system such that the optical axis coincides with the Cartesian axis $\hat{\boldsymbol{z}}$.

While, in this thesis, we will precisely explore the deviations from paraxial propagation in a disordered medium, it is instructive to recall the physics expected at the paraxial level. To this aim, in this chapter we apply the paraxial approximation to the Helmholtz equation and derive the corresponding paraxial wave equation in materials whose permittivity profile $\epsilon(\boldsymbol{r})$ is homogeneous along the optical axis $\hat{\boldsymbol{z}}$, but varies in the transverse plane $\boldsymbol{r}_\perp = (x, y)$, i.e.,

$$\epsilon(\boldsymbol{r}) = \epsilon(\boldsymbol{r}_\perp) = \overline{\epsilon} + \delta\epsilon(\boldsymbol{r}_\perp) \, . \tag{2.1}$$

Here $\overline{\epsilon}$ is the homogeneous component of the permittivity and $\delta\epsilon(\boldsymbol{r}_\perp)$ is its spatially-varying part. For a reason that will appear more clearly below, materials satisfying Eq. (2.1) are referred to as (2+1)-dimensional.

To obtain the paraxial wave equation, we express the electric field as

$$\boldsymbol{E}(\boldsymbol{r}_\perp, z) = \boldsymbol{\mathcal{E}}(\boldsymbol{r}_\perp, z) e^{ikz} \, , \tag{2.2}$$

where $k = \sqrt{\overline{\epsilon}}\omega/c$ is the wavenumber in the homogeneous background. Using the first of the Maxwell's equations (1.3a), the Helmholtz equation (1.7) yields for the envelope $\boldsymbol{\mathcal{E}} = (\boldsymbol{\mathcal{E}}_\perp, \boldsymbol{\mathcal{E}}_z)$ [129]:

$$\begin{cases} \Delta_\perp \boldsymbol{\mathcal{E}}_\perp + \partial_z^2 \boldsymbol{\mathcal{E}}_\perp + 2ik\partial_z \boldsymbol{\mathcal{E}}_\perp + \boldsymbol{\nabla}_\perp [\boldsymbol{\nabla}_\perp \ln \epsilon(\boldsymbol{r}_\perp) \cdot \boldsymbol{\mathcal{E}}_\perp] + ik\boldsymbol{\nabla}_\perp \mathcal{E}_z + \dfrac{\omega^2}{c^2} \delta\epsilon(\boldsymbol{r}_\perp) \boldsymbol{\mathcal{E}}_\perp = 0 & \text{(2.3a)} \\ \Delta_\perp \mathcal{E}_z - \partial_z (\boldsymbol{\nabla}_\perp \cdot \boldsymbol{\mathcal{E}}_\perp) - ik\boldsymbol{\nabla}_\perp \cdot \boldsymbol{\mathcal{E}}_\perp + \dfrac{\omega^2}{c^2} [1 + \delta\epsilon(\boldsymbol{r}_\perp)] \mathcal{E}_z = 0 \, . & \text{(2.3b)} \end{cases}$$

At this stage, we assume that the envelope $\boldsymbol{\mathcal{E}}$ varies sufficiently slowly at wavelength scale. This condition imposes

$$|\partial_z^2 \boldsymbol{\mathcal{E}}| \ll k |\partial_z \boldsymbol{\mathcal{E}}| \text{ and } \frac{2\pi}{k} \left| \frac{\boldsymbol{\nabla}_\perp \epsilon(\boldsymbol{r}_\perp)}{\overline{\epsilon}} \right| \ll 1 \tag{2.4}$$

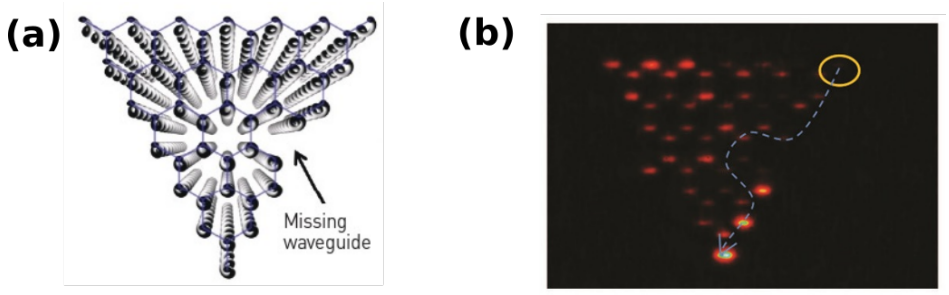

Figure 2.2: (a) Honeycomb array of waveguides with a missing waveguide at the edge simulating a defect. (b) Observation of photonic topological protection in this array. The yellow circle indicates the waveguide where light is injected. Injected light moves clockwise and avoids the defect. Backscattering is suppressed due to topological protection (figures taken from [131]).

to hold true. Under these circumstances, the envelope $\boldsymbol{\mathcal{E}}$ is mostly transverse, i.e., $\mathcal{E}_z \ll |\boldsymbol{\mathcal{E}}_\perp|$. Within the paraxial approximation, the longitudinal component $\mathcal{E}_z$ of the electric field is completely neglected and Eq. (2.3a) leads to the paraxial wave equation [130] for the transverse envelope $\boldsymbol{\mathcal{E}}_\perp$:

$$2ik\partial_z \boldsymbol{\mathcal{E}}_\perp = -\Delta_\perp \boldsymbol{\mathcal{E}}_\perp - \frac{\omega^2}{c^2}\delta\epsilon(\boldsymbol{r}_\perp)\boldsymbol{\mathcal{E}}_\perp \, . \tag{2.5}$$

Since Eq. (2.5) is diagonal, all components of $\boldsymbol{\mathcal{E}}_\perp$ behave equivalently and the propagation problem reduces to that of a single, scalar component that we will denote by $\mathcal{E}$ in the following.

Interestingly, the paraxial wave equation has the same form as the time-dependent Schrödinger equation describing a quantum particle in two dimensions. Once the longitudinal coordinate z is mapped into the time variable t, the two equations have indeed the same structure, with the terms $-\Delta_\perp \boldsymbol{\mathcal{E}}_\perp/(2k)$ and $-\omega\delta\epsilon(\boldsymbol{r}_\perp)\boldsymbol{\mathcal{E}}_\perp/(2c\sqrt{\bar{\epsilon}})$ in the paraxial wave equation corresponding, respectively, to the kinetic and potential terms in the Schrödinger equation. This analogy justifies the expression (2+1)-dimensional system, the third coordinate z playing the role of an effective time.

2.2.2 Examples

Since its initial development to describe laser propagation [132], the paraxial approximation had quite a success history mainly due to its analogy with the Schrödinger equation. In particular, it was largely used to reproduce with light many interesting phenomena of condensed-matter or of quantum gases. In the following, we give a few relevant examples of those.

The first one concerns topological insulators, which represent a fundamentally new phase of matter characterized by a phenomenon of topologically-protected electron conduction mediated by edge states in certain 2D systems [133]. Topological protection means a total absence of scattering by disorder, providing a robustness that is otherwise known for superconductors only. This concept was brought to the photonics domain successfully for the first time after theoretical efforts proposing to exploit the analogy

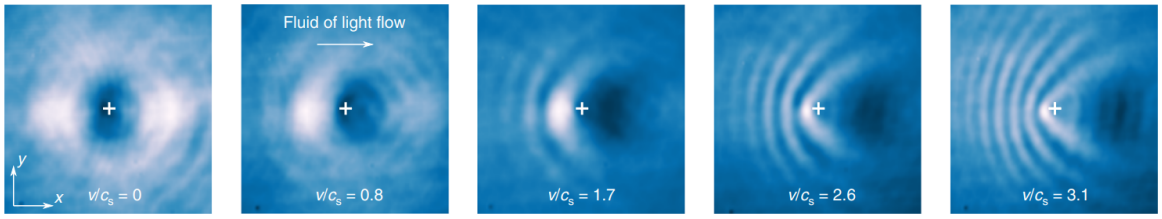

Figure 2.3: Superfluid transition occuring in light propagating inside a Kerr medium, observed in [140]. Pictures show the spatial distribution of light intensity at the output of the Kerr medium for different fluid velocities v at fixed speed of sound c_s. The "fluid of light" flows from left to right. The white cross at the center indicates the position of the obstacle.

between the paraxial wave equation and the Schrödinger equation [134]. The realization of the first photonic topological insulator was theoretically proposed and experimentally demonstrated in [135] using helical waveguides arranged as in a honeycomb lattice (see Fig. 2.2a). By making the waveguides helical along $\hat{\boldsymbol{z}}$, the z-reciprocity is broken and scattering-free edge states appear, enabling light transport around corners without backscattering and light travelling around defects without disruption (see Fig. 2.2b). Given the periodical structure of the material along z, with z playing the role of an effective time, these systems were named photonic Floquet topological insulators.

Another interesting platform where the paraxial wave equation is routinely applied are non-linear Kerr materials (or $\chi^{(3)}$ materials) for which $\delta\epsilon(\boldsymbol{r}_\perp) \propto |\mathcal{E}(\boldsymbol{r}_\perp)|^2$ [136]. In such systems, the paraxial wave equation becomes formally equivalent to the Gross-Pitaevskii equation that governs weakly-interacting Bose-Einstein condensates [137]. This analogy has been recently exploited to experimentally realize optical analogues of quantum fluids phenomena such as interaction-driven thermalization, Bose-Einstein condensation [138, 139] or superfluidity [140] (see Fig. 2.3).

(2+1)-dimensional optical media gained also interest in the context of disorder physics. In [63], the notion of transverse disorder was first introduced. Transversally disordered optical media are characterized by spatial fluctuations of the refractive index taking place in two directions only, the media being homogeneous along the third direction, as described by Eq. (2.12). Such configuration was proposed in [63] in order to facilitate the observation of Anderson localization of light. Indeed, in strictly 2D disordered media, localization is expected to occur at a spatial scale given by the localization length $\xi \sim \ell \exp\big(\pi k\ell/2\big)$, where ℓ is the mean free path and k the optical wave number [141]. Such scale is in general huge since typically $k\ell \gg 1$ in most materials, making the observation of Anderson localization difficult. In the (2+1) disorder geometry, however, this issue can be overcome since, in this case, the wave number entering the expression of the localization length is replaced by the transverse wave number $k \sin\theta$, easily controlled via the angle of incidence θ. Such configuration was first implemented in [64], demonstrating transverse localization of light in a photo-refractive crystal on which a (2+1)-dimensional random refractive index distribution was imprinted with writing beams. Transverse localization of light [142] was also observed in [143] in a photo-refractive material, as well as in disordered optical fibers

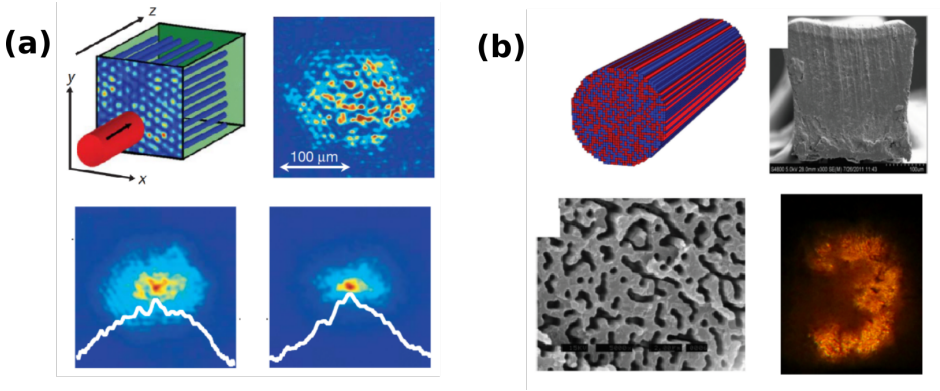

Figure 2.4: (a) Photo-refractive disordered material of dimension (2+1). A narrow incident beam at $z = 0$ undergoes a spreading in the plane (x, y). At sufficiently strong disorder values, 2D Anderson localization is observed in the transverse plane (figures taken from [64]). (b) Transversally disordered optical fiber. An ensemble of points constituting an image of the number "3" are transported along the fiber thanks to the phenomenon of transverse Anderson localization (figures taken from [150]).

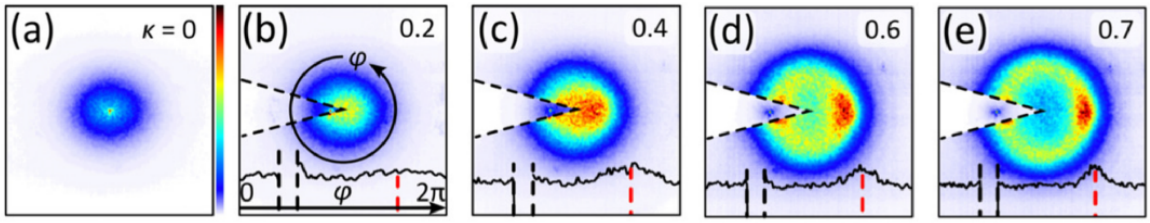

Figure 2.5: Far-field momentum distribution, $|E(\boldsymbol{k}_\perp)|^2$, observed experimentally in [151] at the output of a (2+1) disordered photo-refractive medium. For a tilted incident beam, a diffusive ring together with a coherent backscattering peak (indicated by the red dashed vertical line) becomes visible as a result of scattering in the transverse plane.

in [144]. By using transversally disordered optical fibers, optical image transport using transverse Anderson localization of light was demonstrated in the visible [145, 146], near-infrared [147, 148], and mid-infrared region [149].

A last experimental example exploiting the transverse disorder is the observation of coherent backscattering. If a tilted collimated beam is let evolve through transverse disorder, the transverse projection of its wave vector is randomized due to multiple scattering in the plane (x, y). The optical distribution $|E(\boldsymbol{k}_\perp)|^2$ measured in transmission in the far field then exhibits a diffusive ring with a CBS peak on the top of it. As experimentally observed in [151], both the diffusive ring and the CBS peak become clearly visible at nonzero incident angle. Note that this type of experiment is in direct analogy with measurements of CBS with cold atoms performed in 2012 [152, 153, 154].

2.3 Paraxial propagation in transversally disordered media: coherent mode

2.3.1 Free paraxial propagator

To describe light propagation in a linear medium, a very convenient mathematical tool is the Green's function. Indeed, it allows to simplify the resolution of inhomogeneous, scalar boundary value problems, and to easily compute the electromagnetic fields produced by arbitrary distributions of charges or currents [155]. Green's functions also play a crucial role when it comes to the statistical description of disordered optical media, because it allows to directly apply the perturbation approaches well-known in the context of condensed-matter physics [156].

Let us first introduce the Green's function for the problem of light scattering in an homogeneous medium of permittivity $\bar{\epsilon}$. For paraxial light, the Green's function follows from the paraxial wave equation for the field envelope:

$$i\partial_z \mathcal{E} = -\frac{1}{2k}\Delta_\perp^2 \mathcal{E} \tag{2.6}$$

with $k = \sqrt{\bar{\epsilon}}\omega/c$. The Green's function $G^{(0)}$ is defined as the solution of the equation

$$\left(i\partial_z + \frac{1}{2k}\Delta_\perp\right) G^{(0)}(\boldsymbol{r}_\perp, z) = \delta(\boldsymbol{r}_\perp)\delta(z) \ . \tag{2.7}$$

By introducing the Fourier transform $G^{(0)}(\boldsymbol{k}_\perp, k_z)$, such that

$$G^{(0)}(\boldsymbol{r}_\perp, z) = \int \frac{d^2\boldsymbol{k}_\perp}{(2\pi)^2} \int \frac{dk_z}{2\pi} G^{(0)}(\boldsymbol{k}_\perp, k_z) e^{i(\boldsymbol{k}_\perp \cdot \boldsymbol{r}_\perp - k_z z)} \ , \tag{2.8}$$

we infer that $G^{(0)}(\boldsymbol{k}_\perp, k_z)$ is solution of

$$\hat{\tilde{L}} G^{(0)}(\boldsymbol{k}_\perp, k_z) = 1 \ , \tag{2.9}$$

where $\hat{\tilde{L}} = k_z - \boldsymbol{k}_\perp^2/2k$ is the operator in Fourier space associated with the paraxial wave equation (2.6). The free paraxial propagator in Fourier space then reads

$$G^{(0)}(\boldsymbol{k}_\perp, k_z) = \frac{1}{k_z - \boldsymbol{k}_\perp^2/2k + i0^+} \ , \tag{2.10}$$

where a positive infinitesimal imaginary part in the denominator has been added in order to make the propagator describe an evolution toward positive times, thus consistent with the causality requirement. This type of Green's function is called retarded Green's function in the literature. Correspondingly, the description of propagation toward negative times is obtained by considering the complex conjugate of Eq. (2.10), which defines the "advanced" Green's function, $G^{(0)*}(\boldsymbol{k}_\perp, k_z)$.

2.3.2 Statistical disorder model

Let us now consider light propagation in the presence of transverse disorder in the plane $\boldsymbol{r}_\perp = (x, y)$. Such transversally dielectric disordered medium is naturally described by a permittivity profile of the form of Eq. (2.1), i.e.,

$$\epsilon(\boldsymbol{r}_\perp) = \overline{\epsilon} + \delta\epsilon(\boldsymbol{r}_\perp) \ , \tag{2.11}$$

where $\overline{\epsilon}$ is an homogeneous background and $\delta\epsilon(\boldsymbol{r}_\perp)$ is modeled by a random function with zero mean: $\langle\delta\epsilon(\boldsymbol{r}_\perp)\rangle = 0$ where $\langle ...\rangle$ stands for averaging over disorder realizations. Therefore, $\overline{\epsilon} = \langle\epsilon\rangle$ defines the average (background) permittivity of the medium.

As an input of the theory, we need to specify the statistical properties of $\delta\epsilon(\boldsymbol{r}_\perp)$. To make things simple, here we assume that $\delta\epsilon(\boldsymbol{r}_\perp)$ is drawn from a a normalized Gaussian probability distribution. We then have only one non-zero cumulant. Precisely, the only relevant statistical quantity describing our disordered medium is the two-point correlation function of the disorder fluctuations:

$$B(\boldsymbol{r}_\perp - \boldsymbol{r}'_\perp) = \frac{\langle\delta\epsilon(\boldsymbol{r}_\perp)\delta\epsilon(\boldsymbol{r}'_\perp)\rangle}{\overline{\epsilon}^2} \ . \tag{2.12}$$

In the case of statistically isotropic disorder that will be considered throughout the thesis, the two-point correlation function only depends on $|\boldsymbol{r}_\perp - \boldsymbol{r}'_\perp|$. The function $B(|\boldsymbol{r}_\perp - \boldsymbol{r}'_\perp|)$ decays over a characteristic length scale known as the disorder correlation length, denoted by σ_d in the following.

2.3.3 Dyson equation and self-energy

The paraxial wave equation for a transversally disordered dielectric medium reads

$$i\partial_z\mathcal{E} = -\frac{1}{2k}\Delta_\perp^2\mathcal{E} + V(\boldsymbol{r}_\perp)\mathcal{E} \ , \tag{2.13}$$

where $V(\boldsymbol{r}_\perp) = -k\delta\epsilon(\boldsymbol{r}_\perp)/2\overline{\epsilon}$. Eq. (2.13) is analogous to a Schrödinger equation describing the temporal evolution of a quantum particle subjected to a potential $V(\boldsymbol{r}_\perp)$. Because V only depends on $\boldsymbol{r}_\perp$, the ensuing multiple scattering process takes place in the transverse plane $\boldsymbol{r}_\perp = (x, y)$ only (recall that z plays the role of an effective time).

The Green's function associated with Eq. (2.13) obeys

$$\left(\hat{L} - V\right) G(\boldsymbol{r}_\perp, z) = \delta(\boldsymbol{r}_\perp)\delta(z) \ , \tag{2.14}$$

where $\hat{L} = i\partial_z + \Delta_\perp^2/2k$ is the differential operator associated with Eq. (2.6). The Green's function in the presence of disorder then appears to be linked to the free propagator $G^{(0)}$ by the recursive relation

$$G = G^{(0)} + G^{(0)}VG \ . \tag{2.15}$$

Such recursive relation can be reformulated as a multiple-scattering expansion:

$$G = G^{(0)} + G^{(0)}VG^{(0)} + G^{(0)}VG^{(0)}VG^{(0)} + ... \ . \tag{2.16}$$

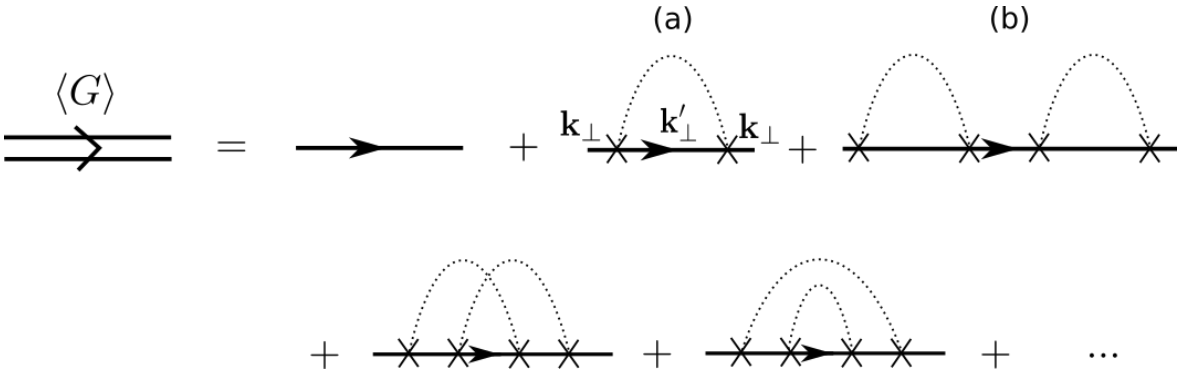

Figure 2.6: Diagrammatic representation of the disorder average of the Born series (2.16). The only irreducible diagram taken into account within the Born approximation is diagram (a). Diagram (b) is an example of reducible diagram, automatically accounted for when Σ is approximated by diagram (a).

As explained above, we wish to study the impact of disorder on light transport on statistical grounds and not at the level of a single, specific disorder realization. An important quantity, from this respect, is the Green's function averaged over disorder realizations. The latter, indeed, precisely describes the evolution of the coherent mode, which constitutes one of the main figures of merit of the thesis. We are then interested not in the disordered paraxial Green's function itself but on its average over an ensemble of disorder realizations. After disorder averaging, Eq. (2.16) simplifies a lot. For Gaussian disorder, the only non-zero contributions stem from second-order disorder pairings $\langle VV \rangle$, with all terms having odd power in V being identically zero. Still, all even terms remain to be dealt with. A convenient way to address this problem is to use a diagrammatic representation. In such diagrammatic theory, solid (dashed) lines with an arrow pointing the direction of propagation stands for retarded (advanced) free Green's functions $G^{(0)}[G^{(0)*}]$, while the crosses stand for scattering events on the disorder potential V and dotted lines for impurity pairings $\langle VV \rangle$. Then, out of all diagrams corresponding to all possible pairings one can distinguish the irreducible diagrams, which are not separable without cutting an impurity line, and the reducible ones, see Fig. 2.6b. Upon averaging, the Dyson equation (2.16) can then be formally written as [16]

$$\langle G \rangle = G^{(0)} + G^{(0)} \Sigma \langle G \rangle \ , \tag{2.17}$$

where Σ, called in literature self-energy, is by definition the infinite sum of all irreducible diagrams. Once an expression for Σ is found, the disorder-average paraxial Green's function follows from

$$\langle G \rangle = \left[G^{(0)-1} - \Sigma \right]^{-1} . \tag{2.18}$$

In this formulation, the knowledge of the average Green's function thus reduces to the calculation of Σ. This calculation, in general, can only be achieved using approximations. The simplest one, the Born approximation, is discussed in the next section.

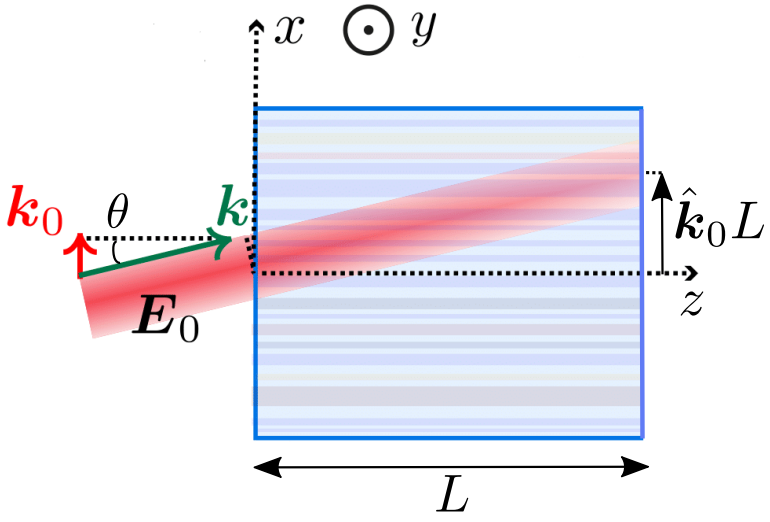

Figure 2.7: A collimated beam impinges on a transversally disordered medium with an angle θ with respect to the axis z. The relevant wave vector involved in scattering is the transverse projection $\boldsymbol{k}_0$ of $\boldsymbol{k}$.

2.3.4 Properties of the paraxial coherent mode at the Born approximation

In the transverse-disorder geometry, the scattering processes take place in the transverse plane (x, y). If a collimated beam impinges on the medium with an angle θ with respect to the axis $\hat{\boldsymbol{z}}$, the relevant wave number involved in scattering is the transverse projection $k_0 = k \sin\theta$ of k in the plane (x, y) (see Fig. 2.7). Introducing the mean free path ℓ in the transverse plane, we are led to define the weak-disorder condition as $k_0\ell \gg 1$. In such a regime, the correlations between successive scattering events become negligible. To compute Σ, it is then sufficient to take into account only the lowest-order irreducible diagram, diagram (a) in Fig. 2.6. This is known as the Born approximation, and it amounts to describing propagation as a succession of independent scattering events. Mathematically, using the Born approximation means neglecting corrections of the order $1/k_0\ell$ and higher to Σ. Within the Born approximation, the self-energy in momentum space $\Sigma(\boldsymbol{k}_\perp, k_z)$ is given by [16]

$$\Sigma(\boldsymbol{k}_\perp, k_z) = \frac{k^2}{4} \int \frac{d^2\boldsymbol{k}'_\perp}{(2\pi)^2} B(\boldsymbol{k}_\perp - \boldsymbol{k}'_\perp) G(\boldsymbol{k}'_\perp, k_z) \;, \tag{2.19}$$

where $B(\boldsymbol{k}_\perp - \boldsymbol{k}'_\perp) = \int d^2(\boldsymbol{r}_\perp - \boldsymbol{r}'_\perp) B(\boldsymbol{r}_\perp - \boldsymbol{r}'_\perp) e^{-i(\boldsymbol{k}_\perp - \boldsymbol{k}'_\perp)\cdot(\boldsymbol{r}_\perp - \boldsymbol{r}'_\perp)}$ is the Fourier transform of the two-point correlation function of the disorder fluctuations defined in Eq. (2.12). Note that, in Eq. (2.19), only the integral over the transverse wave vector $\boldsymbol{k}'_\perp$ appears. Indeed, because the system is homogeneous along $\hat{\boldsymbol{z}}$, in accordance with Noether's theorem [157] the longitudinal Fourier component k_z is conserved in the multiple scattering process.

The simplest way to compute the self-energy is to consider uncorrelated permittivity fluctuations, corresponding to a two-point disorder correlator with zero correlation

length, i.e., having the following form:

$$B(\boldsymbol{r}_\perp - \boldsymbol{r}'_\perp) = \gamma\delta(\boldsymbol{r}_\perp - \boldsymbol{r}'_\perp) \,, \tag{2.20}$$

where $\delta(\boldsymbol{r}_\perp - \boldsymbol{r}'_\perp)$ is a Dirac delta and the parameter γ quantifies the strength of disorder fluctuations. Eq. (2.20) typically constitutes a good approximation as long as the "transverse" wavelength $\lambda_0 = 2\pi/k_0$ is much larger than the disorder correlation length σ_d. For uncorrelated disorder, we have $B(\boldsymbol{k}_\perp - \boldsymbol{k}'_\perp) = \gamma$, leaving us with the following expression for the self-energy:

$$\Sigma(k_z) = \frac{\gamma k^2}{4} \int \frac{d^2\boldsymbol{k}'_\perp}{(2\pi)^2} \frac{1}{k_z - \boldsymbol{k}'^2_\perp/2k + i0^+} \,. \tag{2.21}$$

Note that for the model of uncorrelated disorder, Σ is independent of $\boldsymbol{k}_\perp$. By performing the angular integration and using the Sokhotski–Plemelj theorem [158] to separate explicitly the real and imaginary parts of the self-energy Σ, we get

$$\Sigma(k_z) = \frac{\gamma k^2}{4} \int_0^\infty \frac{dk'_\perp k'_\perp}{2\pi} \left[p.v. \left(\frac{1}{k_z - \boldsymbol{k}'^2_\perp/2k + i0^+} \right) - i\pi\delta(k_z - \boldsymbol{k}'^2_\perp/2k) \right] , \tag{2.22}$$

where $p.v.$ refers to the principal value.

We observe that the real part of Σ diverges at high momenta. This represents a pathology related to the nonphysical nature of uncorrelated disorder. This pathology will not arise in the subsequent chapters, where we will consider more realistic forms of disorder. Here, however, we will simply discard the real part of the self-energy in the rest of this chapter and focus on the role of the imaginary part of the self-energy $\operatorname{Im}\Sigma$, which plays a crucial role. The second term in the right-hand-side of Eq. (2.22) gives $\operatorname{Im}\Sigma = -\gamma k^3/8$. The disorder-average paraxial Green's function in Fourier space then follows from Eq. (2.18):

$$\langle G(\boldsymbol{k}_\perp, k_z) \rangle = \frac{1}{k_z - \boldsymbol{k}^2_\perp/2k - i \operatorname{Im}\Sigma} \,. \tag{2.23}$$

The Green's function (2.23) presents a simple pole in $k_z^{\text{pole}} = \boldsymbol{k}^2_\perp/2k - i \operatorname{Im}\Sigma$. This allows us to easily compute the Green's function in the effective time domain, i.e., $\langle G(\boldsymbol{k}_\perp, z) \rangle = \int \frac{dk_z}{2\pi} \langle G(\boldsymbol{k}_\perp, k_z) \rangle e^{-ik_z z}$ via contour integration [159]:

$$\langle G(\boldsymbol{k}_\perp, z) \rangle = -i \exp\left(-i \frac{\boldsymbol{k}^2_\perp}{2k} z \right) \exp\left(z \operatorname{Im}\Sigma \right) \,. \tag{2.24}$$

Let us now consider the disorder-average field transmitted through a transversally disordered medium of thickness L (see Fig. 2.7). The latter follows by multiplying the Green's function (2.24) evaluated at $z = L$ with the field incident at $z = 0$ according to [160]:

$$\langle \mathcal{E}(\boldsymbol{k}_\perp, z = L) \rangle = i \langle G(\boldsymbol{k}_\perp, L) \rangle \mathcal{E}_0(\boldsymbol{k}_\perp) \,. \tag{2.25}$$

In this relation, $\mathcal{E}_0(\boldsymbol{k}_\perp) = \mathcal{E}(\boldsymbol{k}_\perp, z = 0)$ is the electric field momentum distribution of the light impinging the disordered medium at the $z = 0$ interface and $i\langle G(\boldsymbol{k}_\perp, L) \rangle$

represents the average transmission coefficient of the medium. Considering the incident beam collimated around a transverse wave vector $\boldsymbol{k}_0$, we can Taylor expand the argument in the first exponential of Eq. (2.24) around $\boldsymbol{k}_\perp = \boldsymbol{k}_0$:

$$\frac{\boldsymbol{k}_\perp^2}{2k} \simeq \frac{\boldsymbol{k}_0^2}{2k} + \hat{\boldsymbol{k}}_0 \cdot (\boldsymbol{k}_\perp - \boldsymbol{k}_0) \; , \tag{2.26}$$

where $\hat{\boldsymbol{k}}_0 = \boldsymbol{k}_0/k$, so that

$$\exp\left(-i\frac{\boldsymbol{k}_\perp^2}{2k}L\right) \simeq \exp\left(i\frac{\boldsymbol{k}_0^2}{2k}L\right) \exp\left(-i\hat{\boldsymbol{k}}_0 \cdot \boldsymbol{k}_\perp L\right) \; , \tag{2.27}$$

where the first exponential in the right-hand-side is close to 1, since $k_0 \ll k$ within the paraxial approximation. The intensity of the coherent mode then reads:

$$\begin{aligned} I_c(\boldsymbol{r}_\perp, L) = |\langle \mathcal{E}(\boldsymbol{r}_\perp, L)\rangle|^2 &= \left| \int \frac{d^2\boldsymbol{k}_\perp}{(2\pi)^2} \langle \mathcal{E}(\boldsymbol{k}_\perp, L)\rangle e^{i\boldsymbol{k}_\perp \cdot \boldsymbol{r}_\perp} \right|^2 \\ &= |\mathcal{E}_0(\boldsymbol{r}_\perp - \hat{\boldsymbol{k}}_0 L)|^2 \exp\left(-L/z_s\right) \; , \end{aligned} \tag{2.28}$$

where we have used Eq.s (2.24) and (2.27) in the second equality, and we have introduced $z_s = -(2\,\mathrm{Im}\,\Sigma)^{-1} = 4/(\gamma k^3)$. Within the Schrödinger mapping, the quantity z_s, which will be referred to in the following chapters as the longitudinal mean free path, has in fact the interpretation of an effective scattering mean free *time*. The mean free path in the transverse plane is then defined as

$$\ell = \hat{k}_0 z_s \; , \tag{2.29}$$

with $\hat{k}_0$ having the interpretation of an effective transverse velocity.

From Eq. (2.28) we deduce, first, that the paraxial coherent mode propagates along a straight line, corresponding to a centroid $\boldsymbol{R}_\perp = \int d^2\boldsymbol{r}_\perp \boldsymbol{r}_\perp I_c(\boldsymbol{r}_\perp, L) / \int d^2\boldsymbol{r}_\perp I_c(\boldsymbol{r}_\perp, L) = \hat{\boldsymbol{k}}_0 L$ (see Fig. 2.7). Second, we see that its intensity gets attenuated along the optical axis over a scale given by the longitudinal mean free path z_s. The ballistic propagation, together with the attenuation, reflects the idea that the coherent mode describes the portion of light in the total signal that has not yet undergone multiple scattering after a distance $z = L$ from the interface. Notice, however, that this classical interpretation is rather simplistic, since it misses the true interference nature of the coherent mode: in turn, the coherent mode attenuation originates from the destructive interference between the incident beam and the light scattered by the disorder in the forward direction $\boldsymbol{k}_0$.

2.4 Transverse multiple scattering

As light penetrates deeper in the transversally disordered medium, the coherent mode intensity becomes very small while the multiple scattering signal becomes the main contribution to the total intensity. The intensity of the multiple scattering signal is described by the correlator $\langle GG^* \rangle$, i.e., the disorder average of the product of the retarded Green's function and its complex conjugate, the advanced Green's function.

The Green's function $G(\boldsymbol{r})$ can be seen as the wave amplitude at a generic position $\boldsymbol{r} = (\boldsymbol{r}_\perp, z \geq 0)$ inside the disordered medium resulting from a point source emitting light at $\mathbf{0}$. Such amplitude is built up from all possible infinite multiple scattering sequences from $\mathbf{0}$ to $\boldsymbol{r}$. These sequences involve an arbitrary number of scattering events taking place at the points $\boldsymbol{r}_{\perp 1}, \boldsymbol{r}_{\perp 2}, ..., \boldsymbol{r}_{\perp N}$ of the transverse plane, and are characterized by a complex amplitude $\mathcal{A}^l(\boldsymbol{r})$, with the index l labeling the sequence. The phase of $\mathcal{A}^l(\boldsymbol{r})$ is given by the product $k_0 \mathcal{L}_\perp^l(\boldsymbol{r})$, where k_0 is the incident transverse wave number and $\mathcal{L}_\perp^l(\boldsymbol{r})$ is the path length accumulated during the multiple scattering sequence in the transverse plane. The Green's function $G(\boldsymbol{r})$ can then be expressed formally as

$$G(\boldsymbol{r}) = \sum_l |\mathcal{A}^l(\boldsymbol{r})| e^{ik_0 \mathcal{L}_\perp^l(\boldsymbol{r})} , \tag{2.30}$$

where the sum is over all possible multiple scattering sequences. The product GG^*, therefore, is given by

$$|G(\boldsymbol{r})|^2 = \sum_{l_1, l_2} |\mathcal{A}^{l_1}(\boldsymbol{r}) \mathcal{A}^{l_2}(\boldsymbol{r})| e^{ik_0 [\mathcal{L}_\perp^{l_1}(\boldsymbol{r}) - \mathcal{L}_\perp^{l_2}(\boldsymbol{r})]} . \tag{2.31}$$

When performing the disorder average of the product GG^*, the expression considerably simplifies. Indeed, the difference in transverse path lengths $\mathcal{L}_\perp^{l_1} - \mathcal{L}_\perp^{l_2}$ between non-identical sequences (see Fig. 2.8a) are at least of the order of the transverse mean free path ℓ. In the weak-disorder regime where $\ell \gg k_0^{-1}$, this corresponds to a large dephasing, making all contributions of this type negligible on average due to destructive interference. Then, the relevant trajectory pairs for G and G^* actually contributing to $\langle GG^* \rangle$ are the one for which the scattering sequences are strictly identical, as illustrated in Fig. 2.8b. At weak disorder, the total intensity of the multiple scattering signal is then given by the sum over all possible pairs of paths where interference between the two paths is discarded. Such an approximation is called the *Diffuson* approximation and, as will be shown in the following section, it corresponds to a diffusive process.

In certain cases, multiple scattering processes involving interference can survive the disorder averaging. A celebrated example is found by noting that in time-reversal invariant systems, a trajectory $1 \to 2 \to ... \to N-1 \to N$ paired with its time-reversed partner $N \to N-1 \to ... \to 2 \to 1$ can have the same identical phase factor. In fact, in such term the only accumulated phase difference between the two paths arises at the start and end points of the sequence. Because of this, such a contribution, called in literature the Cooperon, is only significant for $\boldsymbol{k}_\perp \simeq -\boldsymbol{k}_0$: it is responsible for the phenomenon of coherent backscattering. In this thesis we will not discuss more the Cooperon contribution, but we refer the interested reader to [16] for more details.

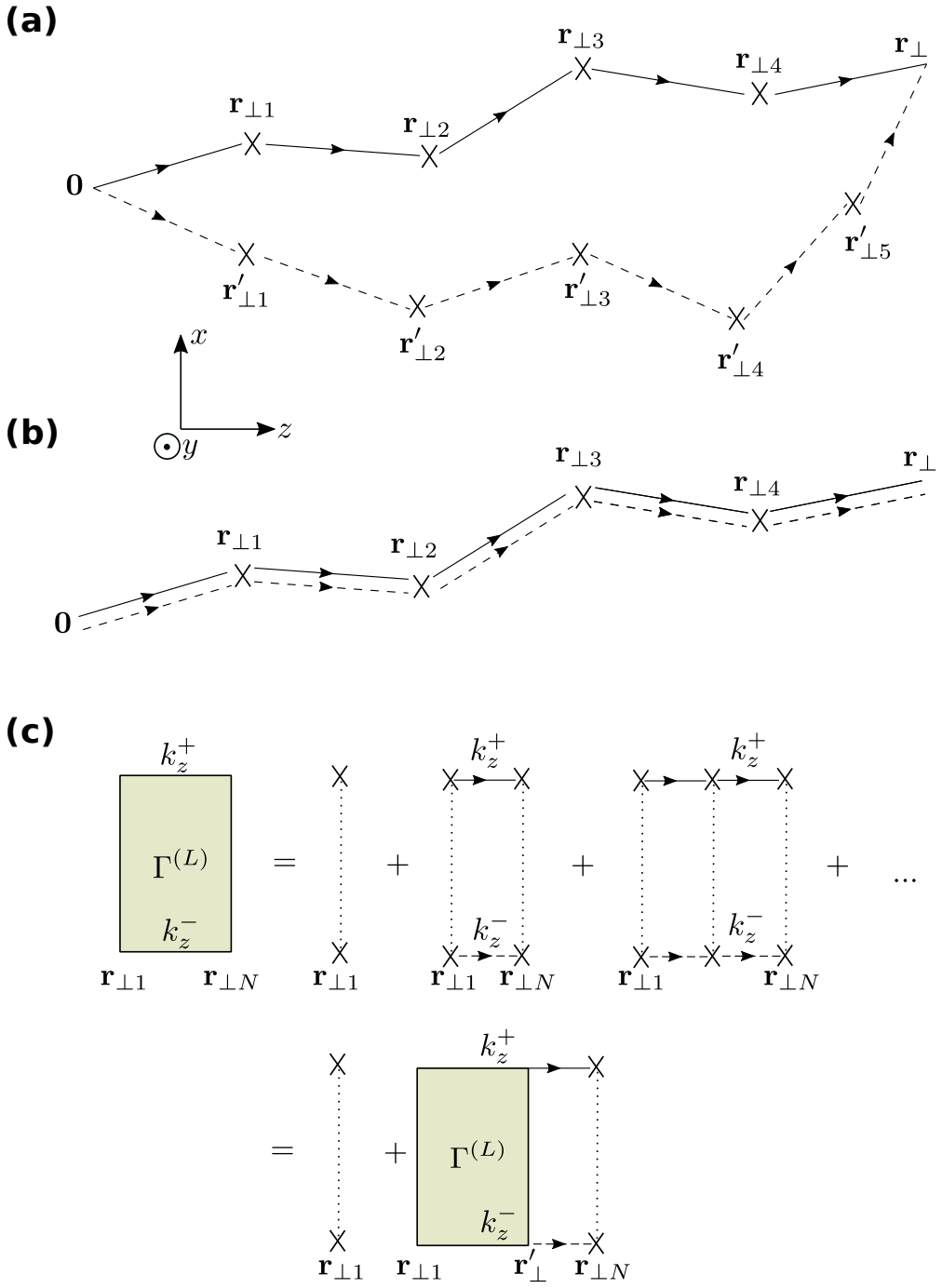

Figure 2.8: **(a)** Real space representation of a multiple scattering term in Eq. (2.31) which, due to the finite path length difference between the two trajectories, does not survive disorder averaging. **(b)** Real space representation of a multiple scattering contribution to the intensity at the Diffuson approximation. Within this approximation, the two wave paths follow the same scattering sequence in the same order. Remember that the scattering events, represented here by crosses, occur in the transverse plane $\boldsymbol{r}_\perp = (x, y)$. **(c)** Diagrammatic representation of all Diffuson sequences involving $1, 2, 3, ...$ scattering events. The second line is an equivalent iterative representation known as the Bethe-Salpeter equation.

2.4.1 Properties of the paraxial Diffuson

The disorder-average correlator of two paraxial Green's functions at a given point $\boldsymbol{r}_\perp$ in the transverse plane can be found in the frequency domain from the relation

$$\begin{aligned}\langle G(\mathbf{0},\boldsymbol{r}_\perp,k_z^+)G^*(\mathbf{0},\boldsymbol{r}_\perp,k_z^-)\rangle_{ms} = &\int d^2\boldsymbol{r}_{\perp 1}d^2\boldsymbol{r}_{\perp N}\langle G(\mathbf{0},\boldsymbol{r}_{\perp 1},k_z^+)\rangle\langle G^*(\mathbf{0},\boldsymbol{r}_{\perp 1},k_z^-)\rangle \\ &\times\Gamma(\boldsymbol{r}_{\perp 1},\boldsymbol{r}_{\perp N},q_z)\langle G(\boldsymbol{r}_{\perp N},\boldsymbol{r}_\perp,k_z^+)\rangle\langle G^*(\boldsymbol{r}_{\perp N},\boldsymbol{r}_\perp,k_z^-)\rangle\ ,\end{aligned} \tag{2.32}$$

where $\mathbf{0}$, $\boldsymbol{r}_\perp$, $\boldsymbol{r}_{\perp 1}$ and $r_{\perp N}$ are, respectively, the positions in the transverse plane of the emission and detection points, and of the first and last scattering events of the sequence. Note that, in order to capture the effective time dependence of the intensity, the Green's functions are here evaluated at the two longitudinal momenta $k_z^\pm = k_z \pm q_z/2$, the variable q_z being the Fourier variable associated with the effective time z. With the subscript ms, we here indicate that only the multiply scattered light signal is considered, i.e. the correlator $\langle GG^*\rangle_{ms}$ does not include the contribution $\langle G\rangle\langle G^*\rangle$ of the coherent mode. Γ, finally, is called the "structure factor". The right-hand side of Eq. (2.32) can be easily interpreted as the succession of three distinct propagation steps. The first factor, $\langle G(\mathbf{0},\boldsymbol{r}_1,k_z^+)\rangle\langle G^*(\mathbf{0},\boldsymbol{r}_{\perp 1},k_z^-)\rangle$, describes the light propagation from the emission point to the first scattering event. The second, $\Gamma(\boldsymbol{r}_{\perp 1},\boldsymbol{r}_{\perp N},q_z)$, encodes all possible scattering sequences between $\boldsymbol{r}_{\perp 1}$ and $\boldsymbol{r}_{\perp N}$. At the Diffuson approximation, Γ is given by $\Gamma^{(L)}$, a series of "ladder diagrams" depicted in Fig. 2.8c. The last term $\langle G(\boldsymbol{r}_{\perp N},\boldsymbol{r}_\perp,k_z^+)\rangle\langle G^*(\boldsymbol{r}_{\perp N},\boldsymbol{r}_\perp,k_z^-)\rangle$, finally, describes the light propagation from the last scattering event to the point $\boldsymbol{r}_\perp$ where light is detected.

The structure factor $\Gamma^{(L)}$ obeys the iterative Bethe-Salpeter equation, which is diagrammatically shown in Fig. 2.8c [16]. The latter mathematically reads:

$$\begin{aligned}\Gamma^{(L)}(\boldsymbol{r}_{\perp 1},\boldsymbol{r}_{\perp N},q_z) = &\frac{\gamma k^2}{4}\delta(\boldsymbol{r}_{\perp 1}-\boldsymbol{r}_{\perp N}) + \int d^2\boldsymbol{r}'_\perp\Gamma^{(L)}(\boldsymbol{r}_{\perp 1},\boldsymbol{r}'_\perp,q_z) \\ &\times\langle G(\boldsymbol{r}'_\perp,\boldsymbol{r}_{\perp N},k_z^+)\rangle\langle G^*(\boldsymbol{r}'_\perp,\boldsymbol{r}_{\perp N},k_z^-)\rangle\ .\end{aligned} \tag{2.33}$$

Generally speaking, solving Eq. (2.33) in an exact way can be a challenging task. If one is only interested in large spatial and temporal scales, however, one may use a hydrodynamic approximation, using that spatial and temporal variations of $\Gamma^{(L)}$ are small at the scales of ℓ and z_s, respectively. We can then expand $\Gamma^{(L)}(\boldsymbol{r}_{\perp 1},\boldsymbol{r}'_\perp,q_z)$ around $\boldsymbol{r}'_\perp = \boldsymbol{r}_{\perp N}$ as:

$$\begin{aligned}\Gamma^{(L)}(\boldsymbol{r}_{\perp 1},\boldsymbol{r}'_\perp,q_z) = &\Gamma^{(L)}(\boldsymbol{r}_{\perp 1},\boldsymbol{r}_{\perp N},q_z) + (\boldsymbol{r}'_\perp-\boldsymbol{r}_{\perp N})\cdot\boldsymbol{\nabla}_{\boldsymbol{r}_{\perp N}}\Gamma^{(L)}(\boldsymbol{r}_{\perp 1},\boldsymbol{r}_{\perp N},q_z) \\ &+\frac{1}{2}[(\boldsymbol{r}'_\perp-\boldsymbol{r}_{\perp N})\cdot\boldsymbol{\nabla}_{\boldsymbol{r}_{\perp N}}]^2\Gamma^{(L)}(\boldsymbol{r}_{\perp 1},\boldsymbol{r}_{\perp N},q_z)+\dots\ .\end{aligned} \tag{2.34}$$

By performing the spatial integration in Eq. (2.33) using the expansion (2.34), and further expanding the product $\langle G\rangle\langle G^*\rangle$ in Eq. (2.33) for $q_z z_s \ll 1$, one finds that the structure factor $\Gamma^{(L)}(\boldsymbol{r}_{\perp 1},\boldsymbol{r}_{\perp N},q_z)$ obeys the diffusion equation

$$(-iq_z + D\Delta_{\boldsymbol{r}_{\perp N}})\Gamma^{(L)}(\boldsymbol{r}_{\perp 1},\boldsymbol{r}_{\perp N},q_z) = \frac{\gamma k^2}{4z_s}\delta(\boldsymbol{r}_{\perp 1}-\boldsymbol{r}_{\perp N})\ , \tag{2.35}$$

where $D = \hat{k}_0^2 z_s/2$ is the diffusion coefficient. Furthermore, due to the slowly-varying behaviour of $\Gamma^{(L)}$ in the hydrodynamic limit, we can take $\Gamma^{(L)}$ out of the integral in

Eq. (2.32), thus obtaining

$$\langle G(\mathbf{0}, \boldsymbol{r}_\perp, k_z^+) G^*(\mathbf{0}, \boldsymbol{r}_\perp, k_z^-) \rangle_D \simeq \frac{4 z_s}{\gamma k^2} \Gamma^{(L)}(\boldsymbol{r}_{\perp 1}, \boldsymbol{r}_{\perp N}, q_z) \,, \tag{2.36}$$

where the subscript D states the fact that the multiply scattered signal has been treated within the Diffuson description. Therefore, $\langle G G^* \rangle_D$ satisfies a diffusion equation as well. Considering a narrow incident beam of waist w_0, the intensity of the multiple scattering signal detected at the point $\boldsymbol{r} = (\boldsymbol{r}_\perp, z = L \gg w_0^2/D)$, $I_D = \langle |\boldsymbol{E}(\boldsymbol{r}_\perp, z = L)|^2 \rangle_D$, is then given by

$$I_D(\boldsymbol{r}_\perp, L) \simeq \langle |G(\mathbf{0}, \boldsymbol{r})|^2 \rangle_D = \frac{e^{-\boldsymbol{r}_\perp^2 / 4DL}}{4\pi DL} \,. \tag{2.37}$$

The hydrodynamic approximation, used to derive Eq. (2.37), is also known as the diffusion approximation. It shows that, on average, light in a scattering medium effectively behaves like a particle undergoing a random walk through the disorder. Looking at the expression of the intensity (2.37) obtained within the diffusion approximation, it seems that its centroid $\boldsymbol{R}_\perp^D = \int d^2\boldsymbol{r}_\perp \boldsymbol{r}_\perp I_D(\boldsymbol{r}_\perp, L) / \int d^2\boldsymbol{r}_\perp I_D(\boldsymbol{r}_\perp, L)$ is zero. Actually, this is not true. An exact computation of the Diffuson centroid done without performing the diffusion approximation (see chapter 5) gives the more accurate result

$$\boldsymbol{R}_\perp^D(L) = \hat{\boldsymbol{k}}_0 z_s \frac{1 - \frac{L}{z_s} e^{-L/z_s} - e^{-L/z_s}}{1 - e^{-L/z_s}} \,. \tag{2.38}$$

The reason why the diffusion approximation fails to accurately describe this observable is due to the fact that $\boldsymbol{R}_\perp^D$ typically varies at short length scales ($\sim \hat{\boldsymbol{k}}_0 z_s$). For the sake of a clearer presentation, we postpone the derivation of Eq. (2.38) to chapter 5.

2.4.2 Total paraxial centroid

Instead of considering separately the ballistic and the multiple scattering components of the light travelling inside the transversally disordered medium, one can also compute the centroid of the full signal, defined as

$$\boldsymbol{R}_\perp^{tot}(L) = \frac{\int d^2\boldsymbol{r}_\perp \boldsymbol{r}_\perp I_c(\boldsymbol{r}_\perp, L) + \int d^2\boldsymbol{r}_\perp \boldsymbol{r}_\perp I_D(\boldsymbol{r}_\perp, L)}{\int d^2\boldsymbol{r}_\perp I_c(\boldsymbol{r}_\perp, L) + \int d^2\boldsymbol{r}_\perp I_D(\boldsymbol{r}_\perp, L)} \,. \tag{2.39}$$

Notice that the normalization factor now includes both I_c and I_D. Using the results (2.28) and (2.38), one finds

$$\boldsymbol{R}_\perp^{tot}(L) = \hat{\boldsymbol{k}}_0 z_s \left(1 - e^{-L/z_s}\right) \,. \tag{2.40}$$

Eq. (2.40) has a very simple classical interpretation: as a result of the finite beam's transverse momentum, the centroid moves ballistically up to a distance of a mean free path $\hat{k}_0 z_s$, and stops there because of the randomization of the transverse momentum associated with multiple scattering.

Interestingly, because of the correspondence between incoherent multiple scattering of light and the random walk of a particle, Eq. (2.40) can be alternatively derived

within a simple scattering approach based on the Boltzmann equation, which we here present in 1D for simplicity (extension to 2D is straightforward). Consider a wave packet with momentum distribution peaked at $\boldsymbol{k}_0 = k_0\hat{\boldsymbol{x}}$ immersed in a 1D disorder. Let $n^{\pm}$ be the population of particles with $\pm\hbar k_0$ momentum. The initial condition, thus, reads $n^+(0) = 1$ and $n^-(0) = 0$ (with the normalization constraint $n^+ + n^- = 1$ holding true throughout the whole evolution). The evolution of the center of mass is given by the Ehrenfest theorem [161]:

$$\partial_t \langle \boldsymbol{x}(t) \rangle = \frac{\langle \boldsymbol{p} \rangle}{m} = \frac{\hbar \boldsymbol{k_0}}{m}(n^+ - n^-)\,, \tag{2.41}$$

where $\langle ... \rangle$ here refers to both the disorder average and quantum expectation value, and m is the particle mass. Neglecting any interference in the disorder, the evolution of $n^{\pm}$ is simply given by coupled Boltzmann equations [162]:

$$\partial_t n^{\pm} = \frac{n^{\mp} - n^{\pm}}{2\tau}\,. \tag{2.42}$$

Solving the differential Eq.s (2.42) is straightforward and gives

$$n^{\pm}(t) = \frac{1 \pm e^{-t/\tau}}{2}\,. \tag{2.43}$$

By inserting these solutions into Eq. (2.41) and using the initial condition $\langle x(t=0) \rangle = 0$, we finally obtain [10]

$$\langle \boldsymbol{x}(t) \rangle = \ell \hat{\boldsymbol{x}} \big(1 - e^{-t/\tau}\big)\,, \tag{2.44}$$

with $\ell = \hbar k_0 \tau / m$ being the transport mean free path, and τ the corresponding mean free time. As anticipated, Eq.s (2.40) and (2.44) have exactly the same structure. By comparing the two, we also have a confirmation that, in our case, z_s plays the role of mean free time, and $\hat{k}_0 z_s$ the role of the mean free path.

2.5 Conclusion

In this chapter, we have presented the problem of light propagation in transversally disordered dielectric media within the framework of the paraxial approximation. This enabled us to introduce some key concepts and tools in a reasonably straightforward way. In the next chapters, we will address the physics of spin-orbit interactions that shows up beyond the paraxial approximation, using the results of the present chapter as a benchmark.

Chapter 3

Oscillating spin Hall effect of light in correlated disorder

In order to capture the phenomenon of spin-orbit interactions of light, it is necessary to employ a description that goes beyond the paraxial approximation. Indeed, the paraxial wave equation constitutes a scalar approximation which completely neglects the polarization degree of freedom of light and its coupling to the light propagation. In 2018, an exact description of light in (2+1)D disordered media fully taking into account the vector nature of light was put forward [42], relying on the simple disorder model introduced in the previous chapter, i.e., a continuous uncorrelated Gaussian disorder discarding the (diverging) real part contribution of the self-energy. It was within this simplified statistical model that, in 2019, the existence of a spin Hall effect of light in (2+1)D disordered media affecting the coherent mode was predicted [62] (see also Sec. 1.7). In this chapter, we propose to fully revisit this physics by employing a more realistic model that takes into account the finite disorder correlation. This will allow us to showcase a novel phenomenon that was missed in [62], namely an *oscillating* spin Hall effect associated with SOI corrections to the real part of the self-energy. Furthermore, by taking advantage of a fine tuning of the correlation length, we will show that various types of spin Hall effects can be realized in a transverse disorder. We will finally present a first possible strategy to make this effect experimentally observable, and discuss its limitations.

3.1 Initial condition and disorder model

In this chapter, we consider a collimated, tilted beam of light impinging on a slab-shaped, transversally disordered dielectric medium lying between $z = 0$ and $z = L$ (see Fig. 3.1). Without any loss of generality, we consider an incident laser beam with a transverse Gaussian-shaped profile. The beam enters the disordered medium with an angle θ with respect to the optical axis $\hat{\boldsymbol{z}}$. Hence, at the interface $z = 0$, the electric field reads

$$\boldsymbol{E}(\boldsymbol{r}_\perp, z = 0) = \sqrt{\frac{2}{\pi w_0^2}} e^{-\boldsymbol{r}_\perp^2/w_0^2 + i\boldsymbol{k}_0 \cdot \boldsymbol{r}_\perp} \boldsymbol{e}_0 \ , \tag{3.1}$$

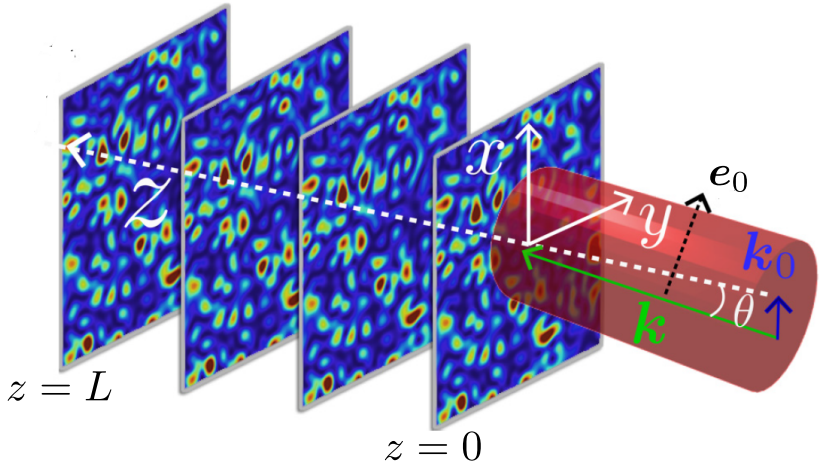

Figure 3.1: We consider the propagation of a tilted, collimated beam of wave vector $\boldsymbol{k}$ with polarization $\boldsymbol{e}_0$ through a medium of thickness L spatially disordered in the (x, y) plane, with a disorder correlation length σ_d (the different planes shown illustrate the disorder invariance along z). The projection of $\boldsymbol{k}$ onto the (x, y) plane is denoted by $\boldsymbol{k}_0$.

where w_0 is the beam waist and $\boldsymbol{k}_0 = k_0\hat{\boldsymbol{x}}$, with $k_0 = k\sin\theta$ the transverse component of the total wave vector $\boldsymbol{k} = k_0\hat{\boldsymbol{x}} + k_z\hat{\boldsymbol{z}}$ (the direction of the Cartesian axis $\hat{\boldsymbol{x}}$ being chosen to be aligned with $\boldsymbol{k}_0$). The hypothesis of collimated beam implies the condition

$$k_0 w_0 \gg 1 \, . \tag{3.2}$$

Eq. (3.1) also fixes the normalization of the intensity:

$$\int d^2\boldsymbol{r}_\perp |\boldsymbol{E}(\boldsymbol{r}_\perp, z = 0)|^2 = 1. \tag{3.3}$$

For the polarization of the incident beam $\boldsymbol{e}_0$, we take the following form:

$$\boldsymbol{e}_0 = \frac{\hat{\boldsymbol{x}}' + e^{i\phi}\hat{\boldsymbol{y}}}{\sqrt{2}} \, , \tag{3.4}$$

where $\hat{\boldsymbol{x}}' = \sin\theta\hat{\boldsymbol{x}} - \cos\theta\hat{\boldsymbol{z}}$ is the unit vector perpendicular to the incident wave vector $\boldsymbol{k}$ lying in the (x, z) plane. By tuning the polarization parameter $\phi \in (-\pi, \pi]$, linearly ($\phi = 0, \pi$), circularly- ($\phi = \pm\pi/2$) and elliptically- (arbitrary ϕ values) polarized beam can be considered.

As in the previous chapter, we consider a dielectric medium homogeneous along z, characterized by a continuous, disordered permittivity distribution in the transverse plane: $\epsilon(\boldsymbol{r}_\perp) = \bar{\epsilon} + \delta\epsilon(\boldsymbol{r}_\perp)$, where $\delta\epsilon(\boldsymbol{r}_\perp)$ is a random Gaussian distribution with zero mean, modelling transverse disorder, and $\bar{\epsilon}$ is the background (uniform) permittivity. In this chapter, we model the disorder correlation by the two-point Gaussian correlation function:

$$B(\boldsymbol{r}_\perp - \boldsymbol{r}'_\perp) = \frac{\langle \delta\epsilon(\boldsymbol{r}_\perp)\delta\epsilon(\boldsymbol{r}'_\perp)\rangle}{\bar{\epsilon}^2} = \frac{\gamma e^{-(\boldsymbol{r}_\perp - \boldsymbol{r}'_\perp)^2/4\sigma_d^2}}{4\pi\sigma_d^2} \, , \tag{3.5}$$

where γ is the disorder amplitude, σ_d is the disorder correlation length and the brackets refer to disorder averaging. Notice that we are dealing with a statistically isotropic transverse disorder. The δ-correlated case discussed in the previous chapter corresponds to the limit $\sigma_d \to 0$.

Given these initial conditions and assumptions, in this chapter we will study the behaviour of the coherent mode in such transverse correlated disorder, employing an "exact" approach, in the sense that it fully accounts for the vector nature of light, and does not rely on the paraxial approximation. In particular, we will be interested in the near-paraxial regime, defined by $\hat{k}_0 = k_0/k \ll 1$, in order to highlight the first-order corrections to the paraxial limit.

3.2 Beyond paraxiality: free electromagnetic propagator and Dyson equation

As seen in the previous chapter for paraxial light, the free propagator constitutes a fundamental building block for the study of light propagation in a disordered medium. As we now wish to take into account the vector character of light, we first need to derive the expression of the free propagator associated with the Helmholtz equation

$$\Delta \boldsymbol{E}(\boldsymbol{r},\omega) + k^2 \boldsymbol{E}(\boldsymbol{r},\omega) - \boldsymbol{\nabla}[\boldsymbol{\nabla}\cdot\boldsymbol{E}(\boldsymbol{r},\omega)] = 0 \tag{3.6}$$

describing light propagation in an homogeneous medium of permittivity $\bar{\epsilon}$ and wave number $k = \sqrt{\bar{\epsilon}}\omega/c$. The linear differential operator associated with Eq. (3.6) is

$$\hat{L}_{ij}(\boldsymbol{r}) = (\Delta + k^2)\delta_{ij} - \nabla_i \nabla_j \ , \tag{3.7}$$

where $i,j = x,y,z$ and δ_{ij} is the Kronecker delta symbol. Contrary to the paraxial case, Eq. (3.6) involves a three-component vector field, such that $\hat{\boldsymbol{L}}$ is a rank-3 tensor. The free electromagnetic Green's tensor $\boldsymbol{G}^{(0)}$ in momentum space $\boldsymbol{k}'$ is then a 3×3 tensor, given by the solution of equation

$$\hat{\tilde{L}}_{ij}(\boldsymbol{k}')G^{(0)}_{jk}(\boldsymbol{k}') = \delta_{ik} \ , \tag{3.8}$$

where $\hat{\tilde{L}}_{ij}(\boldsymbol{k}') = (k^2 - \boldsymbol{k}'^2)\delta_{ij} + k'_i k'_j$. Solving Eq. (3.8), one gets

$$G^{(0)}_{ij}(\boldsymbol{k}') = \frac{\hat{k}'_i \hat{k}'_j}{k^2} + \frac{\delta_{ij} - \hat{k}'_i \hat{k}'_j}{k^2 - \boldsymbol{k}'^2 + i0^+} \ , \tag{3.9}$$

where $\hat{\boldsymbol{k}}' = \boldsymbol{k}'/k$. The first term, proportional to the projector $\hat{\boldsymbol{k}}'\hat{\boldsymbol{k}}'$, represents the longitudinal component of the Green's tensor, while the second term, proportional to the orthogonal projector $\mathbb{1} - \hat{\boldsymbol{k}}'\hat{\boldsymbol{k}}'$, represents its transverse part. The longitudinal part comes from electrostatics and, as such, does not propagate, while the transverse term describes light propagation representing wave solutions of Maxwell's equations. As in the paraxial case, the addition of a positive infinitesimal imaginary component in the denominator of the propagating term ($i0^+$) makes the propagator consistent with the causality constraint (retarded Green's tensor).

The main focus of the thesis concerns light propagation. We are then interested in the far-field electromagnetic region. Throughout the whole thesis we will thus neglect the near-field longitudinal component and use the expression

$$G_{ij}^{(0)}(\boldsymbol{k}') = \frac{\delta_{ij} - \hat{k}'_i \hat{k}'_j}{k^2 - \boldsymbol{k}'^2 + i0^+} \tag{3.10}$$

for the free Green's tensor. The choice can be also justified by the fact that in the thesis we will always restrict ourselves to "dilute" materials, for which the wavelength is typically large compared to the spacing between scatterers.

In a transversally disordered dielectric medium, the Helmholtz equation reads

$$\Delta \boldsymbol{E}(\boldsymbol{r},\omega) + k^2 \boldsymbol{E}(\boldsymbol{r},\omega) - \boldsymbol{\nabla}[\boldsymbol{\nabla}\cdot\boldsymbol{E}(\boldsymbol{r},\omega)] - V(\boldsymbol{r}_\perp)\boldsymbol{E}(\boldsymbol{r},\omega) = 0 \;, \tag{3.11}$$

where the disorder is described by the term $V(\boldsymbol{r}_\perp) = -k^2\delta\epsilon(\boldsymbol{r}_\perp)/\overline{\epsilon}$, which can be interpreted as an effective potential term. The disordered Green's tensor $\boldsymbol{G}$ is then given by the same formal expression as in the paraxial case, see Eq. (2.15), with the only difference that now it has a tensorial form:

$$\boldsymbol{G} = \boldsymbol{G}^{(0)} + \boldsymbol{G}^{(0)}\boldsymbol{V}\boldsymbol{G} \;, \tag{3.12}$$

where $\boldsymbol{V} = V\delta_{ij}$ is the tensor effective potential. Correspondingly, after disorder averaging we obtain the tensor Dyson equation

$$\langle \boldsymbol{G} \rangle = \boldsymbol{G}^{(0)} + \boldsymbol{G}^{(0)}\boldsymbol{\Sigma}\langle \boldsymbol{G} \rangle \;, \tag{3.13}$$

where the self-energy $\boldsymbol{\Sigma}$ is now a 3×3 tensor. The disorder-average Green's tensor is then formally given by

$$\langle \boldsymbol{G} \rangle = \left[\boldsymbol{G}^{(0)-1} - \boldsymbol{\Sigma}\right]^{-1} . \tag{3.14}$$

As in the previous chapter, the quantity $\boldsymbol{\Sigma}$ encodes all effects of disorder on the average field: its real part describes how the phase of the wavefront evolves on average in the disorder (mean refractive index), while its imaginary part governs the attenuation of its amplitude (extinction coefficient), both effects being now described at the vectorial level.

3.3 Disorder-average Green's tensor in correlated transverse disorder

Assuming weak disorder ($k_0\ell \gg 1$), we can evaluate the self-energy tensor $\boldsymbol{\Sigma}$ using the Born approximation [16]. This leads to the following expression:

$$\Sigma_{ij}(\boldsymbol{k}_\perp, k_z) = k^4 \int \frac{d^2\boldsymbol{k}'_\perp}{(2\pi)^2} \frac{B(\boldsymbol{k}_\perp - \boldsymbol{k}'_\perp)(\delta_{ij} - \hat{k}'_i\hat{k}'_j)}{k^2 - \boldsymbol{k}'^2_\perp - k_z^2 + i0^+} \;, \tag{3.15}$$

which is the tensor version of Eq. (2.19). Note that as in the scalar case, here only an integration over $\boldsymbol{k}'_\perp$ is involved, the longitudinal wave number k_z being conserved

due to translation invariance along $\hat{\boldsymbol{z}}$. $B(\boldsymbol{k}_\perp - \boldsymbol{k}'_\perp)$ is the disorder power spectrum, i.e., the Fourier transform of Eq. (3.5). In this section and the next one, we keep the discussion rather general, and only use that the transverse disorder is statistically isotropic, so that $B(\boldsymbol{k}_\perp - \boldsymbol{k}'_\perp) = B(|\boldsymbol{k}_\perp - \boldsymbol{k}'_\perp|)$. Later, we will compute the self-energy tensor (3.15) explicitly, using the Gaussian model of correlations (3.5), for which the power spectrum takes the form $B(\boldsymbol{k}_\perp - \boldsymbol{k}'_\perp) = \gamma \exp\left[-\sigma_d^2(\boldsymbol{k}_\perp - \boldsymbol{k}'_\perp)^2\right]$.

Since we are dealing with a statistically-isotropic disorder in the transverse plane (x, y), to obtain the general expression of the average Green's tensor it is sufficient to compute the self-energy (3.15) in the specific case where the direction of $\boldsymbol{k}_\perp$ is oriented along the $\hat{\boldsymbol{x}}$ axis. Let us then take a closer look to the angular integral of $\boldsymbol{k}'_\perp = (k'_\perp \cos\theta, k'_\perp \sin\theta)$ appearing in Eq. (3.15):

$$\begin{aligned}\int_0^{2\pi} \frac{d\theta}{2\pi} B(|\boldsymbol{k}_\perp - \boldsymbol{k}'_\perp|) \left(\delta_{ij} - \hat{k}'_i \hat{k}'_j\right) = \gamma f(k_\perp, k'_\perp) \int_0^{2\pi} \frac{d\theta}{2\pi} g(k_\perp k'_\perp \cos\theta) \\ \times \left[\delta_{ij} - \begin{pmatrix} \hat{k}'^2_\perp \cos^2\theta & \hat{k}'^2_\perp \sin\theta\cos\theta & \hat{k}_z \hat{k}'_\perp \cos\theta \\ \hat{k}'^2_\perp \sin\theta\cos\theta & \hat{k}'^2_\perp \sin^2\theta & \hat{k}_z \hat{k}'_\perp \sin\theta \\ \hat{k}_z \hat{k}'_\perp \cos\theta & \hat{k}_z \hat{k}'_\perp \sin\theta & \hat{k}_z^2 \end{pmatrix}\right] ,\end{aligned} \tag{3.16}$$

where, as said, $\hat{\boldsymbol{k}}_\perp$ has been aligned to the $\hat{\boldsymbol{x}}$ axis, and $f(k_\perp, k'_\perp)$ and $g(k_\perp k'_\perp \cos\theta)$ are two functions whose expression depends on the specific shape of the disorder correlation function. Looking at Eq. (3.16), it is clear that the self-energy tensor has the following structure:

$$\boldsymbol{\Sigma}(\boldsymbol{k}_\perp, k_z) = \begin{pmatrix} \Sigma_{xx} & 0 & \Sigma_{xz} \\ 0 & \Sigma_{yy} & 0 \\ \Sigma_{xz} & 0 & \Sigma_{zz} \end{pmatrix} . \tag{3.17}$$

Using Eq. (3.17), we perform the two tensor inversions appearing in the Dyson equation (3.14), and obtain the following form for the disorder-average Green's tensor in momentum space:

$$\langle G_{ij}(\boldsymbol{k}_\perp, k_z)\rangle = G_1 \delta_{ij} - G_2 \hat{k}_i \hat{k}_j + \frac{G_1 - G_2}{\hat{k}_\perp^2} \left(\delta_{iz}\hat{k}_j\hat{k}_z + \delta_{jz}\hat{k}_i\hat{k}_z - \delta_{iz}\delta_{jz} - \hat{k}_i\hat{k}_j\right) , \tag{3.18}$$

where

$$G_{1(2)}(\boldsymbol{k}_\perp, k_z) = \frac{1}{k^2 - \boldsymbol{k}_\perp^2 - k_z^2 - \Sigma_{1(2)}(\boldsymbol{k}_\perp, k_z)} \tag{3.19}$$

with

$$\begin{aligned}\Sigma_1(\boldsymbol{k}_\perp, k_z) &= \Sigma_{yy} \\ \Sigma_2(\boldsymbol{k}_\perp, k_z) &= \Sigma_{xx}(1 - \hat{k}_\perp^2) + \Sigma_{zz}(1 - \hat{k}_z^2) - 2\Sigma_{xz}\hat{k}_\perp \hat{k}_z .\end{aligned} \tag{3.20}$$

Note that the matrix structure (3.17) of the self-energy only holds true strictly speaking for $\boldsymbol{k}_\perp$ aligned along $\hat{\boldsymbol{x}}$. Nevertheless, as a result of transverse statistical isotropy, the disorder-average Green's tensor derived from it, and in particular the values of the parameters Σ_1 and Σ_2 entering in its analytical expression, do *not* depend on this particular choice and, thus, can be used for any transverse momentum $\boldsymbol{k}_\perp$.

Since we are interested in the evolution of the coherent mode with z, we need to compute the inverse Fourier transform of Eq. (3.18) with respect to k_z: $\langle \boldsymbol{G}(\boldsymbol{k}_\perp, z)\rangle = \int dk_z \langle \boldsymbol{G}(\boldsymbol{k}_\perp, k_z)\rangle e^{ik_z z}$. The weak disorder condition $k_0\ell \gg 1$ applied to Eq. (3.18) translates into $|\Sigma_{1(2)}| \ll k^2 - k_z^2$. The k_z-poles appearing in Eq. (3.19) can then be Taylor-expanded as

$$k_z^{pole} \simeq \sqrt{k^2 - \boldsymbol{k}_\perp^2} + \frac{\Sigma_{1(2)}(\boldsymbol{k}_\perp, \sqrt{k^2 - \boldsymbol{k}_\perp^2})}{2\sqrt{k^2 - \boldsymbol{k}_\perp^2}} \, . \tag{3.21}$$

Hence, the disorder-average Green's tensor in the effective time domain reads

$$\begin{aligned} \langle G_{ij}(\boldsymbol{k}_\perp, z)\rangle = & -i\frac{e^{ik_z z}}{2k_z}\Bigg[e^{-i\Sigma_1 z/2k_z}\delta_{ij} - e^{-i\Sigma_2 z/2k_z}\hat{k}_i\hat{k}_j \\ & + \frac{e^{-i\Sigma_1 z/2k_z} - e^{-i\Sigma_2 z/2k_z}}{\hat{k}_\perp^2}\Big(\delta_{iz}\hat{k}_j\hat{k}_z + \delta_{jz}\hat{k}_i\hat{k}_z - \delta_{iz}\delta_{jz} - \hat{k}_i\hat{k}_j\Big)\Bigg] \, , \end{aligned} \tag{3.22}$$

where k_z now stands for the "on shell" value $\sqrt{k^2 - \boldsymbol{k}_\perp^2}$ and no longer for the longitudinal Fourier variable. Note that the self-energies $\Sigma_{1(2)}$ appearing in Eq. (3.22) are also to be evaluated on shell: $\Sigma_{1(2)} = \Sigma_{1(2)}(\boldsymbol{k}_\perp, \sqrt{k^2 - \boldsymbol{k}_\perp^2})$ [see Eq. (3.21)].

Before ending this section, let us stress that the expression (3.22) only relies on the transverse nature and the statistical isotropy of the disorder, but it does not depend on the microscopic details of the transverse disorder. As will be elucidated later on, the anisotropic components of the disorder-average Green's tensor (3.22) are associated with a phenomenon of spin-orbit interaction and are responsible for the appearance of a spin Hall effect of light affecting the coherent mode.

3.4 Disorder-average transmitted field

3.4.1 General expression

As in the previous chapter, we now examine the transmission of a light beam through a transversally disordered medium located between the coordinates $z = 0$ and $z = L$. The disorder-average electric field $\langle \boldsymbol{E}(\boldsymbol{k}_\perp, L)\rangle$ is linked to the average Green's tensor via the Fisher-Lee relation [15]:

$$\langle E_i(\boldsymbol{k}_\perp, L)\rangle = \langle t_{ij}(\boldsymbol{k}_\perp, L)\rangle E_j(\boldsymbol{k}_\perp, z = 0) \, , \tag{3.23}$$

where $\langle t_{ij}(\boldsymbol{k}_\perp, L)\rangle = 2i\sqrt{k^2 - \boldsymbol{k}_\perp^2}\langle G_{ij}(\boldsymbol{k}_\perp, L)\rangle$ represents the disorder-average transmission coefficient of the medium, and $\boldsymbol{E}(\boldsymbol{k}_\perp, z = 0) = \sqrt{2\pi}w_0 \exp\big[-(\boldsymbol{k}_\perp - \boldsymbol{k}_0)^2 w_0^2/4\big]\boldsymbol{e}_0$ is the transverse Fourier distribution of the incident beam (3.1).

Using Eq. (3.22), we infer:

$$\langle \boldsymbol{E}(\boldsymbol{k}_\perp, L)\rangle = \boldsymbol{E}(\boldsymbol{k}_\perp, z = 0)e^{ik_z L}\Big[e^{-i\Sigma_1 L/2k_z}\boldsymbol{e}_0 + \Big(e^{-i\Sigma_2 L/2k_z} - e^{-i\Sigma_1 L/2k_z}\Big)\boldsymbol{p}(\boldsymbol{k}_\perp)\Big] \, . \tag{3.24}$$

In this formula, the two complex numbers Σ_1 and Σ_2, already defined in Eq. (3.20), are combinations of matrix elements of the self-energy tensor. Because $\boldsymbol{E}(\boldsymbol{k}_\perp, z = 0)$ is

peaked around $\boldsymbol{k}_\perp = \boldsymbol{k}_0$ (collimated beam hypothesis), Σ_1 and Σ_2 can be evaluated at $\boldsymbol{k}_\perp \simeq \boldsymbol{k}_0$, i.e., approximating $\Sigma_{1(2)} \simeq \Sigma_{1(2)}(\boldsymbol{k}_0, \sqrt{k^2 - \boldsymbol{k}_0^2})$. Their analytical expression depends on the specific form of the disorder power spectrum. In the section below, they will be evaluated explicitly for the Gaussian case (3.5).

In Eq. (3.24), the first term in the right-hand side describes an evolution of the average field without spatial deformation. Its amplitude is controlled by Σ_1, which defines the scattering mean free path along z of the disorder:

$$z_s = -k_z / \operatorname{Im}(\Sigma_1) \,, \tag{3.25}$$

beyond which the coherent mode gets attenuated due to scattering in other directions [17]. This definition of the scattering mean free path, in relation to Σ_1 only, will be discussed more thoroughly below. The second term in the right-hand-side, on the other hand, is proportional to the projection $\boldsymbol{p}(\boldsymbol{k}_\perp) = (\hat{\boldsymbol{e}}_\perp \cdot \boldsymbol{e}_0)\hat{\boldsymbol{e}}_\perp + (\hat{\boldsymbol{z}} \cdot \boldsymbol{e}_0)\hat{\boldsymbol{z}}$ of the polarization vector onto the $(\hat{\boldsymbol{e}}_\perp = \boldsymbol{k}_\perp/k_\perp, \hat{\boldsymbol{z}})$ plane. It describes a wavefront deformation coupling polarization and momentum and, as such, encodes the phenomenon of spin-orbit interaction of light. Notice that this spin-orbit term only exists when $\Sigma_1 \neq \Sigma_2$. The self-energies Σ_1 and Σ_2 being complex numbers, Eq. (3.24) suggests that the SOI term affects both the phase and the amplitude of the average field. As will be shown explicitly below, this property implies a rather rich behavior of the coherent mode.

The existence of two independent self-energies governing light evolution in the disordered medium here stems from the fact that as soon as the incident beam is tilted, i.e., $\boldsymbol{k}_0 \neq 0$, the statistical isotropy in the plane perpendicular to the direction of propagation is broken, making momentum conservation along z (due to translation invariance along that direction) the unique symmetry of the problem. On the other hand, when $\boldsymbol{k}_0 \to 0$ (paraxial limit), an additional symmetry emerges, the statistical isotropy in the (x', y) plane. In this limit, one has $\Sigma_1 \to \Sigma_2$ [see Eq. (3.51)], so spin-orbit interactions disappear (the second term in the right-hand side of Eq. (3.24) vanishes) and the paraxial result obtained in the previous chapter is effectively recovered. Note that no spin-orbit-interaction term ever arises in conventional, three-dimensional isotropic disordered materials, where no direction of propagation is privileged: in 3D the evolution of coherent light is governed by a single self-energy.

3.4.2 Self-energy for Gaussian-correlated transverse disorder

Considering a Gaussian-correlated disorder, see Eq. (3.5), we now explicitly compute the self-energies Σ_1 and Σ_2 appearing in Eq. (3.24). In such a case, the self-energy tensor $\boldsymbol{\Sigma}$ is given by

$$\Sigma_{ij}(\boldsymbol{k}_\perp, k_z) = \gamma k^4 \int \frac{d^2\boldsymbol{k}'_\perp}{(2\pi)^2} \frac{\exp\left[-\sigma_d^2(\boldsymbol{k}_\perp - \boldsymbol{k}'_\perp)^2\right](\delta_{ij} - \hat{k}'_i\hat{k}'_j)}{k^2 - \boldsymbol{k}_\perp'^2 - k_z^2 + i0^+} \,. \tag{3.26}$$

We then rewrite the denominator of Eq. (3.26) as

$$\begin{aligned} \frac{1}{k^2 - \boldsymbol{k}_\perp'^2 - k_z^2 + i0^+} =& p.v.\left(\frac{1}{k^2 - \boldsymbol{k}_\perp'^2 - k_z^2 + i0^+}\right) - i\frac{\pi}{2\sqrt{k^2 - k_z^2}} \\ &\times \left[\delta(k'_\perp - \sqrt{k^2 - k_z^2}) + \delta(k'_\perp + \sqrt{k^2 - k_z^2})\right] \,, \end{aligned} \tag{3.27}$$

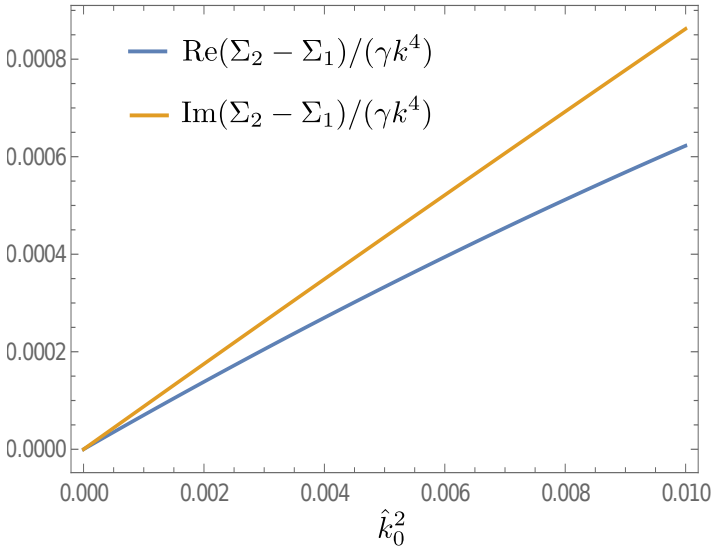

Figure 3.2: Real and imaginary parts of $(\Sigma_2-\Sigma_1)/(\gamma k^4)$ as a function of $\hat{k}_0^2$, in the small $\hat{k}_0$ regime. Here we have set $k_0\sigma_d = 0.5$. Observe that $\Sigma_1 \to \Sigma_2$ when $\hat{k}_0 \to 0$, indicating that SOI vanish in the paraxial limit.

perform the double integral in Eq. (3.26) and evaluate the self-energy matrix elements at $\boldsymbol{k}_\perp \simeq \boldsymbol{k}_0$ and $k_z \simeq \sqrt{k^2-\boldsymbol{k}_0^2}$. This yields the following analytic expression for the real and imaginary parts of the self-energies $\Sigma_{1(2)} \simeq \Sigma_{1(2)}(\boldsymbol{k}_0, \sqrt{k^2-\boldsymbol{k}_0^2})$ governing the evolution of the disorder-average electric field (3.24):

$$\begin{aligned}
\mathrm{Re}\,\Sigma_1 =& \gamma k^4 \int_0^\infty \frac{d\alpha}{2\pi} p.v. \left(\frac{\alpha e^{-k_0^2\sigma_d^2(1+\alpha^2)}}{1-\alpha^2}\right)\left[I_0(2k_0^2\sigma_d^2\alpha) - \frac{\hat{k}_0^2\alpha^2 I_1(2k_0^2\sigma_d^2\alpha)}{2k_0^2\sigma_d^2\alpha}\right] \\
\mathrm{Re}\,\Sigma_2 =& \gamma k^4 \int_0^\infty \frac{d\alpha}{2\pi} p.v. \left(\frac{\alpha e^{-k_0^2\sigma_d^2(1+\alpha^2)}}{1-\alpha^2}\right)\left[(1-2\hat{k}_0^2\alpha^2+\hat{k}_0^4\alpha^4+\hat{k}_0^4)\right. \\
&\left. \times I_0(2k_0^2\sigma_d^2\alpha) + \frac{\hat{k}_0^2\alpha^2(1-\hat{k}_0^2\alpha^2+4k_0^2\sigma_d^2\alpha-4\hat{k}_0^2k_0^2\sigma_d^2\alpha)I_1(2k_0^2\sigma_d^2\alpha)}{2k_0^2\sigma_d^2\alpha}\right],
\end{aligned} \tag{3.28}$$

and

$$\begin{aligned}
\mathrm{Im}\,\Sigma_1 =& -\frac{\gamma k^4}{4} e^{-2k_0^2\sigma_d^2}\left[I_0(2k_0^2\sigma_d^2) - \frac{I_1(2k_0^2\sigma_d^2)}{2k_0^2\sigma_d^2}\hat{k}_0^2\right] \\
\mathrm{Im}\,\Sigma_2 =& -\frac{\gamma k^4}{4} e^{-2k_0^2\sigma_d^2}\left[\left(1-2\hat{k}_0^2+2\hat{k}_0^4\right) I_0(2k_0^2\sigma_d^2)\right. \\
&\left. + \frac{\hat{k}_0^2(1-\hat{k}_0^2)(1+4k_0^2\sigma_d^2)I_1(2k_0^2\sigma_d^2)}{2k_0^2\sigma_d^2}\right],
\end{aligned} \tag{3.29}$$

where I_n are the modified Bessel function of the first kind. Notice that in the case of the real parts, only the angular integration was performed: the remaining radial integration does not appear to have a simple analytic solution and thus requires to be computed numerically.

Eq.s (3.28) and (3.29) indicate that $\Sigma_1 \neq \Sigma_2$ in general, such that spin-orbit interactions of light do impact the propagation of light in the disorder. As mentioned in the previous section, only in the paraxial limit SOI are expected to vanish. This is indeed the case, as demonstrated in Fig. 3.2, which shows both $\mathrm{Re}(\Sigma_2 - \Sigma_1)$ and $\mathrm{Im}(\Sigma_2 - \Sigma_1)$ vs. $\hat{k}_0^2$ at fixed $k_0\sigma_d$. When $\hat{k}_0^2 \to 0$, we have $\Sigma_1 \to \Sigma_2$, the difference $\Sigma_2 - \Sigma_1$ scaling as $\hat{k}_0^2$ at small $\hat{k}_0$.

3.4.3 Limit of uncorrelated disorder

At this stage, it is instructive to examine the limit of uncorrelated disorder from the present approach. This limit, which was considered in the elementary model employed in [62], can be recovered by simply letting $\sigma_d \to 0$ in Eq.s (3.29). For the imaginary parts, we find:

$$\begin{aligned} \mathrm{Im}\,\Sigma_1(\sigma_d \to 0) &= -\frac{\gamma k^4}{8}\left(2 - \hat{k}_0^2\right) \\ \mathrm{Im}\,\Sigma_2(\sigma_d \to 0) &= -\frac{\gamma k^4}{8}\left[2 - 3\hat{k}_0^2\left(1 - \hat{k}_0^2\right)\right] , \end{aligned} \tag{3.30}$$

implying that $\mathrm{Im}(\Sigma_2 - \Sigma_1) = \gamma k^4 \hat{k}_0^2/4 + \mathcal{O}(\hat{k}_0^2)$. We recover that $\Sigma_1 \to \Sigma_2$ in the paraxial regime $\hat{k}_0^2 \to 0$. Taking the limit $\sigma_d \to 0$ in Eq.s (3.28), on the other hand, leads to $\mathrm{Re}\,\Sigma_1 = \mathrm{Re}\,\Sigma_2 = \infty$. This divergence illustrates the unphysical nature of the model of uncorrelated disorder and the need to develop a more precise description.

3.5 Intensity distribution of the coherent mode

We now evaluate the spatial, intensity distribution of the coherent mode, defined as $I_c(\boldsymbol{r}_\perp, L) = |\langle \boldsymbol{E}(\boldsymbol{r}_\perp, L)\rangle|^2$, where $\langle \boldsymbol{E}(\boldsymbol{r}_\perp, L)\rangle$ is the inverse Fourier transform of Eq. (3.24). Introducing the transverse Fourier components $\boldsymbol{k}_\perp^\pm = \boldsymbol{k}_\perp \pm \boldsymbol{q}/2$, we can write

$$I_c(\boldsymbol{r}_\perp, L) = \int \frac{d^2\boldsymbol{k}_\perp}{(2\pi)^2} \int \frac{d^2\boldsymbol{q}}{(2\pi)^2} e^{i\boldsymbol{q}\cdot\boldsymbol{r}_\perp} \langle \boldsymbol{E}(\boldsymbol{k}_\perp^+, L)\rangle \cdot \langle \boldsymbol{E}^*(\boldsymbol{k}_\perp^-, L)\rangle \, . \tag{3.31}$$

The incident beam (3.1) being collimated around $\boldsymbol{k}_\perp = \boldsymbol{k}_0$, the product of the two average fields can be expanded at small $\boldsymbol{q}$:

$$\begin{aligned} \langle \boldsymbol{E}(\boldsymbol{k}_\perp^+, L)\rangle \cdot \langle \boldsymbol{E}(\boldsymbol{k}_\perp^-, L)\rangle \simeq e^{-w_0^2\boldsymbol{q}^2/8}\big\{ &|\langle \boldsymbol{E}(\boldsymbol{k}_\perp, L)\rangle|^2 \\ &+ \boldsymbol{q}\cdot\boldsymbol{\nabla}_{\boldsymbol{q}}[\langle \boldsymbol{E}(\boldsymbol{k}_\perp^+, L)\rangle \cdot \langle \boldsymbol{E}(\boldsymbol{k}_\perp^-, L)\rangle]|_{\boldsymbol{q}\to 0}\big\} \, . \end{aligned} \tag{3.32}$$

This leads to

$$I_c(\boldsymbol{r}_\perp, L) = \int \frac{d^2\boldsymbol{q}}{(2\pi)^2} e^{-w_0^2\boldsymbol{q}^2/8}\big[1 - i\boldsymbol{q}\cdot\boldsymbol{R}_\perp(L)\big] e^{i\boldsymbol{q}\cdot\boldsymbol{r}_\perp} \int \frac{d^2\boldsymbol{k}_\perp}{(2\pi)^2} |\langle \boldsymbol{E}(\boldsymbol{k}_\perp, L)\rangle|^2 \, , \tag{3.33}$$

where

$$\boldsymbol{R}_\perp(L) = \frac{i\int \frac{d^2\boldsymbol{k}_\perp}{(2\pi)^2} \boldsymbol{\nabla}_{\boldsymbol{q}}[\langle \boldsymbol{E}(\boldsymbol{k}_\perp^+, L)\rangle \cdot \langle \boldsymbol{E}(\boldsymbol{k}_\perp^-, L)\rangle]_{\boldsymbol{q}\to 0}}{\int \frac{d^2\boldsymbol{k}_\perp}{(2\pi)^2} |\langle \boldsymbol{E}(\boldsymbol{k}_\perp, L)\rangle|^2} \equiv \frac{\int d^2\boldsymbol{r}_\perp \boldsymbol{r}_\perp I_c(\boldsymbol{r}_\perp, L)}{\int d^2\boldsymbol{r}_\perp I_c(\boldsymbol{r}_\perp, L)} \tag{3.34}$$

is the beam centroid in the transverse plane (x, y). The integral over $\boldsymbol{q}$ in Eq. (3.33) is dominated by small $\boldsymbol{q}-$values, so that we can accurately replace the term inside the squared brackets by an exponential factor. This finally gives the following expression, valid for $\boldsymbol{r}_\perp \lesssim w_0$:

$$I_c(\boldsymbol{r}_\perp, L) \simeq I_c(L) e^{-2|\boldsymbol{r}_\perp - \boldsymbol{R}_\perp(L)|^2/w_0^2} , \tag{3.35}$$

where $I_c(L)$ is the coherent mode intensity taken at the beam center:

$$I_c(L) \equiv I_0 \int \frac{d^2\boldsymbol{k}_\perp}{(2\pi)^2} |\langle \boldsymbol{E}(\boldsymbol{k}_\perp, L)\rangle|^2 = I_c(\boldsymbol{R}_\perp(L), L) \tag{3.36}$$

with $I_0 \equiv 2/(\pi w_0^2)$.

Eq. (3.35) describes a rigid spatial shift $\boldsymbol{R}_\perp(L)$ of the coherent mode in the transverse plane (x, y). We will show that the most interesting effects due to the spin-orbit term in Eq. (3.24) manifest themselves through this shift. Before that, however, let us briefly discuss the intensity $I_c(L)$ of the coherent mode at the beam center, which can be computed from Eq.s (3.24) and (3.36). Due to the spin-orbit term in Eq. (3.24), the profile of $I_c(L)$ depends on the polarization of the incident beam. For $\boldsymbol{e}_0 \propto \hat{\boldsymbol{x}}' + e^{i\phi}\hat{\boldsymbol{y}}$, we have:

$$I_c(L) = \frac{I_0}{2}\left(e^{L\,\mathrm{Im}\,\Sigma_1/k_z} + e^{L\,\mathrm{Im}\,\Sigma_2/k_z}\right) = \frac{I_0}{2} e^{-L/z_s}(1 + e^{L/z_\mathrm{S}}) , \tag{3.37}$$

where we have introduced $z_\mathrm{S} \equiv k_z/(\mathrm{Im}\,\Sigma_2 - \mathrm{Im}\,\Sigma_1)$. Eq. (3.37) effectively describes an exponential decay of the coherent mode with the medium thickness L, mostly governed by $z_s = -k_z/\,\mathrm{Im}\,\Sigma_1$ since $z_\mathrm{S} \propto z_s/\hat{k}_0^2 \gg z_s$. This justifies a posteriori the definition of the mean free path introduced above. The behaviour of the intensity $I_c(L)$ then is very similar to its paraxial counterpart, with the coherent mode intensity getting attenuated at the scale of a mean free path z_s due to scattering in other directions [17]. To conclude this section, we finally provide the explicit expression of z_s:

$$z_s^{-1} = \gamma k^3 \frac{e^{-2k_0^2\sigma_d^2}}{4\sqrt{1-\hat{k}_0^2}} \left[I_0(2k_0^2\sigma_d^2) - \frac{\hat{k}_0^2 I_1(2k_0^2\sigma_d^2)}{2k_0^2\sigma_d^2} \right] , \tag{3.38}$$

which will be used for the numerical plots in the following.

3.6 Centroid of the coherent mode

3.6.1 Calculation of the centroid

In this section, we compute the exact expression of the coherent mode centroid $\boldsymbol{R}_\perp(L)$ defined in Eq. (3.34). To this aim, we calculate the integrand in Eq. (3.34) using the general expression (3.24) of the momentum distribution of the disorder-average electric field. For an arbitrary polarization $\boldsymbol{e}_0$, this integrand reads:

$$\begin{aligned}
\langle \boldsymbol{E}(\boldsymbol{k}_\perp^+, L)\rangle \cdot \langle \boldsymbol{E}^*(\boldsymbol{k}_\perp^-, L)\rangle = {} & 2\pi w_0^2 \exp\left[-w_0^2(\boldsymbol{k}_\perp - \boldsymbol{k}_0)^2/2 - w_0^2\boldsymbol{q}^2/8 + i(k_z^+ - k_z^-)L\right] \\
& \times \Big\{ |e^{-i\Sigma_1 L/2k_z}|^2 - |\boldsymbol{e}_0 \cdot \hat{\boldsymbol{e}}_\perp^-|^2 \left[|e^{-i\Sigma_1 L/2k_z}|^2 - e^{-i(\Sigma_1 - \Sigma_2^*)L/2k_z}\right] \\
& - |\boldsymbol{e}_0 \cdot \hat{\boldsymbol{e}}_\perp^+|^2 \left[|e^{-i\Sigma_1 L/2k_z}|^2 - e^{-i(\Sigma_2 - \Sigma_1^*)L/2k_z}\right] + (\boldsymbol{e}_0 \cdot \hat{\boldsymbol{e}}_\perp^+)(\boldsymbol{e}_0^* \cdot \hat{\boldsymbol{e}}_\perp^-) \\
& \times \left[|e^{-i\Sigma_1 L/2k_z}|^2 + |e^{-i\Sigma_2 L/2k_z}|^2 - e^{-i(\Sigma_1 - \Sigma_2^*)L/2k_z} - e^{-i(\Sigma_2 - \Sigma_1^*)L/2k_z}\right] \Big\} ,
\end{aligned} \tag{3.39}$$

where $\hat{\boldsymbol{e}}_\perp^\pm = \hat{\boldsymbol{e}}_\perp \pm \boldsymbol{q}/(2k_\perp)$, with $\hat{\boldsymbol{e}}_\perp = \boldsymbol{k}_\perp/k_\perp$, and $k_z^\pm = \sqrt{k^2 - \boldsymbol{k}_\perp^\mp}$. In this expression, the only non-zero contributions to the $\boldsymbol{q}$-gradient in Eq. (3.34) are

$$\boldsymbol{\nabla}_{\boldsymbol{q}} \exp\big\{[i(k_z^+ - k_z^-)L]\big\}|_{\boldsymbol{q}\to 0} = -\, i\hat{\boldsymbol{k}}_\perp L \tag{3.40}$$

$$\boldsymbol{\nabla}_{\boldsymbol{q}} |\boldsymbol{e}_0 \cdot \hat{\boldsymbol{e}}_\perp^\pm|^2|_{\boldsymbol{q}\to 0} = \pm\, \frac{1}{k_\perp}\, \mathrm{Re}[\boldsymbol{e}_0(\boldsymbol{e}_0^* \cdot \hat{\boldsymbol{e}}_\perp)] \tag{3.41}$$

$$\boldsymbol{\nabla}_{\boldsymbol{q}} (\boldsymbol{e}_0 \cdot \hat{\boldsymbol{e}}_\perp^+)(\boldsymbol{e}_0^* \cdot \hat{\boldsymbol{e}}_\perp^-)|_{\boldsymbol{q}\to 0} = \frac{i}{k_\perp}\, \mathrm{Im}[\boldsymbol{e}_0(\boldsymbol{e}_0^* \cdot \hat{\boldsymbol{e}}_\perp)]\ . \tag{3.42}$$

Eq.s (3.41) and (3.42) involve a coupling between the beam polarization $\boldsymbol{e}_0$ and the momentum, which will be eventually responsible for a spin Hall effect. It is interesting to notice, however, that this coupling effectively operates only when the incident beam is prepared in a polarization state involving both the $\hat{\boldsymbol{x}}'$ and $\hat{\boldsymbol{y}}$ axis directions. Indeed, if $\boldsymbol{e}_0 = \hat{\boldsymbol{y}}$ the scalar product $\boldsymbol{e}_0 \cdot \boldsymbol{k}_\perp \simeq \boldsymbol{e}_0 \cdot \boldsymbol{k}_0 \propto \hat{\boldsymbol{x}} \cdot \hat{\boldsymbol{y}} = 0$. On the other hand, if $\boldsymbol{e}_0 = \hat{\boldsymbol{x}}'$ the gradients (3.41) and (3.42) provide a contribution that is aligned with the $\hat{\boldsymbol{x}}$ axis and is negligible compared to that of Eq. (3.40).

For a incident polarization of the form

$$\boldsymbol{e}_0 = \frac{\alpha\hat{\boldsymbol{x}}' + \beta\hat{\boldsymbol{y}}}{\sqrt{\alpha^2 + \beta^2}} \tag{3.43}$$

(with $\alpha \in \mathbb{R}$, $\beta \in \mathbb{C}$ and $|\alpha|^2 + |\beta|^2 = 1$), the centroid of the coherent mode $\boldsymbol{R}_\perp$ then acquires the following form:

$$\boldsymbol{R}_\perp(L) \simeq \hat{\boldsymbol{k}}_0 L + R_y(L)\hat{\boldsymbol{y}}\ . \tag{3.44}$$

In addition to the purely ballistic contribution $\hat{\boldsymbol{k}}_0 L$ directed along $\hat{\boldsymbol{k}}_0 = \hat{k}_0\hat{\boldsymbol{x}}$, which coincides with the position of the beam centroid expected in the paraxial regime, a shift of the beam centroid in the $\hat{\boldsymbol{y}}$ direction shows up. This new contribution stems from the spin-orbit correction term in Eq. (3.24), arising beyond the paraxial description. The shift $R_y(L)$ transverse to the direction of light propagation, as will be elucidated below, features a spin Hall effect of light. Such term, contrary to the ballistic contribution, depends strongly on the incident beam polarization. Its value is maximum when the incident polarization is balanced, i.e. $|\alpha|^2 = |\beta|^2 = 1/2$. For this reason, as anticipated in Sec. 3.1, we consider from now on the initial polarization state

$$\boldsymbol{e}_0 = \frac{\hat{\boldsymbol{x}}' + e^{i\phi}\hat{\boldsymbol{y}}}{\sqrt{2}} \tag{3.45}$$

with ϕ being an arbitrary phase. For such initial polarization state, the transverse shift $R_y(L)$ is given by[1]

$$R_y(L) = -\frac{\sin\phi}{k_0}\left[1 - \frac{\cos L/2z_\mathrm{L}}{\cosh L/2z_\mathrm{S}}\right] + \frac{\cos\phi}{k_0}\frac{\sin L/2z_\mathrm{L}}{\cosh L/2z_\mathrm{S}}. \tag{3.46}$$

[1]Eq. (3.46) turns out to hold as well for arbitrary value of $\hat{k}_0$, provided the $1/k_0$ prefactors are replaced by $(1 - \hat{k}_0^2)^{-1/2}/k_0$. This implies the spin Hall effect also exists at large angle of incidence, although its amplitude tends to decrease when approaching the regime of grazing incidence.

The evolution of this transverse motion is governed by the polarization phase ϕ and the two core parameters

$$\begin{aligned} z_{\mathrm{L}} =& \frac{k_z}{\mathrm{Re}\,\Sigma_2 - \mathrm{Re}\,\Sigma_1} \\ z_{\mathrm{S}} =& \frac{k_z}{\mathrm{Im}\,\Sigma_2 - \mathrm{Im}\,\Sigma_1} \,, \end{aligned} \tag{3.47}$$

which represent respectively the longitudinal length scales over which SOI modify the phase and the amplitude of the coherent mode.

3.6.2 Length scales of the spin-orbit interactions

Using the on-shell values of Σ_1 and Σ_2 (3.28)-(3.29), we obtain the following analytic expressions for the SOI lengths z_{L} and z_{S}:

$$\begin{aligned} \frac{1}{z_{\mathrm{L}}} =& \gamma k^3 p.v. \int_0^\infty \frac{\hat{k}_0^2 e^{-k_0^2\sigma_d^2(1+\alpha^2)} \alpha d\alpha}{4\pi k_0^2\sigma_d^2\sqrt{1-\hat{k}_0^2}(1-\alpha^2)} \big\{ 2k_0^2\sigma_d^2 \big[-2\alpha^2 + \hat{k}_0^2(1+\alpha^4) \big] I_0(2k_0^2\sigma_d^2\alpha) \\ &+ \alpha \big[2 + 4(1-\hat{k}_0^2)k_0^2\sigma_d^2\alpha - \hat{k}_0^2\alpha^2 \big] I_1(2k_0^2\sigma_d^2\alpha) \big\} \end{aligned} \tag{3.48}$$

and

$$\begin{aligned} \frac{1}{z_{\mathrm{S}}} =& \gamma k^3 \frac{\hat{k}_0^2 e^{-2k_0^2\sigma_d^2}}{8k_0^2\sigma_d^2\sqrt{1-\hat{k}_0^2}} \big[4(1-\hat{k}_0^2)k_0^2\sigma_d^2 I_0(2k_0^2\sigma_d^2) \\ &- (2 + 4k_0^2\sigma_d^2 - \hat{k}_0^2(1+4k_0\sigma^2)) I_1(2k_0^2\sigma_d^2) \big] \,. \end{aligned} \tag{3.49}$$

Note that both z_{L} and z_{S} are functions of two independent parameter: $\hat{k}_0^2$, the deviation from paraxiality, and $k_0\sigma_d$, the disorder correlation. In particular, according to Sec. 3.4.2 and Fig. 3.2, both z_{L}^{-1} and z_{S}^{-1} vanish in the paraxial limit, where $\hat{\boldsymbol{k}}_0 \to 0$ at fixed $\hat{k}_0\sigma_d$ (since $\Sigma_1 \to \Sigma_2$).

The SOI parameters z_{L} and z_{S} are also shown in Fig. 3.3 as a function of $k_0\sigma_d$, for fixed $\hat{k}_0$. At large $k_0\sigma_d$, both z_{L}^{-1} and z_{S}^{-1} vanish, as expected since at large σ_d everything goes as if no disorder was present. Another interesting property revealed by this plot is the possibility to cancel either z_{L}^{-1} or z_{S}^{-1} by a proper choice of the parameter $k_0\sigma_d$, tunable either via the disorder correlation σ_d or the transverse momentum k_0 (points A and B, respectively). This property will be discussed in detail in the next section. From a mathematical point of view, such a cancellation could have been anticipated given the definition of z_{L} and z_{S}. Indeed, while the sign of both $\mathrm{Im}\,\Sigma_1$ and $\mathrm{Im}\,\Sigma_2$ is always negative (disorder induces extinction), their difference can have an arbitrary sign (with a similar argument for $\mathrm{Re}\,\Sigma_{1(2)}$).

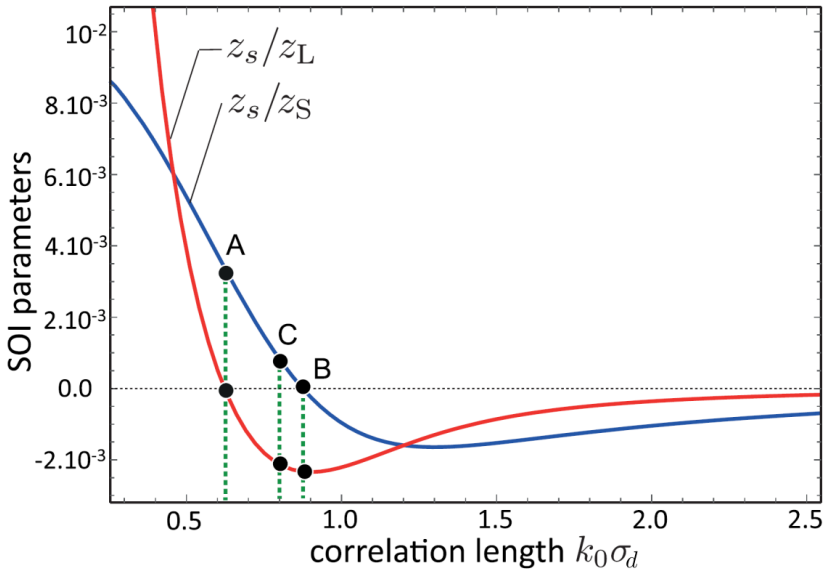

Figure 3.3: Length scales $z_{\rm L}$ and $z_{\rm S}$ controlling the spin Hall effect of light affecting the coherent mode as a function of $k_0\sigma_d$, for $\hat{k}_0 = 0.1$ and in units of the effective scattering mean free time z_s. At the points A ($k_0\sigma_d = 0.6229$) and B ($k_0\sigma_d = 0.8749$), we have $z_{\rm L} = \infty$ and $z_{\rm S} = \infty$, respectively. At the generic point C ($k_0\sigma_d = 0.84$), both $z_{\rm L}$ and $z_{\rm S}$ are finite.

3.6.3 Spin Hall effect of the coherent mode

In order to discuss the various types of transverse trajectories the coherent mode may undergo, let us here recall the obtained expression of the beam centroid transverse shift R_y as a function of the medium longitudinal length L [67]:

$$R_y(L) = -\frac{\sin\phi}{k_0}\left[1 - \frac{\cos L/2z_{\rm L}}{\cosh L/2z_{\rm S}}\right] + \frac{\cos\phi}{k_0}\frac{\sin L/2z_{\rm L}}{\cosh L/2z_{\rm S}}\,. \tag{3.50}$$

The first term in Eq. (3.50) was originally discovered in [62], for an elementary model of uncorrelated disordered and discarding refractive-index effects (i.e., taking $\mathrm{Re}\,\Sigma_1 = \mathrm{Re}\,\Sigma_2 = 0$), see Sec. 1.7. Under these approximations, $z_{\rm L} \to \infty$ and $z_{\rm S} \to z_s/\hat{k}_0^2$, so that $R_y(z) = -\sin\phi/k_0[1 - \cosh^{-1}(z\hat{k}_0^2/2z_s)]$. This describes a monotonic transverse shift existing only for beams having a finite helicity (or spin) $\sigma = \sin\phi$, i.e., a phenomenon fully analogous to an electronic spin Hall effect, where σ plays the role of the electronic spin. In the more realistic case considered here, however, the physics pertaining to Eq. (3.50) is much richer since the presence of the transverse shift is not restricted to incident light having a finite helicity. Furthermore, the modifications of the refractive index due to SOI (associated with $\mathrm{Re}\,\Sigma_{1(2)} \neq 0$) give rise to spatial *oscillations* of the beam at the scale of $z_{\rm L}$, modulating a monotonic component governed by $z_{\rm S}$. Looking carefully at the derivation of $R_y(L)$ and at the expression (3.24) for the disorder-average field, one realizes that these oscillations originate from the interference between the SOI term and itself, and between the SOI term and the paraxial one.

Together with a change of ϕ, the dependence of the SOI parameters $z_{\rm L}$ and $z_{\rm S}$ on the disorder correlation $k_0\sigma_d$ illustrated in Fig. 3.3 makes it possible to significantly change

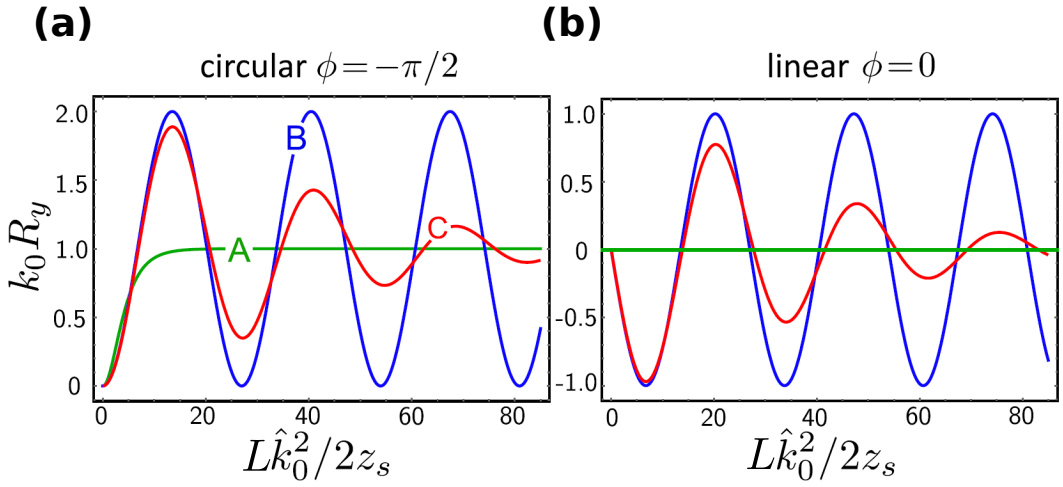

Figure 3.4: (a) $R_y(L)$ for circularly polarized incident light ($\phi = -\pi/2$), at $\hat{k}_0 = 0.1$. The three trajectories correspond to the points A, B, and C of Fig. 3.3, where SOI respectively affect only the amplitude ($z_{\rm L} = \infty$), only the phase ($z_{\rm S} = \infty$), and both the phase and amplitude ($z_{\rm L(S)}$ finite) of the wavefront. In cases B and C, a SHE oscillating around k_0^{-1} appears. (b) For a beam linearly polarized at 45° in the plane (x', y) [$\phi = 0$], a SHE is also present but oscillates around 0.

the behaviour of the transverse trajectory $R_y(L)$ with L, thus offering the possibility to tailor various types of spin Hall effects via a tuning of $k_0\sigma_d$. To illustrate this idea, we show in Fig. 3.4a for a circular incident polarization ($\phi = -\pi/2$) the transverse motion realized at points A and B, where we have, respectively, $z_{\rm L} = \infty$ and $z_{\rm S} = \infty$, as well as at point C which depicts a generic configuration where both $z_{\rm L}$ and $z_{\rm S}$ are finite. In configuration A, SOI only affect the amplitude of the wavefront. This leads to a monotonic increase of $R_y(L)$ toward the asymptotic value $1/k_0$ for $L \gg z_{\rm S}$, effectively reproducing the result of [62]. In case B, in contrast, SOI are purely of phase origin, and $R_y(L)$ exhibits oscillations around $1/k_0$. In the generic case C, finally, the oscillations are present but damped over a length of the order of few $z_{\rm S}$.

Another interesting prediction of Eq. (3.50) is that a SHE, this time oscillating around 0, can arise even for linearly polarized beams ($\phi = 0$), i.e., without initial spin, see Fig. 3.4b. The origin of this a priori surprising phenomenon will be elucidated in Sec. 3.8.

3.7 Polarization evolution

We have seen that the presence of the SOI term in the disorder-average field gives rise to a transverse shift of the beam centroid along $\hat{\boldsymbol{y}}$. This directly illustrates the notion of spin-orbit coupling, where the polarization degree of freedom impacts the trajectory of the coherent mode. The coupling, however, also works the other way around: the change of trajectory should also affect the polarization, i.e., we expect the spin Hall effect of the coherent mode to be accompanied by a complementary evolution with L of its mean polarization direction $\boldsymbol{e}(L)$. The latter follows directly

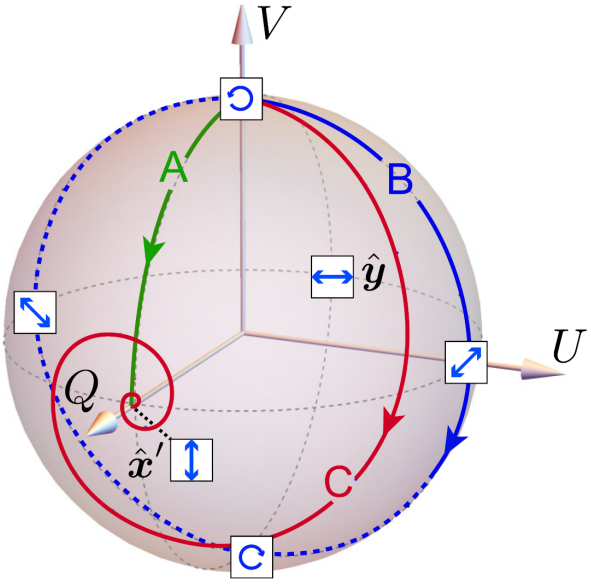

Figure 3.5: Evolution of the polarization state $\boldsymbol{e}(L)$ on the Poincaré sphere when starting from a circularly polarized beam ($\phi = \pi/2$), in configurations A, B, and C. Axes are parametrized by the Stokes parameters U, V, and Q, which give the normalized amount of light polarized linearly along x' or y axis, linearly polarized at $\pm 45°$ in the (x', y) plane, and circularly polarized, respectively (see Appendix A for the definitions of U, V, Q).

from Eq. (3.24). Using the fact that the momentum distribution of the coherent mode always remains peaked around the incident wave vector $\boldsymbol{k}_0$, we have $\boldsymbol{e}(L) \simeq \langle \boldsymbol{E}(\boldsymbol{k}_0, L)\rangle / |\langle \boldsymbol{E}(\boldsymbol{k}_0, L)\rangle|$, with

$$\langle \boldsymbol{E}(\boldsymbol{k}_0, L)\rangle \propto \left(e^{-i\Sigma_2 L/2k_z} \hat{\boldsymbol{x}}' + e^{i\phi} e^{-i\Sigma_1 L/2k_z} \hat{\boldsymbol{y}} \right) \tag{3.51}$$

for $\boldsymbol{e}_0 \propto \hat{\boldsymbol{x}}' + e^{i\phi}\hat{\boldsymbol{y}}$. Notice that Eq. (3.51) showcases the system's anisotropy in the (x', y) plane when $\hat{k}_0 \neq 0$ ($\Sigma_1 \neq \Sigma_2$). It also indicates that SOI naturally imprint simultaneously birefringence and dichroism to the random medium. In fact, Σ_1 and Σ_2 can be seen as the self-energies along the polarization modes $\hat{\boldsymbol{y}}$ and $\hat{\boldsymbol{x}}'$, respectively. From Eq. (3.51), we straightforwardly infer the explicit evolution of the polarization state:

$$\boldsymbol{e}(L) = \frac{\hat{\boldsymbol{x}}' + e^{i\phi + iL/2z_{\mathrm{L}}} e^{-L/2z_{\mathrm{S}}} \hat{\boldsymbol{y}}}{\sqrt{1 + e^{-L/z_{\mathrm{S}}}}} \,, \tag{3.52}$$

which is represented on the Poincaré sphere of Fig. 3.5 for a incident circularly-polarized beam, in the three configurations introduced above. In case A, the polarization directly turns from circular to linear following the shortest path on the Poincaré sphere. As will be discussed in the next section, this describes a direct conversion of the optical spin into orbital momentum [163]. On the other hand, in the generic configuration C where SOI impact both the amplitude and the phase of the wavefront, the transverse damped oscillations of the beam are associated with a spiral trajectory on the Poincaré sphere, i.e., a damped oscillation of the helicity. In the case $z_{\mathrm{S}} > 0$

considered here, these oscillations converge to the attractor state $\boldsymbol{e}(L \gg z_{\mathrm{S}}) = \hat{\boldsymbol{x}}'$, as can be seen from Eq. (3.52). For $z_{\mathrm{S}} < 0$ (corresponding to the right of point B in Fig. 3.3), the evolution would follow a similar trajectory but in the negative-Q plane, converging to the attractor state $\boldsymbol{e}(L \gg |z_{\mathrm{S}}|) = \hat{\boldsymbol{y}}$. In the peculiar configuration B, finally, the undamped oscillations are associated with a periodic evolution of the polarization state on the Poincaré sphere.

3.8 Conservation of angular momentum

In this section, we show how the presented evolutions of $R_y(L)$ and $\boldsymbol{e}(L)$ appear to be dual. Their interconnection originates from the conservation of the total angular momentum of the coherent mode along the optical axis $\hat{\boldsymbol{z}}$, which comes from the statistical isotropy in the (x, y) plane. Generally speaking, analyzing the angular momentum carried by light and its composition is a natural approach for highlighting SOI of light in photonic materials [163]. Indeed, SOI effects typically cause conversions between the different angular momentum degrees of freedom [48]. Here we apply this idea to the spin Hall effect of light of the coherent mode, providing an additional argument for its SOI origin.

The orbital component of the angular momentum carried by the coherent mode in $\epsilon_0/(2\omega)$ units is defined as (see Appendix B) [164]

$$\boldsymbol{L}(L) = -\frac{i\int d^2\boldsymbol{r}_\perp \langle E_i^*(\boldsymbol{r}_\perp, L)\rangle (\boldsymbol{r}\times\boldsymbol{\nabla})\langle E_i(\boldsymbol{r}_\perp, L)\rangle}{\int d^2\boldsymbol{r}_\perp |\langle \boldsymbol{E}(\boldsymbol{r}_\perp, L)\rangle|^2} , \tag{3.53}$$

where the summation over repeated polarization indices (Einstein convention) is understood. Such notational convention will be use throughout the thesis. In the transverse Fourier domain, the integrand in the numerator reads

$$\begin{aligned}\langle E_i^*(\boldsymbol{r}_\perp, L)\rangle (\boldsymbol{r}\times\boldsymbol{\nabla})\langle E_i(\boldsymbol{r}_\perp, L)\rangle = \int \frac{d^2\boldsymbol{K}_\perp}{(2\pi)^2}\int \frac{d^2\boldsymbol{q}}{(2\pi)^2}\langle E_i^*(\boldsymbol{k}_\perp^-, L)\rangle[(-i\boldsymbol{\nabla}_{\boldsymbol{q}} + L\hat{\boldsymbol{z}})\\ \times (i\boldsymbol{k}_\perp^+ + ik_z^+\hat{\boldsymbol{z}})]\langle E_i(\boldsymbol{k}_\perp^+, L)\rangle e^{i\boldsymbol{q}\cdot\boldsymbol{r}_\perp} ,\end{aligned} \tag{3.54}$$

where $\boldsymbol{k}_\perp^\pm = \boldsymbol{K}_\perp \pm \boldsymbol{q}/2$ and $k_z^+ = \sqrt{k^2 - \boldsymbol{k}_\perp^{+2}}$. After performing the integrations over $\boldsymbol{r}_\perp$ and $\boldsymbol{q}$, one gets

$$\boldsymbol{L}(L) = \boldsymbol{R}(L)\times\boldsymbol{k} , \tag{3.55}$$

where $\boldsymbol{R}(L) = \boldsymbol{R}_\perp(L) + L\hat{\boldsymbol{z}}$ and $\boldsymbol{k} = \boldsymbol{k}_0 + k_z\hat{\boldsymbol{z}}$. The orbital angular momentum along z then reads

$$L_z(L) = k_0 R_y(L) . \tag{3.56}$$

On the other hand, the spin component of the coherent mode's total angular momentum is given in $\epsilon_0/(2\omega)$ units by (see Appendix B) [164]

$$\boldsymbol{S}(L) = -\frac{i\int d^2\boldsymbol{r}_\perp \langle \boldsymbol{E}^*(\boldsymbol{r}_\perp, L)\rangle \times \langle \boldsymbol{E}(\boldsymbol{r}_\perp, L)\rangle}{\int d^2\boldsymbol{r}_\perp |\langle \boldsymbol{E}(\boldsymbol{r}_\perp, L)\rangle|^2} . \tag{3.57}$$

Its projection along z, $S_z(L)$, coincides with $V(L) = 2\int d^2\boldsymbol{r}_\perp \mathrm{Im}(\langle E_x^*\rangle\langle E_y\rangle)/\int d^2\boldsymbol{r}_\perp I_c$, the Stokes parameter appearing in the vertical axis of Fig. 3.5, which gives the amount

of circularly polarized light in the beam. In our system, the longitudinal spin angular momentum carried by the coherent mode then equals to

$$S_z(L) = V(L) = \frac{\sin\big(\phi + L/2z_{\mathrm{L}}\big)}{\cosh L/2z_{\mathrm{S}}} \,. \tag{3.58}$$

Putting together Eq.s (3.56) and (3.58), the following equalities hold true

$$J_z = L_z(L) + S_z(L) = k_0 R_y(L) + V(L) = \sin\phi = V(0) = \text{constant} \,. \tag{3.59}$$

Eq. (3.59) illustrates the fundamental dual nature of the $R_y(L)$ and $\boldsymbol{e}(L)$ evolutions, originating from the conservation of the coherent mode's total angular momentum. Note that the value of the conserved quantity $L_z + S_z$ is solely fixed by the incident beam helicity $\sigma = \sin\phi$. Eq. (3.59) implies a mutual conversion between orbital and spin angular momentum [163]. For $\phi = \pi/2$, for instance, with the system in configuration A the initial spin is monotonically converted into orbital momentum while the beam is monotonically shifted. In cases B and C, in contrast, the exchange between $V(L)$ and $R_y(L)$ involves successive mutual conversions, hence the periodic trajectories.

Together with Eq. (3.51), the conservation of total angular momentum also sheds light on the second term in Eq. (3.50) for the transverse shift $R_y(L)$, $\frac{\cos\phi}{k_0}\frac{\sin L/2z_{\mathrm{L}}}{\cosh L/2z_{\mathrm{S}}}$, which predicts a SHE for a spinless incident beam, i.e., $V(0) = 0$. In this case, the coherent mode *spontaneously* acquires a finite spin thanks to the birefringence effect brought by SOI, Eq. (3.51). A transverse motion then spontaneously appears, satisfying Eq. (3.59). Interestingly, the SOI birefringence resembles the magneto-optic Voigt (or Cotton-Mouton) effect, where a magnetic field perpendicular to the direction of propagation converts a linear polarization into an elliptic one [165]. In our scenario, the role of the magnetic field is played by $\boldsymbol{k}_0$. The analogy ends here though, since no transverse motion arises in the Voigt effect.

3.9 Practical observation

Under normal conditions, the oscillating spin Hall effect described above is difficult to detect experimentally for two main reasons. First, because it occurs at the scale k_0^{-1}. Although this scale greatly exceeds the optical wavelength since $k_0 \ll k$ for near-paraxial light, it remains small compared to the beam width w_0 given that, by hypothesis, the beam is well collimated, $k_0 w_0 \gg 1$. Second, because the coherent mode attenuates as $\exp\big(-L/z_s\big)$ due to multiple scattering. Generally speaking, the oscillating SHE occurs at the scales of the SOI parameters, i.e., at $L \sim z_{L(S)} \propto z_s/\hat{k}_0^2 \gg z_s$. At such optical thickness, however, the intensity of the diffusive halo is dominant over the one of the coherent mode, making the experimental detection of the latter and of its transverse displacement difficult. In this section, we provide first insights on what one could do to nevertheless make this phenomenon experimentally observable.

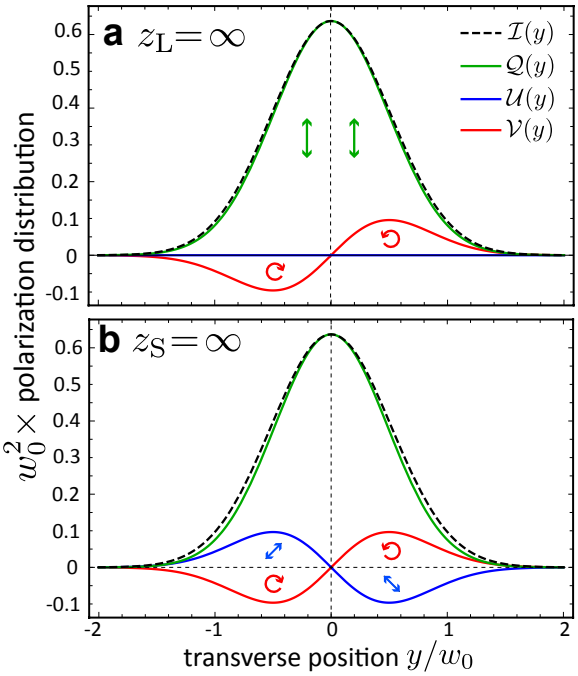

Figure 3.6: Spatially resolved Stokes parameters along direction y of a beam prepared with initial polarization $\boldsymbol{e}_0 = \hat{\boldsymbol{x}}'$, after a propagation distance $z = L$ in the random medium, for $\hat{k}_0 = 0.1$. Axes are normalized using the beam width w_0, and we set $k_0 w_0 = 8$. $I(y)$ is the total intensity distribution, $Q(y)$ and $U(y)$ are, respectively, the distribution of light linearly polarized along $\hat{\boldsymbol{x}}'(\hat{\boldsymbol{y}})$ and $(\hat{\boldsymbol{x}}' \pm \hat{\boldsymbol{y}})/\sqrt{2}$, and $V(y)$ is the distribution of circularly polarized light. Panel (a) corresponds to configuration A ($z_L = \infty$), with $L/z_S = 3\pi$. Panel (b) corresponds to configuration B ($z_S = \infty$), with $L/z_L = -\pi$.

3.9.1 Weak measurement via polarimetry

As mentioned in the first chapter, the spin Hall effect of light at interfaces, although naturally small as it occurs at sub-wavelength scales, has been successfully observed thanks to a pre-selection and post-selection polarimetric technique inspired by weak-measurement methods [51, 52, 166]. This measuring procedure was first proposed in 1988 within a quantum mechanics framework [167] and later extended with profit to the optical domain [168], and now represents a standard laboratory tool [169].

As in deterministic systems, the method of weak quantum measurements makes it possible to amplify the spin Hall effect in a random dielectric medium as well. Here we explain how it can be exploited to selectively amplify both contributions to the transverse shift of the coherent mode centroid appearing in Eq. (3.50). To this aim, we consider an incident beam linearly polarized along $\boldsymbol{e}_0 = \hat{\boldsymbol{x}}'$. As mentioned in Sec. 3.6.1, with this initial state, the transverse shift of the coherent beam $R_y(L)$ is zero. This means that there is no overall SHE of the coherent mode. This is, however, not the case at the level of the *spatial* distribution of the latter. To see this, in Fig. 3.6 we show the spatially-resolved Stokes parameters of the coherent mode along the transverse direction y at a fixed, finite value of $z = L$. Such parameters respectively

represent the distributions of circularly polarized light

$$\mathcal{V}(y) = \frac{2\,\mathrm{Im}[\langle E_x^*(x=0,y,L)\rangle\langle E_y(x=0,y,L)\rangle]}{\int d^2\boldsymbol{r}_\perp I_c(\boldsymbol{r}_\perp,L)}\,, \tag{3.60}$$

the distribution of light linearly polarized along the x' or y axes

$$\mathcal{Q}(y) = \frac{|\langle E_x^*(x=0,y,L)\rangle|^2 - |\langle E_y(x=0,y,L)\rangle|^2}{\int d^2\boldsymbol{r}_\perp I_c(\boldsymbol{r}_\perp,L)}\,, \tag{3.61}$$

and the distribution of light linearly polarized at $\pm 45°$ in the (x',y) plane

$$\mathcal{U}(y) = \frac{2\,\mathrm{Re}[\langle E_x^*(x=0,y,L)\rangle\langle E_y(x=0,y,L)\rangle]}{\int d^2\boldsymbol{r}_\perp I_c(\boldsymbol{r}_\perp,L)}\,. \tag{3.62}$$

These polarization distributions satisfy $\mathcal{Q}^2+\mathcal{V}^2+\mathcal{U}^2=\mathcal{I}^2$, with

$$\mathcal{I}(y) = \frac{|\langle E_x^*(x=0,y,L)\rangle|^2 + |\langle E_y(x=0,y,L)\rangle|^2}{\int d^2\boldsymbol{r}_\perp I_c(\boldsymbol{r}_\perp,L)}\,, \tag{3.63}$$

the intensity distribution along y.

We first discuss the case of a disorder prepared in configuration A ($z_\mathrm{L}=\infty$, Fig. 3.6a), where SOI do not affect the phase of the wavefront and, hence, only the first term in the right-hand-side of Eq. (3.50) is expected. In terms of polarization distributions, this now manifests itself by the fact that $\mathcal{U}(y)=0$, namely no SHE involving light polarized at $\pm 45°$ in the (x',y) plane will be present in such configuration. The effect of SOI is then to split a small portion of the incident beam into two components of circularly polarized light with opposite helicity, as described by the asymmetric shape of the $\mathcal{V}$ distribution in Fig. 3.6a. By detecting light by means of a nearly-orthogonal polarizer $\boldsymbol{e}_\mathrm{out}\propto\hat{\boldsymbol{y}}+i\delta\hat{\boldsymbol{x}}'$ with $|\delta|\ll 1$, one can then eliminate the main $\mathcal{Q}$ component, and select out either the positive or negative $\mathcal{V}$ contributions depending on the sign of δ. Spatially, these contributions are typically shifted by the beam width w_0.

Let us now consider the general scenario where z_L is finite. In this case, we find that $\mathcal{U}(y)$ is not zero any more, i.e., a small part of the beam further splits into two components linearly polarized along $(\hat{\boldsymbol{x}}'\pm\hat{\boldsymbol{y}})/\sqrt{2}$ during propagation. This is displayed in Fig. 3.6b in the particular limit $z_\mathrm{S}=\infty$ (configuration B). This more general polarization structure offers the possibility to selectively magnify either the first or the second term in Eq. (3.50), by respectively post-selecting out the V or U components. To select and amplify the first term, the procedure is as described above, i.e., one detects the beam using a post-selection polarizer $\boldsymbol{e}_\mathrm{out}\propto\hat{\boldsymbol{y}}+i\delta\hat{\boldsymbol{x}}'$. If, on the other hand, one wishes to observe and amplify the second term in Eq. (3.50), the U component of the polarization distribution must be selected out. In the same spirit, this can be achieved using a post-selection polarizer $\boldsymbol{e}_\mathrm{out}\propto\hat{\boldsymbol{y}}+\delta\hat{\boldsymbol{x}}'$.

In the weak-measurement scheme just described, one performs a post-selection of the transmitted light along a polarization direction $\boldsymbol{e}_\mathrm{out}$, so that the beam centroid is now defined as

$$\boldsymbol{R}_\perp(L) = \frac{\int d^2\boldsymbol{r}_\perp \boldsymbol{r}_\perp |\langle \boldsymbol{e}_\mathrm{out}^*\cdot\boldsymbol{E}(\boldsymbol{r}_\perp,L)\rangle|^2}{\int d^2\boldsymbol{r}_\perp |\langle \boldsymbol{e}_\mathrm{out}^*\cdot\boldsymbol{E}(\boldsymbol{r}_\perp,L)\rangle|^2}. \tag{3.64}$$

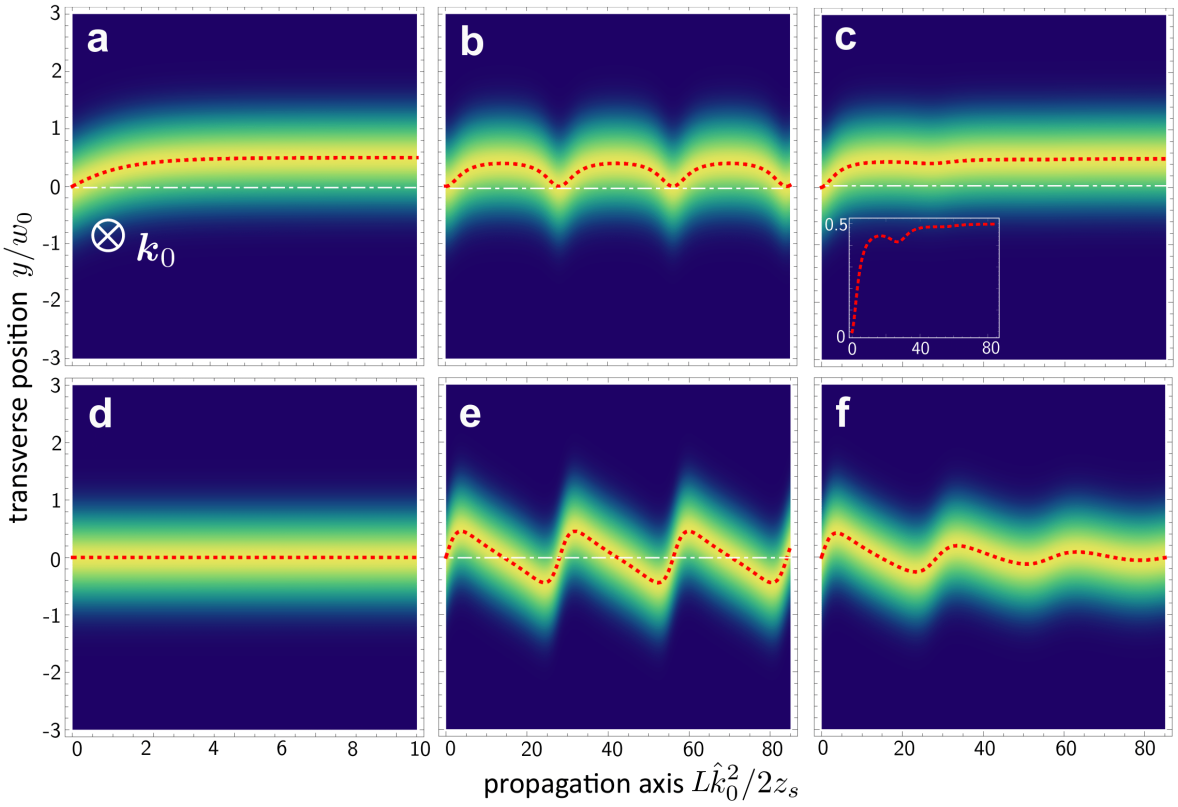

Figure 3.7: Normalized intensity of the coherent mode post-selected by a polarizer $\boldsymbol{e}_{\rm out}$ ("weak measurement"):$|\langle \boldsymbol{e}^*_{\rm out} \cdot \boldsymbol{E}(\boldsymbol{r}_\perp, L)\rangle|^2 / \int d^2\boldsymbol{r}_\perp |\langle \boldsymbol{e}^*_{\rm out} \cdot \boldsymbol{E}(\boldsymbol{r}_\perp, L)\rangle|^2$. In panels (a), (b), and (c) $\boldsymbol{e}_{\rm out} \propto \hat{\boldsymbol{y}} + i\delta\hat{\boldsymbol{x}}'$ with $\delta = (k_0 w_0)^{-1}$ was employed, while in panels (d), (e), and (f) $\boldsymbol{e}_{\rm out} \propto \hat{\boldsymbol{y}} + \delta\hat{\boldsymbol{x}}'$ was used. Panels (a) and (d) have been computed in configuration A, while panels (b) and (e) at the B point, and panels (c) and (f) in configuration C. Dotted curves indicate the beam centroid along y, $R^\delta_y(L)$ [in panel (c) the inset also shows a zoom of $R^\delta_y(L)$]. Notice that the SHE is here of the order of the beam width w_0.

The intensity distributions of the coherent mode following the weak measurement post-selection are obtained by inserting Eq. (3.24) and the definitions of the SOI parameters $z_{\rm S}$ and $z_{\rm L}$ into Eq. (3.64). This gives the following expressions for the projection of the beam centroid onto the y axis:

$$R_y^{\delta}(L) = -\frac{\delta}{k_0}\frac{1 - e^{-L/2z_{\rm S}}\cos\big(L/2z_{\rm L}\big)}{\delta^2 + \big(\frac{1}{k_0 w_0}\big)^2|1 - e^{-L/2z_{\rm S}}e^{iL/2z_{\rm L}}|^2} \tag{3.65}$$

for $\boldsymbol{e}_{\rm out} \propto \hat{\boldsymbol{y}} + i\delta\hat{\boldsymbol{x}}'$, yielding an effective amplification of the first term in Eq. (3.50), and

$$R_y^{\delta}(L) = \frac{\delta}{k_0}\frac{e^{-L/2z_{\rm S}}\sin\big(L/2z_{\rm L}\big)}{\delta^2 + \big(\frac{1}{k_0 w_0}\big)^2|1 - e^{-L/2z_{\rm S}}e^{iL/2z_{\rm L}}|^2} \tag{3.66}$$

for $\boldsymbol{e}_{\rm out} \propto \hat{\boldsymbol{y}} + \delta\hat{\boldsymbol{x}}'$, yielding an effective amplification of the second term in Eq. (3.50). In Fig. 3.7, we show several types of transverse trajectories of the coherent mode obtained via the weak-measurement technique. The intensity distribution displayed follows from

$$\frac{|\langle \boldsymbol{e}_{\rm out}^* \cdot \boldsymbol{E}(\boldsymbol{r}_\perp, L)\rangle|^2}{\int d^2\boldsymbol{r}_\perp |\langle \boldsymbol{e}_{\rm out}^* \cdot \boldsymbol{E}(\boldsymbol{r}_\perp, L)\rangle|^2} \propto \exp\left[-\frac{(y - R_y^{\delta}(L))^2}{w_0^2}\right] . \tag{3.67}$$

For the plots in Fig. 3.7, we choose $|\delta| = (k_0 w_0)^{-1}$, a value around which $R_y(L)$ is maximized. This results in a macroscopic spin Hall effect, i.e., a shift of the same order as the beam width w_0. Remember that without the post-selection scheme, a displacement equal to at most $k_0^{-1} \ll w_0$ is achievable. Note that the only drawback of this procedure stands in the reduction of the intensity detected at the output. Indeed, upon passing through the post-selection polarizer, the optical signal gets further attenuated by a factor δ^2.

3.9.2 Is the spin Hall effect visible?

We now discuss whether or not the spin Hall effect could be experimentally measured in the present configuration. To do so, we need to examine the condition under which the coherent mode is not masked by the contribution of multiply-scattered photons at the typical thicknesses where the spin Hall effect takes place, i.e., at thicknesses L of the order of $z_{\rm L(S)}$.

The intensity of the coherent mode after a propagation distance L inside the disordered medium and passing through the post-selection polarizer is

$$I_c(L) \simeq \frac{2\delta^2 e^{-L/z_s}}{\pi w_0^2} . \tag{3.68}$$

with $|\delta| = (k_0 w_0)^{-1}$. On the other hand, the intensity of the (diffusive) multiple-scattering signal is given by [42]

$$I_D(L) \simeq \frac{1 - e^{-L/z_p}}{8\pi D L} , \tag{3.69}$$

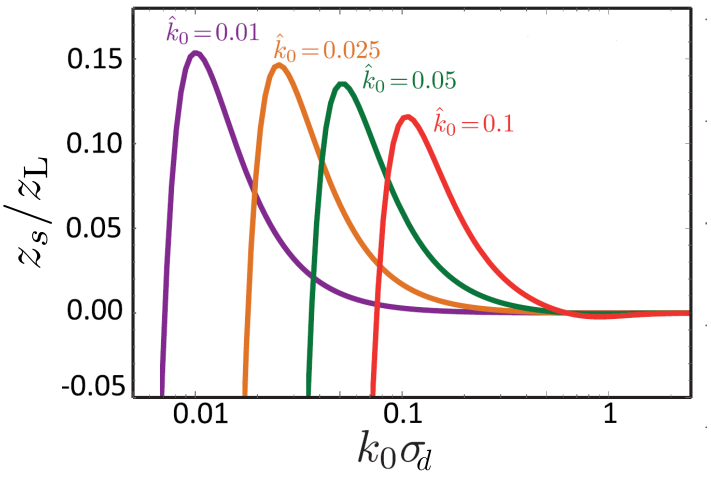

Figure 3.8: Looking at lower correlation lengths, we observe that the SOI parameter z_L^{-1} reaches a maximum value just above the diffraction limit. Near this maximum, the oscillating SHE occurs at the scale of a few z_s.

where $D = \hat{k}_0^2 z_s/2$ is the diffusion coefficient. Note that Eq. (3.69) slightly differs from the expression $(4\pi DL)^{-1}$ of Eq. (2.37) due to factor $1 - e^{-L/z_p}$. This factor corresponds to non-paraxial corrections to the diffusive signal, calculated in [42], with $z_p = z_s/\hat{k}_0^4$ the length scale over which the polarization direction is randomized due to multiple scattering. Hence, within the weak-measurement scheme, the condition for the coherent mode to be more intense than the diffusive halo at a given thickness L reads:

$$\frac{I_D(L)}{I_c(L)} = \frac{w_0^2}{z_s^2}\frac{(kw_0)^2}{8}\frac{1 - e^{-L/z_p}}{L/z_s e^{-L/z_s}} < 1\,. \tag{3.70}$$

In order to distinguish the coherent mode at large thicknesses, it is then necessary to work with a waist w_0 significantly smaller than the scattering mean free path z_s. Considering realistic situations, it is possible to satisfy the condition (3.70) up to L/z_s ratio of the order of 10. For example, given $z_s = 1$cm, $w_0 = 100\mu$m, $\lambda = 500$nm and $\hat{k}_0 = 0.1$ (the product $k_0 w_0$ is then fixed to $\simeq 125$), Eq. (3.70) holds true as long as $L/z_s \lesssim 6.2$. However, according to the above analysis, generally speaking the SHE phenomenon takes place at much larger thicknesses $L/z_s \sim \hat{k}_0^{-2} \sim 100$. This indicates that, at least with a Gaussian beam, observing the SHE in a random medium requires an additional strategy.

3.9.3 Optimal $(\hat{k}_0, k_0\sigma_d)$ choice

In order to make the SHE observable, it is thus require to reduce the distance over which the SHE appears as close as possible to the scattering length z_s. To do so, a first possibility is to take advantage of the strong dependence of the ratio z_s/z_L on $k_0\sigma_d$ at small correlation lengths, well visible in Fig. 3.3. To better see this dependence, in Fig. 3.8 we replot the ratio z_s/z_L of the mean free path to the SOI parameter z_L at smaller values of $k_0\sigma_d$, for several values of $\hat{k}_0$. We observe that for a given angle $\hat{k}_0$, this ratio reaches a maximum where z_L is of the order of a few z_s only. This maximum

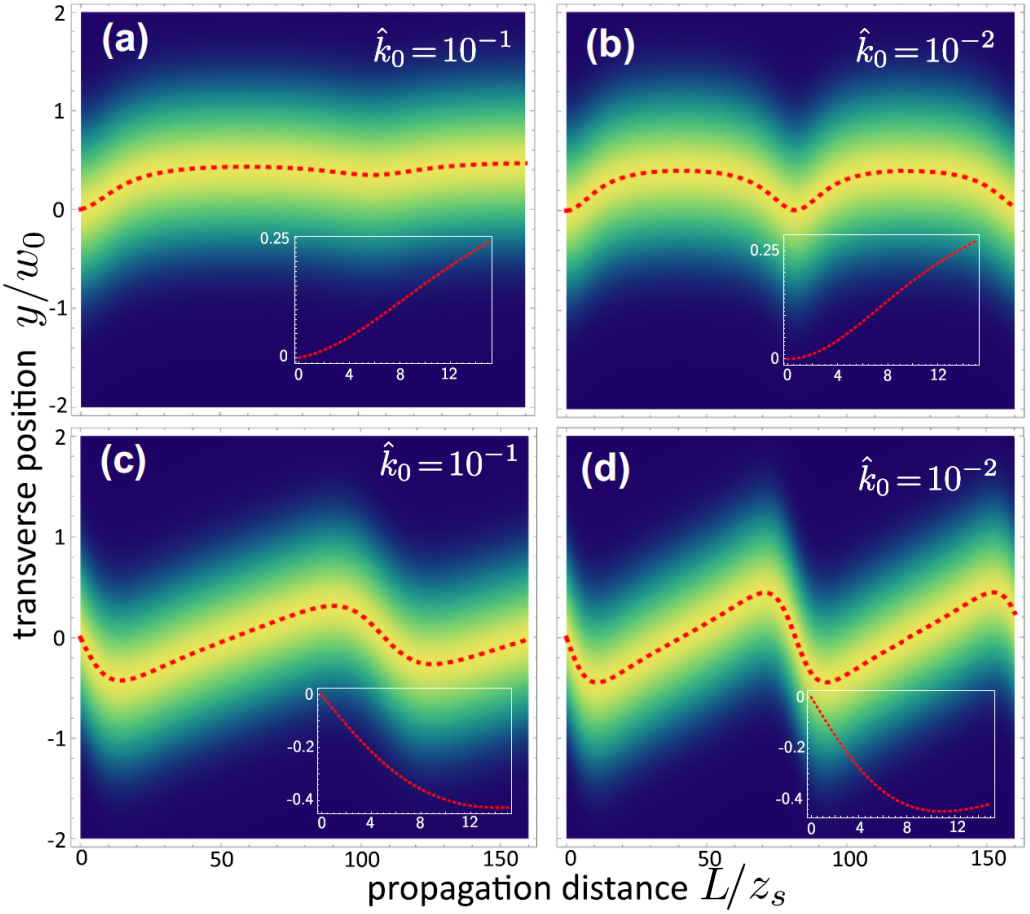

Figure 3.9: Normalized intensity of the coherent mode post-selected by a polarizer $\boldsymbol{e}_{\text{out}}$. In panels (a) and (b), we have $\boldsymbol{e}_{\text{out}} \propto \hat{\boldsymbol{y}} + i\delta\hat{\boldsymbol{x}}'$ with $\delta = (k_0 w_0)^{-1}$, while in panels (c) and (d), $\boldsymbol{e}_{\text{out}} \propto \hat{\boldsymbol{y}} + \delta\hat{\boldsymbol{x}}'$, corresponding to an amplification of the first and second term in Eq. (3.50), respectively. Dotted curves mark the centroid position $R_y^\delta(L)$. Here, $k_0\sigma_d$ is chosen at the point where the ratio z_s/z_{L} is maximum (see Fig. 3.8): $k_0\sigma_d = 0.1056$ in panels (a) and (c), $k_0\sigma_d = 0.01005$ in panels (b) and (d). Insets show zooms of $R_y^\delta(L)$ at the scale of a few z_s.

takes places at a characteristic correlation length close to the limit $k\sigma_d = 1$. By sufficiently decreasing σ_d, it is therefore in principle possible to make the SHE appear at a pretty short scale, where the condition (3.70) is satisfied. In Fig. 3.9, we show several types of transverse trajectories of the coherent mode obtained by combining the weak-measurement technique together with the maximization of z_s/z_{L} via σ_d. The insets demonstrate the possibility to realize a sizable $R_y(L)$ over pretty small optical thicknesses L/z_s. A drawback of this method, nevertheless, is that it requires to employ very small disorder correlation length (σ_d of the order of k^{-1}), which is a challenging task in practice.

3.10 Conclusion

Taking into account the vector nature of light, we have studied the evolution of the coherent mode in continuous isotropic transversally disordered media. We have shown how spin-orbit interactions non-trivially emerge from the system's anisotropy. As a result, a spin Hall shift affecting the coherent mode appears. In particular, considering a realistic model of correlated disorder enabled us to take into account the effect of disorder on the phase of the coherent mode. This allowed us to predict the existence of a variety of oscillating spin Hall effects, which can be tailored by tuning the deviation to paraxiality $\hat{k}_0$, the incident polarization $\boldsymbol{e}_0$ and the amount of disorder correlation $k_0\sigma_d$. In the chapter we have focused on Gaussian-shaped correlations but the approach employed is general and can be straightforwardly generalized to any type of disorder correlation. Tailoring the range of the latter so to gain additional control on SOI parameters could be interesting.

In the last section we have discussed the issues related to the experimental observation of the spin Hall effect, and also the possible solutions. First, the spin Hall shift can be amplified up to the beam width scale via polarimetry and, thanks to a thoughtful tuning of the disorder correlation length and the deviation from paraxiality, can be brought to an optical thickness regime where the coherent mode is still detectable within the multiple scattering signal. Within the model of continuous disorder discussed in this chapter, however, the potential detection of the spin Hall shift, even if in principle possible, remains very challenging due to the very small values of the disorder correlation required to decrease enough the ratio z_{L}/z_s.

In the next chapter, we will show how, by considering discrete resonant scatterers and exploiting the additional degree of freedom given by the frequency of the incident light, it is possible to overcome these limitations and detect a giant spin Hall shift, in both optically-thin and optically-thick media.

Chapter 4

Resonant spin Hall effect of light in random photonic arrays

In the previous chapter, we have seen that the main obstacle to the detection of the spin Hall effect of light in a transversally disordered medium of thickness L is the exponential attenuation of the coherent mode as $\exp\big(-L/z_s\big)$, where z_s is the scattering mean free path along the optical axis, perpendicular to the disordered plane. Indeed, in the case where the disorder consists of continuous spatial fluctuations of the permittivity, without special care the spin Hall effect appears at a characteristic scale $z_{\mathrm{S(L)}} \sim z_s/\sin^2\theta \gg z_s$ where the coherent mode is no longer easily detectable.

In this chapter, we provide a decisive solution to this problem by considering the propagation of light in transversally disordered photonic arrays made of discrete, *resonant* dielectric tubes. In particular, within a minimal model of scattering by a cylinder based on Mie theory, we demonstrate the possibility of achieving sizeable spin Hall shifts of the coherent mode at a scale of the order of the mean free path z_s by properly tuning the frequency of the incident light, making the effect observable in optically-thin media. This constitutes the most important result of the thesis.

Finally, we examine the time dependence of the spin Hall effect, following the abrupt extinction of the incoming laser. In that scenario, the radiation of the resonant scatterers right after the laser extinction gives rise to a flash of light that makes the coherent mode brighter than the diffusive signal in the limit of large optical thicknesses. During the time scale of the flash effect, we show evidence for a significant SHE, thus observable in optically-thick media as well.

4.1 Scattering of light by a narrow cylinder

In this section, we recall the main elements of the scattering theory of light by a single, infinitely-long dielectric cylinder. Our goal here is to provide a simple expression for the T-matrix of such a scatterer, which will be used in the next section as the building block of the problem of light scattering by a transversally random photonic array.

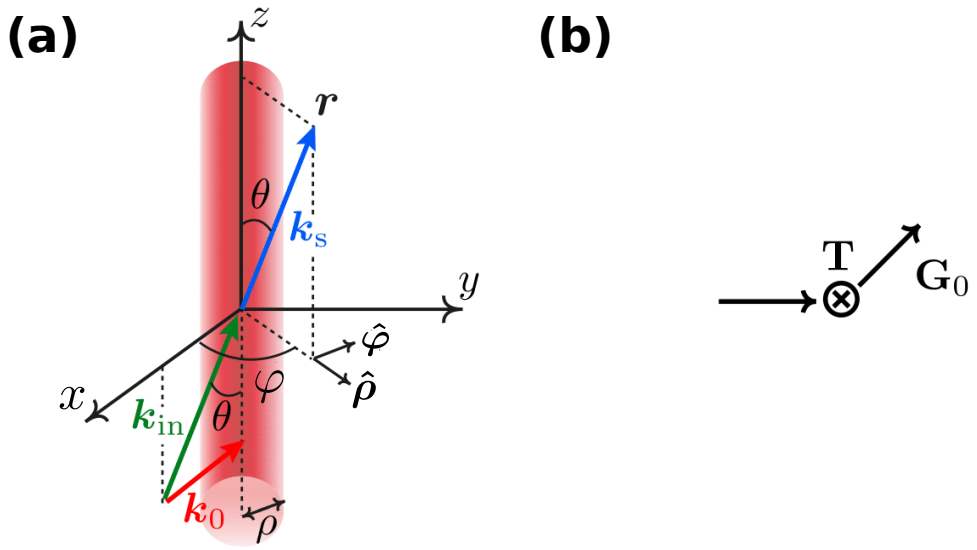

Figure 4.1: (a) Scattering of light by a single, infinitely-long cylinder of radius ρ. The incident wave vector $\boldsymbol{k}_{\rm in}$ makes an angle θ with the cylinder axis z. During the scattering process, the $z-$component of the wave vector, $k_z = (\omega/c)\cos\theta$, is conserved. The projection of $\boldsymbol{k}_{\rm in}$ in the transverse plane (x, y) is denoted by $\boldsymbol{k}_0$. (b) Diagrammatic representation of the field (4.1) scattered by a single cylinder. The circled cross symbol represents the T-matrix of the cylinder.

4.1.1 T-matrix

Let us consider an incident, monochromatic plane wave $\boldsymbol{E}_{\rm in}(\boldsymbol{r}) = \boldsymbol{E}_{\rm in}\exp(i\boldsymbol{k}_{\rm in}\cdot\boldsymbol{r})$, impinging on a dielectric cylinder of radius ρ, see Fig. 4.1a. The incident wave vector $\boldsymbol{k}_{\rm in} = \omega/c(-\sin\theta\hat{\boldsymbol{x}} + \cos\theta\hat{\boldsymbol{z}})$ makes an angle θ with the cylinder axis z. We express the constant field amplitude as $\boldsymbol{E}_{\rm in} = E_i^{\rm TM}\boldsymbol{e}_i^{\rm TM} + E_i^{\rm TE}\boldsymbol{e}_i^{\rm TE}$, where the unit vectors $\boldsymbol{e}_i^{\rm TM} = \cos\theta\hat{\boldsymbol{x}} + \sin\theta\hat{\boldsymbol{z}}$ and $\boldsymbol{e}_i^{\rm TE} = -\hat{\boldsymbol{y}}$ are such that $\boldsymbol{e}_i^{\rm TE}\times\boldsymbol{e}_i^{\rm TM} = \hat{\boldsymbol{k}}_{\rm in}$. The cases $E_i^{\rm TM} = 0$ and $E_i^{\rm TE} = 0$ define the transverse-electric (TE) and transverse-magnetic (TM) modes, where the incident electric field has a zero (nonzero) component along the cylinder axis, respectively.

In the presence of the cylinder, the total electric field decomposes as $\boldsymbol{E}(\boldsymbol{r}) = \boldsymbol{E}_{\rm in}(\boldsymbol{r}) + \boldsymbol{E}_s(\boldsymbol{r})$, where the scattered field $\boldsymbol{E}_s(\boldsymbol{r})$ at any point $\boldsymbol{r} = [\boldsymbol{r}_\perp = (x, y), z]$ is given by the following Lippmann–Schwinger type equation [170]

$$\boldsymbol{E}_s(\boldsymbol{r}) = \int \frac{d^3\boldsymbol{k}'}{(2\pi)^3} e^{i\boldsymbol{k}'\cdot\boldsymbol{r}}\boldsymbol{G}_0(\boldsymbol{k}')\cdot\boldsymbol{T}(\boldsymbol{k}'-\boldsymbol{k}_{\rm in})\cdot\boldsymbol{E}_{\rm in}\ . \tag{4.1}$$

Here $\boldsymbol{T}$ is the T-matrix of the cylinder, i.e., the scattering amplitude for the elastic process $\boldsymbol{k}_{\rm in}\to\boldsymbol{k}'$, and $\boldsymbol{G}^{(0)}$ is the free-space Green's tensor:

$$\boldsymbol{G}^{(0)}(\boldsymbol{k}') = \left(\mathbb{1} - \frac{\boldsymbol{k}'\otimes\boldsymbol{k}'}{\omega^2/c^2}\right)\frac{1}{\omega^2/c^2 - \boldsymbol{k}'^2 + i0^+}\ , \tag{4.2}$$

where the $\otimes$ symbol refers to a dyadic product. A compact, diagrammatic representation of the scattered field (4.1) is represented in Fig. 4.1b.

For a cylinder infinitely extended along z, the z-component of the wave vector is conserved during the scattering process. This imposes $T(\boldsymbol{k}'-\boldsymbol{k}_{\rm in}) = 2\pi\delta(k'_z-k_z)T(\boldsymbol{k}'_\perp-\boldsymbol{k}_0)$, with $\boldsymbol{k}'_\perp$ and $\boldsymbol{k}_0 = -(\omega/c)\sin\theta\hat{\boldsymbol{x}}$ respectively the projections of $\boldsymbol{k}'$ and $\boldsymbol{k}_{\rm in}$ onto the transverse plane (x,y), and k'_z and $k_z = (\omega/c)\cos\theta$ their projections onto the z-axis. Hence, Eq. (4.1) becomes:

$$\begin{aligned}\boldsymbol{E}_s(\boldsymbol{r}) =& \left[\mathbb{1} - \frac{(k_z\hat{\boldsymbol{z}} - i\boldsymbol{\nabla}_\perp)\otimes(k_z\hat{\boldsymbol{z}} - i\boldsymbol{\nabla}_\perp)}{\omega^2/c^2}\right] \\ &\times \int \frac{d^2\boldsymbol{k}'_\perp}{(2\pi)^2}\frac{e^{i\boldsymbol{k}'_\perp\cdot\boldsymbol{r}_\perp + ik_z z}}{\omega^2/c^2 - k_z^2 - k_\perp'^2 + i0^+}\boldsymbol{T}(\boldsymbol{k}'_\perp - \boldsymbol{k}_0)\cdot\boldsymbol{E}_{\rm in}\ .\end{aligned} \tag{4.3}$$

Far from the cylinder axis, i.e., for $k_0 r_\perp \gg 1$, the angular integral is dominated by the stationary phase corresponding to $\boldsymbol{k}'_\perp$ aligned with $\boldsymbol{r}_\perp$. The integral over $\boldsymbol{k}'_\perp$ then simplifies to

$$\int_0^\infty \frac{k'_\perp dk'_\perp}{(2\pi)^2}\sqrt{\frac{2\pi}{ik'_\perp r_\perp}}\frac{e^{ik'_\perp r_\perp + ik_z z}}{\omega^2/c^2 - k_z^2 - k_\perp'^2 + i0^+}\boldsymbol{T}(k'_\perp\hat{\boldsymbol{\rho}} - \boldsymbol{k}_0)\cdot\boldsymbol{E}_{\rm in}\ , \tag{4.4}$$

where $\hat{\boldsymbol{\rho}} \equiv \boldsymbol{r}_\perp/r_\perp$. The remaining integral is computed by the residue theorem, yielding:

$$\boldsymbol{E}_s(\boldsymbol{r}) \simeq i\frac{e^{3i\pi/4}}{4}\sqrt{\frac{2}{\pi k_0 r_\perp}}e^{i\boldsymbol{k}_s\cdot\boldsymbol{r}}\big(\mathbb{1} - \hat{\boldsymbol{k}}_s\otimes\hat{\boldsymbol{k}}_s\big)\cdot\boldsymbol{T}(k_0\hat{\boldsymbol{\rho}} - \boldsymbol{k}_0)\cdot\boldsymbol{E}_{\rm in}\ , \tag{4.5}$$

where $k_0 \equiv |\boldsymbol{k}_0| = \sqrt{\omega^2/c^2 - k_z^2}$ and we have introduced $\boldsymbol{k}_s \equiv k_0\hat{\boldsymbol{\rho}} + k_z\hat{\boldsymbol{z}}$, the wave vector of the scattered field at point $\boldsymbol{r}$, see Fig. 4.1a. Note that due to transversality, $\hat{\boldsymbol{k}}_s\cdot\boldsymbol{E}_s = 0$. Therefore, the scattered field can naturally be decomposed along the vectors $\boldsymbol{e}^{\rm TM} = -\cos\theta\hat{\boldsymbol{\rho}} + \sin\theta\hat{\boldsymbol{z}}$ and $\boldsymbol{e}_s^{\rm TE} = \hat{\boldsymbol{\varphi}}$, so that $\boldsymbol{e}_s^{\rm TE}\times\boldsymbol{e}_s^{\rm TM} = \hat{\boldsymbol{k}}_s$. Denoting by $E_s^{\rm TM}$ and $E_s^{\rm TE}$ the two components of the electric field in this local basis, we can formally rewrite Eq. (4.5) as

$$\begin{bmatrix}E_s^{\rm TM}\\ E_s^{\rm TE}\end{bmatrix} = e^{3i\pi/4}\sqrt{\frac{2}{\pi k_0 r_\perp}}e^{i\boldsymbol{k}_s\cdot\boldsymbol{r}}\begin{bmatrix}T_1 & T_4\\ T_3 & T_2\end{bmatrix}\begin{bmatrix}E_i^{\rm TM}\\ E_i^{\rm TE}\end{bmatrix}\ . \tag{4.6}$$

The explicit expression of the coefficients T_i can be calculated from Mie theory. Mie theory [171] provides an exact solution to electromagnetic-wave scattering by objects of arbitrary size by imposing the continuity of tangential components of electric and magnetic fields at the object's boundaries. In the cylinder geometry, by expanding the total field on the basis of vector cylindrical harmonics and imposing the continuity condition at the cylinder boundary (see Appendix C for more details), one gets [172]

$$\begin{aligned}T_1 &= b_{0\rm I} + 2\sum_{\rm n=1}^{\infty} b_{\rm nI}\cos\big(\mathrm{n}(\pi-\varphi)\big)\\ T_2 &= a_{0\rm II} + 2\sum_{\rm n=1}^{\infty} a_{\rm nII}\cos\big(\mathrm{n}(\pi-\varphi)\big)\\ T_3 &= -2i\sum_{\rm n=1}^{\infty} a_{\rm nI}\sin\big(\mathrm{n}(\pi-\varphi)\big) = -T_4\ ,\end{aligned} \tag{4.7}$$

where $\pi - \varphi$ is the angle between $\boldsymbol{k}_0$ and $k_0\hat{\boldsymbol{\rho}}$, see Fig. 4.1a. The a_n and b_n are Mie coefficients that are functions of the size parameter $k\rho$, where $k \equiv \omega/c$ and ρ is the radius of the cylinder. They exhibit an infinite set of resonances, see the example (4.9) below and Appendix C for their analytical expressions.

4.1.2 Low-frequency limit

Assuming a small angle of incidence ($\theta \ll 1$), we now focus on the low frequency limit (or, equivalently, the narrow-cylinder limit): $k\rho \ll 1$. More precisely, we restrict ourselves to the two lowest Mie resonances of the problem, which turn out to constitute the minimal resonant model to capture the spin Hall effect (see Sec. 4.2). The lowest resonance is included in the Mie coefficients of order n = 1, which further satisfy $a_{1\mathrm{I}} \simeq b_{1\mathrm{I}} \simeq -ia_{1\mathrm{I}}$ at low frequency and small angle, while the next one is in the coefficient $b_{0\mathrm{I}}$. These observations allow us to express the T-matrix in terms of the coefficients $b_{0\mathrm{I}}$ and $a_{1\mathrm{I}}$ only:

$$\boldsymbol{T} = -i\begin{bmatrix} T_1 & T_4 \\ T_3 & T_2 \end{bmatrix} \simeq -i\begin{bmatrix} b_{0\mathrm{I}} + 2ia_{1\mathrm{I}}\cos\varphi & 2ia_{1\mathrm{I}}\sin\varphi \\ -2ia_{1\mathrm{I}}\sin\varphi & 2ia_{1\mathrm{I}}\cos\varphi \end{bmatrix} . \tag{4.8}$$

The exact expression of $b_{0\mathrm{I}}$ is, for instance, given by (see [172] or Appendix C)

$$b_{0\mathrm{I}} = \frac{m^2 k\rho\sin\theta J_1(\eta)J_0(k\rho\sin\theta) - \eta J_0(\eta)J_1(k\rho\sin\theta)}{m^2 k\rho\sin\theta J_1(\eta)H_0^{(1)}(k\rho\sin\theta) - \eta J_0(\eta)H_1^{(1)}(k\rho\sin\theta)} , \tag{4.9}$$

where $\eta = k\rho\sqrt{m^2 - \cos^2\theta}$, with m the ratio of the refractive index of the cylinder to that of the surrounding medium. The ratio (4.9) still includes an infinite set of resonances as a function of $k\rho$. As we wish to focus on the lowest one only, we further simplify Eq. (4.9) by linearizing the various Bessel functions around the first zero of the denominator. This calculation is tedious but straightforward, and leads to the simple Lorentzian approximation:

$$b_{0\mathrm{I}} \simeq \frac{i\Gamma_1/2}{\omega - \omega_1 + i\Gamma_1/2} \tag{4.10}$$

where, at small θ, the resonance frequency ω_1 and its bandwidth Γ_1 are given by

$$\omega_1 \simeq \frac{c\alpha}{\rho\sqrt{m^2-1}} \quad \text{and} \quad \Gamma_1 \simeq \frac{cm\alpha\pi\sin^2\theta}{\rho(m^2-1)} , \tag{4.11}$$

with $\alpha \simeq 2.4048$. Notice that $\Gamma_1(\theta \to 0) \propto \theta^2 \to 0$, a key property that will be at the origin of a giant spin Hall effect in the random array. A similar approximation for $a_{1\mathrm{I}}$ gives:

$$a_{1\mathrm{I}} \simeq -\frac{1}{2}\frac{\Gamma_0/2(\omega/\omega_0)^2}{\omega - \omega_0 + i\Gamma_0/2(\omega/\omega_0)^2} . \tag{4.12}$$

The resonance frequency ω_0 and the bandwidth Γ_0 have more complicated expressions, which are given in Appendix D for clarity. They show, in particular, that in contrast to Γ_1, at small angle Γ_0 varies very weakly with θ. Eq.s (4.8), (4.10) and (4.12) constitute a minimal model for light scattering by a cylinder at low frequency, where only the two lowest Mie resonances are considered.

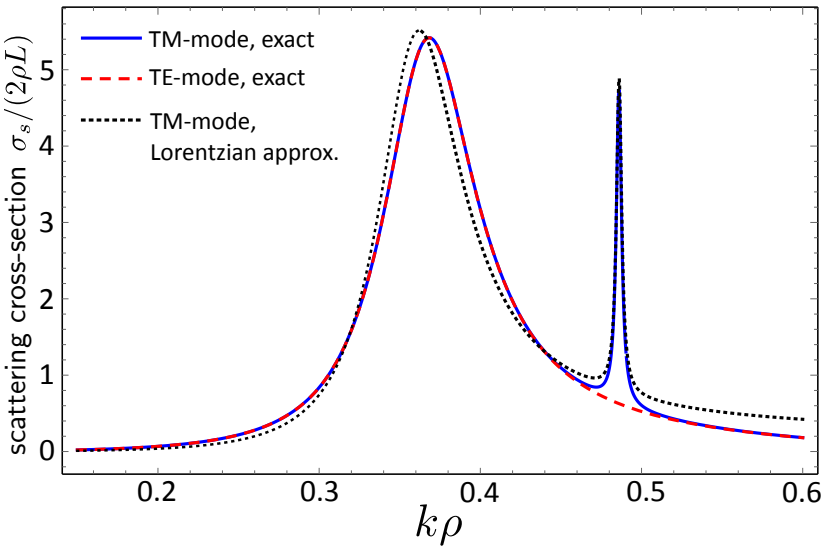

Figure 4.2: Scattering cross-section for the TE and TM modes, computed from Eq. (4.14) using $m = 5$ and $\sin\theta = 0.05$. Here we only show the two lowest Mie resonances. The solid and dashed curve are the result of the exact Mie calculation for the TM and TE modes, respectively. In the TM case, a very sharp resonance of width $\propto \sin^2\theta$ generically shows up at $\omega = \omega_1$. The dotted curve shows the Lorentzian approximation, Eq.s (4.10) and (4.12), in the TM mode for comparison.

4.1.3 Properties of lowest Mie resonances

To conclude this section, we briefly discuss the main properties of the two resonances (4.10) and (4.12), as well as the accuracy of the Lorentzian approximations made. To this aim, it is convenient to evaluate the scattering cross section σ_s of the cylinder, defined as

$$\sigma_s = \frac{\int_A \mathbf{\Pi}_s \cdot \hat{\boldsymbol{\rho}}\, dA}{|\mathbf{\Pi}_i|}\,, \tag{4.13}$$

where $\mathbf{\Pi}_{i,s} = 1/(2i\omega\mu_0)\,\mathrm{Re}[\boldsymbol{E}_{i,s} \times (\boldsymbol{\nabla} \times \boldsymbol{E}^*_{i,s})]$ is the Poynting vector of the incident and scattered fields [173], and A is a fictitious surface enclosing the cylinder in the far field. Inserting Eq. (4.6) into this definition, we find

$$\frac{\sigma_s^{\mathrm{TE}}}{2\rho L} = \frac{2}{k\rho}\langle |T_2|^2 + |T_4|^2\rangle_\varphi \qquad \frac{\sigma_s^{\mathrm{TM}}}{2\rho L} = \frac{2}{k\rho}\langle |T_1|^2 + |T_3|^2\rangle_\varphi \tag{4.14}$$

for the TE ($E_i^{\mathrm{TM}} = 0$) and TM ($E_i^{\mathrm{TE}} = 0$) polarization modes. In Eq. (4.14), $\langle \ldots \rangle_\varphi$ refers to an angular average over φ and we have normalized σ_s by the geometrical cross section $2\rho L$ of the cylinder. The scattering cross section in the two polarization modes is shown in Fig. 4.2. The prediction of Mie theory, based on the exact expressions (4.7) of the coefficients of the T-matrix, is displayed together with the Lorentzian approximation in the TM case, based on Eq.s (4.8), (4.10) and (4.12). The plot confirms the good accuracy of the simple Lorentzian model, on which we will rely in the rest of the chapter.

Fig. 4.2 also confirms that the resonance at ω_0 is the lowest one. This resonance shows up both in the TE and TM modes, and is rather broad even for large values

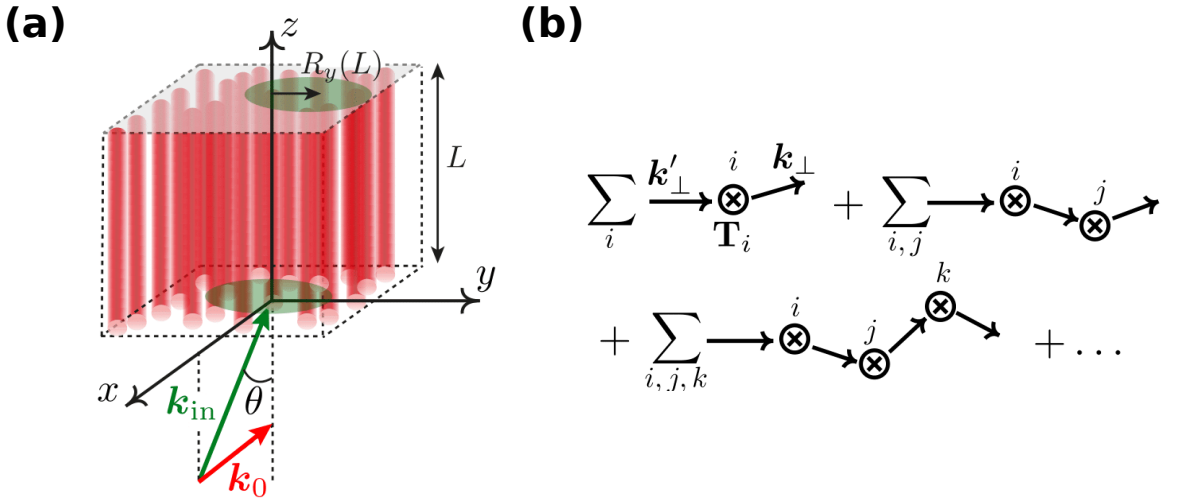

Figure 4.3: (a) Transmission of light through a random photonic array of dielectric cylinders (of thickness L). Upon crossing the array, the coherent mode intensity exhibits a spin Hall shift $R_y(L)$ along the y axis. (b) Diagrammatic representation of the multiply scattered field (4.15). The sums run over the number N of cylindrical scatterers. Remember that multiple scattering here takes place in the (x, y) plane only.

of the relative refractive index m of the cylinder. As mentioned above, both ω_0 and Γ_0 weakly depend on the angle of incidence θ. The second resonance, at $\omega_1 > \omega_0$, only shows up in the TM mode, and for this reason will be referred to as the "TM resonance" in the following. Its most remarkable property is its sharpness, which stems from the proportionality of Γ_1 to $\sin^2\theta \ll 1$ at small θ, see Eq. (4.11).

4.2 Scattering of light by a random photonic array

Let us now consider the scattering of light by an array made of a large number of identical, randomly distributed cylindrical scatterers with parallel axes (see Fig. 4.3a).

4.2.1 Dyson equation

The electric field $\boldsymbol{E}(\boldsymbol{r})$ at some point $\boldsymbol{r}$ within the array is now given by a sum over multiple scattering trajectories, as sketched in Fig. 4.3b. In terms of the Fourier components $\boldsymbol{E}(\boldsymbol{k}_\perp, k_z) = \int d^2\boldsymbol{r}_\perp dz e^{-i\boldsymbol{k}_\perp\cdot\boldsymbol{r}_\perp - ik_z z}\boldsymbol{E}(\boldsymbol{r})$, the multiple scattering sequence is iterated by the relation

$$\boldsymbol{E}(\boldsymbol{k}_\perp, k_z) = \boldsymbol{E}_{\rm in}(\boldsymbol{k}_\perp, k_z) + \sum_j \int \frac{d^2\boldsymbol{k}'_\perp}{(2\pi)^2}\boldsymbol{G}^{(0)}(\boldsymbol{k}_\perp, k_z)\cdot\boldsymbol{T}_j(\boldsymbol{k}_\perp - \boldsymbol{k}'_\perp)\cdot\boldsymbol{E}(\boldsymbol{k}'_\perp, k_z)\ , \quad (4.15)$$

where $\boldsymbol{T}_j$ refers to the T-matrix of the cylinder j and the sum runs over the number of cylinders of the array. This relation generalizes the single-scattering solution (4.1). Notice the conservation of k_z due to translation invariance along z. Denoting by $\boldsymbol{r}_{\perp j}$

the (random) position of the cylinder j in the transverse plane (x, y), we have $\boldsymbol{T}_j(\boldsymbol{k}_\perp - \boldsymbol{k}'_\perp) \simeq \boldsymbol{T}\, e^{-i(\boldsymbol{k}_\perp - \boldsymbol{k}'_\perp)\cdot \boldsymbol{r}_{\perp j}}$, where $\boldsymbol{T}$ is the $T-$matrix of the cylinder located at $\boldsymbol{r}_{\perp j} = 0$.

As in the previous chapter, we focus on the disorder-average electric field $\langle \boldsymbol{E} \rangle$, which governs the evolution of the coherent mode. In our random photonic array where the scatterers are discrete, disorder averaging corresponds to a statistical average of Eq. (4.15) over the cylinder positions in the transverse plane. In general, this average can not be computed analytically exactly due to the multiple correlations between the scatterers [174, 175, 176]. Here, however, we assume a dilute distribution of the cylinders, i.e., $nk_0^{-2} \ll 1$, with n the density of the cylinders in the transverse plane (x, y) and $k_0 = \omega/c_0 \sin\theta$ the transverse wave number. Together with the low-frequency limit introduced in Sec. 4.1.2, we have: $\rho \ll k_0^{-1} \ll n^{-1/2}$.

The diluteness condition $nk_0^{-2} \ll 1$ implies that the probability that the scattered light "returns" to a scatterer already visited is very small, such that we have $\langle \boldsymbol{T}_j \cdot \boldsymbol{E}_s \rangle \simeq \langle \boldsymbol{T}_j \rangle \cdot \langle \boldsymbol{E}_s \rangle$. This approximation is known in the literature as the independent-scattering approximation (ISA) and is often used when dealing with discrete scatterers [177]. On the other hand, the condition $n^2\rho \ll 1$ implies that spatial correlations between tubes, caused by their finite size, are negligible. This allows us to employ a simple model of disorder where the cylinder positions $\boldsymbol{r}_{\perp j}$ are uniformly distributed, such that:

$$\sum_j \langle e^{-i(\boldsymbol{k}_\perp - \boldsymbol{k}'_\perp)\cdot \boldsymbol{r}_{\perp j}} \rangle = \sum_j \int \frac{d^2\boldsymbol{r}_{\perp j}}{S} e^{-i(\boldsymbol{k}_\perp - \boldsymbol{k}'_\perp)\cdot \boldsymbol{r}_{\perp j}} \simeq \frac{N}{S} \delta(\boldsymbol{k}_\perp - \boldsymbol{k}'_\perp) \,, \tag{4.16}$$

with $N/S = n$, S being the area occupied by the array in the transverse plane (x, y). The disorder average of Eq. (4.15) thus reads

$$\langle \boldsymbol{E}(\boldsymbol{k}_\perp, k_z) \rangle = \boldsymbol{E}_{\rm in}(\boldsymbol{k}_\perp, k_z) + \boldsymbol{G}^{(0)}(\boldsymbol{k}_\perp, k_z) \cdot n\boldsymbol{T} \cdot \langle \boldsymbol{E}(\boldsymbol{k}_\perp, k_z) \rangle \,. \tag{4.17}$$

For a point-source emitting light within the array, this relation is simply generalized in terms of the disorder-average Green's tensor $\langle \boldsymbol{G} \rangle$, which obeys

$$\langle \boldsymbol{G}(\boldsymbol{k}_\perp, k_z) \rangle = \boldsymbol{G}^{(0)}(\boldsymbol{k}_\perp, k_z) + \boldsymbol{G}^{(0)}(\boldsymbol{k}_\perp, k_z) \cdot n\boldsymbol{T} \cdot \langle \boldsymbol{G}(\boldsymbol{k}_\perp, k_z) \rangle \,. \tag{4.18}$$

Eq. (4.18) is known as the Dyson equation at the independent-scattering approximation [177]. From the knowledge of the T-matrix of a single cylinder, the average Green's tensor of the random array thus follows from

$$\langle \boldsymbol{G}(\boldsymbol{k}_\perp, k_z) \rangle = [\boldsymbol{G}^{(0)-1}(\boldsymbol{k}_\perp, k_z) - \boldsymbol{\Sigma}]^{-1} \,, \tag{4.19}$$

where $\boldsymbol{\Sigma} \equiv n\boldsymbol{T}$ is the self-energy tensor describing the disordered system. Eq. (4.19) is nothing but the Dyson Eq. (3.14), here obtained for a model of discrete scatterers.

4.2.2 Disorder-average transmitted field

As illustrated in Fig. 4.3a, we aim at describing the coherent component of light transmitted through a random photonic array of thickness L. The coherent mode is described by the disorder average of the transmitted field, whose Fourier distribution follows from the input-output relation [cf. Eq. (3.23)]

$$\langle \boldsymbol{E}(\boldsymbol{k}_\perp, z = L) \rangle = \boldsymbol{t}(\boldsymbol{k}_\perp, L) \cdot \boldsymbol{E}(\boldsymbol{k}_\perp, z = 0) \,, \tag{4.20}$$

where $\boldsymbol{E}(\boldsymbol{k}_\perp, z=0)$ is the Fourier distribution of the field at the entrance of the array. In the following, we take the latter of the form

$$\boldsymbol{E}(\boldsymbol{k}_\perp, z=0) = \sqrt{2\pi} w_0 \exp\big[-(\boldsymbol{k}_\perp - \boldsymbol{k}_0)^2 w_0^2/4\big] \boldsymbol{e}_0 \tag{4.21}$$

with $k_0 w_0 \gg 1$. This is the same initial state as considered in the previous chapter [see Eq. (3.1)], which models a collimated beam of intensity distribution normalized to unity, i.e., $\int d^2\boldsymbol{k}_\perp/(2\pi)^2 |\boldsymbol{E}(\boldsymbol{k}_\perp, z=0)|^2 = 1$, and of unit polarization vector $\boldsymbol{e}_0$. A fundamental quantity in Eq. (4.20) is the average transmission matrix of the array $\boldsymbol{t}$, given by [178]:

$$\boldsymbol{t}(\boldsymbol{k}_\perp, L) = 2i\sqrt{k^2 - \boldsymbol{k}_\perp^2}\, \langle \boldsymbol{G}(\boldsymbol{k}_\perp, z=L)\rangle \ , \tag{4.22}$$

where $\langle \boldsymbol{G}(\boldsymbol{k}_\perp, z)\rangle \equiv \int dk_z/(2\pi) e^{ik_z z} \langle \boldsymbol{G}(\boldsymbol{k}_\perp, k_z)\rangle$.

From Eq.s (4.20) and (4.22), the problem thus reduces to evaluating the average Green's tensor of the array. This can be done by computing the tensor inverse in the right-hand side of the Dyson equation (4.19). But before doing so, let us rewrite the $T-$matrix (4.8) of a single scatterer in the global basis (x, y, z). Within the minimal two-Mie-resonances model at small angle $\theta \ll 1$, we find after the basis change:

$$\boldsymbol{\Sigma} = \begin{bmatrix} \Sigma_{xx} & 0 & 0 \\ 0 & \Sigma_{xx} & 0 \\ 0 & 0 & \Sigma_{zz} \end{bmatrix}_{(x,y,z)} \ , \tag{4.23}$$

where

$$\Sigma_{xx} = -8n a_{1\mathrm{I}} = 4n \frac{\Gamma_0/2(\omega/\omega_0)^2}{\omega - \omega_0 + i\Gamma_0/2(\omega/\omega_0)^2} \tag{4.24}$$

and

$$\Sigma_{zz} = -\frac{4inb_{0\mathrm{I}}}{\sin^2\theta} = \frac{4n}{\sin^2\theta} \frac{\Gamma_1/2}{\omega - \omega_1 + i\Gamma_1/2} \ . \tag{4.25}$$

Contrary to (3.17), the structure of the self-energy tensor (4.23) is diagonal. This reflects the fact that, within the narrow-cylinder limit considered here, the disorder in the photonic array is effectively uncorrelated and exhibits a uniaxial anisotropy. This diagonal structure, however, is not specifically related to the resonant character of the disorder. In particular, the same structure was found in [62] within a non-resonant, continuous model of uncorrelated transverse disorder.

From Eq. (4.23), the calculation of the disorder-average Green's tensor in momentum follows the same lines as in the previous chapter [cf. Eq. (3.18)]. It yields the following expression for the disorder-average transmission matrix of the array [68]

$$\begin{aligned} \boldsymbol{t}(\boldsymbol{k}_\perp, L) =& e^{ik_z L}\Big[e^{-i\Sigma_{\mathrm{TE}} L/2k_z}\delta_{ij} - e^{-i\Sigma_{\mathrm{TM}} L/2k_z}\hat{k}_i\hat{k}_j \\ &+ \frac{e^{-i\Sigma_{\mathrm{TE}} L/2k_z} - e^{-i\Sigma_{\mathrm{TM}} L/2k_z}}{\hat{k}_\perp^2}(\delta_{iz}\hat{k}_j\hat{k}_z + \delta_{jz}\hat{k}_i\hat{k}_z - \delta_{iz}\delta_{jz} - \hat{k}_i\hat{k}_j)\Big] \ , \end{aligned} \tag{4.26}$$

where $k_z = \sqrt{\omega^2/c^2 - \boldsymbol{k}_\perp^2}$ and the two complex quantities Σ_{TE} and Σ_{TM}, corresponding to Σ_1 and Σ_2 in the previous chapter, are defined as

$$\Sigma_{\mathrm{TE}} = \Sigma_{xx}, \qquad \Sigma_{\mathrm{TM}} = \Sigma_{xx} + (\Sigma_{zz} - \Sigma_{xx})\sin^2\theta \ . \tag{4.27}$$

The labels "TE" and "TM" that we preferably use in this chapter will be clarified shortly. Combining Eq.s (4.20), (4.21) and (4.26), we finally obtain the exact expression of the disorder-average transmitted field:

$$\begin{aligned}\langle \boldsymbol{E}(\boldsymbol{k}_\perp, L)\rangle =& \sqrt{2\pi} w_0 e^{-(\boldsymbol{k}_\perp - \boldsymbol{k}_0)^2 w_0^2/4} e^{ik_z L}\big[e^{-i\Sigma_{\rm TE} L/2k_z}\boldsymbol{e}_0 \\ &+ (e^{-i\Sigma_{\rm TM} L/2k_z} - e^{-i\Sigma_{\rm TE} L/2k_z})\boldsymbol{p}(\boldsymbol{k}_\perp)\big] ,\end{aligned} \tag{4.28}$$

where $\boldsymbol{p}(\boldsymbol{k}_\perp) = (\hat{\boldsymbol{e}}_\perp \cdot \boldsymbol{e}_0)\hat{\boldsymbol{e}}_\perp + (\hat{\boldsymbol{z}} \cdot \boldsymbol{e}_0)\hat{\boldsymbol{z}}$ is the projection of the initial polarization $\boldsymbol{e}_0$ onto the $(\hat{\boldsymbol{e}}_\perp = \boldsymbol{k}_\perp/k_\perp, \hat{\boldsymbol{z}})$ plane. This is the same form as Eq. (3.24) of the previous chapter, where a continuous model of (non-resonant) transverse disorder was considered. Therefore, we again expect the appearance of a spin Hall effect of light affecting the coherent mode. Nevertheless, as we will show below, the characteristics of the spin Hall effect in the photonic array can be significantly different from those of the model of continuous disorder due to the different resonant character of the two scalar self-energies $\Sigma_{\rm TE}$ and $\Sigma_{\rm TM}$.

4.3 Intensity distribution of the coherent mode

In this section, we examine the intensity distribution of the coherent mode of the photonic array, defined as $I_c(\boldsymbol{r}_\perp, L) = |\langle \boldsymbol{E}(\boldsymbol{r}_\perp, L)\rangle|^2$, where $\langle \boldsymbol{E}(\boldsymbol{r}_\perp, L)\rangle$ is the Fourier transform of Eq. (4.28). As in chapter 3, the spatial intensity distribution of the coherent mode has the following structure:

$$I_c(\boldsymbol{r}_\perp, L) \simeq I_c(L) e^{-2|\boldsymbol{r}_\perp - \boldsymbol{R}_\perp(L)|^2/w_0^2} , \tag{4.29}$$

where $I_c(L) = I_0 \int \frac{d^2\boldsymbol{k}_\perp}{(2\pi)^2} |\langle \boldsymbol{E}(\boldsymbol{k}_\perp, L)\rangle|^2 = I_c(\boldsymbol{R}_\perp(L), L)$ with $I_0 \equiv 2/(\pi w_0^2)$. The derivation of Eq. (4.29) is fully analogous to the one presented in Sec. 3.5. Let us recall that Eq. (4.29) describes the fact that the coherent mode undergoes a rigid spatial shift $\boldsymbol{R}_\perp(L)$ in the transverse plane (x, y), detected at the output of the medium. It is through this shift that the phenomenon of spin Hall effect of light shows up.

4.3.1 Intensity at the beam center

We here discuss the properties of $I_c(L)$, the intensity of the coherent mode at the beam center detected at the disordered media output. For TE- or TM-polarized light (i.e., $\boldsymbol{e}_0 = \boldsymbol{e}_i^{\rm TE}$ or $\boldsymbol{e}_i^{\rm TM}$), Eq. (4.28) reduces to $\langle \boldsymbol{E}(\boldsymbol{k}_0, z)\rangle \propto e^{-i\Sigma_{\rm TE(TM)} z/2k_z} \boldsymbol{e}_i^{\rm TE(TM)}$, respectively. The two different self-energies $\Sigma_{\rm TE}$ and $\Sigma_{\rm TM}$ thus turn out to correspond to the self-energies of the two polarization modes TE and TM of the problem discussed in Sec. 4.1. At small angle, the intensity at the beam center $I_c(L)$ for TE-(TM-) polarized light is then simply equal to:

$$I_c(L) = I_0 \exp\left(\frac{L\,{\rm Im}\Sigma_{\rm TE(TM)}}{k}\right), \tag{4.30}$$

describing an exponential decay respectively governed by the imaginary parts ${\rm Im}\,\Sigma_{\rm TE} < 0$ or ${\rm Im}\Sigma_{\rm TM} < 0$. As usually in a disordered medium, this decay provides an effective-medium description for the propagation of the ballistic mode, which gets depleted at

the scale of a mean free path due to scattering in other directions [17]. A difference with standard isotropic random media is that the decay here involves two different mean free paths $-k/\operatorname{Im}\Sigma_{\mathrm{TE(TM)}}$, one for each mode.

In the following, we will use as a benchmark for all length scales along z the TE scattering mean free path, denoted by z_s [1]:

$$\frac{1}{z_s} = -\frac{1}{k}\mathrm{Im}\,\Sigma_{\mathrm{TE}} = \frac{4n}{k}\frac{(\Gamma_0/2)^2(\omega/\omega_0)^4}{(\omega-\omega_0)^2+(\Gamma_0/2)^2(\omega/\omega_0)^4}\ , \tag{4.31}$$

where we have used Eq.s (4.24) and (4.27) in the second equality. We will also frequently use the value of the mean free path evaluated at the lowest Mie resonance ω_0, $z_s^0 \equiv z_s(\omega_0) = k/4n$.

Let us here open a small parenthesis about the exact value of z_s in the static regime (i.e., at $\omega \to 0$). For small incident angles ($\theta \ll 1$), one finds from the exact expression of $b_{0\mathrm{I}}$ and $a_{1\mathrm{I}}$ in Eq. (4.8) the result

$$z_s^{-1}(\omega=0) = n\left(\frac{m^2-1}{m^2+1}\right)^2\pi^2k^3\rho^4 = \frac{n\alpha_s^2k^3}{4}\ , \tag{4.32}$$

where in the second equality the polarizability of an infinite tube $\alpha_s = 2S(m^2-1)/(m^2+1)$ [179], with $S=\pi\rho^2$ being the tube section, has been introduced. Comparing Eq. (4.32) with the non-resonant uncorrelated disorder result, $z_s = 4/(\gamma k^3)$ of chapter 2 [62], we observe that in the photonic array the disorder amplitude γ maps onto the product $n\alpha_s^2$.

For an arbitrary polarization of the incident beam, $I_c(L)$ is given by a weighted sum of the two exponential decays (4.30). In particular, for a balanced mixture of the two modes

$$\boldsymbol{e}_0 = \frac{\boldsymbol{e}_i^{\mathrm{TM}} + e^{i\phi}\boldsymbol{e}_i^{\mathrm{TE}}}{\sqrt{2}}\ , \tag{4.33}$$

which is the most favourable configuration to observe a SHE (see Sec. 3.6.1), we have:

$$I_c(L) = \frac{I_0}{2}\left(e^{L\,\mathrm{Im}\Sigma_{\mathrm{TE}}/k} + e^{L\,\mathrm{Im}\Sigma_{\mathrm{TM}}/k}\right)\ . \tag{4.34}$$

It is instructive, at this stage, to display the coherent mode intensity (4.34) as a function of the frequency $\omega-\omega_0$ relative to the lowest Mie resonance, see Fig. 4.4. The intensity exhibits two local minima, corresponding to the two resonances at ω_0 and ω_1 [with the TM resonance at ω_1 originating from Σ_{TM} only, see Eq. (4.27)]. The plot, in particular, showcases the sharp character of the TM resonance, whose width $\Gamma_1 \propto \sin^2\theta$. Note that the distance $(\omega_1-\omega_0)/(\Gamma_0/2)$ between the resonances increases as the angle of incidence θ decreases. This is essentially due to the θ-dependence of ω_0 and Γ_0, which are slowly decreasing functions of θ [ω_1 is, on the contrary, nearly independent of θ, see Eq. (4.11)].

[1] For the balanced polarization mixture (4.33), the coherent intensity (4.34) involves both the TE and TM mean free paths. However, as discussed in the next section, away from the TM resonance we have $\mathrm{Im}\Sigma_{\mathrm{TM}} \simeq \mathrm{Im}\Sigma_{\mathrm{TE}}$, while at the TM resonance $\mathrm{Im}\Sigma_{\mathrm{TM}} \gg \mathrm{Im}\Sigma_{\mathrm{TE}}$. Therefore, in both cases $I(L) \propto \exp\big(L\mathrm{Im}\Sigma_{\mathrm{TE}}/k\big)$ at large enough L.

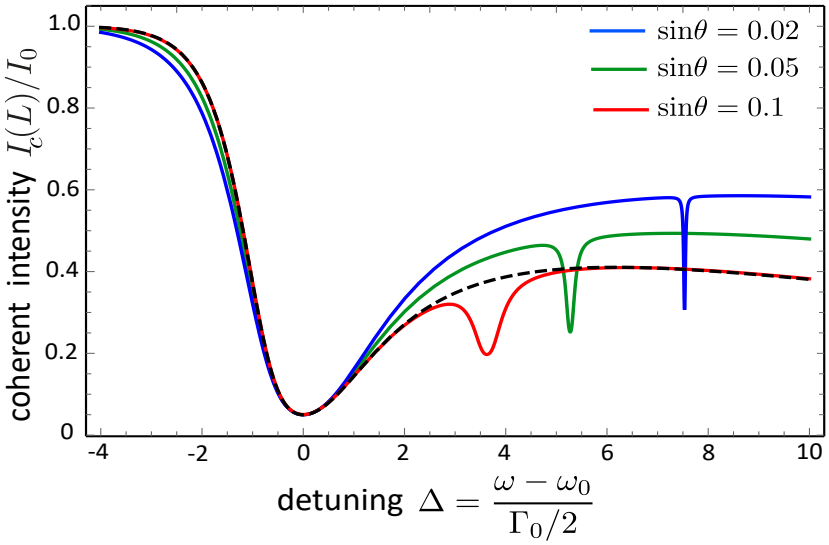

Figure 4.4: Intensity $I_c(L)$ of the coherent mode at the beam center for a balanced mixture of TE and TM modes, Eq. (4.34), as a function of the detuning $\Delta = (\omega - \omega_0)/(\Gamma_0/2)$ relative to the lowest Mie resonance of the photonic array. The curves correspond to three values of the angle of incidence θ. In each case, the sharp resonance at $\omega = \omega_1$ is visible, and becomes narrower as θ decreases. The relative cylinder refractive index is set to $m = 3$ and the optical thickness to $L = 3z_s^0$. The dashed curve shows the intensity in the TE mode for comparison, i.e., $I_c(L) = I_0 \exp\big(-L/z_s\big)$.

4.3.2 Resonant spin Hall effect

We now move to examine the centroid $\boldsymbol{R}_\perp(L)$ of the coherent mode. Its derivation is the same as in Sec. 3.6 and, when considering Eq. (4.33) as the initial polarization state, gives:

$$\boldsymbol{R}_\perp(L) \simeq \hat{\boldsymbol{k}}_0 L + R_y(L)\hat{\boldsymbol{y}} \,, \tag{4.35}$$

where on top of the usual ballistic contribution $\hat{\boldsymbol{k}}_0 L$ appears the SHE contribution:

$$R_y(L) = -\frac{\sin\phi}{k_0}\left[1 - \frac{\cos L/2z_{\rm L}}{\cosh L/2z_{\rm S}}\right] + \frac{\cos\phi}{k_0}\frac{\sin L/2z_{\rm L}}{\cosh L/2z_{\rm S}} \,, \tag{4.36}$$

which is identical to Eq. (3.46), the only difference residing in the microscopic expression of the parameters $z_{\rm L}$ and $z_{\rm S}$, still defined as

$$\begin{aligned} z_{\rm L} &= [{\rm Re}(\Sigma_{\rm TM} - \Sigma_{\rm TE})/k]^{-1} \\ z_{\rm S} &= [{\rm Im}(\Sigma_{\rm TM} - \Sigma_{\rm TE})/k]^{-1} \,. \end{aligned} \tag{4.37}$$

As in chapter 3, the shift (4.36) stems from the interference between spin-orbit coupled photons propagating in the effective medium at the two spatial frequencies $k - \Sigma_{\rm TE}/k$ and $k - \Sigma_{\rm TM}/k$, this interference involving both oscillation and relaxation effects because of the complex nature of the self energies $\Sigma_{\rm TE(TM)}$.

As compared to the model of continuous disorder, the SOI parameters $z_{\rm L}$ and $z_{\rm S}$ now resonantly depend on frequency, which can be used as a new degree of freedom regarding the physics of the spin Hall effect. Indeed, what makes the discrete random

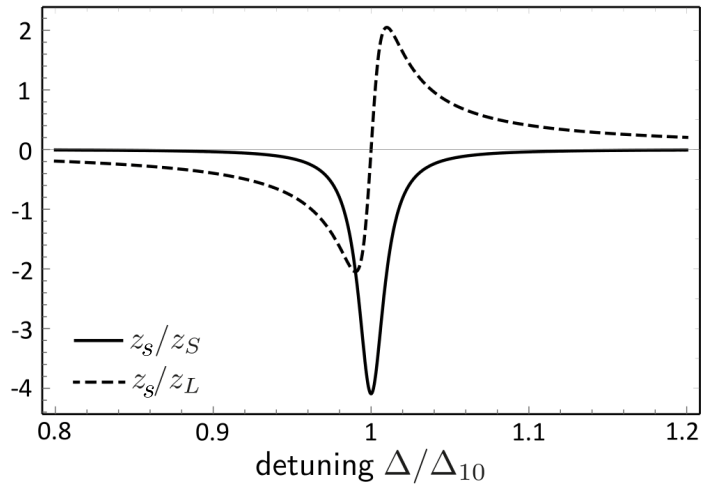

Figure 4.5: Ratios $z_s/z_{\mathrm{S(L)}}$ of the scattering mean free path along z to the spin Hall mean free paths, as a function of the detuning relative to the Mie resonance at $\omega = \omega_1$ [here $\Delta = (\omega - \omega_0)/(\Gamma_0/2)$ is expressed in units of $\Delta_{10} = (\omega_1 - \omega_0)/(\Gamma_0/2)$; $\Delta = \Delta_{10}$ thus corresponds to $\omega = \omega_1$]. Observe that the ratios exceed unity in the vicinity of the resonance.

array of special interest here is that, by exploiting the highly resonant character of the scatterers together with the strong dependence of the TM resonance width upon the angle of incidence θ, it is possible to access a regime where z_{S} and z_{L} are comparable to the mean free path z_s. This is in marked contrast with non-resonant media, where we have found that (see Sec. 3.6.2)

$$z_{\mathrm{L(S)}} \sim z_s/\sin^2\theta\ , \tag{4.38}$$

so that the spin Hall effect arises at a scale where the coherent mode is significantly attenuated and is, consequently, not easily detectable.

To illustrate the above property, we show in Fig. 4.5 the ratios z_s/z_{L} and z_s/z_{S} as a function of detuning, in the close vicinity of the TM resonance. These ratios are computed by inserting Eq.s (4.24), (4.25) and (4.27) in the definitions (4.37). Observe that in the vicinity of this resonance, one can easily achieve $|z_s/z_{\mathrm{S(L)}}| > 1$. The reason for this striking effect is the ultra-narrow character of the TM resonance at small angle of incidence (see Fig. 4.2), together with the fact that this resonance directly governs the magnitude of $z_{\mathrm{L(S)}}$ via Σ_{TM} [see Eq.s (4.25) and (4.27)] but not of the mean free path z_s (which only depends on Σ_{TE}, i.e., on the lowest Mie resonance).

4.3.3 Tailoring the spin Hall effect via the incident frequency

In the previous chapter, we have shown that a variety of coherent mode's transverse trajectories can be tailored by changing the disorder correlation length. In the random array, a similar idea can be implemented, this time by tuning the incident laser frequency. In Fig. 4.6, we illustrate this possibility by showing the ratio $|z_{\mathrm{S}}/z_{\mathrm{L}}|$ vs. the detuning for different sets of the parameters (m, θ), focusing our attention on the frequency window close to the TM resonance where, as shown above, the spin Hall effect

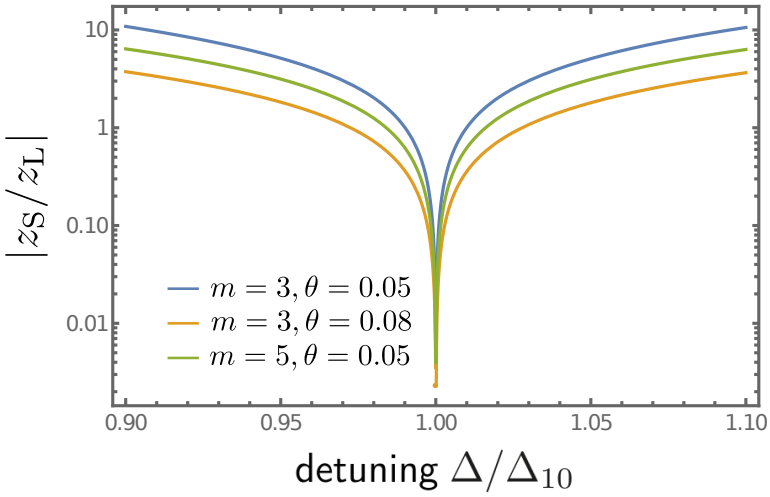

Figure 4.6: Parameter $|z_S/z_L|$, whose value controls which type of SHE trajectory will appear in the coherent mode, as a function of the incident laser frequency. In the frequency window of interest close to the TM resonance, one can realize both $|z_S/z_L| \ll 1$, $|z_S/z_L| \sim 1$ and $|z_S/z_L| \gg 1$. The different curves here stand for different values of (m, θ).

occurs at the scale of the mean free path. When this ratio is small the SHE typically varies monotonically with L, while for large $|z_S/z_L|$ it exhibits oscillations. To illustrate this, we show in Fig.s 4.7a and 4.7b the spin Hall shift R_y vs. L near the TM resonance for circularly and linearly polarized light, respectively, at fixed $m = 3, \theta = 0.05$. When $|z_S/z_L| \ll 1$ one has a monotonic shift only involving circularly polarized light, while for $|z_S/z_L| \sim 1$ and $|z_S/z_L| \gg 1$ one observes, respectively, the presence of damped and undamped transverse oscillations with a non-zero shift also appearing for linearly polarized light. Notice that exactly at resonance, the spin Hall effect appears at a scale *smaller* than the mean free path, whose position is indicated by the vertical dotted line. On the contrary, as one deviates from the resonance, R_y becomes sizeable at a much larger scale than z_s, with $z_{L(S)}$ converging to the non-resonant result (4.38).

4.3.4 Asymptotic limits of the spin-orbit parameters

To gain a better insight on the behavior of the SHE described above, it is instructive to examine the analytical expressions of z_S and z_L in some characteristic limits. The explicit frequency dependence of these parameters is obtained by inserting Eq.s (4.24), (4.25) and (4.27) into the definitions (4.37):

$$\frac{1}{z_S} = \frac{4n}{k}\left[\sin^2\theta \frac{(\Gamma_0/2)^2(\omega/\omega_0)^4}{(\omega-\omega_0)^2 + (\Gamma_0/2)^2(\omega/\omega_0)^4} - \frac{(\Gamma_1/2)^2}{(\omega-\omega_1)^2 + (\Gamma_1/2)^2}\right] \tag{4.39}$$

$$\frac{1}{z_L} = \frac{4n}{k}\left[\frac{(\Gamma_1/2)(\omega-\omega_1)}{(\omega-\omega_1)^2 + (\Gamma_1/2)^2} - \sin^2\theta \frac{(\Gamma_0/2)(\omega-\omega_0)(\omega/\omega_0)^2}{(\omega-\omega_0)^2 + (\Gamma_0/2)^2(\omega/\omega_0)^4}\right] . \tag{4.40}$$

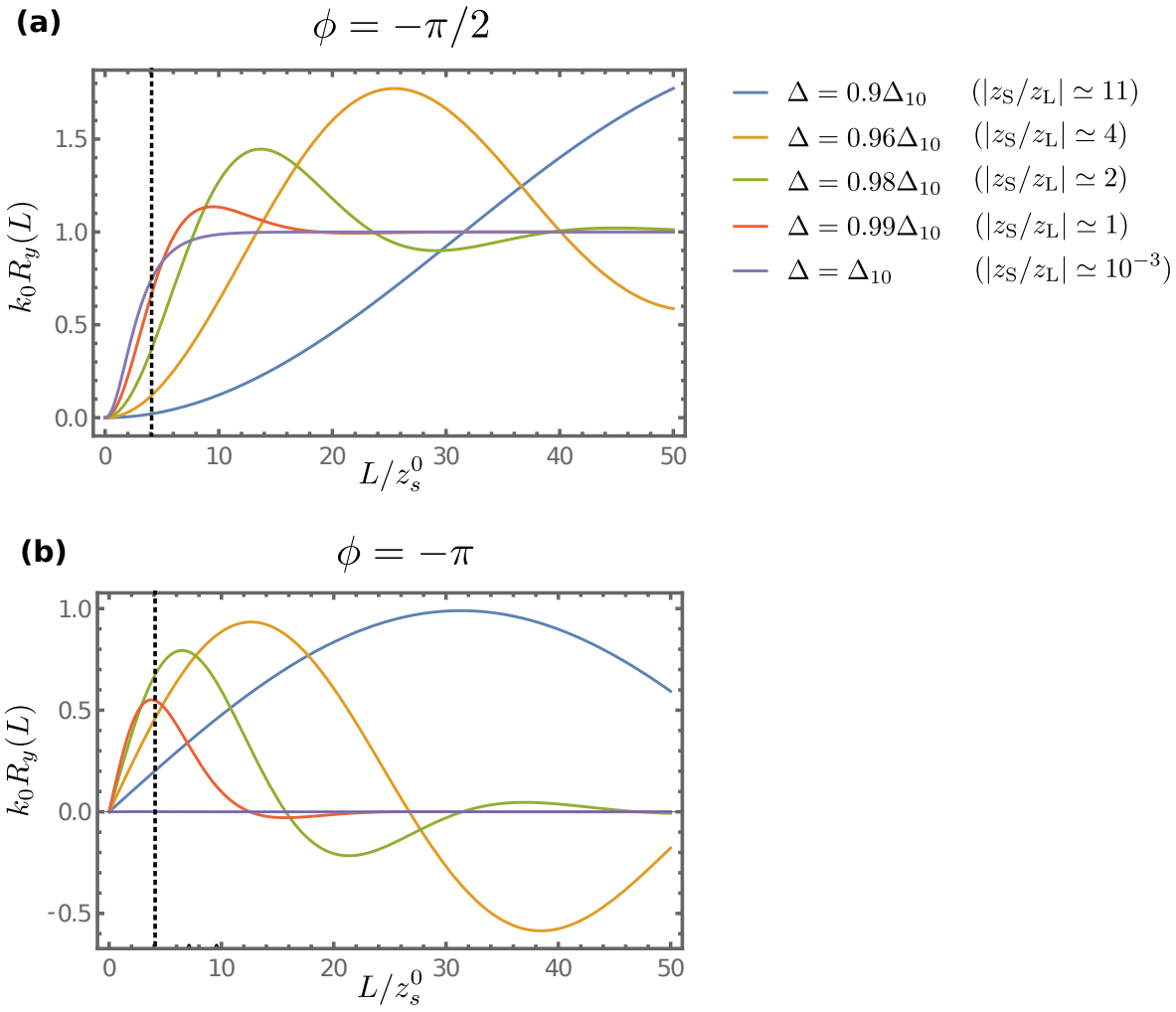

Figure 4.7: Transverse shift R_y of the beam centroid as a function of L for various detunings close to the TM resonance. In panels (a) and (b), incident light circularly ($\phi = -\pi/2$) and linearly ($\phi = -\pi$) polarized is considered, respectively. The vertical dotted line indicates the location of the mean free path z_s (for the considered near-resonant detunings, z_s is nearly independent of Δ). For all plots we set $m = 3$, $\theta = 0.05$. The plots demonstrate that in the vicinity of the TM resonance, various spin Hall shifts appearing at scales of the order of z_s can be realized.

Let us first consider the static limit $\omega \to 0$, which formally corresponds to the model of non-resonant dielectric media discussed in [62, 67]. Equation (4.39) gives

$$z_{\mathrm{S}}(\omega \to 0) \simeq \frac{1}{\sin^2\theta}\frac{k}{4n}\left(\frac{2\omega_0}{\Gamma_0}\right)^2\left(\frac{\omega_0}{\omega}\right)^4 = \frac{z_s(\omega \to 0)}{\sin^2\theta}\,, \tag{4.41}$$

where we have neglected the second term in the right-hand side of Eq. (4.39) using that $\Gamma_1 \sim \sin^2\theta\Gamma_0$, and we have used the expression (4.31) of the mean free path in the second equality. Similarly, from Eq. (4.40) we find $z_{\mathrm{L}}(\omega \to 0) \sim z_s(\omega \to 0)/\sin^2\theta$. We thus recover the generic relation (4.38) for non-resonant materials.

Second, we examine the situation where the laser is tuned at the TM resonance, i.e., $\omega \simeq \omega_1$. In that case, the second term in the right-hand side of Eq. (4.39) becomes dominant and leads to

$$|z_{\mathrm{S}}(\omega \simeq \omega_1)| \simeq \frac{k}{4n} = z_s^0 < z_s\,. \tag{4.42}$$

This confirms the result of the previous section, namely that the SHE occurs at a spatial scale shorter than the mean free path. Note, on the other hand, that $z_{\mathrm{L}} \sim z_s^0/\sin^2\theta \gg z_s$ exactly at the TM resonance. This explains the absence of oscillations in the spin Hall shift visible in Fig. 4.7 for $\Delta = \Delta_{10}$.

In the case, finally, where the laser is tuned near the TE resonance ($\omega \simeq \omega_0$), we find from Eq.s (4.39) and (4.40) the same behavior as in the static limit: $z_{\mathrm{L(S)}}(\omega \simeq \omega_0) \simeq z_s/\sin^2\theta \gg z_s$, so that there is no significant SHE at the scale of the mean free path.

4.3.5 Giant spin Hall effect

According to Eq. (4.36), the maximum value of the spin Hall shift in a random array is $R_y \sim k_0^{-1}$. As already done in Sec. 3.9.1, by performing a proper polarimetry measurement ("weak quantum measurement" optical analogue) one can amplify the shift up to the scale of the beam width w_0 (recall that $k_0 w_0 \gg 1$ holds true by hypothesis). Combining the TM resonance excitation with the weak quantum measurement enables us to achieve a giant spin Hall effect, a priori accessible to experimental detection.

In the weak-measurement scheme, we recall that the coherent mode centroid is given by

$$\boldsymbol{R}_\perp(L) = \frac{\int d\boldsymbol{r}_\perp \boldsymbol{r}_\perp |\boldsymbol{e}_{\mathrm{out}}^* \cdot \langle \boldsymbol{E}(\boldsymbol{r}_\perp, L)\rangle|^2}{\int d\boldsymbol{r}_\perp |\boldsymbol{e}_{\mathrm{out}}^* \cdot \langle \boldsymbol{E}(\boldsymbol{r}_\perp, L)\rangle|^2}\,, \tag{4.43}$$

where $\boldsymbol{e}_{\mathrm{out}}$ is the direction of the post-selection polarizer through which the transmitted light is detected.

Similarly to what was explained in Sec. 3.9.1, by starting from a linearly polarized beam $\boldsymbol{e}_0 = \boldsymbol{e}_i^{\mathrm{TM}}$, the first and second term of Eq. (4.7) composing the microscopic SHE can be effectively enhanced by choosing, respectively, a post-selection polarizer of the form $\boldsymbol{e}_{\mathrm{out}} \propto \boldsymbol{e}_i^{\mathrm{TE}} + i\delta\boldsymbol{e}_i^{\mathrm{TM}}$ and $\boldsymbol{e}_{\mathrm{out}} \propto \boldsymbol{e}_i^{\mathrm{TE}} + \delta\boldsymbol{e}_i^{\mathrm{TM}}$ with $|\delta| \ll 1$. The analytical expressions for the beam centroid within the weak-measurement scheme in the two

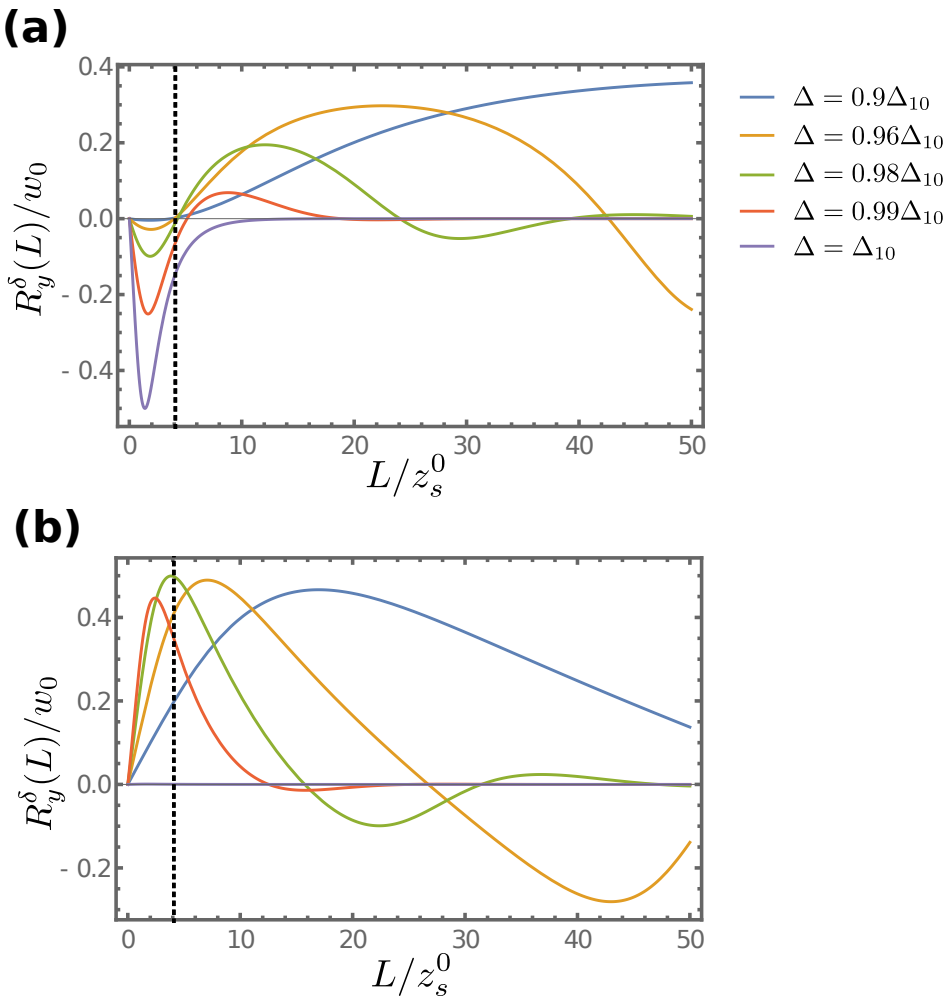

Figure 4.8: Weak-measurement-based spin Hall shift $R_y^\delta(L)$ vs. L for various detunings, in the vicinity of the TM resonance. The vertical dotted line indicates the position of the mean free path z_s. For all plots we set $m = 3$, $\theta = 0.05$ and $\delta = -(k_0 w_0)^{-1}$. In panels (a) and (b), we consider, respectively, $\boldsymbol{e}_{\text{out}} \propto \boldsymbol{e}_i^{\text{TE}} + i\delta \boldsymbol{e}_i^{\text{TM}}$ and $\boldsymbol{e}_{\text{out}} \propto \boldsymbol{e}_i^{\text{TE}} + \delta \boldsymbol{e}_i^{\text{TM}}$ as post-selection polarizer effectively amplifying the first (second) term in Eq. (4.36). As in Fig. 4.7, the shift appears at the same scale of z_s, but its maximum value is now of the order of the beam width w_0 thanks to the post-selection scheme.

configurations are the following:

$$\begin{aligned} R_y^{\delta}(L) &= -\frac{\delta}{k_0}\frac{1-e^{-L/2z_{\rm S}}\cos\big(L/2z_{\rm L}\big)}{\delta^2+\big(\frac{1}{k_0w_0}\big)^2|1-e^{-L/2z_{\rm S}}e^{iL/2z_{\rm L}}|^2} \text{ for } \boldsymbol{e}_{\rm out}\propto \boldsymbol{e}_i^{\rm TE}+i\delta\boldsymbol{e}_i^{\rm TM} \\ R_y^{\delta}(L) &= \frac{\delta}{k_0}\frac{e^{-L/2z_{\rm S}}\sin\big(L/2z_{\rm L}\big)}{\delta^2+\big(\frac{1}{k_0w_0}\big)^2|1-e^{-L/2z_{\rm S}}e^{iL/2z_{\rm L}}|^2} \text{ for } \boldsymbol{e}_{\rm out}\propto \boldsymbol{e}_i^{\rm TE}+\delta\boldsymbol{e}_i^{\rm TM} \end{aligned} \tag{4.44}$$

Compared to Eq. (4.36), which does not involve any post-selection, the shifts (4.44) are now of the order of the beam width w_0 if one chooses $|\delta| \sim 1/(k_0 w_0) \ll 1$. This is shown in Fig. 4.8, where Eq.s (4.44) have been plotted for various detunings in the close vicinity of the TM Mie resonance. Again, the spin Hall shift occurs at a smaller scale than the mean free path (indicated by a vertical dotted line), but contrary to Fig. 4.7 its maximum value is now of the order of w_0. This result can be seen as a giant SHE in a random array, where the spin Hall shift is both macroscopic and occurs at a $z-$scale where the coherent mode is fully visible.

4.4 Spin-orbit coupled flash of light

In the previous section, we have shown that a giant spin Hall effect can emerge in the coherent mode by operating in the close vicinity of the TM resonance. This manifests itself by a spatial shift of the beam in the transverse plane of the random array, visible for optically-thin arrays of thickness $L \sim z_s$ of the order of the scattering mean free path. The next natural question is whether the SHE can also be observed in an optically-thick random array of length $L \gg z_s$. In the case of a stationary laser excitation considered so far, this is clearly hopeless due to the exponential attenuation of the coherent mode as $\exp\big(-L/z_s\big)$. For a time-dependent excitation, on the other hand, the resonant character of the system makes this possible by exploiting the "coherent flash" phenomenon, as we now show.

The coherent flash belongs to a class of coherence-related phenomena that occur after rapid source extinction when dealing with resonant scatterers. Such coherent transient phenomena are rather ubiquitous in physics. The first observation of coherent emission after source excitation comes from free induction decay in nuclear magnetic resonances [180, 181]. Later, free induction decay was also observed in the optical domain, with electromagnetic resonances in atoms [182, 183], molecules [184, 185] and nuclei [186, 187]. In the context of disordered media, the coherent flash corresponds to a strong, transient enhancement of coherent light intensity occurring after a sudden source extinction in the regime $L/z_s \gg 1$, where for a stationary excitation the coherent mode would be completely depleted by multiple scattering. The time duration of this flash of light is reduced with respect to the single scatterer lifetime by a factor of the order of the optical thickness [188].

The origin of the flash effect can be understood from the decomposition (4.15) of the total field

$$\boldsymbol{E}(\boldsymbol{r}) = \boldsymbol{E}_{\rm in}(\boldsymbol{r}) + \boldsymbol{E}_s(\boldsymbol{r}) \tag{4.45}$$

as the sum of the incoming and scattered fields, $\boldsymbol{E}_{\rm in}$ and $\boldsymbol{E}_s$, respectively. In the stationary regime, the coherently transmitted field stems from the destructive interference be-

tween $\boldsymbol{E}_{\rm in}$ and the part of $\boldsymbol{E}_s$ scattered in the same (forward) direction $\boldsymbol{k}_{\rm in}$[2], resulting in the Beer-Lambert attenuation of the coherent mode intensity as $I_c(L) = \exp\big(-L/z_s\big)$. If the laser is switched off, this interference is suppressed while the resonant scatterers continue to radiate over a time scale of the order of the inverse of the resonance width, leading to a flash of light. This can be mathematically formulated as follows. When the laser is switched off, $\boldsymbol{E}_{\rm in}(t=0^+)=0$ such that $\boldsymbol{E}(t=0^+)=\boldsymbol{E}_s(t=0^+)$. On the other hand, if the medium is optically thick, $\boldsymbol{E}(t=0^-)\simeq 0$ is exponentially attenuated, such that $\boldsymbol{E}_s(t=0^-)=-\boldsymbol{E}_{\rm in}(t=0^-)$. Combining these relations assuming the continuity of the scattered field at $t=0$ leads to $\boldsymbol{E}(t=0^+)=-\boldsymbol{E}_{\rm in}(t=0^-)$, i.e., a flash of light of same intensity as the incoming beam. Because of the cooperative effect of scatterers in the forward direction lying at the basis of the phenomenon, the coherent flash takes place at large enough optical thickness $L/z_s \gg 1$ and its duration is much shorter than the excited lifetime of the single scatterer.

Coherent flashes of light in optically-thick media have been theoretically described and experimentally observed in resonant cold atomic gases [188]. Later on, it was also shown that "super-flashes" of intensity larger than that of the incoming laser could even be achieved by operating slightly away from resonance, with a maximum theoretical value of $4|\boldsymbol{E}_{\rm in}|^2$ stemming from the general inequality $|\boldsymbol{E}_{\rm in}+\boldsymbol{E}_s|^2 \leq |\boldsymbol{E}_{\rm in}|^2$ imposed by energy conservation [189, 190]. The coherent super-flash represents a form of cooperative forward emission of the atoms, which can be regarded as a phenomenon of superradiance. Beyond the coherent flash, the physics of cooperative emission from an ensemble of radiation dipoles, opened by the Dicke's seminal work in 1954 [191], has been widely explored [192], representative examples being superradiant lasers [193, 194] and superradiance of a single photon emission [195].

The coherent flash is expected to take place in our system as well, due to the resonant nature of our scatterers. This suggests the possibility to observe a time-dependent SHE in optically-thick random arrays, provided the associated spin Hall shift exists on the time scale where the flash occurs. To describe this problem, let us here again consider an incident laser beam of the form (4.21), but now suppose that the beam is suddenly switched off at some time $t=0$:

$$\boldsymbol{E}(\boldsymbol{k}_\perp, z=0, t) = \sqrt{2\pi} w_0 \exp\big[-(\boldsymbol{k}_\perp-\boldsymbol{k}_0)^2 w_0^2/4 - i\omega_l t\big]\boldsymbol{e}_0\theta(-t)\ , \tag{4.46}$$

the Heaviside theta function $\theta(t)$ models the abrupt extinction of the source and ω_l is the laser carrier frequency. We then insert the relation

$$\exp(-i\omega_l t)\theta(-t) = \int \frac{d\omega}{2\pi} e^{-i\omega t}\left[\pi\delta(\omega-\omega_l) - ip.v.\left(\frac{1}{\omega-\omega_l}\right)\right] \tag{4.47}$$

into Eq. (4.46). This leads to the temporal version of Eq. (4.28): which reads:

$$\begin{aligned}\langle \boldsymbol{E}(\boldsymbol{k}_\perp, z=L, t)\rangle = \sqrt{2\pi w_0^2}\exp\big[-\frac{w_0^2}{4}(\boldsymbol{k}_\perp-\boldsymbol{k}_0)^2\big]\int\frac{d\omega}{2\pi}e^{-i\omega t}\Big[\pi\delta(\omega-\omega_l)\\ - ip.v.\left(\frac{1}{\omega-\omega_l}\right)\Big]\times\big[e^{-i\Sigma_{\rm TE}L/2k_z}\boldsymbol{e}_0 + \big(e^{-i\Sigma_{\rm TM}L/2k_z}-e^{-i\Sigma_{\rm TE}L/2k_z}\big)\boldsymbol{p}(\boldsymbol{k}_\perp)\big]\ .\end{aligned} \tag{4.48}$$

[2]Indeed, although, in an arbitrary direction, the light emitted from the scatterers is incoherent with the respect to the incoming beam due to the randomness of the scatterers' positions, this is not the case in the forward direction where the phase of the scattered field, for geometric reasons, turns out to be independent of the scatterers' position.

The space-time intensity distribution of the coherent mode follows from

$$I_c(\boldsymbol{r}_\perp, L, t) = \int \frac{d^2\boldsymbol{k}_\perp}{(2\pi)^2} \int \frac{d^2\boldsymbol{q}}{(2\pi)^2} e^{i\boldsymbol{q}\cdot\boldsymbol{r}_\perp} \langle \boldsymbol{E}(\boldsymbol{k}_\perp^+, L, t)\rangle \cdot \langle \boldsymbol{E}^*(\boldsymbol{k}_\perp^-, L, t)\rangle \tag{4.49}$$

with $\boldsymbol{k}_\perp^\pm = \boldsymbol{k}_\perp \pm \boldsymbol{q}/2$. Following the same lines as in Sec. 3.5, we end up with

$$I_c(\boldsymbol{r}_\perp, L, t) \simeq I_c(L, t) e^{-2|\boldsymbol{r}_\perp - \boldsymbol{R}_\perp(L,t)|^2/w_0^2} , \tag{4.50}$$

where

$$I_c(L, t) = I_0 \int \frac{d^2\boldsymbol{k}_\perp}{(2\pi)^2} |\langle \boldsymbol{E}(\boldsymbol{k}_\perp, L, t)\rangle|^2 = I(\boldsymbol{R}_\perp(L), L, t) \tag{4.51}$$

with $I_0 = 2/(\pi w_0^2)$, and

$$\begin{aligned} \boldsymbol{R}_\perp(L, t) =& \frac{i \int \frac{d^2\boldsymbol{K}}{(2\pi)^2} \boldsymbol{\nabla}_{\boldsymbol{q}} [\langle \boldsymbol{E}(\boldsymbol{K}_+, L, t)\rangle \cdot \langle \boldsymbol{E}^*(\boldsymbol{K}_-, L, t)]\rangle_{\boldsymbol{q}\to 0}}{\int \frac{d^2\boldsymbol{K}}{(2\pi)^2} |\overline{\boldsymbol{E}}(\boldsymbol{K}, L, t)|^2} \\ \equiv& \frac{\int d^2\boldsymbol{r}_\perp \boldsymbol{r}_\perp I_c(\boldsymbol{r}_\perp, L, t)}{\int d\boldsymbol{r}_\perp I_c(\boldsymbol{r}_\perp, L, t)} . \end{aligned} \tag{4.52}$$

Eq.s (4.50, 4.51, 4.52) are the time-dependent versions of Eq.s (3.34, 3.35, 3.36). To evaluate the coherent mode intensity (4.51) and the beam centroid (4.52), we need to perform the Fourier transforms with respect to ω coming from Eq. (4.48), taking into account the explicit frequency dependence of $\Sigma_{\mathrm{TE(TM)}}$. To this aim and for the sake of simplicity, we drop the quadratic frequency corrections in Eq. (4.24), and thus use:

$$\begin{aligned} \Sigma_{\mathrm{TE}}(\omega) =& \frac{4n\Gamma_0/2}{\omega - \omega_0 + i\Gamma_0/2} \\ \Sigma_{\mathrm{TM}}(\omega) =& \frac{4n\Gamma_1/2}{\omega - \omega_0 + i\Gamma_1/2} + \frac{4n\Gamma_0/2\cos^2\theta}{\omega - \omega_0 + i\Gamma_0/2} . \end{aligned} \tag{4.53}$$

This allows us to derive closed formulas for $I_c(L, t)$ and $\boldsymbol{R}_\perp(L, t)$, which can be used for numerical simulations. These expressions are a little cumbersome and are therefore given in Appendix E for clarity.

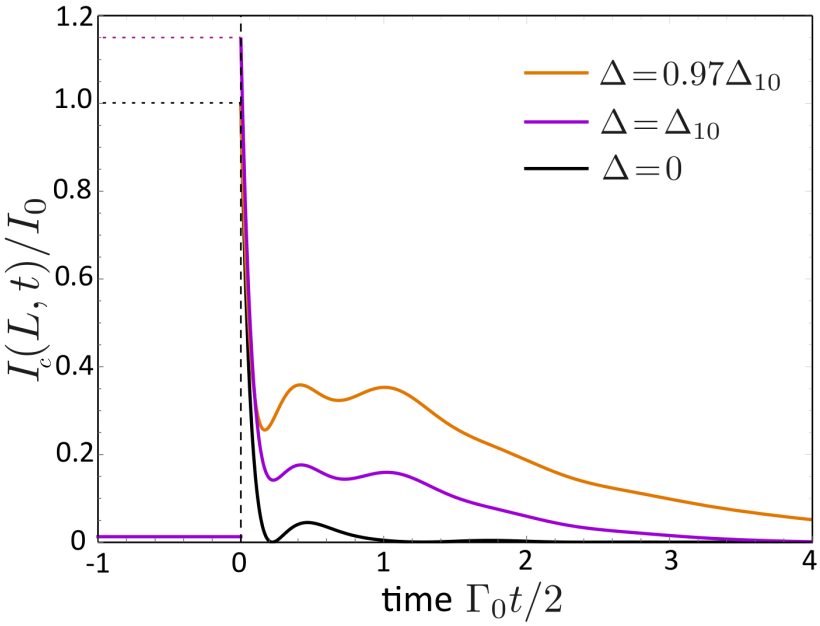

Figure 4.9: Time evolution of the coherent mode intensity $I_c(L,t)$ transmitted through the random array, for three values of the detuning $\Delta = (\omega_l - \omega_0)/(\Gamma_0/2)$. In each case the incident laser is switched off at $t = 0$, which results in a flash of light at $t = 0^+$. In the vicinity of the TM resonance ($\Delta = \Delta_{10}$), the flash exhibits a long-lived tail.

We first show in Fig. 4.9 the coherent mode intensity vs. time following the laser extinction for three values of the detuning $\Delta = (\omega - \omega_0)/(\Gamma_0/2)$, setting the optical thickness L/z_s^0 to a relatively large value. At $\Delta = 0$, we observe a coherent flash of maximum amplitude $I_c = I_0$ decaying over a typical time scale $\sim \Gamma_0^{-1} z_s/L$, i.e., a fraction of the lifetime of the TE Mie resonance. This behavior is similar to that observed in resonant cold atomic gases [188, 189]. On the other hand, at detunings $\Delta \simeq \Delta_{10}$ the temporal shape of the coherent intensity acquires a bimodal structure, with a short transient flash followed by a slowly decaying tail that persists up to the much longer time scale $\sim \Gamma_1^{-1} z_s/L \sim \Gamma_0^{-1} z_s/(L \sin^2\theta)$. This long-lived tail is a direct manifestation of the resonance at ω_1, whose contribution to $I_c(L,t)$ becomes significant when $\omega_l \sim \omega_1$ and adds up to the contribution of the resonance at ω_0. In this doubly-resonant regime, the magnitude of the flash also slightly exceeds I_0.

Following the laser extinction, not only the intensity but also the spin Hall shift undergoes a temporal evolution. Its analytical expression is given in Appendix E, in both cases where a polarization post-selection is performed or not. We show in Fig. 4.10 its macroscopic value $R_y^\delta(L,t)$ along the $y-$axis obtained using the weak-measurement procedure explained in Sec. 4.3.5, for two different detunings (one near TM resonance and one not) at a fixed value $L/z_s^0 \gg 1$ of the optical thickness. For $\boldsymbol{e}_{\rm out} \propto \boldsymbol{e}_i^{\rm TE} + i\delta \boldsymbol{e}_i^{\rm TM}$ as post-selection polarizer, we demonstrate the possibility of achieving a significant spin Hall shift of the order of the beam width w_0 in a time-window where, thanks to the coherent flash phenomenon, the coherent mode is visible at large optical thicknesses. Specifically, we find that, when the incident laser frequency is tuned near the TM

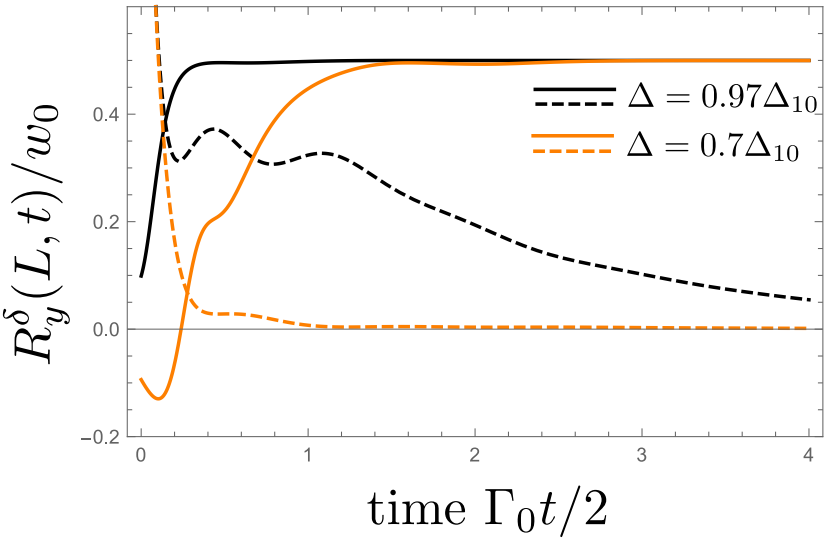

Figure 4.10: Time evolution of the macroscopic spin Hall shift, based on the weak-measurement scheme with $\boldsymbol{e}_{\rm out} \propto \boldsymbol{e}_i^{\rm TE} - i(k_0 w_0)^{-1}\boldsymbol{e}_i^{\rm TM}$ as post-selection polarizer, for two values of the detuning (solid curves). The corresponding intensities $I_c(L,t)/I_0$ are superimposed (dashed curves, same vertical scale). Near the TM resonance ($\Delta = \Delta_{10}$), a large spin Hall shift appears over a time window where the coherent flash is still significant. We set $m = 3$, $\theta = 0.05$, and an optical thickness $L/z_s^0 = 15$.

resonance ($\Delta \simeq \Delta_{10}$), the shift reaches a value $w_0/2$ over a time scale $\Gamma_0^{-1} z_s/L$, much shorter than the duration $\Gamma_1^{-1} z_s/L$ of the coherent flash. As one moves away from the TM resonance, on the other hand, the shift takes a longer and longer time to appear while the flash duration becomes shorter and shorter (see Fig. 4.10).

4.5 Conclusion

We have described the propagation of light in transversally disordered photonic arrays, and have shown evidence for an enhanced spin Hall effect of light in the vicinity of the second Mie resonance of the system. This resonance is associated with the TM polarization component of the beam impinging on the medium at an angle of incidence θ, and exhibits a narrow spectral width scaling as θ^2. This gives rise to a SHE shift taking place at longitudinal length scales $z_{\rm S(L)}$ smaller than the mean free path z_s, in strong contrast with non-resonant materials for which $z_{\rm S(L)} \sim z_s/\theta^2 \gg z_s$. This implies that the SHE occurs at a spatial scale where the coherent mode is still significant. Furthermore, we have provided a temporal description of the SHE following the abrupt switch off of the incoming beam. In this scenario, the resonant nature of the photonic array leads to a flash of light in the coherently transmitted signal, which allows to detect the coherent mode in the regime of large optical thickness. Again, in the vicinity of the TM resonance, we have shown evidence for a long-lived flash of light together with the emergence of a sizeable spin Hall effect in the same time window.

Chapter 5

Effect of spin-orbit interactions in transverse multiple scattering

So far we have mainly focused our attention on the impact of spin-orbit interactions on the coherent mode in transversally disordered media. But, as discussed in Sec. 2.1, the coherent mode represents just a fraction of the light propagating in a disordered medium, with the multiple scattering component becoming dominant in optically-thick media, i.e., of thickness $L \gg z_s$.

A first vectorial (i.e., beyond-paraxial) description of light multiple scattering in (2+1)-dimensional disordered media was developed in 2018 [42], based on the hydrodynamic (diffusion) approximation. Through the computation of the disorder-average distribution of transverse momenta $\langle \left| \boldsymbol{E}(\boldsymbol{k}_\perp, L) \right|^2 \rangle$ detected at the longitudinal coordinate $z = L$, a crossover from a scalar to a vectorial regime was identified. Precisely, it was shown that at a certain longitudinal scale $L \sim z_s/\hat{k}_0^4$, the polarization vector of the multiply scattered photons was getting randomized, marking the full breakdown of the paraxial description. Furthermore, the polarization dependence of the coherent backscattering peak on both sides of this crossover was also analyzed in terms of incident and detection polarization channels.

In this chapter, we present a preliminary study of the role of spin-orbit interactions in the multiple scattering signal of a transversally disordered medium, restricting ourselves to the Diffuson approximation. In particular, considering a near-paraxial light evolution ($\hat{k}_0 \ll 1$), we examine the spin-orbit corrections to the centroid of the Diffuson. For this purpose (and unlike the approach used in [42]), we employ a full vectorial description of the Diffuson that does *not* use the diffusion approximation. This is indeed required, since, as stated in Sec. 2.4.1, the centroid of the multiple scattering component evolves at scales of the order of the mean free path or smaller, where a diffusion approximation would be clearly inaccurate.

5.1 Diffuson center of mass

Within the Diffuson approximation, i.e., neglecting all interference effects in multiple scattering, the centroid of a beam propagating inside the transversally disordered medium is given by

$$\boldsymbol{R}_\perp^{tot}(L) = \frac{\int d^2\boldsymbol{r}_\perp \boldsymbol{r}_\perp I_c(\boldsymbol{r}_\perp, L) + \int d^2\boldsymbol{r}_\perp \boldsymbol{r}_\perp I_D(\boldsymbol{r}_\perp, L)}{\int d^2\boldsymbol{r}_\perp I_c(\boldsymbol{r}_\perp, L) + \int d^2\boldsymbol{r}_\perp I_D(\boldsymbol{r}_\perp, L)} \,, \tag{5.1}$$

where both the coherent mode (I_c) and the Diffuson (I_D) signals are included. When only the first term of both the numerator and the denominator is counted, one obtains the coherent mode centroid that we have studied exhaustively in the previous chapters.

Similarly to what we have done in the previous chapters for the coherent mode, one could imagine now to detect only the light coming from the multiple scattering component (i.e., including single, double, etc. scattering processes). Experimentally, this would mean collecting the output light coming from any direction with the exception of the forward one. The corresponding Diffuson centroid is then defined as

$$\boldsymbol{R}_\perp^{D}(L) = \frac{\int d^2\boldsymbol{r}_\perp \boldsymbol{r}_\perp I_D(\boldsymbol{r}_\perp, L)}{\int d^2\boldsymbol{r}_\perp I_D(\boldsymbol{r}_\perp, L)} \,. \tag{5.2}$$

Expressing the optical intensity in Fourier space, Eq. (5.2) can be re-expressed as

$$\boldsymbol{R}_\perp^{D}(L) = \frac{i\int \frac{d^2\boldsymbol{K}}{(2\pi)^2} \boldsymbol{\nabla}_{\boldsymbol{q}} \langle \boldsymbol{E}(\boldsymbol{K}_+, L)\cdot \boldsymbol{E}(\boldsymbol{K}_-, L)\rangle_D|_{\boldsymbol{q}\to 0}}{\int \frac{d^2\boldsymbol{K}}{(2\pi)^2} \langle \left|\boldsymbol{E}(\boldsymbol{K}, L)\right|^2\rangle_D} \,, \tag{5.3}$$

where $\boldsymbol{K}_\pm = \boldsymbol{K} \pm \boldsymbol{q}/2$. Notice that Eq. (5.3) differs from the corresponding expression (3.34) for the coherent mode centroid in that it involves a disorder average over the product of fields, instead of the product of the disorder-averaged fields. This difference makes the computation of $\boldsymbol{R}_\perp^D(L)$ very different and much more complex.

In the rest of this section, we are going to work out Eq. (5.3) to get a formal expression of $\boldsymbol{R}_\perp^D(L)$ suitable for an explicit computation. Since the procedure is similar for both the numerator and denominator in Eq. (5.2), we here detail the procedure for the numerator only. Expressing the numerator of Eq. (5.3) in terms of the Green's tensor, using the input-output relation

$$\boldsymbol{E}(\boldsymbol{k}_\perp, L) = 2ik_z \int \frac{d^2\boldsymbol{k}'_\perp}{(2\pi)^2} \langle \boldsymbol{k}_\perp | \, G_{ij}(L) \left|\boldsymbol{k}'_\perp\right\rangle \boldsymbol{E}(\boldsymbol{k}'_\perp, z=0) \,, \tag{5.4}$$

we get

$$\begin{aligned}\int d^2\boldsymbol{r}_\perp \boldsymbol{r}_\perp \langle \left|\boldsymbol{E}(\boldsymbol{r}_\perp, L)\right|^2\rangle_D = 4ik_z^2 \int \frac{d^2\boldsymbol{K}}{(2\pi)^2} \int \frac{d^2\boldsymbol{Q}'}{(2\pi)^2} \int \frac{d^2\boldsymbol{q}'}{(2\pi)^2} E_j(\boldsymbol{Q}'_+, z=0) \\ \times E_l^*(\boldsymbol{Q}'_-, z=0) \boldsymbol{\nabla}_{\boldsymbol{q}} \langle [\left\langle \boldsymbol{K}_+\right| G_{ij}(L) \left|\boldsymbol{Q}'_+\right\rangle \left\langle \boldsymbol{K}_-\right| G_{il}(L) \left|\boldsymbol{Q}'_-\right\rangle^*] \rangle_D|_{\boldsymbol{q}\to 0} \,,\end{aligned} \tag{5.5}$$

where $\boldsymbol{Q}'_\pm = \boldsymbol{Q}' \pm \boldsymbol{q}'/2$ are the transverse Fourier components of the incident light, and $\boldsymbol{E}(\boldsymbol{Q}'_\pm, z=0) = \sqrt{2\pi} w_0 \exp\left[-(\boldsymbol{Q}'_\pm - \boldsymbol{k}_0)^2 w_0^2/4\right] \boldsymbol{e}_0$ with $k_0 w_0 \gg 1$ is the transverse Fourier distribution of the incident (collimated) field, the same considered in the

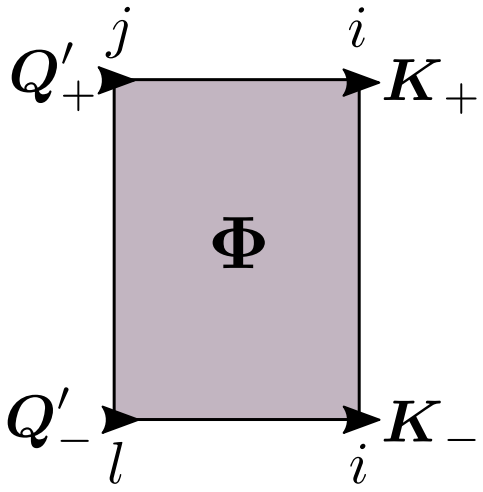

Figure 5.1: Diagrammatic representation of the correlator $\Phi_{jl}(\boldsymbol{Q},\boldsymbol{K},\boldsymbol{q},\boldsymbol{q}') = \langle[\langle \boldsymbol{K}_+|\, G_{ij}(L)\,|\boldsymbol{Q}'_+\rangle\,\langle \boldsymbol{K}_-|\, G_{il}(L)\,|\boldsymbol{Q}'_-\rangle^*]\rangle_D \propto (2\pi)^2\delta(\boldsymbol{q}-\boldsymbol{q}')$. The diagram satisfies the momentum conservation constraint (5.6).

previous chapters. Due to the conservation of transverse momentum, corresponding to the statistical translation invariance in the transverse plane (see Fig. 5.1), we have

$$\boldsymbol{Q}'_+ + \boldsymbol{K}_- = \boldsymbol{K}_+ + \boldsymbol{Q}'_- \Rightarrow \boldsymbol{q} = \boldsymbol{q}' \,. \tag{5.6}$$

Then, looking at the product

$$E_j(\boldsymbol{Q}'+\boldsymbol{q}/2, z=0)E_l^*(\boldsymbol{Q}'-\boldsymbol{q}/2, z=0) = 2\pi w_0^2 e^{-w_0^2 q^2/8} e^{-w_0^2(\boldsymbol{Q}'-\boldsymbol{k}_0)^2/2} e_{0j}e_{0l}^* \,, \tag{5.7}$$

we observe that the first exponential in Eq. (5.7) introduces terms of order q^2 or higher and, therefore, does not contribute to the $\boldsymbol{q}$-gradient in Eq. (5.5). The second exponential, instead, is peaked around $\boldsymbol{Q}' \simeq \boldsymbol{k}_0$ due to the collimated nature of the incident beam, making it possible to effectively replace it by a Dirac delta function $(2\pi)^2\delta(\boldsymbol{Q}'-\boldsymbol{k}_0)$. Such an approximation corresponds to effectively neglecting all contributions to the centroid proportional to $(k_0 w_0)^{-2}$ and higher. We are, thus, left with the following expression

$$\begin{aligned}\int d^2\boldsymbol{r}_\perp \boldsymbol{r}_\perp \langle \big|\boldsymbol{E}(\boldsymbol{r}_\perp, z)\big|^2\rangle_D = 4ik_z^2 e_{0j}e_{0l}^* \int \frac{dK_z}{2\pi}\int\frac{dq_z}{2\pi}\int\frac{d^2\boldsymbol{K}}{(2\pi)^2} e^{iq_z L} \\ \times \boldsymbol{\nabla}_{\boldsymbol{q}}\langle[\langle \boldsymbol{K}_+|\, G_{ij}(K_z^+)\,\big|\boldsymbol{k}_0^+\big\rangle\,\langle \boldsymbol{K}_-|\, G_{il}^*(K_z^-)\big|\boldsymbol{k}_0^-\big\rangle]\rangle_D|_{\boldsymbol{q}\to 0}\,,\end{aligned} \tag{5.8}$$

where $\boldsymbol{k}_0^\pm = \boldsymbol{k}_0 \pm \boldsymbol{q}/2$. Notice that we have here introduced the longitudinal Fourier variables of the retarded and advanced Green's tensor $K_z^\pm = K_z \pm q_z/2$ with respect to $z = L$. Finally, we decompose the disorder-average product of the two Green's tensors in the following standard way [16]:

$$\begin{aligned}\langle[\langle \boldsymbol{K}_+|\, G_{ij}(K_z^+)\,\big|\boldsymbol{k}_0^+\big\rangle\,\big\langle \boldsymbol{K}_-\big|G_{il}(K_z^-)\,\big|\boldsymbol{k}_0^-\big\rangle^*]\rangle_D = \langle G_{j\alpha}(\boldsymbol{k}_0^+, K_z^+)\rangle\langle G_{l\beta}^*(\boldsymbol{k}_0^-, K_z^-)\rangle \\ \times \langle G_{\gamma i}(\boldsymbol{K}_+, K_z^+)\rangle\langle G_{\delta i}^*(\boldsymbol{K}_-, K_z^-)\rangle \Gamma^{(L)}_{\alpha\beta,\gamma\delta}(K_z, q_z, \boldsymbol{q})\,,\end{aligned} \tag{5.9}$$

where $\Gamma^{(L)}_{\alpha\beta,\gamma\delta}(K_z, q_z, \boldsymbol{q})$ is the structure factor that encodes multiple scattering within the Diffuson approximation.

Proceeding analogously with the denominator of Eq. (5.2), we then find that the Diffuson centroid $\boldsymbol{R}^D_\perp(z)$ is given by the ratio of

$$\begin{aligned}\int d^2\boldsymbol{r}_\perp \boldsymbol{r}_\perp \langle \left|\boldsymbol{E}(\boldsymbol{r}_\perp, z)\right|^2\rangle_D = 4ik_z^2 e_{0j}e^*_{0l}\int\frac{dK_z}{2\pi}\int\frac{dq_z}{2\pi}\int\frac{d^2\boldsymbol{K}}{(2\pi)^2}e^{iq_zL}\\ \times \boldsymbol{\nabla}_{\boldsymbol{q}}\langle G_{j\alpha}(\boldsymbol{k}_0^+, K_z^+)\rangle\langle G^*_{l\beta}(\boldsymbol{k}_0^-, K_z^-)\rangle\langle G_{\gamma i}(\boldsymbol{K}_+, K_z^+)\rangle\\ \times \langle G^*_{\delta i}(\boldsymbol{K}_-, K_z^-)\rangle\Gamma^{(L)}_{\alpha\beta,\gamma\delta}(K_z, q_z, \boldsymbol{q})|_{\boldsymbol{q}\to 0}\end{aligned} \tag{5.10}$$

to

$$\begin{aligned}\int d^2\boldsymbol{r}_\perp \langle \left|\boldsymbol{E}(\boldsymbol{r}_\perp, z)\right|^2\rangle_D = 4k_z^2 e_{0j}e^*_{0l}\int\frac{dK_z}{2\pi}\int\frac{dq_z}{2\pi}\int\frac{d^2\boldsymbol{K}}{(2\pi)^2}e^{iq_zL}\langle G_{j\alpha}(\boldsymbol{k}_0, K_z^+)\rangle\\ \times \langle G^*_{l\beta}(\boldsymbol{k}_0, K_z^-)\rangle\langle G_{\gamma i}(\boldsymbol{K}, K_z^+)\rangle\langle G^*_{\delta i}(\boldsymbol{K}, K_z^-)\rangle\Gamma^{(L)}_{\alpha\beta,\gamma\delta}(K_z, q_z, \boldsymbol{0})\ .\end{aligned} \tag{5.11}$$

The explicit calculation of the Diffuson centroid being rather involved, to keep the formalism as simple as possible in this chapter we restrict ourselves to the simplest model of transverse disorder, i.e., we consider an uncorrelated, Gaussian disorder and take into account only the imaginary self-energy in the disorder-average Green's tensors. This is the same disorder model used in [42, 62]. Within this framework, the disorder-average Green's tensor is given by

$$\begin{aligned}\langle G_{ij}(\boldsymbol{k}_\perp, k_z)\rangle = G_1(\boldsymbol{k}_\perp, k_z)\delta_{ij} + \left[\frac{\hat{k}_z^2}{1-\hat{k}_z^2}G_2(\boldsymbol{k}_\perp, k_z) - \frac{1}{1-\hat{k}_z^2}G_1(\boldsymbol{k}_\perp, k_z)\right]\hat{k}_i\hat{k}_j\\ + \left[\frac{1}{1-\hat{k}_z^2}G_1(\boldsymbol{k}_\perp, k_z) - \frac{1}{1-\hat{k}_z^2}G_2(\boldsymbol{k}_\perp, k_z)\right](\delta_{iz}\hat{k}_j\hat{k}_z + \delta_{jz}\hat{k}_i\hat{k}_z - \delta_{iz}\delta_{jz})\,,\end{aligned} \tag{5.12}$$

where

$$G_{1(2)}(\boldsymbol{k}_\perp, k_z) = \frac{1}{k^2 - \boldsymbol{k}_\perp^2 - k_z^2 - i\,\mathrm{Im}\,\Sigma_{1(2)}(\boldsymbol{k}_\perp, k_z)}\ . \tag{5.13}$$

Let us remind that at first order in the parameter $\hat{k}_0$, small for near-paraxial light, we have

$$\begin{aligned}\mathrm{Im}\,\Sigma_1(\boldsymbol{k}_\perp, k_z) &\simeq -\frac{k}{z_s}\\ \mathrm{Im}\left[\Sigma_2(\boldsymbol{k}_\perp, k_z) - \Sigma_1(\boldsymbol{k}_\perp, k_z)\right] &= \frac{k}{z_\mathrm{S}} \simeq \frac{k}{z_s}\hat{k}_0^2\ ,\end{aligned} \tag{5.14}$$

where $z_s = 4/(\gamma k^4)$ with γ the strength of the disorder power spectrum (see Sec. 3.4.3).

5.2 Paraxial limit

Before analyzing the exact expression of $\boldsymbol{R}_\perp^D(L)$, it is useful and pedagogical to first show how the computation proceeds in the paraxial regime. Indeed, in this limit all the tensors present in Eq.s (5.10) and (5.11) can be replaced by scalar quantities. The calculation is then more straightforward and can be used as a benchmark for the full vectorial computation. To calculate the Diffuson center of mass in the paraxial regime, we simply replace the Green's tensor by the Green's function associated with the scalar Helmholtz equation (1.9). This corresponds to considering only the scalar ("paraxial") term in Eq. (5.12), namely:

$$\langle G(\boldsymbol{k}_\perp, k_z)\rangle = \frac{1}{k^2 - \boldsymbol{k}_\perp^2 - k_z^2 + ik/z_s} \,. \tag{5.15}$$

Note that, alternatively, one could also calculate the centroid in the paraxial limit by directly starting from the paraxial wave equation, as we did in chapter 2. Even though the paraxial wave equation relies on some additional assumptions compared to the scalar Helmholtz equation, in the following we show that we recover the same expected result for the center of mass.

Since the computation of the centroid involves only contributions that are linear in $\boldsymbol{q}$ [due to gradient $\boldsymbol{\nabla}_{\boldsymbol{q}}|_{\boldsymbol{q}\to 0}$ in Eq. (5.3)], all terms proportional to q^2 and of higher order can be safely neglected in the computations. Thus, for instance, for the $\boldsymbol{q}$-dependent Green's functions we can use the following expansion without loss of generality:

$$\langle G(\boldsymbol{k}_\perp \pm \boldsymbol{q}/2, k_z)\rangle \simeq \langle G(\boldsymbol{k}_\perp, k_z)\rangle \pm (\boldsymbol{k}_\perp \cdot \boldsymbol{q})\langle G(\boldsymbol{k}_\perp, k_z)\rangle^2 + \mathcal{O}(\boldsymbol{q}^2) \,. \tag{5.16}$$

That said, the first natural step to compute the Diffuson centroid is to evaluate the integral $\int \frac{d^2\boldsymbol{K}}{(2\pi)^2}\langle G(\boldsymbol{K}_+, K_z^+)\rangle\langle G^*(\boldsymbol{K}_-, K_z^-)\rangle$ in Eq.s (5.10) and (5.11). The integration over the direction of $\boldsymbol{K}$ makes all the linearly $\boldsymbol{q}$-dependent terms vanish since they are all proportional to $\boldsymbol{K}\cdot\boldsymbol{q}$. Using the contour integration method we have

$$\int \frac{d^2\boldsymbol{K}}{(2\pi)^2}\langle G(\boldsymbol{K}_+, K_z^+)\rangle\langle G^*(\boldsymbol{K}_-, K_z^-)\rangle = \frac{1}{4\big(k/z_s + iK_z q_z\big)} \,. \tag{5.17}$$

For scalar light, the structure factor $\Gamma^{(L)}$ at the Diffuson approximation is given by the series of ladder diagrams, which obeys the following scalar Bethe-Salpeter equation [16]

$$\Gamma^{(L)}(K_z, q_z, \boldsymbol{q}) = \gamma k^4 + \gamma k^4 \Gamma^{(L)}(K_z, q_z, \boldsymbol{q}) \int \frac{d^2\boldsymbol{K}}{(2\pi)^2}\langle G(\boldsymbol{K}_+, K_z^+)\rangle\langle G^*(\boldsymbol{K}_-, K_z^-)\rangle \,. \tag{5.18}$$

Solving Eq. (5.18) for $\Gamma^{(L)}$ and using Eq. (5.17), we get

$$\begin{aligned}\Gamma^{(L)}(K_z, q_z, \boldsymbol{q}) =& \frac{\gamma k^4}{1 - \gamma k^4 \int \frac{d^2\boldsymbol{K}}{(2\pi)^2}\langle G(\boldsymbol{K}_+, K_z^+)\rangle\langle G^*(\boldsymbol{K}_-, K_z^-)\rangle} \\ =& \gamma k^4 \left[1 - \frac{\gamma k^4}{4\big(k/z_s + iK_z q_z\big)}\right]^{-1} .\end{aligned} \tag{5.19}$$

The denominator of $\boldsymbol{R}_\perp^D(L)$ is then given by:

$$\int d^2\boldsymbol{r}_\perp \langle \left|\boldsymbol{E}(\boldsymbol{r}_\perp, L)\right|^2 \rangle_D = 4k_z^2 \int \frac{dK_z}{2\pi} \int \frac{dq_z}{2\pi} \gamma k^4 \frac{e^{iq_z L}}{4iK_z q_z} \langle G(\boldsymbol{k}_0, K_z^+)\rangle \langle G^*(\boldsymbol{k}_0, K_z^-)\rangle \ . \quad (5.20)$$

The integration over K_z yields

$$\int \frac{dK_z}{2\pi K_z} \langle G(\boldsymbol{k}_0, K_z^+)\rangle \langle G^*(\boldsymbol{k}_0, K_z^-)\rangle = \frac{1}{4k_z^2}\left[\frac{i}{k_z q_z + ik/z_s} - \frac{i}{k_z q_z - ik/z_s}\right] , \quad (5.21)$$

where $k_z = \sqrt{k^2 - k_0^2}$. The first term in the right-hand side has its pole lying in the lower part of the complex plane. Hence, it can be neglected in the following since it does not contribute to the integration over q_z. We are then left with

$$\int d^2\boldsymbol{r}_\perp \langle \left|\boldsymbol{E}(\boldsymbol{r}_\perp, L)\right|^2 \rangle_D = \frac{k}{z_s} \int \frac{dq_z}{2\pi} \frac{e^{iq_z L}}{iq_z} \frac{1}{ik_z q_z + k/z_s} \ . \quad (5.22)$$

Given the following results for the integration over q_z:

$$\begin{aligned} \int \frac{dq_z}{2\pi} \frac{e^{iq_z L}}{iq_z + 0^+} &= 1 \\ \int \frac{dq_z}{2\pi} \frac{e^{iq_z L}}{ik_z q_z + k/z_s} &= \frac{1}{k_z} \exp\left(-\frac{k}{k_z}\frac{L}{z_s}\right) \end{aligned} \quad (5.23)$$

and $k_z \simeq k$ (for $\hat{k}_0 \ll 1$), we obtain

$$\int d^2\boldsymbol{r}_\perp \langle \left|\boldsymbol{E}(\boldsymbol{r}_\perp, L)\right|^2 \rangle_D = 1 - e^{-L/z_s} \ . \quad (5.24)$$

Note that by considering both the coherent mode and Diffuson contributions [see Eq. (2.28)], we recover the conservation of normalization: $\int d^2\boldsymbol{r}_\perp \langle \left|\boldsymbol{E}(\boldsymbol{r}_\perp, L)\right|^2 \rangle_{tot} = \int d^2\boldsymbol{r}_\perp (\left|\langle \boldsymbol{E}(\boldsymbol{r}_\perp, L)\rangle\right|^2 + \langle \left|\boldsymbol{E}(\boldsymbol{r}_\perp, L)\right|^2 \rangle_D) = 1$.

In order to get the numerator of $\boldsymbol{R}_\perp^D(L)$, we need instead to compute

$$\begin{aligned} \int d^2\boldsymbol{r}_\perp \boldsymbol{r}_\perp \langle \left|\boldsymbol{E}(\boldsymbol{r}_\perp, L)\right|^2 \rangle_D = & 4ik_z^2 \int \frac{dK_z}{2\pi} \int \frac{dq_z}{2\pi} \frac{\gamma k^4 e^{iq_z L}}{4iK_z q_z} \\ & \times \boldsymbol{\nabla}_{\boldsymbol{q}} \langle G(\boldsymbol{k}_0^+, K_z^+)\rangle \langle G^*(\boldsymbol{k}_0^-, K_z^-)\rangle|_{\boldsymbol{q}\to 0} \ . \end{aligned} \quad (5.25)$$

Given that

$$\begin{aligned} \boldsymbol{\nabla}_{\boldsymbol{q}} \langle G(\boldsymbol{k}_0^+, K_z^+)\rangle \langle G^*(\boldsymbol{k}_0^-, K_z^-)\rangle|_{\boldsymbol{q}\to 0} = & \boldsymbol{k}_0 \big[\langle G(\boldsymbol{k}_0, K_z^+)^2\rangle \langle G^*(\boldsymbol{k}_0, K_z^-)\rangle \\ & - \langle G(\boldsymbol{k}_0, K_z^+)\rangle \langle G^*(\boldsymbol{k}_0, K_z^-)^2\rangle\big] \ , \end{aligned} \quad (5.26)$$

the integration over K_z yields

$$\begin{aligned} \int \frac{dK_z}{2\pi K_z} \boldsymbol{\nabla}_{\boldsymbol{q}} \langle G(\boldsymbol{k}_0^+, K_z^+)\rangle \langle G^*(\boldsymbol{k}_0^-, K_z^-)\rangle|_{\boldsymbol{q}\to 0} = & \frac{\boldsymbol{k}_0}{4k_z^2}\left[\frac{i}{(k_z q_z + ik/z_s)^2}\right. \\ & \left. + \frac{i}{(k_z q_z - ik/z_s)^2}\right] . \end{aligned} \quad (5.27)$$

The first term in the right-hand-side has again its pole lying in the lower part of the complex plane and can thus be dropped since it does not contribute to the integration over q_z. We then have

$$\int d^2\boldsymbol{r}_\perp \boldsymbol{r}_\perp \langle \left|\boldsymbol{E}(\boldsymbol{r}_\perp, L)\right|^2 \rangle_D = -\,\boldsymbol{k}_0 \frac{k}{z_s} \int \frac{dq_z}{2\pi} \frac{e^{iq_z L}}{iq_z} \frac{1}{(k_z q_z - ik/z_s)^2}\ . \tag{5.28}$$

Using

$$\int \frac{dq_z}{2\pi} e^{iq_z L} \frac{1}{(k_z q_z - ik/z_s)^2} = -\frac{L}{k_z^2} \exp\left(-\frac{k}{k_z}\frac{L}{z_s}\right) \tag{5.29}$$

and $k_z \simeq k$, we finally get

$$\int d^2\boldsymbol{r}_\perp \boldsymbol{r}_\perp \langle \left|\boldsymbol{E}(\boldsymbol{r}_\perp, L)\right|^2 \rangle_D = \hat{\boldsymbol{k}}_0 z_s \left(1 - \frac{L}{z_s} e^{-L/z_s} - e^{-L/z_s}\right)\ . \tag{5.30}$$

Combining Eq.s (5.24) and (5.30), we obtain the paraxial expression of $\boldsymbol{R}_\perp^D(L)$, which, as anticipated in Sec. 2.4.1, is given by

$$\boldsymbol{R}_\perp^D(L) = \hat{\boldsymbol{k}}_0 z_s \frac{1 - \frac{L}{z_s} e^{-L/z_s} - e^{-L/z_s}}{1 - e^{-L/z_s}}\ . \tag{5.31}$$

In the next sections, our goal will be to identify the vectorial corrections associated with spin-orbit interactions to Eq. (5.31) which, therefore, will constitute our reference point.

At this stage, let us say a word about the *total* paraxial centroid (5.1), which includes both the coherent mode and the multiple scattering signal. The latter reads:

$$\boldsymbol{R}_\perp^{tot}(L) = \hat{\boldsymbol{k}}_0 z_s \left(1 - e^{-L/z_s}\right) = \underbrace{\hat{\boldsymbol{k}}_0 L e^{-L/z_s}}_{\text{coherent mode}} + \underbrace{\hat{\boldsymbol{k}}_0 z_s \left(1 - \frac{L}{z_s} e^{-L/z_s} - e^{-L/z_s}\right)}_{\text{multiple scattering (Diffuson)}}\ . \tag{5.32}$$

In Fig. 5.2, we show Eq. (5.32), together with the contributions coming from the coherent mode and the Diffuson. When $L \ll z_s$, $\boldsymbol{R}_\perp^{tot}(L) \simeq \hat{\boldsymbol{k}}_0 L$ is mainly given by the coherent mode contribution, whereas at $L \gg z_s$, $\boldsymbol{R}_\perp^{tot}(L) \simeq \hat{\boldsymbol{k}}_0 z_s$ is dominated by the multiple scattering contribution. Note that, as expected, the result (5.32) is analogous to the one for a Boltzmann particle scattered in a two-dimensional disordered potential (see Sec. 2.4.2 and [10]).

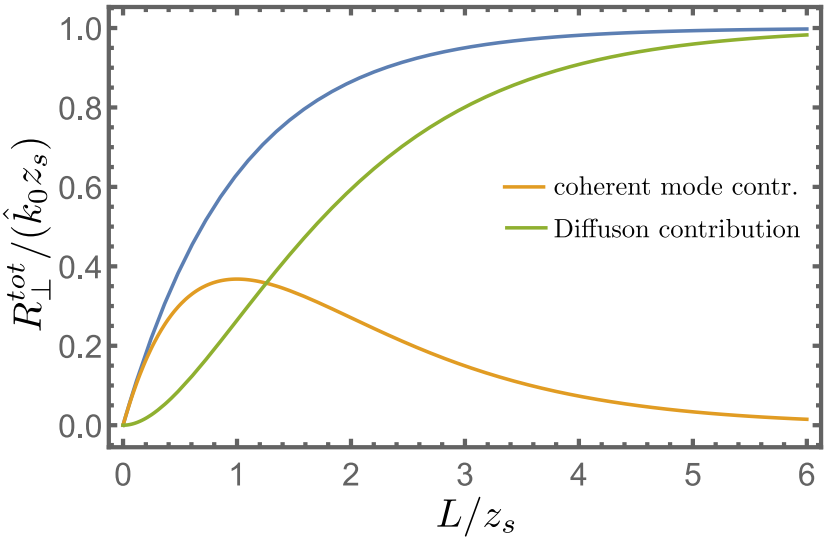

Figure 5.2: Blue curve: total beam centroid $|\boldsymbol{R}_\perp^{tot}(L)|$ vs. L/z_s in the paraxial regime, Eq. (5.32). The orange and green curves, instead, stand for the contributions to $|\boldsymbol{R}_\perp^{tot}(L)|$ coming from the coherent mode ($L/z_s e^{-L/z_s}$) and the Diffuson ($1 - L/z_s e^{-L/z_s} - e^{-L/z_s}$), respectively.

5.3 Full vectorial calculation: flux conservation

We now examine the Diffuson centroid by fully taking into account the vector nature of light. To this aim, we first consider the denominator of Eq. (5.3), i.e., the flux of the multiple scattering component, which together with the flux $\int d^2\boldsymbol{r}_\perp I_c(\boldsymbol{r}_\perp, L)$ of the coherent mode must satisfy the flux conservation. This conservation is an essential, but also fragile property that needs to be recovered in our description. Otherwise, any subsequent statement on the centroid would be inconsistent. We thus compute

$$\begin{aligned}\int d^2\boldsymbol{r}_\perp \langle\, |\boldsymbol{E}(\boldsymbol{r}_\perp,L)|^2\rangle_D = 4k_z^2 e_{0j} e_{0l}^* \int \frac{dK_z}{2\pi} \int \frac{dq_z}{2\pi} \int \frac{d^2\boldsymbol{K}}{(2\pi)^2} e^{iq_z L} \langle G_{j\alpha}(\boldsymbol{k}_0, K_z^+)\rangle \\ \times \langle G_{l\beta}^*(\boldsymbol{k}_0, K_z^-)\rangle \langle G_{\gamma i}(\boldsymbol{K}, K_z^+)\rangle \langle G_{\delta i}^*(\boldsymbol{K}, K_z^-)\rangle \Gamma^{(L)}_{\alpha\beta,\gamma\delta}(K_z, q_z, \boldsymbol{0})\ ,\end{aligned} \tag{5.33}$$

where we now have to take into account the full vectorial expression (5.12) for the disorder-average Green's tensor. As done in Sec. 5.2, the first natural step is to perform the integration over $\boldsymbol{K}$. This time the integral is a tensor, which we denote by

$$\int \frac{d^2\boldsymbol{K}}{(2\pi)^2} \langle G_{\gamma i}(\boldsymbol{K}_+, K_z^+)\rangle \langle G_{\delta i}^*(\boldsymbol{K}_-, K_z^-)\rangle \equiv Q_{\gamma\delta}(K_z, q_z, \boldsymbol{q})\ . \tag{5.34}$$

After multiplying the two disorder-average Green's tensor, the integrand will be composed of several terms, whose relevant contributions are at most linear in $\boldsymbol{q}$. This

calculation involves the following integrals over the modulus of $\boldsymbol{K}$:

$$\begin{aligned}
F_{11} \equiv& \int \frac{KdK}{2\pi}\langle G_1^+\rangle\langle G_1^{-*}\rangle = -\frac{1}{4(\mathrm{Im}\,\Sigma_1 - iq_zK_z)} - \frac{i\sqrt{k^2-K_z^2}(\boldsymbol{K}_u\cdot\boldsymbol{q})}{4(\mathrm{Im}\,\Sigma_1 - iq_zK_z)^2} \\
\equiv& F_{11}^{(0)} + F_{11}^{(1)}(\boldsymbol{K}_u\cdot\boldsymbol{q}) \\
F_{22} \equiv& \int \frac{KdK}{2\pi}\langle G_2^+\rangle\langle G_2^{-*}\rangle = -\frac{1}{4(\mathrm{Im}\,\Sigma_2 - iq_zK_z)} - \frac{i\sqrt{k^2-K_z^2}(\boldsymbol{K}_u\cdot\boldsymbol{q})}{4(\mathrm{Im}\,\Sigma_2 - iq_zK_z)^2} \\
\equiv& F_{22}^{(0)} + F_{22}^{(1)}(\boldsymbol{K}_u\cdot\boldsymbol{q}) \\
F_{12} \equiv& \int \frac{KdK}{2\pi}\langle G_1^+\rangle\langle G_2^{-*}\rangle \equiv \int \frac{KdK}{2\pi}\langle G_2^+\rangle\langle G_1^{-*}\rangle \equiv F_{12}^{(0)} + F_{12}^{(1)}(\boldsymbol{K}_u\cdot\boldsymbol{q}) \\
=& -\frac{1}{2(\mathrm{Im}\,\Sigma_1 + \mathrm{Im}\,\Sigma_2 - 2iq_zK_z)} - \frac{i\sqrt{k^2-K_z^2}(\boldsymbol{K}_u\cdot\boldsymbol{q})}{(\mathrm{Im}\,\Sigma_1 + \mathrm{Im}\,\Sigma_2 - 2iq_zK_z)^2}\,,
\end{aligned} \tag{5.35}$$

where $\boldsymbol{K}_u$ is the unit vector associated with $\boldsymbol{K}$, $\boldsymbol{K}_u \equiv \boldsymbol{K}/K$, as well as the following integrals over the direction of $\boldsymbol{K}$

$$\begin{aligned}
\langle \hat{k}_\alpha \hat{k}_\beta\rangle_{\boldsymbol{K}_u} =& \delta_{\alpha\beta}\frac{1-\hat{K}_z^2}{2} + \delta_{\alpha z}\delta_{\beta z}\frac{3\hat{K}_z^2-1}{2} \\
\langle \hat{k}_\alpha^{\pm}\rangle_{\boldsymbol{K}_u} =& \delta_{\alpha z}\hat{K}_z \pm \frac{\hat{q}_\alpha}{4}(1+\hat{K}_z^2) \\
\langle \hat{k}_\alpha^{+}\hat{k}_\beta^{-}\rangle_{\boldsymbol{K}_u} =& \langle \hat{k}_\alpha\hat{k}_\beta\rangle_{\boldsymbol{K}_u} + \frac{\hat{K}_z}{2}(\delta_{\beta z}\hat{q}_\alpha - \delta_{\alpha z}\hat{q}_\beta) \\
\langle \hat{k}_\alpha^{\pm}\hat{k}_\beta^{\pm}\rangle_{\boldsymbol{K}_u} =& \langle \hat{k}_\alpha\hat{k}_\beta\rangle_{\boldsymbol{K}_u} \pm \frac{\hat{K}_z^3}{2}(\delta_{\beta z}\hat{q}_\alpha + \delta_{\alpha z}\hat{q}_\beta)\,,
\end{aligned} \tag{5.36}$$

where $\boldsymbol{k}$ in the left-hand sides stands here for $(\boldsymbol{K}, K_z)$. By handling with patience every term one by one, one obtains the following expression for the $Q_{\gamma\delta}$ tensor

$$\begin{aligned}
Q_{\gamma\delta} =& \delta_{\gamma\delta}\frac{F_{11}^{(0)} + \hat{K}_z^2 F_{22}^{(0)}}{2} + \delta_{\gamma z}\delta_{\delta z}\frac{(2-3\hat{K}_z^2)F_{22}^{(0)} - F_{11}^{(0)}}{2} \\
&+ (\delta_{\delta z}\hat{q}_\gamma - \delta_{\gamma z}\hat{q}_\delta)\frac{\hat{K}_z F_{12}^{(0)}}{2} + (\delta_{\delta z}\hat{q}_\gamma + \delta_{\gamma z}\hat{q}_\delta)\frac{\hat{K}_z}{2}(\hat{K}_z^2-1)F_{22}^{(1)}\,.
\end{aligned} \tag{5.37}$$

The second step consists in computing the structure factor (series of ladder diagrams) $\boldsymbol{\Gamma}^{(L)}$. In the vectorial case, $\boldsymbol{\Gamma}^{(L)}$ is a fourth-rank tensor with respect to the polarization indices, obeying the following Bethe-Salpeter equation

$$\begin{aligned}
\Gamma^{(L)}_{\alpha\beta,\gamma\delta}(K_z, q_z, \boldsymbol{q}) =& \gamma k^4 \delta_{\alpha\gamma}\delta_{\beta\delta} + \gamma k^4 \Gamma^{(L)}_{mn,\gamma\delta}(K_z, q_z, \boldsymbol{q}) \\
&\times \underbrace{\int \frac{d^2\boldsymbol{K}}{(2\pi)^2}\langle G_{\alpha m}(\boldsymbol{K}_+, K_z^+)\rangle\langle G^*_{\beta n}(\boldsymbol{K}_-, K_z^-)\rangle}_{\equiv Q_{\alpha\beta,mn}}\,.
\end{aligned} \tag{5.38}$$

A significant simplification of this equation can be used by observing that $\boldsymbol{\Gamma}^{(L)}$ cannot depend linearly on $\boldsymbol{q}$ because of statistical isotropy in the transverse plane. For our purpose, we then need just to compute its $\boldsymbol{q} = 0$ contribution, $\Gamma^{(L)}_{\alpha\beta,\gamma\delta}(K_z, q_z, \boldsymbol{0})$.

The latter has been previously studied in [42], but on the basis of the diffusion approximation corresponding to low values of q_z. Since the physics we want to address, however, typically involves small scales, this approximation is not adequate and also possibly large q_z values should be properly computed. To this aim, we rewrite the tensor Bethe-Salpeter equation as

$$\boldsymbol{\Gamma}^{(L)} = \gamma k^4 \boldsymbol{I} + \gamma k^4 \boldsymbol{Q} \cdot \boldsymbol{\Gamma}^{(L)} = \gamma k^4 \sum_{m=0}^{\infty} \left(\gamma k^4 \boldsymbol{Q}\right)^m \ , \tag{5.39}$$

where $\boldsymbol{I} \equiv \delta_{\alpha\gamma}\delta_{\beta\delta}$. To compute explicitly the infinite sum, one strategy is to decompose the 9×9 matrix $\boldsymbol{Q}$ on the complete basis of orthogonal, irreducible tensors $\boldsymbol{\Pi}^{(n)}$, satisfying $\boldsymbol{\Pi}^{(n)} \cdot \boldsymbol{\Pi}^{(n')} = \delta_{nn'}$ and $\sum_n \boldsymbol{\Pi}^{(n)} = \boldsymbol{I}$ [196]. Indeed, denoting by λ_n the corresponding eigenvalues of this decomposition, we have

$$\gamma k^4 \boldsymbol{Q} = \sum_n \gamma k^4 \lambda_n \boldsymbol{\Pi}^{(n)} \ , \tag{5.40}$$

so that

$$\boldsymbol{\Gamma}^{(L)} = \sum_n \frac{\gamma k^4}{1 - \gamma k^4 \lambda_n} \boldsymbol{\Pi}^{(n)} \ . \tag{5.41}$$

The aforementioned decomposition of $Q_{\alpha\beta,\gamma\delta}(K_z, q_z, \mathbf{0})$ is very involved, but it can be done with the help of Wolfram Mathematica© software. From this we find that the polarization space of the matrix $Q_{\alpha\beta,\gamma\delta}$ is decomposable into six eigensubspaces, three of them being associated with a twice degenerate eigenvalue. The exact expressions of $(\lambda_n, \boldsymbol{\Pi}^{(n)})$ are rather cumbersome and are reported in Appendix F.

The next step of the calculation is to contract $\Gamma_{\alpha\beta,\gamma\delta}$ with $Q_{\gamma\delta}$. From Appendix F and Mathematica, we find that

$$\begin{aligned}
\Pi^{(n)}_{\alpha\beta,\gamma\delta}\delta_{\gamma\delta} &= 0 \text{ for } n = 1,2,3,4 \\
\Pi^{(n)}_{\alpha\beta,\gamma\delta}\delta_{\gamma\delta}(\delta_{\delta z}\hat{q}_\gamma + \delta_{\gamma z}\hat{q}_\delta) &= 0 \text{ for } n \neq 3 \\
\Pi^{(n)}_{\alpha\beta,\gamma\delta}\delta_{\gamma\delta}(\delta_{\delta z}\hat{q}_\gamma - \delta_{\gamma z}\hat{q}_\delta) &= 0 \text{ for } n \neq 4 \\
\Pi^{(n)}_{\alpha\beta,\gamma\delta}\delta_{\gamma z}\delta_{\delta z} &= 0 \text{ for } n = 1,2,3,4 \ .
\end{aligned} \tag{5.42}$$

The aforementioned contraction thus yields

$$\begin{aligned}
\Gamma^{(L)}_{\alpha\beta,\gamma\delta} \cdot Q_{\gamma\delta} = \gamma k^4 \Bigg[& \frac{\delta_{\alpha\beta}(1+\hat{K}_z^2)}{8iK_z q_z} + \frac{\delta_{\alpha z}\delta_{\beta z}(1-3\hat{K}_z^2)}{8iK_z q_z} + (\delta_{\beta z}\hat{q}_\alpha + \delta_{\alpha z}\hat{q}_\beta) \\
& \times \frac{\hat{K}_z(\hat{K}_z^2 - 1)F^{(1)}_{22}}{2(1-\gamma k^4\lambda_3)} + \frac{\hat{K}_z F^{(0)}_{12}}{2(1-\gamma k^4\lambda_4)}(\delta_{\beta z}\hat{q}_\alpha - \delta_{\alpha z}\hat{q}_\beta)\Bigg] \ .
\end{aligned} \tag{5.43}$$

Recalling that we are interested in computing the SOI correction to the Diffuson centroid in the limit of small angles of incidence which, as shown in the previous chapters, basically involves only the transverse components of the electric field, it is sufficient to restrict ourselves to the first term in the right-hand-side of Eq. (5.43):

$$\Gamma^{(L)}_{\alpha\beta,\gamma\delta} \cdot Q_{\gamma\delta} \simeq \gamma k^4 \frac{\delta_{\alpha\beta}(1+\hat{K}_z^2)}{8iK_z q_z} \ , \tag{5.44}$$

where all components directed along the z axis have been neglected. We then arrive at the following expression:

$$\begin{aligned}\int d^2\boldsymbol{r}_\perp \langle \left|\boldsymbol{E}(\boldsymbol{r}_\perp, L)\right|^2 \rangle_D = 4k_z^2 e_{0j} e_{0l}^* \int \frac{dK_z}{2\pi} \int \frac{dq_z}{2\pi} e^{iq_z L} \gamma k^4 \\ \times \frac{1+\hat{K}_z^2}{8iK_z q_z} \langle G_{j\alpha}(\boldsymbol{k}_0, K_z^+)\rangle \langle G_{l\alpha}^*(\boldsymbol{k}_0, K_z^-)\rangle \ .\end{aligned} \tag{5.45}$$

Since we do not have to perform any integration of Green's tensors over transverse wave vectors anymore, it is of practical convenience for the rest of the chapter to work with $\langle G_{ij}\rangle$ rewritten in the following way

$$\langle G_{ij}(\boldsymbol{K}, k_z)\rangle = G_1 \delta_{ij} - G_2 \hat{k}_i \hat{k}_j + \frac{G_1 - G_2}{1-\hat{k}_z^2}\left[\delta_{iz}\delta_{jz}(\hat{k}_z^2 - 1) - \hat{K}_i \hat{K}_j\right] . \tag{5.46}$$

Introducing the integrals

$$\begin{aligned} H_{11}^{(0)} &\equiv \int \frac{dK_z}{2\pi} \langle G_1\rangle \langle G_1^*\rangle = -\frac{i}{4k_z} \frac{1}{k_z q_z + i\,\mathrm{Im}\,\Sigma_1} \\ H_{12}^{(0)} &\equiv \int \frac{dK_z}{2\pi} \langle G_1\rangle \langle G_2^*\rangle = -\frac{i}{2k_z} \frac{1}{2k_z q_z + i\,\mathrm{Im}\,\Sigma_1 + i\,\mathrm{Im}\,\Sigma_2} \\ H_{22}^{(0)} &\equiv \int \frac{dK_z}{2\pi} \langle G_2\rangle \langle G_2^*\rangle = -\frac{i}{4k_z} \frac{1}{k_z q_z + i\,\mathrm{Im}\,\Sigma_2} \ , \end{aligned} \tag{5.47}$$

in the near paraxial limit $\hat{k}_z \to 1$, one obtains

$$\int d^2\boldsymbol{r}_\perp \langle \left|\boldsymbol{E}(\boldsymbol{r}_\perp, L)\right|^2 \rangle_D = 4k_z^2 \gamma k^4 \int \frac{dq_z}{2\pi} e^{iq_z L} \frac{1}{4ik_z q_z} \left[H_{11}^{(0)} + \left(H_{22}^{(0)} - H_{11}^{(0)}\right) |\hat{\boldsymbol{x}} \cdot \boldsymbol{e}_0|^2\right] , \tag{5.48}$$

where we have used $\boldsymbol{k}_0/k_0 = \hat{\boldsymbol{x}}$, i.e., we have chosen the transverse incident wave vector $\boldsymbol{k}_0$ aligned along the x axis, as in the previous chapters. Using the results (5.23) for integrals over q_z, we finally get

$$\int d^2\boldsymbol{r}_\perp \langle \left|\boldsymbol{E}(\boldsymbol{r}_\perp, L)\right|^2 \rangle_D = 1 - e^{-L/z_s}\left[1 - |\hat{\boldsymbol{x}} \cdot \boldsymbol{e}_0|^2 \left(1 - e^{L/z_\mathrm{S}}\right)\right] , \tag{5.49}$$

where $z_s = -k/\,\mathrm{Im}\,\Sigma_1$ and $z_\mathrm{S} = k/\,\mathrm{Im}(\Sigma_2 - \Sigma_1)$. Recalling the result obtained for the coherent mode:

$$\int d^2\boldsymbol{r}_\perp \left|\langle \boldsymbol{E}(\boldsymbol{r}_\perp, L)\rangle\right|^2 = e^{-L/z_s}\left[1 - |\hat{\boldsymbol{x}} \cdot \boldsymbol{e}_0|^2 \left(1 - e^{L/z_\mathrm{S}}\right)\right] , \tag{5.50}$$

we infer that

$$\int d^2\boldsymbol{r}_\perp \langle \left|\boldsymbol{E}(\boldsymbol{r}_\perp, L)\right|^2 \rangle_{tot} = 1 , \tag{5.51}$$

which is nothing but the flux conservation, here recovered while taking into account the leading-order vectorial corrections to both the coherent mode and the multiple scattering signals.

5.4 SOI lateral shift of the multiple scattering component

In previous chapters, we have seen that as soon as one describes light propagation beyond the paraxial approximation, a transverse shift associated with spin-orbit interactions shows up in the coherent mode. In order to see if an analogous effect arises also in the Diffuson, we now compute

$$\int d^2\boldsymbol{r}_\perp \boldsymbol{r}_\perp \langle \left|\boldsymbol{E}(\boldsymbol{r}_\perp, L)\right|^2\rangle_D = 4ik_z^2 e_{0j}e_{0l}^* \int \frac{dK_z}{2\pi}\int \frac{dq_z}{2\pi} e^{iq_z L}\gamma k^4 \frac{1+\hat{K}_z^2}{8iK_z q_z} \times \boldsymbol{\nabla}_{\boldsymbol{q}} \langle G_{j\alpha}(\boldsymbol{k}_0^+, K_z^+)\rangle \langle G_{l\alpha}^*(\boldsymbol{k}_0^-, K_z^-)\rangle|_{\boldsymbol{q}\to 0}\ . \tag{5.52}$$

The integration over K_z of the product of retarded and advanced incoming Green's tensors involves the following contributions:

$$\begin{aligned} H_{11} &\equiv \int \frac{dK_z}{2\pi}\langle G_1^+\rangle\langle G_1^{*-}\rangle = H_{11}^{(0)} + (\boldsymbol{k}_0\cdot\boldsymbol{q})H_{11}^{(1)} \\ H_{22} &\equiv \int \frac{dK_z}{2\pi}\langle G_2^+\rangle\langle G_2^{*-}\rangle = H_{22}^{(0)} + (\boldsymbol{k}_0\cdot\boldsymbol{q})H_{22}^{(1)} \\ H_{12} &\equiv \int \frac{dK_z}{2\pi}\langle G_1^+\rangle\langle G_2^{*-}\rangle = H_{12}^{(0)} + (\boldsymbol{k}_0\cdot\boldsymbol{q})H_{12}^{(1)} \end{aligned} \tag{5.53}$$

with

$$\begin{aligned} H_{11}^{(1)} &\equiv \frac{i}{4k_z}\frac{1}{(k_z q_z + i\,\mathrm{Im}\,\Sigma_1)^2} \\ H_{22}^{(1)} &\equiv \frac{i}{4k_z}\frac{1}{(k_z q_z + i\,\mathrm{Im}\,\Sigma_2)^2} \\ H_{12}^{(1)} &\equiv \frac{i}{k_z}\frac{1}{(2k_z q_z + i\,\mathrm{Im}\,\Sigma_1 + i\,\mathrm{Im}\,\Sigma_2)^2}\ . \end{aligned} \tag{5.54}$$

Note that terms which involve a q_z pole in the lower half complex plane and/or are quadratic in $\boldsymbol{q}$ are not reported here since they give no contribution to the centroid. Performing the integration over K_z then yields the following expression for the Diffuson centroid

$$\int d^2\boldsymbol{r}_\perp \boldsymbol{r}_\perp \langle \left|\boldsymbol{E}(\boldsymbol{r}_\perp, L)\right|^2\rangle_D = 4ik_z^2\gamma k^4 \int \frac{dq_z}{2\pi}\frac{e^{iq_z L}}{4ik_z q_z}\Big\{ \boldsymbol{k}_0\big[H_{11}^{(1)} + |\hat{\boldsymbol{x}}\cdot\boldsymbol{e}_0|^2\left(H_{22}^{(1)} - H_{11}^{(1)}\right)\big] + \frac{i}{k_0}\,\mathrm{Im}[\boldsymbol{e}_0(\hat{\boldsymbol{x}}\cdot\boldsymbol{e}_0^*)]\big(H_{11}^{(0)} - 2H_{12}^{(0)} + H_{22}^{(0)}\big)\Big\}\ . \tag{5.55}$$

Keeping in mind the integrals in Eq.s (5.23), together with the following integral over q_z:

$$\int \frac{dq_z}{2\pi}\frac{e^{iq_z L}}{(k_z q_z + i\,\mathrm{Im}\,\Sigma)^2} = -\frac{L}{k_z}\exp\left(L\,\mathrm{Im}\,\Sigma/k_z\right)\ , \tag{5.56}$$

we obtain:

$$\int d^2\boldsymbol{r}_\perp \boldsymbol{r}_\perp \langle\, |\boldsymbol{E}(\boldsymbol{r}_\perp, L)|^2 \rangle_D = \hat{\boldsymbol{k}}_0 z_s \Bigg\{ 1 - \frac{L}{z_s} e^{-L/z_s} - e^{-L/z_s} - |\hat{\boldsymbol{x}} \cdot \boldsymbol{e}_0|^2 \Bigg[-2\hat{k}_0^2 - \frac{L}{z_s} e^{-L/z_s} \big(1 - (1+\hat{k}_0^2) e^{L/z_\mathrm{S}}\big) - e^{-L/z_s} \big(1 - (1+2\hat{k}_0^2) e^{L/z_\mathrm{S}}\big) \Bigg] \Bigg\} + \frac{\mathrm{Im}[\boldsymbol{e}_0 (\hat{\boldsymbol{x}} \cdot \boldsymbol{e}_0^*)]}{k_0} e^{-L/z_s} (1 - e^{L/2z_\mathrm{S}})^2 \,. \tag{5.57}$$

The vectorial description of the Diffuson centroid brings a first correction proportional to $|\hat{\boldsymbol{x}} \cdot \boldsymbol{e}_0|^2$ along $\hat{\boldsymbol{k}}_0$ direction. Such correction being in the same direction as the paraxial contribution but of much smaller amplitude (proportional to $\hat{k}_0^2$), we drop it from now on. The other correction, corresponding to the last term in the right-hand side of Eq. (5.57), is instead responsible for the emergence of a SOI-related lateral shift R_y^D transverse to both the incident transverse wave vector and the longitudinal axis, as we will see in the following. When compared with the lateral term affecting the coherent mode centroid, one realizes that such term is actually equal in magnitude but of opposite sign. Therefore, *no* lateral shift is predicted to show up when looking at the centroid of the *total* signal:

$$\boldsymbol{R}_\perp^{tot}(L) = \hat{\boldsymbol{k}}_0 z_s \big(1 - e^{-L/z_s}\big) \Rightarrow R_y^{tot}(L) = 0 \,. \tag{5.58}$$

Hence, it seems that spin-orbit interactions of light effectively do not play any role when recording both the diffusive light and the ballistic components, at least at the level of the beam centroid and within the uncorrelated disorder model. It would be interesting to check if this property holds true even when considering correlated disorder where the scattering mean free path and the transport mean free path can differ significantly.

However, spin-orbit interactions are responsible for the appearance of a lateral displacement along y of opposite sign for the two components when considered separately. Considering the usual incident polarization $\boldsymbol{e}_0 = (\hat{\boldsymbol{x}}' + e^{i\phi}\hat{\boldsymbol{y}})/\sqrt{2}$, we find the following expression for the lateral shift Diffuson centroid taken alone:

$$R_y^D(L) = \frac{\sigma}{k_0} \frac{e^{-L/z_s}(1 - e^{L/2z_\mathrm{S}})^2}{2 - e^{-L/z_s}\big(1 + e^{L/z_\mathrm{S}}\big)} \,, \tag{5.59}$$

where $\sigma = \sin\phi$ is the helicity of the incident beam. Looking carefully at the calculations leading to Eq. (5.59), one notes that the Diffuson spin Hall effect actually originates from the SOI corrections impacting the propagation of light from the source point to the first scattering event, but not the multiple scattering process itself (i.e., no spin-orbit corrections occur in the structure factor $\Gamma^{(L)}$). For comparison, we recall the corresponding result for the coherent mode [62]:

$$R_y(L) = -\frac{\sigma}{k_0} \left[1 - \frac{1}{\cosh\left(L/2z_\mathrm{S}\right)} \right] . \tag{5.60}$$

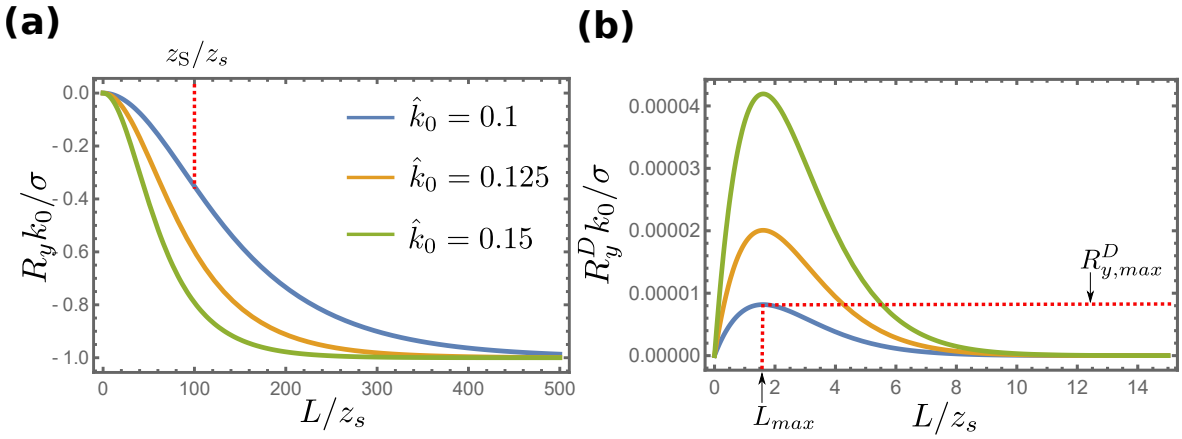

Figure 5.3: Centroid of the coherent mode R_y (panel a) and of the multiple scattering signal R_y^D (panel b) vs. L/z_s for three values of $\hat{k}_0 \ll 1$. The centroids are expressed in units of σ/k_0, with σ the helicity of the incident beam.

Both lateral shifts (5.59) and (5.60) are proportional to the incident beam helicity and, as already pointed out, have different signs. We also observe that, while for the coherent mode only the z_S parameter governs the evolution of the shift with L, in the case of R_y^d both z_s and z_S come into play. The evolutions of R_y and R_y^D with L are depicted in Fig. 5.3. In the case of the coherent mode centroid, after a longitudinal propagation length of a few z_S, a plateau value of the shift of magnitude σ/k_0 is reached. On the other hand, a lateral shift of the Diffuson centroid reaches a maximum $R^D_{y,max}$ at a certain $L \equiv L_{max}$, and then goes to zero at large L. Because in the present chapter we have considered a simple model of (non-resonant) Gaussian uncorrelated disorder, we have $z_S = z_s/\hat{k}_0^2 \gg 1$. In this model, we observe a clear separation between the longitudinal scales at which the two lateral shifts R_y and R_y^D become significant. Indeed, while the spin Hall effect of the coherent mode emerges at the scale $L \sim z_S$, the Diffuson SHE takes place at $L \sim L_{max}$, which is of the order of z_s, see Fig. 5.4a. The maximum value of the Diffuson lateral shift, on the other hand, is shown in Fig. 5.4b. It can be approximated as

$$R^D_{y,max} \simeq 0.1 \frac{\sigma}{k_0} \left(\frac{z_s}{z_S} \right)^2 \simeq 0.1 \frac{\sigma}{k} \hat{k}_0^3. \tag{5.61}$$

Hence, the lateral shift of the Diffuson centroid is very small compared to that of the coherent mode $[R_y(L \gg z_S) \simeq -\sigma/k_0]$, due to the additional factor $0.1\hat{k}_0^4 \ll 1$. This small amplitude of the multiple scattering shift is a priori extremely difficult to detect experimentally. However, by naively substituting in Eq. (5.59) the values of z_s and z_S computed in the previous chapter in the case of a random photonic array with the incident laser frequency tuned at the TM resonance ω_1, for which we have $z_s/z_S \simeq -4$ (see Fig. 4.5), one obtains a significant amplification of the effect: $R^D_{y,max}(L_{max} \simeq 0.65 z_s) \simeq 0.19\sigma/k_0$.

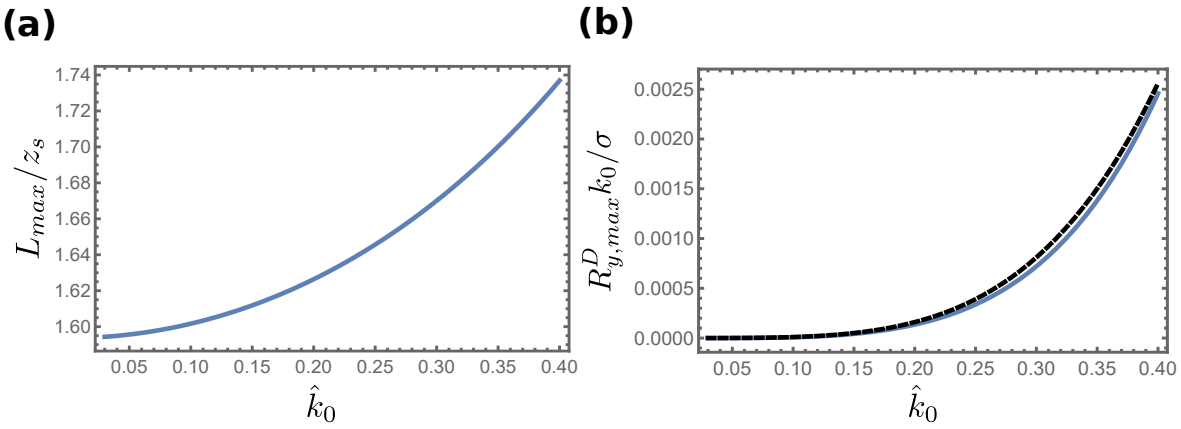

Figure 5.4: (a) Medium thickness L_{max} where the Diffuson lateral shift R_y^D is maximum and (b) corresponding maximum value $R^D_{y,max}$ as a function of $\hat{k}_0 = \sin\theta \ll 1$, with θ the angle of incidence. The dashed black curve is the approximation (5.61).

5.5 Conclusion

In this chapter, we have provided first theoretical insights of the existence of a spin Hall effect in the multiple scattering component of light propagating in transverse disorder. The results here presented are to be considered as preliminary as they have been only derived in the framework of the simple model of continuous uncorrelated disorder. An extension to the case of a photonic array, however, is rather straightforward. Furthermore, a clear physical interpretation of the change of sign with respect to the spin Hall effect of the coherent mode, as well as a computation of the evolution of the different Diffuson angular momentum contributions, still need to be formulated. Possible amplification of the phenomenon via the weak-measurement scheme, finally, could also be the focus of future works.

General conclusion and outlook

In this thesis, we have explored the effects of spin-orbit interactions on light propagation in transversally disordered dielectric media. On general grounds, we have shown by employing a full vectorial description that, as soon as the incident beam wave vector is tilted with respect to the optical axis along which the medium is homogeneous, an anisotropic component encoding spin-orbit interactions of light appears in the disorder-average electric field, with SOI of light effectively imprinting birefringence and dichroism to the random medium. This component is responsible for the emergence of a spin Hall effect of light in the coherent mode, i.e., a lateral shift of the ballistic component of the beam, both transverse to the optical axis and to the projection of the incident wave vector in the disordered transverse plane. In particular, we have demonstrated the existence of an oscillating spin Hall effect affecting the coherent mode in the case of continuous transverse disorder, controllable via incident polarization, the angle of incidence and the disorder correlation length. The spin Hall effect is also accompanied by a complementary evolution of the polarization of the coherent mode, mediated by the conservation of the longitudinal component of the total angular momentum. In this model of disorder, we have shown that this lateral shift -which typically occurs at the scale of the transverse wavelength- can be amplified up to the much larger scale of the beam width, by employing a weak-measurement scheme based on polarimetry. Nevertheless, in non-resonant disorder, the spin Hall effect remains difficult to measure as it typically occurs at a longitudinal scale much larger than the mean free path ($z_{\mathrm{L(S)}} \sim z_s/\hat{k}_0 \gg z_s$), where the coherent mode is exponentially attenuated. To overcome this issue, we have further considered a discrete model of resonant transverse disorder, a transversally disordered photonic array made of parallel tubes. By describing the disorder-average propagation of light in such a structure using a model based on Mie scattering, we have showcased the possibility of tailoring the spin Hall effect of the coherent mode via a tuning of the frequency of the incident laser. In particular, by operating in the vicinity of the second Mie resonance of the system, we have identified a novel regime where the spin Hall effect arises at a scale $z_{\mathrm{L(S)}} \lesssim z_s$, making the effect *a priori* observable experimentally. We have also investigated the time dependence of the spin Hall effect following the abrupt extinction of the laser. In that case, the appearance of a flash of light in the coherent mode makes the spin Hall effect observable at large optical thicknesses. Finally, we have explored for the first time the role of SOI in transverse multiple scattering, and have found evidence for a SHE for the diffusive photons.

There are several possible lines of research for future works on the role of spin-orbit interactions in disordered media. A first one would consist in more systematically exploring the spin Hall effect with numerical simulations in transverse disorder, for instance using an electromagnetic transfer-matrix approach. This would allow, in particular, to characterize the SHE at the level of single disorder realizations. Second, providing a geometric-phase description of spin-orbit interactions in random media would be of high interest, not only from a fundamental point of view, but also as a practical tool. Indeed, this might lead to a significant simplification of the problem, making accessible the computation of more complex observables while avoiding the full vectorial resolution of the problem, as done in the present thesis. A theoretical implementation of the Berry phase in the context of disordered systems is, however, not straightforward since it must rely on a wave description, rather than on a (semi-classical) ray approach as we presented in the beginning of the manuscript. Precisely, this would require introducing the Berry phase at the level of the Green's function, in the spirit of the Aharonov-Bohm effect for electrons in vector-potential fields. Another possible direction is to try to export this SOI physics beyond the geometry of transverse disorder. Although spin-orbit interactions average out when considering a standard isotropic 3D disorder, the origin of the spin Hall effect in transversally disordered media pointed out in this thesis, i.e., the anisotropy between the $\hat{\boldsymbol{y}}$ and $\hat{\boldsymbol{x}}'$ axes, may suggest the possible presence of similar effects in 3D disorder composed of scatterers with certain anisotropic properties. As far as the multiple scattering signal is concerned, the spin Hall effect of the Diffuson certainly requires further investigation. As already stated, only first insights into this physics have been presented in this thesis. Extending it to correlated disorder and to the case of transversally disordered photonic arrays or investigating a possible amplification via weak measurements, together with a better understanding of the phenomenon and of the conservation laws at play, constitute important questions to be addressed. Other open questions, finally, are the effect of spin-orbit interactions of light on the centroid corrections associated with coherent backscattering, and in the Anderson localization regime.

Appendix A

Stokes parameters

In weakly inhomogeneous optical media satisfying $\lambda|\boldsymbol{\nabla}\epsilon|/\epsilon \ll 1$, light can be effectively described as transverse waves. Given a monochromatic plane wave characterized by a frequency ω and a wave vector $\boldsymbol{k}$, both the electric and magnetic fields then appear to always be orthogonal to $\boldsymbol{k}$, transverse to the direction of propagation. Once an orthonormal basis $(\hat{\boldsymbol{e}}_{\mathbf{1}}, \hat{\boldsymbol{e}}_2)$ for the plane transverse to $\boldsymbol{k}$ is chosen, the polarization of light can be determined by looking at the complex component of the electric field projected onto the basis $(\hat{\boldsymbol{e}}_{\mathbf{1}}, \hat{\boldsymbol{e}}_2)$. Jones vector is a two-component vector composed of such complex numbers. Jones vectors (and Jones calculus) are only applicable to light that is already fully polarized, such as the case of a monochromatic plane wave here taken as an example.

In order to describe the polarization state of more complex beams, such as randomly or partially polarized light, one needs to employ the Stokes parameters. The Stokes parameters are a set of four values often combined into a vector, known as the Stokes vectors, $(I, Q, U, V)^T$, which require the use of the so-called Mueller calculus to be manipulated.

Once the $(\hat{\boldsymbol{e}}_{\mathbf{1}}, \hat{\boldsymbol{e}}_2)$ basis is fixed, the Stokes parameters are defined as follows [197]:

$$\begin{aligned} I =& |E_1|^2 + |E_2|^2 \\ Q =& |E_1|^2 - |E_2|^2 \\ U =& 2\,\mathrm{Re}[E_1^* E_2] \\ V =& 2\,\mathrm{Im}[E_1^* E_2] \end{aligned} \tag{A.1}$$

with $E_{1(2)} = \hat{\boldsymbol{e}}_{1(2)} \cdot \boldsymbol{E}$. I is the total intensity of the beam, Q and U give the amount of light linearly polarized along the ($\hat{\boldsymbol{e}}_{\mathbf{1}}$ or $\hat{\boldsymbol{e}}_2$) axes and linealy polarized at $\pm 45°$ in the $(\hat{\boldsymbol{e}}_{\mathbf{1}}, \hat{\boldsymbol{e}}_2)$ plane, respectively, while V describes the amount of light in the beam which is circularly polarized.

An efficient graphical tool useful for visualizing the polarization state of a light beam and its evolution is provided by the Poincaré sphere, a unity-radius sphere lying in a three-dimensional space whose Cartesian axis are given by the Stokes parameters Q, U and V (as done in Fig. 3.5). All possible normalized polarization states are mapped into points on the surface of the Poincaré sphere. The depiction of the evolution of such polarization states translates into a curve lying on the Poincaré sphere surface.

Appendix B

Angular momentum of light

Within the classical physics framework, the angular momentum of a physical entity is given by the pseudovector resulting from the cross product between its position and its linear momentum. This holds true for classical particles as well as for light. Thus, the electromagnetic angular momentum contained in a volume V reads

$$\boldsymbol{J} = \frac{\epsilon_0}{2} \int_V d^3\boldsymbol{r} \big\{ \boldsymbol{r} \times \big[\boldsymbol{E}(\boldsymbol{r}) \times \boldsymbol{B}^*(\boldsymbol{r}) \big] \big\} \, . \tag{B.1}$$

In the thesis we are studying light propagation along an optical axis $\hat{\boldsymbol{z}}$. Rather than the total angular momentum contained inside a certain space region, we are then interested in the total angular momentum along the longitudinal axis z, which reads

$$\boldsymbol{J}(z) = \frac{\epsilon_0}{2} \int d^2\boldsymbol{r}_\perp \big\{ \boldsymbol{r} \times \big[\boldsymbol{E}(\boldsymbol{r}) \times \boldsymbol{B}^*(\boldsymbol{r}) \big] \big\} \, , \tag{B.2}$$

where the integration is now over the transverse plane (x, y). By using the Maxwell equation $i\omega \boldsymbol{B} = \boldsymbol{\nabla} \times \boldsymbol{E}$, it is possible to eliminate from all equations the explicit dependence of the magnetic field $\boldsymbol{B}$ [198]. For Eq. (B.2), this procedure yields

$$\boldsymbol{J}(z) = \frac{\epsilon_0}{2i\omega} \int d^2\boldsymbol{r}_\perp E_i^*(\boldsymbol{r} \times \boldsymbol{\nabla}) E_i + \frac{\epsilon_0}{2i\omega} \int d^2\boldsymbol{r}_\perp \boldsymbol{E}^* \times \boldsymbol{E} \, , \tag{B.3}$$

where the summation over repeated polarization indices (Einstein convention) is understood.

The first term in the right-hand side of Eq. (B.3) is related to the spatial variation of the electric field and is interpreted as an orbital angular momentum:

$$\boldsymbol{L}(z) = \frac{\epsilon_0}{2i\omega} \int d^2\boldsymbol{r}_\perp E_i^*(\boldsymbol{r} \times \boldsymbol{\nabla}) E_i \, . \tag{B.4}$$

When speaking of orbital angular momentum of light, it is customary to distinguish its "intrinsic" and "extrinsic" components [199]. The extrinsic component is related to a displacement of the light beam with respect to an origin. The extrinsic orbital angular momentum then represents the optical analogous to the mechanical angular momentum of classical particles. On the other hand, the intrinsic orbital angular momentum is associated with a variation of the phase of the field, thus concerning the deformation

of the light wavefronts. Beams displaying optical vortexes, known in literature as helical modes, for instance, carry a non-zero intrinsic orbital angular momentum. The Laguerre-Gaussian beams [200] constitute a notable example of such helical beams. In the present thesis, however, only the extrinsic orbital angular momentum is involved.

On the contrary, the second term of Eq. (B.3) is associated to the vector nature of light and thus to the light polarization degrees of freedom. Indeed, such term is interpreted as the spin angular momentum of light:

$$\boldsymbol{S}(z) = \frac{\epsilon_0}{2i\omega} \int d^2\boldsymbol{r}_\perp \boldsymbol{E}^* \times \boldsymbol{E} \; . \tag{B.5}$$

Discriminating the different contributions to the angular momentum of light beams and the conservation rules that relate them is in general crucial to highlight the presence of spin-orbit interactions in an optical system.

Appendix C

Scattering by a cylinder: Mie coefficients

Mie theory provides an exact solution to electromagnetic-wave scattering by objects of arbitrary size. We summarize here the main steps of the derivation of the Mie coefficients in the case of interest in the thesis, namely an infinite circular right cylinder. Nevertheless, the *modus operandi* is general to any Mie theory. For more details, together with a step by step derivation, we refer the interested reader to [172].

The starting point is the scalar Helmholtz equation, which, once expressed in polar coordinates (r, φ, z), admits the separable solutions

$$\psi_{\mathrm{n}}(r, \varphi, z) = Z_{\mathrm{n}}(rk_0)e^{i\mathrm{n}\varphi}e^{ik_z z} \,, \tag{C.1}$$

where Z_{n} is a solution to the Bessel equation [201] and $\mathrm{n} \in \mathbb{Z}$. The scalar functions ψ_{n} are functions from which it is possible to generate the special class of solutions of the vector Helmholtz equation, given by:

$$\boldsymbol{M}_{\mathrm{n}} = \boldsymbol{\nabla} \times (\hat{\boldsymbol{z}}\psi_{\mathrm{n}}) \qquad \boldsymbol{N}_{\mathrm{n}} = \frac{\boldsymbol{\nabla} \times \boldsymbol{M}_{\mathrm{n}}}{k} \,. \tag{C.2}$$

$\boldsymbol{M}_{\mathrm{n}}$ and $\boldsymbol{N}_{\mathrm{n}}$, known as vector cylindrical harmonics, constitute an infinite orthogonal complete vector basis of the real space. One can then expand both the incident and scattered field, as well as the field inside the cylinder, on this basis. This decomposition is suitable for imposing the continuity of the tangential components of both electric and magnetic fields at the cylindrical interface $r = \rho$, which as a result returns the values of the Mie coefficients, i.e., the expansion coefficients on this basis of the scattered field $\boldsymbol{E}_s$. The latter reads

$$\boldsymbol{E}_s = \begin{bmatrix} \boldsymbol{E}_s^{\mathrm{TM}} \\ \boldsymbol{E}_s^{\mathrm{TE}} \end{bmatrix} \propto \begin{bmatrix} \sum_{\mathrm{n}=-\infty}^{\infty} b_{\mathrm{nI}}\boldsymbol{N}_{\mathrm{n}}^{(3)} + ia_{\mathrm{nI}}\boldsymbol{M}_{\mathrm{n}}^{(3)} \\ \sum_{\mathrm{n}=-\infty}^{\infty} b_{\mathrm{nII}}\boldsymbol{N}_{\mathrm{n}}^{(3)} + ia_{\mathrm{nII}}\boldsymbol{M}_{\mathrm{n}}^{(3)} \end{bmatrix} \,, \tag{C.3}$$

where the superscript (3) indicates that the vector cylindrical harmonics are here generated using the Hankel function of the first kind [201] as solution of Bessel equation Z_{n}. The subscripts I and II applied to the Mie coefficients a and b indicate if they come, respectively, from the component E_s^{TM} or E_s^{TE} of the scattered field, while the subscript n indicates its order in the harmonic expansion. In the case of an infinitely-long

cylinder, the Mie coefficients have analytical expressions, which we report below:

$$\begin{aligned} a_{\mathrm{nI}} &= \frac{C_{\mathrm{n}}V_{\mathrm{n}} - B_{\mathrm{n}}D_{\mathrm{n}}}{W_{\mathrm{n}}V_{\mathrm{n}} + iD_{\mathrm{n}}^2} = -b_{\mathrm{nII}} \\ b_{\mathrm{nI}} &= \frac{W_{\mathrm{n}}B_{\mathrm{n}} + iD_{\mathrm{n}}C_{\mathrm{n}}}{W_{\mathrm{n}}V_{\mathrm{n}} + iD_{\mathrm{n}}^2} \\ a_{\mathrm{nII}} &= -\frac{A_{\mathrm{n}}V_{\mathrm{n}} - iC_{\mathrm{n}}D_{\mathrm{n}}}{W_{\mathrm{n}}V_{\mathrm{n}} + iD_{\mathrm{n}}^2}\ , \end{aligned} \tag{C.4}$$

where

$$\begin{aligned} A_{\mathrm{n}} =& i\xi\left[\xi J_{\mathrm{n}}'(\eta)J_{\mathrm{n}}(\xi) - \eta J_{\mathrm{n}}(\eta)J_{\mathrm{n}}'(\xi)\right] \\ B_{\mathrm{n}} =& \xi\left[m^2\xi J_{\mathrm{n}}'(\eta)J_{\mathrm{n}}(\xi) - \eta J_{\mathrm{n}}(\eta)J_{\mathrm{n}}'(\xi)\right] \\ C_{\mathrm{n}} =& \mathrm{n}\cos\theta\eta J_{\mathrm{n}}(\eta)J_{\mathrm{n}}(\xi)(\xi^2/\eta^2 - 1) \\ D_{\mathrm{n}} =& \mathrm{n}\cos\theta\eta J_{\mathrm{n}}(\eta)H_{\mathrm{n}}^{(1)}(\xi)(\xi^2/\eta^2 - 1) \\ V_{\mathrm{n}} =& \xi\left[m^2\xi J_{\mathrm{n}}'(\eta)H_{\mathrm{n}}^{(1)}(\xi) - \eta J_{\mathrm{n}}(\eta)H_{\mathrm{n}}^{(1)\prime}(\xi)\right] \\ W_{\mathrm{n}} =& i\xi\left[\eta J_{\mathrm{n}}(\eta)H_{\mathrm{n}}^{(1)\prime}(\xi) - \xi J_{\mathrm{n}}'(\eta)H_{\mathrm{n}}^{(1)}(\xi)\right] \end{aligned} \tag{C.5}$$

with $\xi = k\rho\sin\theta$, $\eta = k\rho\sqrt{m^2 - \cos^2\theta}$, and J_{n} and $H_{\mathrm{n}}^{(1)}$ being the Bessel and Hankel functions of the first kind, respectively.

Eq. (4.6) of the main text, where the Mie coefficients (C.4) enter, is obtained by expanding at large distances ($k_0 r_\perp \gg 1$) the scattered field obtained in the above Mie theory.

Appendix D

Parameters of lowest Mie resonances

In this appendix, we provide the analytical expressions of the resonance frequencies $\omega_{0(1)}$ and widths $\Gamma_{0(1)}$ of the two lowest Mie resonances of a dielectric cylinder. These expressions are obtained by linearizing the Bessel functions in Eq. (C.5) in the vicinity of the first zeros of the denominators of $b_{0\mathrm{I}}$ and $a_{1\mathrm{I}}$. For the lowest Mie resonance we find

$$\begin{aligned}\omega_0 =&\frac{c_0/8\rho}{\gamma+\ln\frac{a\sin\theta}{2\sqrt{m^2-1}}}\left[\frac{adm^2}{c\sqrt{m^2-1}}\right.\\&\left.-\sqrt{\frac{a^2d^2m^4}{c^2(m^2-1)}-\left(8+\frac{4a^2dm^2}{c(m^2-1)}\right)\left(4\gamma+4\ln\frac{a\sin\theta}{2\sqrt{m^2-1}}\right)}\right]\end{aligned} \tag{D.1}$$

and

$$\Gamma_0=\frac{\rho}{c_0}\frac{4\pi\omega_0^2}{\sqrt{\frac{a^2d^2m^4}{c^2(m^2-1)}-\left(8+\frac{4a^2dm^2}{c(m^2-1)}\right)\left(4\gamma+4\ln\frac{a\sin\theta}{2\sqrt{m^2-1}}\right)}}\,, \tag{D.2}$$

where γ is the Euler's constant and $a = 1.84118378$, $b = 0.2051107$, $c = 0.581865$ and $d = 0.8204428$. We also recall that θ is the angle of incidence of the laser on the cylinder, ρ is the cylinder radius and m is the refractive index of the cylinder with respect to the surrounding medium. Similarly, for the TM Mie resonance we find

$$\omega_1=\frac{c_0}{\rho}\left[\frac{\alpha}{\sqrt{m^2-1}}+\frac{m\alpha\sin^2\theta}{m^2-1}\left(\gamma+\ln\frac{\alpha\sin\theta}{2\sqrt{m^2-1}}\right)\right] \tag{D.3}$$

and

$$\Gamma_1=\frac{c_0}{\rho}\frac{m\alpha\pi\sin^2\theta}{m^2-1}, \tag{D.4}$$

where $\alpha = 2.4048$. In particular, at very small angle Eq. (D.3) reduces to Eq. (4.11) of the main text. In the limit $\theta \to 0$ the width Γ_0 goes to zero very slowly, whereas Γ_1 vanishes very fast due to the $\sin^2\theta$ scaling.

Appendix E

Coherent mode intensity and spin Hall shift following laser extinction

To compute the coherent-mode intensity $I_c(L,t)$ following a laser extinction, we insert Eq. (4.48) into Eq. (4.51) and perform the integral over momentum. This gives

$$\begin{aligned} I_c(L,t) =& I_0 \Bigg| \int \frac{d\omega}{2\pi} e^{-i\omega t} \left[\pi\delta(\omega-\omega_l) - ip.v.\left(\frac{1}{\omega-\omega_l}\right)\right] \\ & \times \left[e^{-i\Sigma_{\mathrm{TE}}L/2k_z}\boldsymbol{e}_0 - \left(e^{-i\Sigma_{\mathrm{TE}}L/2k_z} - e^{-i\Sigma_{\mathrm{TM}}L/2k_z}\right)\boldsymbol{p}(\boldsymbol{k}_0)\right] \Bigg|^2 . \end{aligned} \tag{E.1}$$

Then we express the exponential terms $\exp\left(-i\Sigma_{\mathrm{TE(TM)}}L/2k_z\right)$ as infinite series using Eq.s (4.53), for instance:

$$\exp\left(-i\Sigma_{\mathrm{TE}}L/2k_z\right) = \sum_{p=0}^{\infty} \frac{1}{p!}\left(-\frac{iz}{2z_s^0}\frac{\Gamma_0/2}{\omega-\omega_0+i\Gamma_0/2}\right)^p , \tag{E.2}$$

and perform the frequency integrals in Eq. (E.1) using the residue theorem. The calculation is tedious but straightforward. It gives

$$I(L,t) = \frac{I_0}{2}\left[|F(L,t)|^2 + |G(L,t)|^2\right] , \tag{E.3}$$

where

$$G(L,t) = \sum_{p=0}^{\infty} \frac{1}{p!}\left(-\frac{L}{2z_s^0}\frac{i\Gamma_0/2}{\delta_0+i\Gamma_0/2}\right)^p \frac{\Gamma(p,(\Gamma_0/2-i\delta_0)t)}{\Gamma(p)} \tag{E.4}$$

and

$$
\begin{aligned}
F(L,t) =& \exp\left(-\frac{L}{2z_s^0}\frac{i\Gamma_1/2}{-\Delta\omega - i\Delta\Gamma/2}\right)\sum_{p=0}^{\infty}\frac{1}{p!}\left(-\frac{L\cos^2\theta}{2z_s^0}\frac{i\Gamma_0/2}{\delta_0+i\Gamma_0/2}\right)^p \\
&\times\frac{\Gamma(p,(\Gamma_0/2-i\delta_0)t)}{\Gamma(p)} + \exp\left(-\frac{L\cos^2\theta}{2z_s^0}\frac{i\Gamma_0/2}{\Delta\omega+i\Delta\Gamma/2}\right) \\
&\qquad\times\sum_{p=0}^{\infty}\frac{1}{p!}\left(-\frac{L}{2z_s^0}\frac{i\Gamma_1/2}{\delta_1+i\Gamma_1/2}\right)^p\frac{\Gamma(p,(\Gamma_1/2-i\delta_1)t)}{\Gamma(p)} \\
&+\sum_{p=0}^{\infty}\sum_{s=1}^{p-1}\frac{1}{p!}\left(-\frac{L\cos^2\theta}{2z_s^0}\frac{i\Gamma_0/2}{\delta_0+i\Gamma_0/2}\right)^p\frac{\Gamma(p-s,(\Gamma_0/2-i\delta_0)t)}{\Gamma(p-s)} \\
&\qquad\times\left(\frac{\delta_0+i\Gamma_0/2}{\Delta\omega+i\Delta\Gamma/2}\right)^s M_s\left(-\frac{L}{2z_s^0}\frac{i\Gamma_1/2}{-\Delta\omega-i\Delta\Gamma/2}\right) \\
&+\sum_{p=0}^{\infty}\sum_{s=1}^{p-1}\frac{1}{p!}\left(-\frac{L}{2z_s^0}\frac{i\Gamma_1/2}{\delta_1+i\Gamma_1/2}\right)^p\frac{\Gamma(p-s,(\Gamma_1/2-i\delta_1)t)}{\Gamma(p-s)} \\
&\qquad\times\left(\frac{\delta_1+i\Gamma_1/2}{-\Delta\omega-i\Delta\Gamma/2}\right)^s M_s\left(-\frac{L\cos^2\theta}{2z_s^0}\frac{i\Gamma_0/2}{\Delta\omega+i\Delta\Gamma/2}\right).
\end{aligned}
\tag{E.5}
$$

Here $\Gamma(n,x)$ is the upper incomplete Gamma function, $M_s(x) = {}_1F_1(1+s,2,x)x$ with ${}_1F_1$ being the Kummer's confluent hypergeometric function [201], and the various detunings are defined as

$$
\begin{aligned}
\delta_0 =& \omega_l - \omega_0 \\
\delta_1 =& \omega_l - \omega_1 \\
\Delta\omega =& \omega_1 - \omega_0 \\
\Delta\Gamma =& \Gamma_1 - \Gamma_0\,.
\end{aligned}
\tag{E.6}
$$

The calculation of the spin Hall shift of the coherent mode after the laser extinction is performed using Eq. (4.52) and follows the same strategy as in the stationary case. For $\boldsymbol{e}_0 \propto \boldsymbol{e}_i^{\mathrm{TM}} + e^{i\phi}\boldsymbol{e}_i^{\mathrm{TE}}$, we find:

$$
R_y(L,t) = -\frac{\sin\phi}{k_0}\left[1 - \frac{2\,\mathrm{Re}[F^*(L,t)G(L,t)]}{|F(L,t)|^2+|G(L,t)|^2}\right] + \frac{\cos\phi}{k_0}\frac{2\,\mathrm{Im}[F^*(L,t)G(L,t)]}{|F(L,t)|^2+|G(L,t)|^2}\,. \tag{E.7}
$$

The time-dependent spin Hall shifts following from the weak-measurement procedure, finally, are given by:

$$
R_y^{\delta}(L,t) = -\frac{\delta}{k_0}\frac{|F(L,t)|^2 - \mathrm{Re}[F^*(L,t)G(L,t)]}{\delta^2|F(L,t)|^2 + \left(\frac{1}{k_0 w_0}\right)^2|G(L,t)-F(L,t)|^2} \tag{E.8}
$$

for $\boldsymbol{e}_{\mathrm{out}} \propto \boldsymbol{e}_i^{\mathrm{TE}} + i\delta\boldsymbol{e}_i^{\mathrm{TM}}$ as a post-selection polarizer, and

$$
R_y^{\delta}(L,t) = \frac{\delta}{k_0}\frac{\mathrm{Im}[F^*(t,z)G(t,z)]}{\delta^2|F(t,z)|^2 + \left(\frac{1}{k_0 w_0}\right)^2|G(t,z)-F(t,z)|^2} \tag{E.9}
$$

for $\boldsymbol{e}_{\mathrm{out}} \propto \boldsymbol{e}_i^{\mathrm{TE}} + \delta\boldsymbol{e}_i^{\mathrm{TM}}$.

Appendix F

Decomposition of the structure factor on orthonormal projectors

In the following we report the full expressions for the eigentensors $\mathbf{\Pi}^{(n)}$ and eigenvalues λ_n of the 9×9 matrix $Q_{\alpha\beta,\gamma\delta}$. From this decomposition, as reported in the main text, comes the following decomposition of the structure factor $\mathbf{\Gamma}^{(L)}(K_z, q_z, \mathbf{0})$:

$$\Gamma^{(L)}_{\alpha\beta,\gamma\delta} = \sum_n \frac{\gamma k^4}{1-\gamma k^4 \lambda_n} \Pi^{(n)}_{\alpha\beta,\gamma\delta} \,. \tag{F.1}$$

The eigentensors $\mathbf{\Pi}^{(n)}$ are given by

$$\begin{aligned}
\Pi^{(1)}_{\alpha\beta,\gamma\delta} =& \frac{1}{2}[\delta_{\alpha\gamma}\delta_{\beta\delta} - \delta_{\alpha\delta}\delta_{\beta\gamma} - \delta_{\alpha\gamma}\delta_{\beta z}\delta_{\delta z} + \delta_{\alpha\delta}\delta_{\beta z}\delta_{\gamma z} + \delta_{\beta\gamma}\delta_{\alpha z}\delta_{\delta z} \\
& - \delta_{\beta\delta}\delta_{\alpha z}\delta_{\gamma z}] \\
\Pi^{(2)}_{\alpha\beta,\gamma\delta} =& \frac{1}{2}[-\delta_{\alpha\beta}\delta_{\gamma\delta} + \delta_{\alpha\gamma}\delta_{\beta\delta} + \delta_{\alpha\delta}\delta_{\beta\gamma} - \delta_{\alpha\gamma}\delta_{\beta z}\delta_{\delta z} - \delta_{\alpha\delta}\delta_{\beta z}\delta_{\gamma z} - \delta_{\beta\gamma}\delta_{\alpha z}\delta_{\delta z} \\
& - \delta_{\beta\delta}\delta_{\alpha z}\delta_{\gamma z} + \delta_{\alpha\beta}\delta_{\gamma z}\delta_{\delta z} + \delta_{\gamma\delta}\delta_{\alpha z}\delta_{\beta z} + \delta_{\alpha z}\delta_{\beta z}\delta_{\gamma z}\delta_{\delta z}] \\
\Pi^{(3)}_{\alpha\beta,\gamma\delta} =& \frac{1}{2}[\delta_{\alpha\gamma}\delta_{\beta z}\delta_{\delta z} + \delta_{\alpha\delta}\delta_{\beta z}\delta_{\gamma z} + \delta_{\beta\gamma}\delta_{\alpha z}\delta_{\delta z} + \delta_{\beta\delta}\delta_{\alpha z}\delta_{\gamma z} - 4\delta_{\alpha z}\delta_{\beta z}\delta_{\gamma z}\delta_{\delta z}] \\
\Pi^{(4)}_{\alpha\beta,\gamma\delta} =& \frac{1}{2}[\delta_{\alpha\gamma}\delta_{\beta z}\delta_{\delta z} - \delta_{\alpha\delta}\delta_{\beta z}\delta_{\gamma z} - \delta_{\beta\gamma}\delta_{\alpha z}\delta_{\delta z} + \delta_{\beta\delta}\delta_{\alpha z}\delta_{\gamma z}] \\
\Pi^{(5)}_{\alpha\beta,\gamma\delta} =& \frac{F^{(0)}_{11} - F^{(0)}_{22}(2 - 4\hat{K}_z^2 + \hat{K}_z^4) - S}{-4S}\delta_{\alpha\beta}\delta_{\gamma\delta} + [\delta_{\alpha\beta}\delta_{\gamma z}\delta_{\delta z} + \delta_{\gamma\delta}\delta_{\alpha z}\delta_{\beta z}] \\
& \times \frac{-F^{(0)}_{11} + F^{(0)}_{22}(2 - 3\hat{K}_z^4) + S}{-4S} + \frac{-F^{(0)}_{11} + F^{(0)}_{22}(2 - 12\hat{K}_z^2 + 9\hat{K}_z^4) - 3S}{-4S} \\
& \times \delta_{\alpha z}\delta_{\beta z}\delta_{\gamma z}\delta_{\delta z} \doteq \Pi^{(5)}_{\alpha\beta,\gamma\delta}(S) \\
\Pi^{(6)}_{\alpha\beta,\gamma\delta} =& \Pi^{(5)}_{\alpha\beta,\gamma\delta}(-S) \,,
\end{aligned} \tag{F.2}$$

where

$$S = \sqrt{\left[F^{(0)}_{11}\right]^2 - 2F^{(0)}_{11}F^{(0)}_{22}(2 - 4\hat{K}_z^2 + \hat{K}_z^4) + \left[F^{(0)}_{22}\right]^2(2 - 4\hat{K}_z^2 + 3\hat{K}_z^4)^2} \,. \tag{F.3}$$

From these expressions one can verify the orthonormal $\mathbf{\Pi}^{(n)} \cdot \mathbf{\Pi}^{(n')} = \delta_{nn'}$ and completeness $\sum_n \mathbf{\Pi}^{(n)} = \mathbb{1}$ relations. The corresponding eigenvalues λ_n are instead given by

$$\begin{aligned}
\lambda_1 =& F_{12}^{(0)} \hat{K}_z^2 \\
\lambda_2 =& \frac{F_{11}^{(0)} + 2F_{12}^{(0)} \hat{K}_z^2 + F_{22}^{(0)} \hat{K}_z^4}{4} \\
\lambda_3 =& \frac{1}{2}(1 - \hat{K}_z^2)(F_{12}^{(0)} + 2F_{22}^{(0)} \hat{K}_z^2) \\
\lambda_4 =& \frac{1}{2}(1 - \hat{K}_z^2) F_{12}^{(0)} \\
\lambda_5 =& \frac{1}{4}[F_{11}^{(0)} + F_{22}^{(0)}(2 - 4\hat{K}_z^2 + 3\hat{K}_z^4) - S] \\
\lambda_6 =& \frac{1}{4}[F_{11}^{(0)} + F_{22}^{(0)}(2 - 4\hat{K}_z^2 + 3\hat{K}_z^4) + S] \, .
\end{aligned} \tag{F.4}$$

The quantities $F_{11}^{(0)}$, $F_{12}^{(0)}$, and $F_{22}^{(0)}$ are those introduced in Eq. (5.35) of the main text.

Bibliography

[1] L. P. Gor'kov, A. I. Larkin, and D. E. Khmel'nitskii. Particle conductivity in a two-dimensional random potential. *JETP Lett.*, 30:228, 1979.

[2] G. Bergmann. Weak localization in thin films: a time-of-flight experiment with conduction electrons. *Physics Reports*, 107(1):1–58, 1984.

[3] P.-E. Wolf and G. Maret. Weak Localization and Coherent Backscattering of Photons in Disordered Media. *Phys. Rev. Lett.*, 55:2696–2699, 1985.

[4] M. P. van Albada and A. Lagendijk. Observation of Weak Localization of Light in a Random Medium. *Phys. Rev. Lett.*, 55:2692–2695, 1985.

[5] P. W. Anderson. Absence of Diffusion in Certain Random Lattices. *Phys. Rev.*, 109:1492–1505, 1958.

[6] E. Abrahams. *50 Years of Anderson Localization*. World Scientific, Singapore, 2010.

[7] T. Karpiuk, N. Cherroret, K. L. Lee, B. Grémaud, C. A. Müller, and C. Miniatura. Coherent Forward Scattering Peak Induced by Anderson Localization. *Phys. Rev. Lett.*, 109:190601, 2012.

[8] V. N. Prigodin, B. L. Altshuler, K. B. Efetov, and S. Iida. Mesoscopic dynamical echo in quantum dots. *Phys. Rev. Lett.*, 72:546–549, 1994.

[9] C. Hainaut, I. Manai, J.-F. Clément, J. C. Garreau, P. Szriftgiser, G. Lemarié, N. Cherroret, D. Delande, and R. Chicireanu. Controlling symmetry and localization with an artificial gauge field in a disordered quantum system. *Nature Communications*, 9:1382, 2018.

[10] T. Prat, D. Delande, and N. Cherroret. Quantum boomeranglike effect of wave packets in random media. *Phys. Rev. A*, 99:023629, 2019.

[11] J. Janarek, D. Delande, N. Cherroret, and J. Zakrzewski. Quantum boomerang effect for interacting particles. *Phys. Rev. A*, 102:013303, 2020.

[12] F. Scheffold, W. Härtl, G. Maret, and E. Matijević. Observation of long-range correlations in temporal intensity fluctuations of light. *Phys. Rev. B*, 56:10942–10952, 1997.

[13] F. Scheffold and G. Maret. Universal Conductance Fluctuations of Light. *Phys. Rev. Lett.*, 81:5800–5803, 1998.

[14] S. Feng and P. A. Lee. Mesoscopic Conductors and Correlations in Laser Speckle Patterns. *Science*, 251(4994):633–639, 1991.

[15] R. Berkovits and S. Feng. Correlations in coherent multiple scattering. *Physics Reports*, 238(3):135–172, 1994.

[16] E. Akkermans and G. Montambaux. *Mesoscopic Physics of Electrons and Photons*. Cambridge University Press, Cambridge, 2007.

[17] P. Sheng. *Introduction to Wave Scattering, Localization, and Mesoscopic Phenomena*. Academic Press, San Diego, 1995.

[18] G. Hertel, D. J. Bishop, E. G. Spencer, J. M. Rowell, and R. C. Dynes. Tunneling and Transport Measurements at the Metal-Insulator Transition of Amorphous Nb: Si. *Phys. Rev. Lett.*, 50:743–746, 1983.

[19] M. A. Paalanen, T. F. Rosenbaum, G. A. Thomas, and R. N. Bhatt. Critical Scaling of the Conductance in a Disordered Insulator. *Phys. Rev. Lett.*, 51:1896–1899, 1983.

[20] T. F. Rosenbaum, G. A. Thomas, and M. A. Paalanen. Critical behavior of Si:P at the metal-insulator transition. *Phys. Rev. Lett.*, 72:2121–2121, 1994.

[21] H. Hu, A. Strybulevych, J. H. Page, S. E. Skipetrov, and B. A. van Tiggelen. Localization of ultrasound in a three-dimensional elastic network. *Nature Physics*, 4:945–948, 2008.

[22] S. Faez, A. Strybulevych, J. H. Page, A. Lagendijk, and B. A. van Tiggelen. Observation of Multifractality in Anderson Localization of Ultrasound. *Phys. Rev. Lett.*, 103:155703, 2009.

[23] J. Chabé, G. Lemarié, B. Grémaud, D. Delande, P. Szriftgiser, and J. C. Garreau. Experimental Observation of the Anderson Metal-Insulator Transition with Atomic Matter Waves. *Phys. Rev. Lett.*, 101:255702, 2008.

[24] F. Jendrzejewski, A. Bernard, K. Müller, P. Cheinet, V. Josse, M. Piraud, L. Pezzé, L. Sanchez-Palencia, A. Aspect, and P. Bouyer. Three-dimensional localization of ultracold atoms in an optical disordered potential. *Nature Physics*, 8:398, 2012.

[25] G. Semeghini, M. Landini, P. Castilho, S. Roy, G. Spagnolli, A. Trenkwalder, M. Fattori, M. Inguscio, and G. Modugno. Measurement of the mobility edge for 3D Anderson. *Nature Physics*, 11:554–559, 2015.

[26] D. S. Wiersma, P. Bartolini, A. Lagendijk, and R. Righini. Localization of light in a disordered medium. *Nature*, 390:671–673, 1997.

[27] A. Z. Genack and N. Garcia. Observation of photon localization in a three-dimensional disordered system. *Phys. Rev. Lett.*, 66:2064–2067, 1991.

[28] F. Scheffold, R. Lenke, R. Tweer, and G. Maret. Localization or classical diffusion of light? *Nature*, 398:206–207, 1999.

[29] M. Störzer, P. Gross, C. M. Aegerter, and G. Maret. Observation of the Critical Regime Near Anderson Localization of Light. *Phys. Rev. Lett.*, 96:063904, 2006.

[30] T. Sperling, W. Bührer, C. Aegerter, and G. Maret. Direct determination of the transition to localization of light in three dimensions. *Nature Photonics*, 7:48–52, 2013.

[31] T. Sperling, L. Schertel, M. Ackermann, G. J. Aubry, C. M. Aegerter, and G. Maret. Can 3D light localization be reached in 'white paint'? *New Journal of Physics*, 18(1):013039, 2016.

[32] S. John. Electromagnetic absorption in a disordered medium near a photon mobility edge. *Phys. Rev. Lett.*, 53:2169–2172, 1984.

[33] S. E. Skipetrov and I. M. Sokolov. Absence of Anderson Localization of Light in a Random Ensemble of Point Scatterers. *Phys. Rev. Lett.*, 112:023905, 2014.

[34] L. Bellando, A. Gero, E. Akkermans, and R. Kaiser. Cooperative effects and disorder: A scaling analysis of the spectrum of the effective atomic Hamiltonian. *Phys. Rev. A*, 90:063822, 2014.

[35] C. E. Máximo, N. Piovella, P. W. Courteille, R. Kaiser, and R. Bachelard. Spatial and temporal localization of light in two dimensions. *Phys. Rev. A*, 92:062702, 2015.

[36] M. J. Stephen and G. Cwilich. Rayleigh scattering and weak localization: Effects of polarization. *Phys. Rev. B*, 34:7564–7572, 1986.

[37] P.-E. Wolf, G. Maret, E. Akkermans, and R. Maynard. Optical coherent backscattering by random media : an experimental study. *J. Phys. France*, 49(1):63–75, 1988.

[38] E. Akkermans, P.-E. Wolf, R. Maynard, and G. Maret. Theoretical study of the coherent backscattering of light by disordered media. *J. Phys. France*, 49(1):77–98, 1988.

[39] F. C. MacKintosh, J. X. Zhu, D. J. Pine, and D. A. Weitz. Polarization memory of multiply scattered light. *Phys. Rev. B*, 40:9342–9345, 1989.

[40] G. Labeyrie, F. de Tomasi, J.-C. Bernard, C. A. Müller, C. Miniatura, and R. Kaiser. Coherent Backscattering of Light by Cold Atoms. *Phys. Rev. Lett.*, 83:5266–5269, 1999.

[41] C. A. Müller, T. Jonckheere, C. Miniatura, and D. Delande. Weak localization of light by cold atoms: The impact of quantum internal structure. *Phys. Rev. A*, 64:053804, 2001.

[42] N. Cherroret. Coherent multiple scattering of light in $(2+1)$ dimensions. *Phys. Rev. A*, 98:013805, 2018.

[43] G. L. J. A. Rikken and B. A. van Tiggelen. Observation of magnetically induced transverse diffusion of light. *Nature*, 381:54–55, 1996.

[44] I. Freund, M. Kaveh, R. Berkovits, and M. Rosenbluh. Universal polarization correlations and microstatistics of optical waves in random media. *Phys. Rev. B*, 42:2613–2616, 1990.

[45] A. A. Chabanov, N. P. Trégourès, B. A. van Tiggelen, and A. Z. Genack. Mesoscopic Correlation with Polarization Rotation of Electromagnetic Waves. *Phys. Rev. Lett.*, 92:173901, 2004.

[46] A. A. Chabanov, B. Hu, and A. Z. Genack. Dynamic Correlation in Wave Propagation in Random Media. *Phys. Rev. Lett.*, 93:123901, 2004.

[47] N. Cherroret, A. Peña, A. A. Chabanov, and S. E. Skipetrov. Nonuniversal dynamic conductance fluctuations in disordered systems. *Phys. Rev. B*, 80:045118, 2009.

[48] K. Y. Bliokh, F. J. Rodríguez-Fortuño, F. Nori, and A. V. Zayats. Spin–orbit interactions of light. *Nature Photonics*, 9:796–808, 2015.

[49] X. Ling, X. Zhou, K. Huang, Y. Liu, C.-W. Qiu, H. Luo, and S. Wen. Recent advances in the spin Hall effect of light. *Reports on Progress in Physics*, 80(6):066401, 2017.

[50] M. Onoda, S. Murakami, and N. Nagaosa. Hall Effect of Light. *Phys. Rev. Lett.*, 93:083901, 2004.

[51] O. Hosten and P. Kwiat. Observation of the Spin Hall Effect of Light via Weak Measurements. *Science*, 319(5864):787–790, 2008.

[52] Y. Gorodetski, K. Y. Bliokh, B. Stein, C. Genet, N. Shitrit, V. Kleiner, E. Hasman, and T. W. Ebbesen. Weak Measurements of Light Chirality with a Plasmonic Slit. *Phys. Rev. Lett.*, 109:013901, 2012.

[53] K. Y. Bliokh, A. Niv, V. Kleiner, and E. Hasman. Geometrodynamics of spinning light. *Nature Photonics*, 2:748–753, 2008.

[54] F. Cardano and L. Marrucci. Spin–orbit photonics. *Nature Photonics*, 9:776–778, 2015.

[55] A. Aiello, P. Banzer, M. Neugebauer, and G. Leuchs. From transverse angular momentum to photonic wheels. *Nature Photonics*, 9:789–795, 2015.

[56] I. M. Vellekoop and A. P. Mosk. Focusing coherent light through opaque strongly scattering media. *Opt. Lett.*, 32(16):2309–2311, 2007.

[57] S. Popoff, G. Lerosey, M. Fink, A. C. Boccara, and S. Gigan. Image transmission through an opaque material. *Nature Communications*, 1:81, 2010.

[58] I. M. Vellekoop, A. Lagendijk, and A. P. Mosk. Exploiting disorder for perfect focusing. *Nature Photonics*, 4:320–322, 2010.

[59] O. Katz, E. Small, and Y. Silberberg. Looking around corners and through thin turbid layers in real time with scattered incoherent light. *Nature Photonics*, 6:549–553, 2012.

[60] O. Katz, P. Heidmann, M. Fink, and S. Gigan. Non-invasive single-shot imaging through scattering layers and around corners via speckle correlations. *Nature Photonics*, 8:784–790, 2014.

[61] S. Rotter and S. Gigan. Light fields in complex media: Mesoscopic scattering meets wave control. *Rev. Mod. Phys.*, 89:015005, 2017.

[62] T. Bardon-brun, D. Delande, and N. Cherroret. Spin Hall Effect of Light in a Random Medium. *Phys. Rev. Lett.*, 123:043901, 2019.

[63] H. De Raedt, A. Lagendijk, and P. de Vries. Transverse Localization of Light. *Phys. Rev. Lett.*, 62:47–50, 1989.

[64] T. Schwartz, G. Bartal, S. Fishman, and M. Segev. Transport and Anderson localization in disordered two-dimensional photonic lattices. *Nature*, 446:52–55, 2007.

[65] G. I. Martone, T. Bienaimé, and N. Cherroret. Spin-orbit-coupled fluids of light in bulk nonlinear media. *Phys. Rev. A*, 104:013510, 2021.

[66] G. I. Martone and N. Cherroret. Spontaneous breaking of time translation symmetry in a spin-orbit-coupled fluid of light, 2022. https://arxiv.org/abs/2206.11714.

[67] F. Carlini and N. Cherroret. Tailoring propagation of light via spin-orbit interactions in correlated disorder. *Phys. Rev. A*, 105:053508, 2022.

[68] F. Carlini and N. Cherroret. Resonant Spin Hall Effect of Light in Random Photonic Arrays, 2022. https://arxiv.org/abs/2210.16379.

[69] E. H. Hall. On a New Action of the Magnet on Electric Currents. *American Journal of Mathematics*, 2(3):287–292, 1879.

[70] R. S. Popovic. *Hall Effect Devices (2nd ed.)*. CRC Press, Boca Raton, 2003.

[71] N. Nagaosa, J. Sinova, S. Onoda, A. H. MacDonald, and N. P. Ong. Anomalous Hall effect. *Rev. Mod. Phys.*, 82:1539–1592, 2010.

[72] D. Yoshioka. *The Quantum Hall Effect*. Springer, Berlin, 2002.

[73] K. von Klitzing, T. Chakraborty, P. Kim, V. Madhavan, X. Dai, J. McIver, Y. Tokura, L. Savary, D. Smirnova, A. M. Rey, C. Felser, J. Gooth, and X. Qi. 40 years of the quantum Hall effect. *Nature Reviews Physics*, 2:397–401, 2020.

[74] H. L. Stormer, D. C. Tsui, and A. C. Gossard. The fractional quantum Hall effect. *Rev. Mod. Phys.*, 71:S298–S305, 1999.

[75] M. I. Dyakonov and V. I. Perel. Current-induced spin orientation of electrons in semiconductors. *Physics Letters A*, 35(6):459–460, 1971.

[76] J. E. Hirsch. Spin Hall Effect. *Phys. Rev. Lett.*, 83:1834–1837, 1999.

[77] M. I. Dyakonov. *Spin Hall Effect. In Future Trends in Microelectronics (eds S. Luryi, J. Xu and A. Zaslavsky).* Wiley, New York, 2010.

[78] N. F. Mott and H. S. W. Massey. *The theory of atomic collisions.* Clarendon Press, Oxford, 1965.

[79] Y. A. Bychkov and É. I. Rashba. Properties of a 2D electron gas with lifted spectral degeneracy. *Soviet Journal of Experimental and Theoretical Physics Letters*, 39:78, 1984.

[80] R. Winkler. *Spin-orbit Coupling Effects in Two-Dimensional Electron and Hole Systems.* Springer, Berlin, 2003.

[81] A. Manchon, H. C. Koo, J. Nitta, S. M. Frolov, and R. A. Duine. New perspectives for Rashba spin–orbit coupling. *Nature Materials*, 14:871–882, 2015.

[82] Y. K. Kato, R. C. Myers, A. C. Gossard, and D. D. Awschalom. Observation of the Spin Hall Effect in Semiconductors. *Science*, 306(5703):1910–1913, 2004.

[83] J. Wunderlich, B. Kaestner, J. Sinova, and T. Jungwirth. Experimental Observation of the Spin-Hall Effect in a Two-Dimensional Spin-Orbit Coupled Semiconductor System. *Phys. Rev. Lett.*, 94:047204, 2005.

[84] J. Sinova, S. O. Valenzuela, J. Wunderlich, C. H. Back, and T. Jungwirth. Spin Hall effects. *Rev. Mod. Phys.*, 87:1213–1260, 2015.

[85] S. D. Bader and S. S. P. Parkin. Spintronics. *Annual Review of Condensed Matter Physics*, 1(1):71–88, 2010.

[86] I. Białynicki-Birula. On the Wave Function of the Photon. *Acta Physica Polonica A*, 86(1):97–116, 1994.

[87] Encyclopedia Britannica. https://www.britannica.com/science/electromagnetic-radiation/Gamma-rays#ref11353.

[88] L. D. Landau, E. M. Lifshitz, and L. P. Pitaevskii. *Electrodynamics of Continuous Media. Vol. 8 (2nd ed.).* Butterworth-Heinemann, Oxford, 1984.

[89] Y. A. Kravtsov and Y. I. Orlov. *Geometrical Optics of Inhomogeneous Media.* Springer-Verlag, Berlin, 1990.

[90] R. G. González-Acuña and H. A. Chaparro-Romo. *Stigmatic Optics.* IOP Publishing, Bristol, 2020.

[91] M. Born, E. Wolf, A. B. Bhatia, P. C. Clemmow, D. Gabor, A. R. Stokes, A. M. Taylor, P. A. Wayman, and W. L. Wilcock. *Principles of Optics: Electromagnetic Theory of Propagation, Interference and Diffraction of Light.* Cambridge University Press, Cambridge, 1999.

[92] K. Y. Bliokh and A. Aiello. Goos–Hänchen and Imbert–Fedorov beam shifts: an overview. *Journal of Optics*, 15(1):014001, 2013.

[93] F. Goos and H. Hänchen. Ein neuer und fundamentaler Versuch zur Totalreflexion. *Annalen der Physik*, 436(7-8):333–346, 1947.

[94] F. I. Fedorov. *Dokl. Akad. Nauk SSSR*, 105:465, 1955.

[95] K. Artmann. Berechnung der Seitenversetzung des totalreflektierten Strahles. *Annalen der Physik*, 437(1-2):87–102, 1948.

[96] C. Imbert. Calculation and Experimental Proof of the Transverse Shift Induced by Total Internal Reflection of a Circularly Polarized Light Beam. *Phys. Rev. D*, 5:787–796, 1972.

[97] H. Schilling. Die Strahlversetzung bei der Reflexion linear oder elliptisch polarisierter ebener Wellen an der Trennebene zwischen absorbierenden Medien. *Annalen der Physik*, 471(3-4):122–134, 1965.

[98] M. A. Player. Angular momentum balance and transverse shifts on reflection of light. *Journal of Physics A: Mathematical and General*, 20(12):3667, 1987.

[99] V. G. Fedoseyev. Conservation laws and transverse motion of energy on reflection and transmission of electromagnetic waves. *Journal of Physics A: Mathematical and General*, 21(9):2045, 1988.

[100] V. S. Liberman and B. Y. Zel'dovich. Spin-orbit interaction of a photon in an inhomogeneous medium. *Phys. Rev. A*, 46:5199–5207, 1992.

[101] A. V. Dooghin, N. D. Kundikova, V. S. Liberman, and B. Y. Zel'dovich. Optical Magnus effect. *Phys. Rev. A*, 45:8204–8208, 1992.

[102] H. G. Magnus. Über die Abweichung der Geschosse, und: Über eine abfallende Erscheinung bei rotierenden Körpern. *Annalen der Physik*, 164:1–29, 1853.

[103] S. M. Rytov. *Dokl. Akad. Nauk. SSSR*, 18:263, 1938.

[104] V. V. Vladimirski. *Dokl. Akad. Nauk. SSSR*, 31:222, 1941.

[105] M.-C. Chang and Q. Niu. Berry phase, hyperorbits, and the Hofstadter spectrum: Semiclassical dynamics in magnetic Bloch bands. *Phys. Rev. B*, 53:7010–7023, 1996.

[106] G. Sundaram and Q. Niu. Wave-packet dynamics in slowly perturbed crystals: Gradient corrections and Berry-phase effects. *Phys. Rev. B*, 59:14915–14925, 1999.

[107] J. Sinova, D. Culcer, Q. Niu, N. A. Sinitsyn, T. Jungwirth, and A. H. MacDonald. Universal Intrinsic Spin Hall Effect. *Phys. Rev. Lett.*, 92:126603, 2004.

[108] J. Anandan. The geometric phase. *Nature*, 360:307–313, 1992.

[109] S. Pancharatnam. Generalized theory of interference, and its applications. *Proceedings of the Indian Academy of Sciences*, 44(5):247–262, 1956.

[110] M. V. Berry. Quantal phase factors accompanying adiabatic changes. *Proceedings of the Royal Society of London. A. Mathematical and Physical Sciences*, 392(1802):45–57, 1984.

[111] M. Kolodrubetz, D. Sels, P. Mehta, and A. Polkovnikov. Geometry and non-adiabatic response in quantum and classical systems. *Physics Reports*, 697:1–87, 2017. Geometry and non-adiabatic response in quantum and classical systems.

[112] S.-D. Liang and G.-Y. Huang. Topological invariance and global Berry phase in non-Hermitian systems. *Phys. Rev. A*, 87:012118, 2013.

[113] K. Y. Bliokh. Geometrodynamics of polarized light: Berry phase and spin Hall effect in a gradient-index medium. *Journal of Optics A: Pure and Applied Optics*, 11(9):094009, 2009.

[114] Y. Aharonov and D. Bohm. Significance of Electromagnetic Potentials in the Quantum Theory. *Phys. Rev.*, 115:485–491, 1959.

[115] M. Peshkin and A. Tonomura. *The Aharonov-Bohm effect*. Springer, Berlin, 1989.

[116] S. Murakami, N. Nagaosa, and S.-C. Zhang. Dissipationless Quantum Spin Current at Room Temperature. *Science*, 301(5638):1348–1351, 2003.

[117] K. Y. Bliokh and Y. P. Bliokh. Topological spin transport of photons: the optical Magnus effect and Berry phase. *Physics Letters A*, 333(3):181–186, 2004.

[118] A. Tomita and R. Y. Chiao. Observation of Berry's Topological Phase by Use of an Optical Fiber. *Phys. Rev. Lett.*, 57:937–940, 1986.

[119] P. W. Anderson. More Is Different. *Science*, 177(4047):393–396, 1972.

[120] B. L. Al'tshuler and P. A. Lee. Disordered Electronic Systems. *Physics Today*, 41(12):36, 1988.

[121] R. A. Webb and S. Washburn. Quantum Interference Fluctuations in Disordered Metals. *Physics Today*, 41(12):46, 1988.

[122] V. L. Bonch-Bruevich. Problems of the electron theory of disordered semiconductors. *Soviet Physics Uspekhi*, 26(8):664, 1983.

[123] S. Datta. *Electronic Transport in Mesoscopic Systems*. Cambridge University Press, Cambridge, 1997.

[124] B. Shapiro. Cold atoms in the presence of disorder. *Journal of Physics A: Mathematical and Theoretical*, 45(14):143001, 2012.

[125] J. W. Goodman. *Speckle Phenomena in Optics: Theory and Applications*. Roberts and Company Publishers, Greenwood Village, 2007.

[126] E. Akkermans, P.-E. Wolf, and R. Maynard. Coherent Backscattering of Light by Disordered Media: Analysis of the Peak Line Shape. *Phys. Rev. Lett.*, 56:1471–1474, 1986.

[127] A. Lagendijk, B. van Tiggelen, and D. S. Wiersma. Fifty years of Anderson localization. *Physics Today*, 62(8):24, 2009.

[128] F. Evers and A. D. Mirlin. Anderson transitions. *Rev. Mod. Phys.*, 80:1355–1417, 2008.

[129] M. Lax, W. H. Louisell, and W. B. McKnight. From Maxwell to paraxial wave optics. *Phys. Rev. A*, 11:1365–1370, 1975.

[130] B. E. A. Saleh and M. C. Teich. *Fundamentals of Photonics*. John Wiley & Sons, New York, 1991.

[131] M. C. Rechtsman, Y. Plotnik, Y. Lumer, M. Segev, J. M. Zeuner, and A. Szameit. Photonic Topological Insulators. *Opt. Photon. News*, 24(12):42–42, 2013.

[132] H. Kogelnik and T. Li. Laser Beams and Resonators. *Appl. Opt.*, 5(10):1550–1567, 1966.

[133] M. Z. Hasan and C. L. Kane. Colloquium: Topological insulators. *Rev. Mod. Phys.*, 82:3045–3067, 2010.

[134] T. Ozawa, H. M. Price, A. Amo, N. Goldman, M. Hafezi, L. Lu, M. C. Rechtsman, D. Schuster, J. Simon, O. Zilberberg, and I. Carusotto. Topological photonics. *Rev. Mod. Phys.*, 91:015006, 2019.

[135] M. C. Rechtsman, J. M. Zeuner, Y. Plotnik, Y. Lumer, D. Podolsky, F. Dreisow, S. Nolte, M. Segev, and A. Szameit. Photonic Floquet topological insulators. *Nature*, 496:196–200, 2013.

[136] J. Kerr. A new relation between electricity and light: Dielectrified media birefringent. *Philosophical Magazine*, 50(332):337–348, 1875.

[137] I. Carusotto. Superfluid light in bulk nonlinear media. *Proceedings of the Royal Society A*, 470:20140320, 2014.

[138] C. Sun, S. Jia, C. Barsi, S. Rica, A. Picozzi, and J. W. Fleischer. Observation of the kinetic condensation of classical waves. *Nature Physics*, 8(6):470–474, 2012.

[139] N. Šantić, A. Fusaro, S. Salem, J. Garnier, A. Picozzi, and R. Kaiser. Nonequilibrium Precondensation of Classical Waves in Two Dimensions Propagating through Atomic Vapors. *Phys. Rev. Lett.*, 120:055301, 2018.

[140] C. Michel, O. Boughdad, M. Albert, P.-É. Larré, and M. Bellec. Superfluid motion and drag-force cancellation in a fluid of light . *Nature Communications*, 9:2108, 2018.

[141] P. Wölfle and D. Vollhardt. Self-consistent theory of anderson localization: General formalism and applications. In Elihu Abrahams, editor, *50 Years of Anderson Localization*, chapter 10, page 43. World Scientific, Singapore, 2010.

[142] M. Segev, Y. Silberberg, and D. Christodoulides. Anderson localization of light. *Nature Photonics*, 7:197–204, 2013.

[143] M. Boguslawski, S. Brake, J. Armijo, F. Diebel, P. Rose, and C. Denz. Analysis of transverse Anderson localization in refractive index structures with customized random potential. *Opt. Express*, 21(26):31713–31724, 2013.

[144] S. Karbasi, C. R. Mirr, P. G. Yarandi, R. J. Frazier, K. W. Koch, and A. Mafi. Observation of transverse Anderson localization in an optical fiber. *Opt. Lett.*, 37(12):2304–2306, 2012.

[145] S. Karbasi, R. J. Frazier, K. W. Koch, T. Hawkins, J. Ballato, and A. Mafi. Image transport through a disordered optical fibre mediated by transverse Anderson localization. *Nature Communications*, 5:3362, 2014.

[146] J. Zhao, J. E. A. Lopez, Z. Zhu, D. Zheng, S. Pang, R. A. Correa, and A. Schülzgen. Image Transport Through Meter-Long Randomly Disordered Silica-Air Optical Fiber. *Scientific Reports*, 8:3065, 2018.

[147] T. H. Tuan, S. Kuroyanagi, K. Nagasaka, T. Suzuki, and Y. Ohishi. Near-infrared optical image transport through an all-solid tellurite optical glass rod with transversely-disordered refractive index profile. *Opt. Express*, 26(13):16054–16062, 2018.

[148] T. H. Tuan, S. K., K. Nagasaka, T. Suzuki, and Y. Ohishi. Characterization of an all-solid disordered tellurite glass optical fiber and its NIR optical image transport. *Japanese Journal of Applied Physics*, 58(3):032005, 2019.

[149] A. Nakatani, H. T. Tong, M. Matsumoto, G. Sakai, T. Suzuki, and Y. Ohishi. Transverse Anderson localization of mid-infrared light in a chalcogenide transversely disordered optical fiber. *Opt. Express*, 30(4):5159–5166, 2022.

[150] A. Mafi, S. Karbasi, K. W. Koch, T. Hawkins, and J. Ballato. Transverse Anderson Localization in Disordered Glass Optical Fibers: A Review. *Materials*, 7(8):45520–5527, 2014.

[151] M. Boguslawski, S. Brake, D. Leykam, A. S. Desyatnikov, and C. Denz. Observation of transverse coherent backscattering in disordered photonic structures. *Scientific Reports*, 7:10439, 2017.

[152] F. Jendrzejewski, K. Müller, J. Richard, A. Date, T. Plisson, P. Bouyer, A. Aspect, and V. Josse. Coherent Backscattering of Ultracold Atoms. *Phys. Rev. Lett.*, 109:195302, 2012.

[153] K. Müller, J. Richard, V. V. Volchkov, V. Denechaud, P. Bouyer, A. Aspect, and V. Josse. Suppression and Revival of Weak Localization through Control of Time-Reversal Symmetry. *Phys. Rev. Lett.*, 114:205301, 2015.

[154] N. Cherroret, T. Karpiuk, C. A. Müller, B. Grémaud, and C. Miniatura. Coherent backscattering of ultracold matter waves: Momentum space signatures. *Phys. Rev. A*, 85:011604, 2012.

[155] J. D. Jackson. *Classical electrodynamics (2nd ed.)*. Wiley, New York, 1975.

[156] A. A. Abrikosov, L. P. Gorkov, and I. E. Dzyaloshinskii. *Methods of Quantum Field Theory in Statistical Physics*. Dover Books, New York, 1963.

[157] G. Sardanashvily. *Noether's Theorems: Applications in Mechanics and Field Theory*. Springer-Verlag, Berlin, 2016.

[158] V. S. Vladimirov. *Methods of the Theory of Generalized Functions (Analytical Methods and Special Functions)*. Taylor & Francis, London, 2002.

[159] J. Stalker. *Complex Analysis: Fundamentals of the Classical Theory of Functions*. Springer, Berlin, 1998.

[160] S. Feng, C. Kane, P. A. Lee, and A. D. Stone. Correlations and Fluctuations of Coherent Wave Transmission through Disordered Media. *Phys. Rev. Lett.*, 61:834–837, 1988.

[161] C. Cohen-Tannoudji, B. Diu, and F. Laloë. *Quantum Mechanics, Volume 1: Basic Concepts, Tools, and Applications (2nd ed.)*. John Wiley & Sons, New York, 2019.

[162] S. Harris. *An introduction to the theory of the Boltzmann equation*. Dover Books, New York, 1971.

[163] D. L. Andrews and M. Babiker. *The Angular Momentum of Light*. Cambridge University Press, Cambridge, 2013.

[164] F. J. Belinfante. On the current and the density of the electric charge, the energy, the linear momentum and the angular momentum of arbitrary fields. *Physica*, 7(5):449–474, 1940.

[165] D. Budker, W. Gawlik, D. F. Kimball, S. M. Rochester, V. V. Yashchuk, and A. Weis. Resonant nonlinear magneto-optical effects in atoms. *Rev. Mod. Phys.*, 74:1153–1201, 2002.

[166] Y. Qin, Y. Li, H. He, and Q. Gong. Measurement of spin Hall effect of reflected light. *Opt. Lett.*, 34(17):2551–2553, 2009.

[167] Y. Aharonov, D. Z. Albert, and L. Vaidman. How the result of a measurement of a component of the spin of a spin-1/2 particle can turn out to be 100. *Phys. Rev. Lett.*, 60:1351–1354, 1988.

[168] M. R. Dennis and J. B. Götte. The analogy between optical beam shifts and quantum weak measurements. *New Journal of Physics*, 14(7):073013, 2012.

[169] J. Dressel, M. Malik, F. M. Miatto, A. N. Jordan, and R. W. Boyd. Colloquium: Understanding quantum weak values: Basics and applications. *Rev. Mod. Phys.*, 86:307–316, 2014.

[170] B. A. Lippmann and J. Schwinger. Variational Principles for Scattering Processes. I. *Phys. Rev.*, 79:469–480, 1950.

[171] W. Hergert and T. Wriedt. *The Mie Theory:Basics and Applications*. Springer, Berlin, 2012.

[172] C. F. Bohren and D. Huffman. *Absorption and Scattering of Light by Small Particles*. John Wiley & Sons, New York, 1983.

[173] D. J. Griffiths. *Introduction to Electrodynamics*. Prentice-Hall, New Jersey, 1981.

[174] B. A. van Tiggelen and A. Lagendijk. Resonantly induced dipole-dipole interactions in the diffusion of scalar waves. *Phys. Rev. B*, 50:16729–16732, 1994.

[175] N. Cherroret, D. Delande, and B. A. van Tiggelen. Induced dipole-dipole interactions in light diffusion from point dipoles. *Phys. Rev. A*, 94:012702, 2016.

[176] C. C. Kwong, D. Wilkowski, D. Delande, and R. Pierrat. Coherent light propagation through cold atomic clouds beyond the independent scattering approximation. *Phys. Rev. A*, 99:043806, 2019.

[177] A. Lagendijk and B. A. van Tiggelen. Resonant multiple scattering of light. *Physics Reports*, 270(3):143–215, 1996.

[178] D. S. Fisher and P. A. Lee. Relation between conductivity and transmission matrix. *Phys. Rev. B*, 23:6851–6854, 1981.

[179] J. Venermo and A. Sihvola. Dielectric polarizability of circular cylinder. *Journal of Electrostatics*, 63(2):101–117, 2005.

[180] N. Bloembergen, E. M. Purcell, and R. V. Pound. Relaxation Effects in Nuclear Magnetic Resonance Absorption. *Phys. Rev.*, 73:679–712, 1948.

[181] E. L. Hahn. Nuclear Induction Due to Free Larmor Precession. *Phys. Rev.*, 77:297–298, 1950.

[182] K. Toyoda, Y. Takahashi, K. Ishikawa, and T. Yabuzaki. Optical free-induction decay of laser-cooled ^{85}Rb. *Phys. Rev. A*, 56:1564–1568, 1997.

[183] S. Zamith, J. Degert, S. Stock, B. de Beauvoir, V. Blanchet, M. A. Bouchene, and B. Girard. Observation of Coherent Transients in Ultrashort Chirped Excitation of an Undamped Two-Level System. *Phys. Rev. Lett.*, 87:033001, 2001.

[184] R. G. Brewer and R. L. Shoemaker. Optical Free Induction Decay. *Phys. Rev. A*, 6:2001–2007, 1972.

[185] R. G. Brewer and A. Z. Genack. Optical Coherent Transients by Laser Frequency Switching. *Phys. Rev. Lett.*, 36:959–962, 1976.

[186] P. Helistö, E. Ikonen, T. Katila, and K. Riski. Coherent Transient Effects in Mössbauer Spectroscopy. *Phys. Rev. Lett.*, 49:1209–1213, 1982.

[187] E. Ikonen, P. Helistö, T. Katila, and K. Riski. Coherent transient effects due to phase modulation of recoilless γ radiation. *Phys. Rev. A*, 32:2298–2315, 1985.

[188] M. Chalony, R. Pierrat, D. Delande, and D. Wilkowski. Coherent flash of light emitted by a cold atomic cloud. *Phys. Rev. A*, 84:011401, 2011.

[189] C. C. Kwong, T. Yang, M. S. Pramod, K. Pandey, D. Delande, R. Pierrat, and D. Wilkowski. Cooperative Emission of a Coherent Superflash of Light. *Phys. Rev. Lett.*, 113:223601, 2014.

[190] C. C. Kwong, T. Yang, D. Delande, R. Pierrat, and D. Wilkowski. Cooperative Emission of a Pulse Train in an Optically Thick Scattering Medium. *Phys. Rev. Lett.*, 115:223601, 2015.

[191] R. H. Dicke. Coherence in Spontaneous Radiation Processes. *Phys. Rev.*, 93:99–110, 1954.

[192] M. Gross and S. Haroche. Superradiance: An essay on the theory of collective spontaneous emission. *Physics Reports*, 93(5):301–396, 1982.

[193] D. Meiser, J. Ye, D. R. Carlson, and M. J. Holland. Prospects for a Millihertz-Linewidth Laser. *Phys. Rev. Lett.*, 102:163601, 2009.

[194] J. G. Bohnet, Z. Chen, J. M. Weiner, D. Meiser, M. J. Holland, and J. K. Thompson. A steady-state superradiant laser with less than one intracavity photon. *Nature*, 484:78–81, 2012.

[195] M. O. Scully and A. A. Svidzinsky. The Super of Superradiance. *Science*, 325(5947):1510–1511, 2009.

[196] C. A. Müller and C. Miniatura. Multiple scattering of light by atoms with internal degeneracy. *Journal of Physics A: Mathematical and General*, 35(47):10163, 2002.

[197] G. G. Stokes. On the Composition and Resolution of Streams of Polarized Light from different Sources. *Transactions of the Cambridge Philosophical Society*, 9:399, 1851.

[198] S. J. van Enk and G. Nienhuis. Eigenfunction description of laser beams and orbital angular momentum of light. *Optics Communications*, 94(1):147–158, 1992.

[199] A. T. O'Neil, I. MacVicar, L. Allen, and M. J. Padgett. Intrinsic and Extrinsic Nature of the Orbital Angular Momentum of a Light Beam. *Phys. Rev. Lett.*, 88:053601, 2002.

[200] L. Allen, M. W. Beijersbergen, R. J. C. Spreeuw, and J. P. Woerdman. Orbital angular momentum of light and the transformation of Laguerre-Gaussian laser modes. *Phys. Rev. A*, 45:8185–8189, 1992.

[201] M. Abramowitz. *Handbook of Mathematical Functions, With Formulas, Graphs, and Mathematical Tables*. Dover Publications, Inc., USA, 1974.